Measurements of Inclusive and Differential Cross-sections of Single-top t-channel Production at $\sqrt{s} = 8$ TeV with the CMS Detector

By

Wajid Ali Khan

SUBMITTED IN PARTIAL FULFILLMENT OF THE
REQUIREMENTS FOR THE DEGREE OF
DOCTOR OF PHILOSOPHY
AT
DEPARTMENT OF PHYSICS
QUAID-E-AZAM UNIVERSITY, ISLAMABAD
January 2015

Certificate

The undersigned hereby certify that they have read and recommend to the Department of Physics for acceptance of thesis entitled "**Measurements of Inclusive and Differential Cross-sections of Single-top *t*-channel Production at $\sqrt{s}$ = 8 TeV with the CMS Detector**" by **Wajid Ali Khan** in partial fulfillment of the requirements for the degree of **Doctor of Philosophy**.

Supervisor:

Prof. Dr. Hafeez Hoorani
Director General
National Center For Physics
Islamabad, Pakistan

Submitted Through:

Prof. Dr. Arshad Majeed Mirza
Chairman
Department of Physics
Quaid-e-Azam University
Islamabad, Pakistan

QUAID-E-AZAM UNIVERSITY

Date: **January 2015**

Author: **Wajid Ali Khan**

Title: **Measurements of Inclusive and Differential Cross-sections of Single-top *t*-channel Production at $\sqrt{s} = 8$ TeV with the CMS Detector**

Department: **Physics**

Degree: **Ph.D** Convocation: **January** Year: **2015**

Permission is herewith granted to Quaid-e-Azam University to circulate and to have copied for non-commercial purposes, at its discretion, the above title upon the request of individuals or institutions.

Signature of Author

To my wonderful father (late), sweet mother and loving wife ...

Table of Contents

List of Tables

List of Figures

List of Acronyms

CERN	**E**uropean **O**rganization for **N**uclear **R**esearch
CMS	**C**ompact **M**uon **S**olenoid
LHC	**L**arge **H**adron **C**ollider
CMS	**C**ompact **M**uon **S**olenoid
ATLAS	**A** **T**oroidal LHC **A**pparatu**S**
LHC-*b*	**L**arge **H**adron **C**ollider **b**eauty
ALICE	**A** **L**arge **I**on **C**ollider **E**xperiment
FNAL	**F**ermi **N**ational **A**ccelerator **L**aboratory
LEP	**L**arge **E**lectron **P**ositron Collider
CDF	**C**ollider **D**etector at **F**ermilab
DØ	**D**etector **Z**ero at Fermilab
RPC	**R**esistive **P**late **C**hambers
DT	**D**rift **T**ube
L1T	**L**evel-1 **T**rigger
HLT	**H**igher **L**evel **T**rigger
CSC	**C**athode **S**tripe **C**hamber
POG	**P**hysics **O**bject **G**roup
PAG	**P**hysics **A**nalysis **G**roup
PAS	**P**hysics **A**nalysis **S**ummary
TeV/GeV	**T**era/**G**iga **E**lectron **V**olts
SM	**S**tandard **M**odel
QED	**Q**uantum **E**lectro **D**ynamics

QCD	**Q**uantum **C**hromo **D**ynamics
CKM	**C**abibbo-**K**obayashi-**M**askawa
LO	**L**eading **O**rder
NLO	**N**ext to **L**eading **O**rder
NNLO	**N**ext to **N**ext to **L**eading **O**rder
NNLL	**N**ext to **N**ext to **L**eading **L**ogarithms
FCNC	**F**lavour **C**hanging **N**eutral **C**urrent
SUSY	**SU**per **SY**mmetry
EWSB	**E**lectro **W**eak **S**ymmetry **B**reaking
PDF	**P**arton **D**ensity **F**unction
MET	**M**issing **T**ransverse **E**nergy
p_{T}	Transverse Momentum
PF	**P**article-**F**low Algorithm
SV	**S**econdary **V**ertex
CSV	**C**ombined **S**econdary **V**ertex

زمانۂ حاضر کا انسان

عشق ناپید و خرد می گزدش صُورتِ مار
عقل کو تابعِ فرمانِ نظر کر نہ سکا

ڈُھونڈنے والا ستاروں کی گزر گاہوں کا
اپنے افکار کی دنیا میں سفر کر نہ سکا

اپنی حِکمت کے خم و پیچ میں اُلجھا ایسا
آج تک فیصلہ نفع و ضرر کر نہ سکا

جس نے سورج کی شُعاوں کو گرفتار کیا
زندگی کی شبِ تاریک سحرَ کر نہ سکا!

Sir Dr. Allama Muhammad Iqbal (1877 – 1938)
Zarb-e-Kaleem

Modern Man

Love fled, Mind stung him like a snake,
He could not force it to visions will;

He tracked the orbits of the stars,
Yet could not travel his own thoughts world;

Entangled in the labyrinth of his science,
Lost counts of good and ill;

Took captive the sun's rays,
Yet no sunrise on life's thick night unfurled.

Acknowledgements

I am grateful to my advisors Prof. Dr. Hafeez Hoorani and Prof. Dr. Thomas Müller for their constant support and help throught out the duration of Ph.D studies. They imparted their knowledge and provided many useful suggestions and friendly encouragements. They are and they will be the source of inspiration for me. I am thankful to my colleages at NCP and many colleages at Karlsruhe Institute of Technology (KIT) Karlsruhe, Germany. I would like to express my profound thanks to Dr. Jeanine Wagner-Kuhr, Dr. Thorsten Chwalek and Steffen for their help, suggestions and guidance. Steffen was always there to answer my stupid questions and helping me out. I will always remember eating "Donar" with Steffen, disscussing various issues related to our daily life and the term "Donar Police" coined by Dr. Thorsten Chwalek. It was really a great time with lots of nice memories.

I am grateful to chairperson, Department of Physics, Quaid-e-Azam University, Islamabad for allowing me to do research at National Center for Physics, Islamabad. I am grateful to Prof. Dr. Thomas Müller for giving me opportunity and the efforts he made for me to come and work with his group at Karlsruhe Institute of Technology (KIT) to complete the Ph.D studies. I am thankful to all of my teachers who taught me, their knowledge, efforts and guidance helped me alot to change my life from worse to bad. They made an ever lasting impact on my personality, thoughts and helped me to develop my aptitude and attitude towards physics.

Above all, I don't have any words for my sweet mother for her eternal love, affections, prayers and all the hardships she faced for my education, I wish my father was alive, I can feel the gap been created in my life because of his absence, I really miss him. Brothers and sisters for their support and care through out my education. How can I forget my loving wife, without her help and support this manuscript would have never came into existance, I am sorry for being so careless, I was not able to keep a balance between you and research, please accept my appologies. *I contributed with "heart and soul"!*

Wajid Ali Khan

Abstract

The Large Hadron Collider (LHC) is a top-quark factory, the large number of the top-quarks are produced which can be used to measure various properties of the top-quark with a much higher precision. This thesis describes the single-top-quark t-channel inclusive and differential cross-section measurements in a proton-proton collisions at a center-of-mass energy of 8 TeV using lepton+jets in the final state. The results for the inclusive cross-section and the differential cross-section measurements are based on a data set which corresponds to an integrated luminosity of 19.7 fb^{-1} recorded with the CMS detector at the LHC. The measured inclusive production cross-section of the t-channel single-top-quark is:

$$\sigma_{t-\mathrm{ch.}} = 83.6 \pm 2.3\,(\mathrm{stat.}) \pm 7.4\,(\mathrm{syst.})\,\mathrm{pb}.$$

The measured single t and $\bar{\mathrm{t}}$ production cross-sections in the t-channel is:

$$\sigma_{t-\mathrm{ch.}}(\mathrm{t}) = 53.8 \pm 1.5\,(\mathrm{stat.}) \pm 4.4\,(\mathrm{syst.})\,\mathrm{pb},$$
$$\sigma_{t-\mathrm{ch.}}(\bar{\mathrm{t}}) = 27.6 \pm 1.3\,(\mathrm{stat.}) \pm 3.7\,(\mathrm{syst.})\,\mathrm{pb}.$$

The measured cross-section ratio, top-quark(t) and the anti-top-quark($\bar{\mathrm{t}}$), when separated on the basis of charged lepton at $\sqrt{s}$ = 8 TeV is:

$$\mathrm{R}_{t-\mathrm{ch.}} = \sigma_{t-\mathrm{ch.}}(\mathrm{t})/\sigma_{t-\mathrm{ch.}}(\bar{\mathrm{t}}) = 1.95 \pm 0.10\,(\mathrm{stat.}) \pm 0.19\,(\mathrm{syst.}),$$

and the measurement of CKM matrix element,

$$|f_{\mathrm{Lv}} V_{\mathrm{tb}}| = 0.979 \pm 0.045\,(\mathrm{exp.}) \pm 0.016\,(\mathrm{theo.}),$$

comes out to be in good agreement with the standard model predictions. The single-top-quark differential cross-section measurements as a function of the top-quark p_{T} and $|y|$ are performed. The differential cross-section measurements are essential for the comparison of the QCD predictions in the standard model. The measured normalized differential cross-sections come out to be in a remarkable agreement with the various theoretical predictions.

Introduction

Particle physics is a field of science which investigates the basic principles behind matter and its interaction. The recent developments in the field of science and technology has made it possible to build the high energy particle accelerators and then use them as a tool to look deep into the mysteries behind the matter, its interactions and the creation of new particles at higher and higher energies.

The world biggest particle accelerator, The LHC, is situated at CERN near France-Swiss border, began operating at the end of year 2008 by smashing the two proton beams at a $\sqrt{s} = 7\,\mathrm{TeV}$. The LHC will be operating later at a higher center-of-mass energy of 14 TeV with an instantaneous luminosity of $10^{34}\,\mathrm{cm}^{2}\,\mathrm{s}^{-1}$. We have seen, from the physics results derived from the data delivered by LHC at $\sqrt{s} = 7, 8\,\mathrm{TeV}$, that it has done quite a marvelous job by reproducing quite a number of different physical results from various previous experiments at TeV energy scale.

The first experimental evidence of the top-quark was made by the CDF and DØ experiments at the FNAL in which proton and anti-proton beams were brought into collisions [1]. Although, the top-quark was discovered about 20 years ago but its properties are still investigated at higher precision. The existence of the top-quark was made by Kobayashi and Maskawa in 1973 [2, 3] along with a quark of lighter mass known as b-quark which was later discovered in the year 1977. There are two modes for the production of the top-quark, the strong interaction and electroweak interaction. In the strong interaction the top-quark are produced in pairs and in electroweak interaction we have have either a top or anti top-quark. The single top-quark can be produced in three possible modes, i.e., via t-channel, s-channel and tW in association with W-boson. The t-channel has the largest production cross-section. The first experimental evidence for the top-quark was seen in pair production while in the year 2009 the CDF and DØ collaboration gave the first experimental results of the single-top-quark [4]. The LHC started running in the year in 2010, the higher center-of-mass energy available for colliding partons makes the LHC a top-quark factory by producing about 1 $\mathrm{t\bar{t}}$ pair event per second and about 30 single-top-quark events per minute. During the early running of the LHC, there was enough early data delivered by LHC to ATLAS [5] and CMS [6] experiments to re-discover the top-quark pair production. Similarly the electroweak signatures of the single-top-quark were also seen by the ATLAS and the CMS experiments [7, 8].

This thesis consists of the inclusive production cross-section (CMS-TOP-PAS-12-038) and the differential cross-section (CMS-TOP-PAS-13-004) measurements of the single-top-quark in the t-channel with lepton+jets (μ/e) in the final state using the data collected by the CMS experiment in the year 2012 at a $\sqrt{s} = 8\,\mathrm{TeV}$. The measurement of the inclusive t-channel production cross-section and the ratio of cross-sections, (t to $\bar{\mathrm{t}}$), comes out to be in a very good agreement with the standard model predictions [9]. The natural step forward would be to study the normalized differential cross-section as a function of some kinematic variables related to the single-top-quark. The differential cross-section measurement helps us to compare the various theoretical models with the measurement. In this thesis, the normalized differential cross-section as a function of the top-quark p_{T} and $|y|$ are presented. The various models implemented in POWHEG, aMC@NLO and CompHEP are compared with the CMS data [10].

The top-quark is the most heaviest quark in the three known quark families. Due to the large mass of the top-quark $173.1 \pm 1.1\,\mathrm{GeV}$[1] [11] it decays before it can form a bound state, thus the single-top-quark processes can be used to study the properties of bare quark. A study of the single-top-quark production modes and their properties are very interesting because the production takes place via exchange of W-boson and this gives us an opportunity to study the Wtb vertex. The production cross-section is directly proportional to CKM matrix element $|V_{\mathrm{tb}}|^{2}$ and it gives us a direct access to measure the CKM matrix element V_{tb}. The standard model of elementary particle predicts the value of $V_{\mathrm{tb}} \approx 1$ and any deviation of V_{tb} from unity will hint towards a new physics or physics beyond the standard model, e.g., 4^{th} generation of quarks. The study of the single-top-quark will give us a chance to probe into anomalous couplings and FCNC. The single-top-quark production also serves as a major backgrounds to Higgs and SUSY searches. Moreover, the number of top-quarks produced is greater than the number of anti-top produced due to the valance quark distribution in colliding partons. An interesting quantity in this regard is the ratio of cross-section, t to $\bar{\mathrm{t}}$. This quantity depends on the PDF of valance quarks and from this measurement PDF fitters will have an insight to constrain the parton density functions.

The structure of thesis is as follows: The thesis starts with an introduction to the standard model of particle physics, motivations to study the top-quark physics and the main results of the thesis. Chapter 1 gives a brief history, production and properties of the top-quarks. Followed by a description of the LHC and the CMS detector in Chapter 2. In Chapter 3, the event generation, simulation and reconstruction of the single-top-quark is described and a comparison between the simulations from CompHEP and PowHEG are given, also an introduction to the tools used during the analysis are presented. Chapter 4 describes the selection performed on lepton, jets, $E\!\!\!/_{\mathrm{T}}$, m_{T} which are used for the reconstruction of the top-quark are presented. Chapter 5 describes the results on the inclusive cross-section measurements, ratio of cross-sections and the systematics uncertainties quoted on the measurement. Chapter 6 describes the measurement of normalized differential cross-section as a function of the top-quark p_{T} and $|y|$ which is based on the neural network separation of signal from background processes. In Chapter 7, the results obtained for the inclusive and differential cross-sections are listed with summary and outlook to future developments are presented in the final section.

[1]Natural units ($\hbar$ = c = 1), are used else where.

Chapter 1

Theoretical Perspective

1.1 The Standard Model of Elementary Particles

The standard model [12–22] is a name given to a mathematical framework based on quantum mechanics and relativity that describes all the known fermions and all the forces except gravity. The theory was established in early 70's and with the passage of time, the theory has done really well by explaining many interesting experimental results and there are large number of phenomenon which are predicted by this theoretical frame work and have experimentally verified. It provides an elegant way to describe the particles and the fundamental interactions among them. It describes how the elementary particles interact with each other. The interaction can be described by a Lagrangian, which is a function that describes the dynamics of the theory behind the standard model of particle physics. Irrespective of the fact the standard model of particle physics explains many phenomenon beautifully but the theory does not incorporate gravity nor it explain open questions like nature of dark matter, dark energy, neutrino oscillations and matter anti-matter asymmetry. It also does not explain why there are only three generations of quarks and lepton which such a huge differences in their mass. The standard model of particles physics will serve as a basis for building more exotic models such as Super-Symmetry, String Theory, Grand Unification Theories and the Theory of Large Extra Dimensions.

The foundation and formulation of the standard model was done in 1960's and 1970's in a way to combine the combine the electromagnetic and weak interactions. According to the standard model all the elementary particle gain masses via Higgs mechanism, these include the mass of W, Z-bosons and all the fermions. With the discovery of W and Z-bosons at CERN in 1981 the electroweak theory became a widely accepted theory and their masses were found to be in very good agreement with the standard model predictions. Also, the discovery of Higgs boson in 2012 by ATLAS and CMS collaborations is an another success story of the standard model of particle physics.

In the standard model there are two categories in which the particles can be placed, fermions and bosons. Fermions are the constituents of matter and have a half-integer spin, e.g., $\frac{1}{2}$. The bosons are the carrier of the forces and have integer spin, e.g., 1.

Table 1.1: The fundamental forces and their characteristics

Force	Couples	Rel. Strength	Force-Carrier
Strong force	force between protons and neutrons inside nucleus	100	gluon
Electromagnetic force	force between charges (electricity and magnetism)	1	photon
Weak force	involved in radioactive decay	10^{-11}	$W^{\pm}$, Z
Gravitational force	force between masses	10^{-36}	graviton

Fundamental Forces and Interactions

In the present world where we live in, there are four types of fundamental forces present namely the gravitational force, the electromagnetic force, the weak force and the strong force. Out of these four fundamental forces, three of them have been very well incorporated in the standard model of particle physics and are well tested, where as the gravitational force, described by the general theory of relativity, has not been included in the standard model of particle physics. Since the gravitational force becomes more and more important as the mass of interacting bodies increases and the gravitational effects become more and more effective. Where as for the other three forces they dominate on nuclear scale and therefore we can neglect their effect on large scale masses.

The mediator of the force between two masses has not yet been observed but is given a name Graviton. The Graviton is supposed to be a spin = 2 particle. Interactions between the electrically charged particles are described by the QED [23–28]. In QED the mediator of electromagnetic interaction is a mass-less photon and it is due to the zero mass of the photon which makes the range of electromagnetic force infinite. The theory which describes the interaction between the quarks and gluon is known as QCD. The QED and QCD are well verified and tested in various experiments and the experimental results are in well agreement to the predictions made by them.

In the standard model the mediator of electroweak force are two gauge bosons, the W-boson and the Z-bosons which are quite massive as compared to the mass of photon or gluon for the QED and QCD. It is due the large mass of these mediators which limits the range of weak force to the dimensions of a nucleus. This force is also known as Weak Nuclear Force. Due to this weak force the quarks change their flavor from one to anther type with the exchange of W-boson, as a result the weak interaction are not identical to the mass eigenstates. The force carrying bosons gluons, photons, W and Z-bosons have spin = 1, since they represent a vectorial fields, where as the Higgs boson has a spin = 0 and it corresponds to a scaler field. As discussed earlier, the gravition of spin = 2 particle corresponds to a tenorial field.

Fermions

The particles obeying the Pauli exclusion principal are known as fermions, i.e., two particles cannot share the same quantum mechanical state. They have half integer spin s = $\frac{1}{2}$ and follow the Fermi-Dirac statistics. According to the standard model of particle

Table 1.2: The three generations of the quarks and leptons with their mass, charge $e = 1.602176487 \times 10^{-19}$C. The uncertainties are quoted on the muon and electron masses are of the order of 10^{-8} and 10^{-6} MeV.

Generation	Quark Flavor	Fermion	Symbol	Charge	Mass [MeV]
	up	quark	u	$+\frac{2}{3}$	1.5 - 3.3
Ist	down	quark	d	$-\frac{1}{3}$	3.5 - 6.0
	electron	lepton	e	-1	0.511
	e-neutrino	lepton	ν_e	0	$< 2\times10^{-6}$
	charm	quark	c	$+\frac{2}{3}$	$(1.27\ ^{+0.07}_{-0.11})\times 10^3$
2nd	strange	quark	s	$-\frac{1}{3}$	$104\ ^{+26}_{-34}$
	muon	lepton	μ	-1	105.658
	μ-neutrino	lepton	ν_μ	0	< 0.190
	top	quark	t	$+\frac{2}{3}$	$(173.1\pm1.3)\times 10^3$
3rd	bottom	quark	b	$-\frac{1}{3}$	$(4.20^{+0.17}_{-0.07})\times10^3$
	tau	lepton	τ	-1	1776.84 ± 0.17
	τ-neutrino	lepton	ν_τ	0	< 18.2

physics there are twelve elementary particles. The six leptons and six quarks which are categorized in three families. Each family consist of a up quark, down quark, a charged lepton and the neutrino associated with the charged lepton. The standard model predicts only three lepton and quark family. Every member of the quark or lepton family has the corresponding anti fermion which has the same properties but opposite charge. It has been observed that all the visible matter is composed of particles belonging to first family. The properties of leptons and quarks are summarized in Table 1.2. The higher generations of fermions are produced in upper atmosphere during the collisions of high energy cosmic rays with the molecules present in the atmosphere or they can be produced in the collider experiments. The masses of fermions increases as one moves towards higher generations. The particles which have larger mass decays into particles which are lighter in mass. According to the standard model the neutrinos are massless. Several experiments have observed that the neutrinos can change the flavor and therefore they have mass [29–31]. This requires an extension [32,33] of the standard model of particle physics by including all the new results. Bare quarks do not exist. They always form a bound state with other quarks. These bound states are known as Hadrons.

The hadrons can be further classified into baryons which consists of three quarks, each quark is of different color. The mesons which consist of quark-anti quark pair and each quark is of different color, as a result mesons are also colorless. In order to satisfy the Pauli exclusion principal quarks are given a quantum number which is known as color quantum number (red, blue, green) [34–36]. When ever we try to separate a quark-anti-quark pair a sort of new color flux tube is formed between the two separating quarks. Now the energy stored in the flux tube is sufficient to produce a quark-anti quark pair. This process continues until all the quarks pair-up to form jets of hadrons. All hadrons are colorless. This is also known as color confinement.

Bosons

The bosons do not obey the Pauli exclusion principal and follow the Bose-Einstein statistics. They have integral spin s = 0, 1, 2. Bosons are force carriers and each interaction mediates its force via gauge bosons. The classical example is the interaction between two electrons and force is mediated via a photon. The photon is a massless and charge less spin-1 gauge boson. Where as the electroweak interaction is mediated via W, Z-gauge bosons. The W-boson has a charge ± 1, where as the Z-boson is neutral. Unlike the photon these gauge bosons are not massless. The W-boson has a mass of 80.398 ± 0.0025 GeV and Z-boson has a mass of 91.188 ± 0.002 GeV. Gluons which are the mediators of strong interactions are massless and have color charge and this results in a eight different possible combinations. The four forces and the properties of the mediators of these forces are given in Table 1.3.

Table 1.3: The three standard model forces, gauge bosons, masses and their charges [37].

Force	Mediator	Symbol	Charge	Mass[GeV]
Strong	8 gluons	g	0	0
Electromagnetic	photon	γ	0	0
Weak	W	$W^{\pm}$	± 1	80.398 ± 0.003
Weak	Z	Z^0	0	91.188 ± 0.002

1.2 Electroweak Decay

One of the four fundamental forces in nature is the electroweak force. It has a unique property that particles change their flavor via exchange of W-bosons. As a result the eigenstates are identical with the mass eigen states of electroweak interaction. The CKM matrix is a unitary 3×3 matrix which gives the probability of transitions of different mass eigen states to the weak eigen states [2,3]. The CKM matrix is given by:

$$\begin{pmatrix} d' \\ s' \\ b' \end{pmatrix} = \begin{pmatrix} V_{ud} & V_{us} & V_{ub} \\ V_{cd} & V_{cs} & V_{cb} \\ V_{td} & V_{ts} & V_{tb} \end{pmatrix} \begin{pmatrix} d \\ s \\ b \end{pmatrix}. \tag{1.2.1}$$

The CKM matrix in general describes that coupling of two quarks, e.g., t and a b-quarks to a W-boson. The values of the matrix elements keeping the unitarity of CKM are given by [38]:

$$V_{\mathrm{CKM}} = \begin{pmatrix} 0.97428 \pm 0.00015 & 0.2253 \pm 0.0007 & 0.00347^{+0.00016}_{-0.00012} \\ 0.2252 \pm 0.0007 & 0.97345^{+0.00015}_{-0.00016} & 0.0410^{+0.0011}_{-0.0007} \\ 0.00862^{+0.00026}_{-0.00020} & 0.0403^{+0.0011}_{-0.0007} & 0.999152^{+0.000030}_{-0.000045} \end{pmatrix}. \tag{1.2.2}$$

The CKM matrix clearly explains that a quark can decay by changing its flavor to another family, but this probability is very small, where as the probability of a quark to decay to its own family is maximum. Thus for example the top-quark decaying to a b-quark is most probable. The decay of the top is an electroweak decay t $\rightarrow$Wb and in weak decays the 'parity' is not conserved. Parity is a discrete transformation such that $\hat{p}\psi \rightarrow -\psi$.

The law of parity conservation states that the physics should remain unchanged upon the reversal of space axis. The strong and electromagnetic interaction respect the law of parity conservation but weak interaction does not obey this law of parity conservation. Any spinor can be written as the super position of left hand and right hand chiral states:

$$\psi = \psi_{\mathrm{L}} + \psi_{\mathrm{R}}. \tag{1.2.3}$$

The chiral states are those states which cannot be mapped onto one another by any linear or rotational transformation. In terms of projection operators the wave function can be written as:

$$\psi = \mathrm{P_R}\psi + \mathrm{P_L}\psi, \qquad \text{where } \mathrm{P_R} = 1/2(1+\gamma^5),\ \mathrm{P_R} = 1/2(1+\gamma^5). \tag{1.2.4}$$

In QED/QCD the interaction vertex is of the form $j_\alpha \propto \bar{u}_\alpha \gamma^\mu u_\alpha$. However in the most general form of the interaction between a fermion and boson is a liner combination of bilinear covariants. For an interaction corresponding to the exchange of a boson or spin-1 particle the possible linear combination of bilinear co-variants is a vector and an axial-vector. The vector plus axial form of the weak interaction has been ruled out by various experiments [39]. In general vector-axial vertex is of the form $j^\mu \propto \bar{u}_{\nu_e}(\gamma^\mu - \gamma^\mu\gamma^5)u_e$ where γ^μ denotes the Dirac matrices and γ^5 is the Chirality operator. In the standard model the W-boson couples only to left hand component of particles and left hand component of anti-particles. In the ultra relativistic limit 'Chiral States' corresponds to the 'Helicity States'. The helicity is the projection of spin onto to its momentum vector, mathematically can be written as:

$$h = \vec{\sigma} \cdot \hat{p}, \quad \text{with } \hat{p} = \frac{\vec{p}}{\mid \vec{p} \mid}. \tag{1.2.5}$$

The helicity operator has the eigen values ± 1. The helicity is positive when the spin and momentum vectors are in the same direction and negative when spin and momentum vector are in opposite direction. The two modes can be termed as right handed and left handed polarization. The Longitudinal polarization takes place when the spin of the particle is perpendicular to its direction of motion. These states are not the eigen states of the helicity operator. The helicity is an experimentally measurable quantity and it shows the angular distribution in the decay of particles while the chirality is a quantum number which can not be measured directly in a detector.

1.3 Top-quark Physics

The first experimental signature of the top-quark was made by CDF and DØ experiments in a proton anti proton collisions [1]. Ever since the top-quark has been discovered, its properties have been studied in great detail and with high precision. The mass of the top-quark is the most interesting quantity and the most recent value obtained from the CDF and DØ combination which yields a value of $173.1 \pm 1.3\,\mathrm{GeV}$ [11]. It is the most heaviest known quark discovered so far. The mass of the top-quark and Rhenium atom (atomic number Z = 75) are of the same size or 40 times the mass of b-quark. Due to the large mass, it was also considered once that it might not be one of the isospin partner of the b-quark. As the top-quark is also heavier than the W-boson so it can decay into $t \to$ Wb, and its decay to its isospin partner the b-quark has almost 100% branching ratio. From this branching ratio it may be inferred that, the standard model which assumes that there are only three quark family, the Cabibbo Kobayashi Maskawa matrix element (CKM) $|V_{tb}|$ is close to one. The top's heavy mass opens up a large phase space for its decay to heavy states, such as Wb, Zq, H $^{0,\pm}$q etc. Also the mass of the top-quark is close to electroweak symmetry scale ($v \approx 246\,\mathrm{GeV}$), v is the vacuum expectation value. The Yukawa coupling to Higgs field ($g_Y = \frac{m_T}{v/\sqrt{2}}$) is close to one, it could play an important role in electroweak symmetry breaking [40, 41] or giving rise to some alternative mechanisms through which elementary particles may acquire mass. It can be assumed that any new physics in Electroweak Symmetry Breaking (EWSB), models would be coupled preferentially to the top-quark. Since the top-quark is quite massive as compared to the other member of the quark family one can argue whether it is an ordinary quark or an exotic?

Due to the large mass, the lifetime of the top-quark is really very short. It decays into other particles before it can form a QCD bound state. The time scale is very short as compared to the the typical time scale needed for the formation of QCD bound states. As a result, the top-quark decays before hadronization takes place and therefore offers an opportunity which one can use to study the properties of a single quark, passing its spin information on to its decay products. Thus it is possible to measure a physical observable that depends on the top-quark spin, providing a unique opportunity to test standard model predictions and physics beyond the standard model searches.

Table 1.4: A historical overview of the top-quark searches in various experiments at $e^+e^-$and $p\overline{p}$.

Year	Collider	Particles	Limit on m_T [GeV]	References
1979-84	PETRA (DESY)	e^+e^-	> 23.3	[42–55]
1987-90	TRISTAN (KEK)	e^+e^-	> 30.2	[56–60]
1989-90	SLC (SLAC), LEP (CERN	e^+e^-	> 45.8	[61–64]
1984	Sp$\overline{p}$S (CERN)	$p\overline{p}$	> 45.0	[65]
1990	Sp$\overline{p}$S (CERN)	$p\overline{p}$	> 69.0	[66,67]
1991	TEVATRON (FNAL)	$p\overline{p}$	> 77.0	[68–70]
1992	TEVATRON	$p\overline{p}$	> 91.0	[71,72]
1994	TEVATRON	$p\overline{p}$	> 131	[73,74]
1995	TEVATRON	$p\overline{p}$	$174 \pm 10^{+13}_{-12}$	[1]
1995	TEVATRON	$p\overline{p}$	$174^{+19}_{-21} \pm 22$	[75]

1.4 Top-quark Pair Production

In the following section, the theoretical aspects for production of the top-quark pair production will be discussed briefly. The detailed theoretical discussions on the top-quark pair production can be found in the Refs. [76–78]. In the standard model the dominant production mechanism of the top-quark is via strong interaction. The top-quark is so heavy that the mass of the top-quark becomes larger than the Λ_{QCD}. Mathematically the total inclusive top pair production initiated by pp or p$\overline{\mathrm{p}}$ at a center-of-mass energy, can be written as [79,80]:

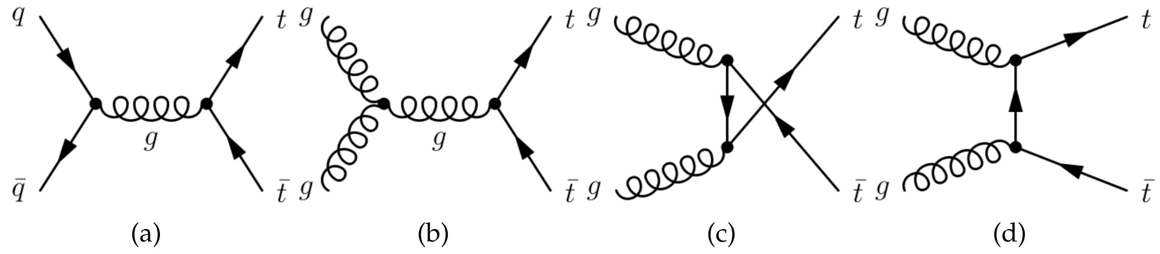

Figure 1.1: Leading order Feynman diagrams of the t$\bar{\mathrm{t}}$ pair production at hadron colliders (a) represents the top quark pair production via quark anti quark annihilation and (b) - (d) represents the top pair production via gluon fusion.

$$\sigma_{pp\to\mathrm{t\bar{t}}}(s,m_{\mathrm{T}}) = \sum_{i,j=q,\bar{q},g} \int \mathrm{d}x_i \mathrm{d}x_j f_i(x_i,\mu_f^2) f_j(x_j,\mu_f^2) \times \hat{\sigma}_{ij\to\mathrm{t\bar{t}}}(\rho, m_{\mathrm{T}}^2, \mu_f, \mu_r^2, \alpha_s), \qquad (1.4.1)$$

where the summation indices i and j presented in the equation 1.4.1 runs over all the partons qq, gg, qg. The x_i, x_j are parton momentum fractions with respect to the colliding quarks, $f_i(x_i,\mu_f^2), f_j(x_j,\mu_f^2)$ are the parton density functions (PDF), μ_f, μ_r are the factorization and re-normalization scales respectively, α_s is the strong coupling constant, $\hat{s} \approx x_i x_j s$ is the partonic center-of-mass energy and $\rho = 4m_{\mathrm{T}}^2/\sqrt{\hat{s}}$. The minimum amount of energy required to produce t$\bar{\mathrm{t}}$ at rest is $\hat{s} = 4m_{\mathrm{T}}^2$ therefore the $x_i x_j = \hat{s}/s \geq 4m_{\mathrm{T}}^2/s$. From the Fig. 1.2 the probability of finding a given quark momentum fraction x decreases by increasing the value of x. The typical value of $x_i x_j$ can be inferred by setting $x_i \approx x_j \equiv x$ gives the values for x where the t$\bar{\mathrm{t}}$ production takes place:

$$\begin{aligned} x &= 2m_{\mathrm{T}}/\sqrt{s} && (1.4.2) \\ &= 0.190 \qquad \text{Tevatron } \sqrt{\mathrm{s}} = 1.80\,\mathrm{TeV}, \\ &= 0.180 \qquad \text{Tevatron } \sqrt{\mathrm{s}} = 1.96\,\mathrm{TeV}, \\ &= 0.035 \qquad \text{LHC } \sqrt{\mathrm{s}} = 10\,\mathrm{TeV}, \\ &= 0.025 \qquad \text{LHC } \sqrt{\mathrm{s}} = 14\,\mathrm{TeV}. \end{aligned}$$

For the typical values of x in case of Tevatron the parton density function for the valance quarks (u,d) is much larger than that of gluon see Fig. 1.2. This explains the fact why the quark-anti quark dominates the t$\bar{\mathrm{t}}$ production at Tevatron, where as for the typical values of x for LHC energies the gluon parton density function is larger than the valance quarks parton density function. Consequently the t$\bar{\mathrm{t}}$ production via gluon fusion dominates at LHC energies. The cross-sections for the hard parton-parton process can be calculated by applying Feynman rules to the diagrams shown in Fig. 1.1. The leading order differential cross-section for the top-quark pair production via quark anti quark annihilation is given by:

$$\frac{\mathrm{d}\hat{\sigma}}{\mathrm{d}\hat{t}}(q\bar{q} \to \mathrm{t\bar{t}}) = \frac{4\pi\alpha_s^2}{9\hat{s}^4}\left[(m_\mathrm{T}^2 - \hat{t})^2 + (m_\mathrm{T}^2 - \hat{u})^2 + 2m_\mathrm{T}^2\hat{s}\right]. \tag{1.4.3}$$

Similarly the leading order $\mathrm{t\bar{t}}$ pair differential cross-section via gluon fusion is given by:

$$\begin{aligned}\frac{\mathrm{d}\hat{\sigma}}{\mathrm{d}\hat{t}}(gg \to \mathrm{t\bar{t}}) = \frac{\pi\alpha_s^2}{8\hat{s}^2}\Bigg[&\frac{6(m_\mathrm{T}^2 - \hat{t})(m_\mathrm{T}^2 - \hat{u})}{s^2} - \frac{m_\mathrm{T}^2(\hat{s} - 4m_\mathrm{T}^2)}{3(m_\mathrm{T}^2 - \hat{t})(m_\mathrm{T}^2 - \hat{u})}\\ &+ \frac{4}{3}\frac{(m_\mathrm{T}^2 - \hat{t})(m_\mathrm{T}^2 - \hat{u}) - 2m_\mathrm{T}^2(m_\mathrm{T}^2 + \hat{t})}{(m_\mathrm{T}^2 - \hat{t})^2}\\ &+ \frac{4}{3}\frac{(m_\mathrm{T}^2 - \hat{t})(m_\mathrm{T}^2 - \hat{u}) - 2m_\mathrm{T}^2(m_\mathrm{T}^2 + \hat{u})}{(m_\mathrm{T}^2 - \hat{t})^2}\\ &- 3\frac{(m_\mathrm{T}^2 - \hat{t})(m_\mathrm{T}^2 - \hat{u}) - m_\mathrm{T}^2(\hat{u} - \hat{t})}{\hat{s}(m_\mathrm{T}^2 - \hat{t})^2}\\ &- 3\frac{(m_\mathrm{T}^2 - \hat{t})(m_\mathrm{T}^2 - \hat{u}) - m_\mathrm{T}^2(\hat{t} - \hat{u})}{\hat{s}(m_\mathrm{T}^2 - \hat{t})^2}\Bigg].\end{aligned} \tag{1.4.4}$$

where $\hat{s}$, $\hat{t}$ and $\hat{u}$ are the Mandelstam variables of the partonic processes.

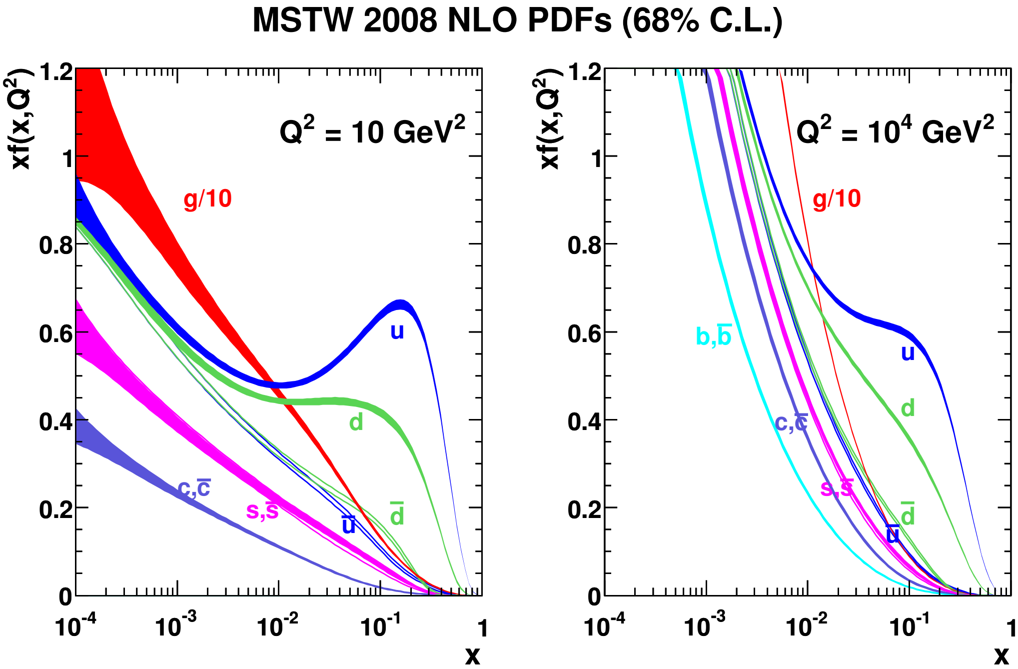

Figure 1.2: The MSTW2008 next-to-leading-order (NLO) parameterization for quark, anti-quarks and gluons momentum densities in a proton as a function of the longitudinal momentum fraction x at $\mu_f^2 = 10\,\text{GeV}$ and at $\mu_f^2 = 10{,}000\,\text{GeV}$ [81].

Table 1.5: The $\mathrm{t\bar{t}}$ production cross-section at next to the leading order, which includes the gluon re-summation corrections at various energies for Tevatron and at LHC for $m_{\mathrm{T}} = 175\,\text{GeV}$. The quoted result includes PDF uncertainty.

	$\sigma_{\text{NLO}}(\text{pb})$		$gg \to \mathrm{t\bar{t}}$	$q\bar{q} \to \mathrm{t\bar{t}}$
Tevatron($\sqrt{s} = 1.8\,\text{TeV}$, $\mathrm{p\bar{p}}$)	5.19 ± 13 %	[82]	10%	90%
	$5.24 \pm 6\%$	[83]	10%	90%
Tevatron($\sqrt{s} = 1.8\,\text{TeV}$, $\mathrm{p\bar{p}}$)	$6.10 \pm 13\%$	[82]	15%	85%
	$6.77 \pm 9\%$	[83]	15%	85%
LHC ($\sqrt{s} = 14\,\text{TeV}$, $\mathrm{p\bar{p}}$)	$833 \pm 15\%$	[84]	90%	10%

1.5 Single-top-quark Production

The single-top-quark production is mediated by electroweak interaction as compared to the $\mathrm{t\bar{t}}$ production which is mediated via strong interaction. There are three possible modes in which single-top-quark can be produced via s-channel, t-channel and tW-associated production. The tree level Feynman diagrams for the single-top-quark production is shown in the Fig. 1.3.

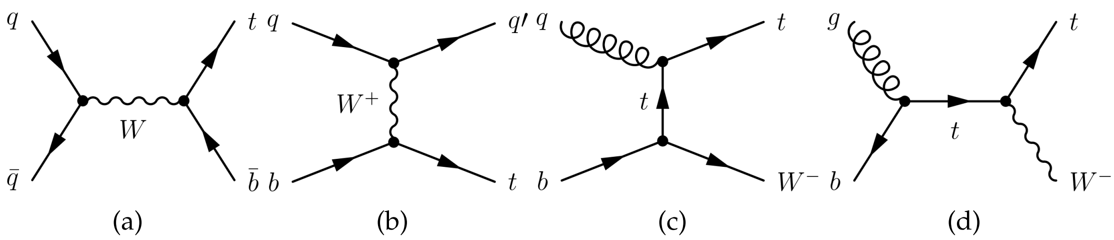

Figure 1.3: The tree level Feynman diagrams for the single-top-quark in a proton proton or proton anti-proton colliders. The diagrams (a), (b), (c) - (d) represents the single-top-quark production via s, t and tW respectively.

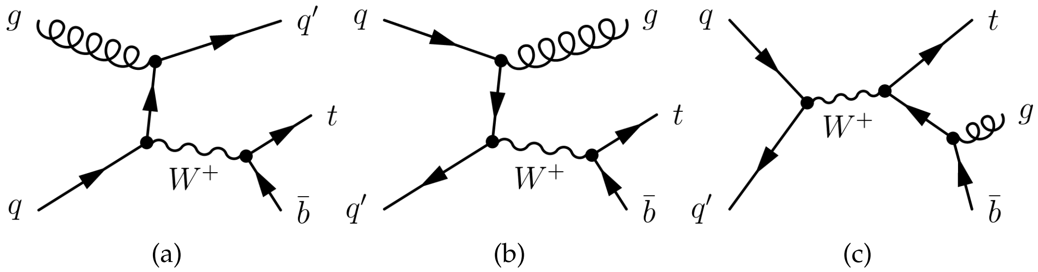

Figure 1.4: The next to leading order Feynman diagrams of the single-top-quark production via s-channel.

The single-top-quark production has a unique feature that in all the possible production modes has the Wtb vertex and thus single-top-quark production gives the best possibility to probe this vertex and to measure the $|V_{\mathrm{tb}}|$ directly. The modes of single-top-quark production can be distinguished from each other on the basis of Q^2 of W-boson, i.e., $Q^2 = -q^2$ where q is the four momentum of the W-boson. For s-channel $q^2 > 0$ for t-channel $q^2 < 0$ and for associated production $q^2 = m_{\mathrm{W}}^2$.

s-channel Production

The s-channel production of the single-top-quark has the smallest cross-section at the LHC. The time like W-boson is produced via quark anti quark annihilation in the s-channel. Since the colliding particles in case of LHC are protons which do not have anti-quark as their valance and this quark has to be the sea quark as a result the s-channel cross-section is very small when compared to the other modes of production.

Figure 1.3(a) and the Fig. 1.4 represents the leading order and next to the leading order Feynman diagrams for the production of single-top-quark via s-channel respectively. The NNLO s-channel production cross-section of the single-top-quark for various energies is given in the Table 1.6

Table 1.6: The NNLO s-channel production cross-section at LHC for m_{T} = 173 GeV and using MSTW2008 NNLO PDF, the first uncertainty is from scale variation $\frac{1}{2}m_{\mathrm{T}} < \mu < 2m_{\mathrm{T}}$ and the second is from the PDF at 90% C.L. [85].

.

s-channel (LHC)	t	$\bar{\mathrm{t}}$	Total
7 TeV	$3.14 \pm 0.06^{+0.12}_{-0.10}$	$1.42 \pm 0.01^{+0.07}_{-0.06}$	$4.56 \pm 0.07^{+0.18}_{-0.17}$
8 TeV	$3.79 \pm 0.07 \pm 0.13$	$1.76 \pm 0.01 \pm 0.08$	$5.55 \pm 0.08 \pm 0.21$
14 TeV	$7.87 \pm 0.14^{+0.31}_{-0.28}$	$3.99 \pm 0.05^{+0.14}_{-0.21}$	$11.86 \pm 0.19^{+0.45}_{-0.49}$

t-channel Production

The single-top-quark production via t-channel is the most dominating production process. It has the largest production cross-section. Due to the large production cross cross-section of the single-top-quark via t-channel it is one of most important electroweak production processes which can be studied at the LHC and because of its large production cross-section the measurement of $|V_{\mathrm{tb}}|$ will therefore has less statistical uncertainty. Figure 1.3(b) shows the LO and Fig. 1.5 represents the NLO production of single-top-quark in t-channel. The NLO is a 2$\rightarrow$3 process in which a gluon splits into b$\bar{\mathrm{b}}$. The initial b-quark contributing in the production process comes from gluon splitting. This is called W-gluon fusion. The other b-quark in the final state is a 2^{nd} b-quark known as spectator quark. This 2^{nd} b-quark has a very soft transverse momentum and it is found along the beam directions in an experiment, care must be taken in the t-channel that this second b-quark is separated from the b-quark coming from the decay of the top-quark and it is not selected as b-jet. The leading order differential cross-sections of t-channel is given by [86–92].

Table 1.7: The NNLO t-channel production cross-section at LHC for m_{T} = 173 GeV and using MSTW2008 NNLO PDF, the first uncertainty is from scale variation $\frac{1}{2}m_{\mathrm{T}} < \mu < 2m_{\mathrm{T}}$ and the second is from the PDF at 90% C.L. [85].

t-channel (LHC)	t	$\bar{\mathrm{t}}$	Total
7 TeV	$43.0^{+1.6}_{-0.2} \pm 0.8$	$22.9 \pm 0.5^{+0.7}_{-0.9}$	$65.9^{+2.1+1.5}_{-0.7-1.7}$
8 TeV	$56.4^{+2.1}_{-0.3} \pm 1.1$	$30.7 \pm 0.7^{+0.9}_{-1.1}$	$87.2^{+2.8+2.0}_{-1.0-2.2}$
14 TeV	$154^{+4.0}_{-1.0} \pm 3.0$	$94^{+2.0+2.0}_{-1.0-3.0}$	$248^{+6.0+5.0}_{-2.0-6.0}$

This 2^{nd} b-quark when treated massless, the resulting scheme is known as 5 Flavour scheme (5FS) which leads to singularities in the collinear of the spectator b-quark and we can remove these singularities by introducing the parton density function of the spectator quark. On the other hand taking the b-quark as a massive particle the resulting scheme is 4 Flavor scheme [93]. The single-top-quark production cross-section at various energies for the LHC experiment are given in Table 1.7.

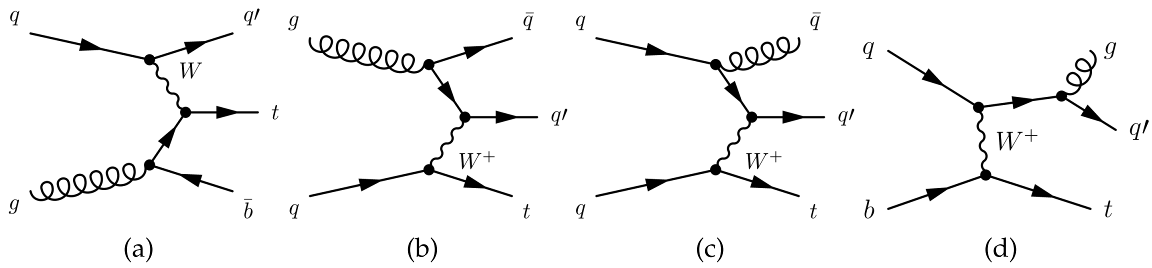

Figure 1.5: Next to the leading order Feynman diagrams for the t-channel single-top-quark production.

Associative Production (tW)

The production of single-top-quark in association with a W-boson has the second largest production cross-section at LHC. The s-channel and t-channel are well understood theoretically while tW, the associative production, is not known with higher precision. Nevertheless tW-channel contributes 20% to the total production cross-section of the single-top-quark. In this process a real W-boson is produced along with the single-top-quark.

The predicted NNLO production cross-sections for the tW-channel at various LHC energies [85] are given in Table 1.8. The processes $\mathrm{t^+W^-}$ and $\mathrm{t^-W^+}$ has the same production cross-section. The leading order production of the tW is well defined but at NLO in QCD there are large corrections due to the presence of possible Feynman diagrams shown in the Fig. 1.7. At the NLO there are some real and virtual corrections to the LO Feynman diagrams but these diagrams also contribute to the $\mathrm{t\bar{t}}$ production at the LO with decay of the $\mathrm{t\bar{t}}$. Especially there is large contribution when the $m_{\mathrm{bW}} \to m_{\mathrm{top}}$. Thus at LO there is a well defined production cross-section for $\sigma_{\mathrm{t\bar{t}}}$ and σ_{tW}, where $\sigma_{\mathrm{tW}} < \sigma_{\mathrm{t\bar{t}}}$. At NLO the σ_{tW} gets a large correction due to the presence of interference diagrams from $\mathrm{t\bar{t}}$ processes. The interference problem between the tW and $\mathrm{t\bar{t}}$ can be solved by introducing the two approaches namely Diagram Removal (DR) and Diagram Subtraction (DS). The difference between them measures the tW- $\mathrm{t\bar{t}}$ interference.

Table 1.8: The associated production cross-sections of single-top-quark measured at 7, 8 and 14 TeV at LHC.

Associated Production (LHC)	7 TeV	8 TeV	14 TeV
	$7.8 \pm 0.2^{+0.5}_{-0.6}$ pb	$11.1 \pm 0.2^{+0.3}_{-0.7}$ pb	$41.8 \pm 1.0^{+1.5}_{-2.4}$ pb

In diagram removal (DR) one removes all diagrams that enter $\mathrm{t\bar{t}}$ production at the amplitude level thus the interference with LO top pair production is completely removed. The removal of these diagrams can lead to the violation of electroweak and QCD gauge invariance.

In diagram subtraction (DS), which is a bit more complicated than the Diagram Removal, the $\mathrm{t\bar{t}}$ contribution is removed at the cross-section level where the cross-section is modified with a local subtraction term which in principal removes the top pair contribution. The

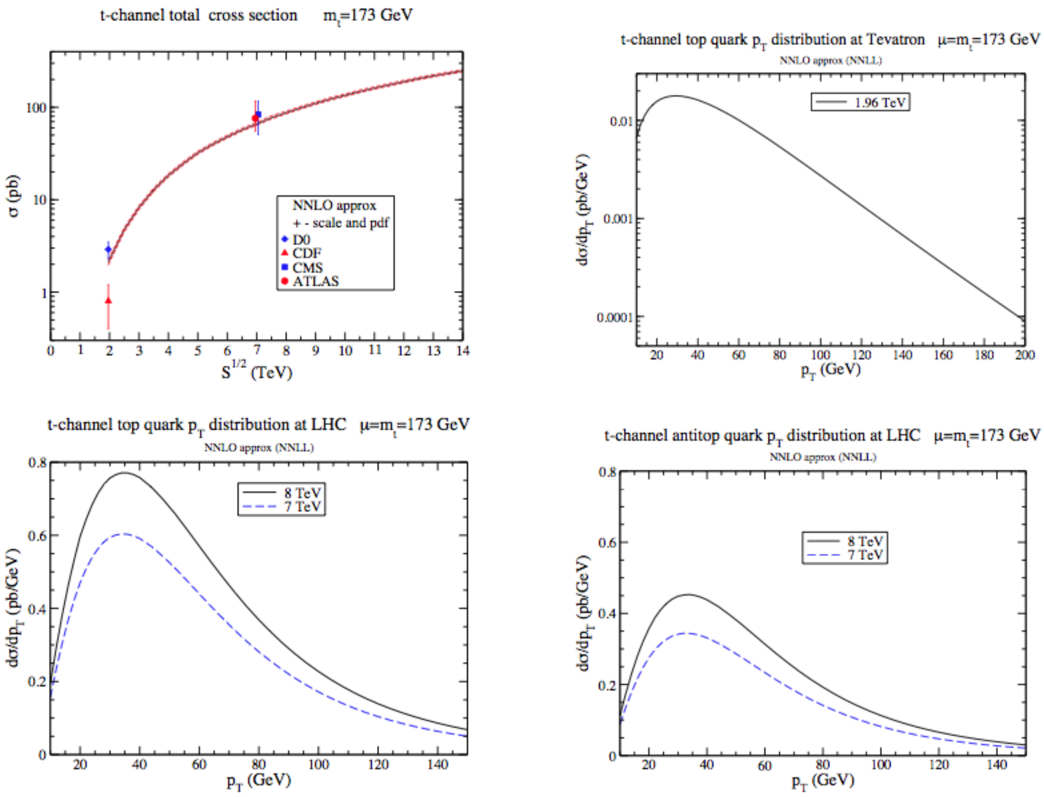

Figure 1.6: t-channel production section and measured cross-section at the ATLAS, CMS, CDF and DØ experiments plotted against the $\sqrt{s} = 7$ and 8 TeV (upper left), p_T distribution of the top-quark at a $\sqrt{s} = 1.96$ TeV (upper right). Lower right and left shows the p_T distribution of the top and anti top-quark in the t-channel at $\sqrt{s} = 7$ and 8 TeV [85].

DS is based on the narrow width approximation. This process of subtracting the cross-section is gauge invariant. Schematically, this can be written as:

$$\sigma_{ab\to tW} = \sigma_{ab} - \sigma_{ab}^{subt}, \tag{1.5.1}$$

where σ_{ab} represents the final state of associated production while the σ_{ab}^{subt} removes the possible contribution coming from the $t\bar{t}$ pair.

1.6 Top-quark Decay and Spin Polarization

The top-quark is the heaviest quark known. Due to the large mass, the top-quark decays into other lighter particles before the bound state formation takes place. The top-quark is 35 times heavier than the next heaviest quark which makes the top-quark even more interesting. With a mass above than the mass of a q-quark and W-boson the decay of the top-quark is expected to be a two body decay. The standard model assumes that the top-quark decay to Wbis almost 100%. Neglecting the terms of order $m_b^2/m_T^2, \alpha_s^2$ and those of order $(\alpha_s/\pi)m_W^2/m_T^2$ in the decay amplitude the standard model predicts the decay width of the top-quark to be [94]:

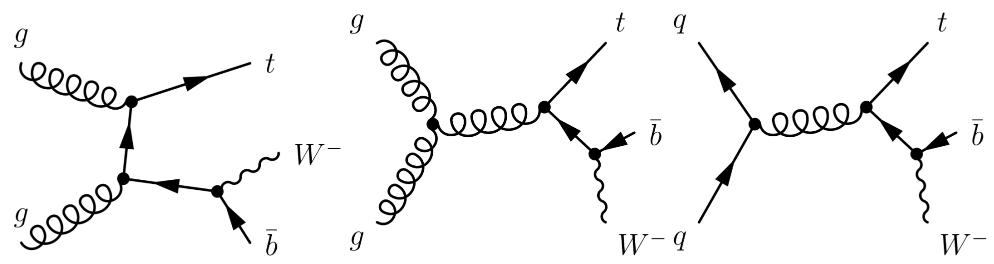

Figure 1.7: Next to the leading order Feynman diagrams for the associated production (tW) of the single-top-quark

$$\Gamma_{\text{top}} = \frac{G_F m_T^3}{8\pi\sqrt{2}}\left(1-\frac{m_W^2}{m_T^2}\right)^2\left(1+\frac{2m_W^2}{m_T^2}\right)\times\left[1-\frac{2\alpha_s}{3\pi}\left(\frac{2\pi^2}{3}-\frac{5}{2}\right)\right], \tag{1.6.1}$$

$$\Gamma_{\text{top}} = 1.40\text{ GeV} \Rightarrow \tau_{\text{top}} \approx 5\times10^{-25}\,\text{s}, \tag{1.6.2}$$

$$\Gamma_{\text{top}} = \Lambda_{\text{QCD}} \approx 3\times10^{-24}\,\text{s}. \tag{1.6.3}$$

The decay width of the top-quark is proportional to the mass and it changes from 1.02 GeV for m_{top} = 160 GeV to 1.56 GeV for m_{top} = 180 GeV. Due to the short life time of the top-quark, which is orders of the magnitude smaller than the typical hadronization timescale, the top-quark decays before it can form a bound state. Because of its short life time the top-quark decaying products retain the spin information. This feature turns out to be a powerful tool to study the vector-axial coupling structure of the Wtb vertex. In t-channel single top quark production, the top-quark are almost 100% polarized due to the vector minus axial structure of the weak interaction. Consequently if there are any new physics model or is there any deviation in the standard model physics the top-quarks polarization will be effected. A significant contribution has been made by the CDF experiment to study the polarization in t-channel [95]. Due to the limited amount of the statistics the precision was not sufficient to exclude the hypothesis of opposite polarization to the one predicted by the standard model.

The top-quark spin asymmetry is used as a probe to study the top-quark coupling structure. The top-quark spin asymmetry is given by:

$$\text{A}_\text{l} \equiv \frac{1}{2}\cdot p_\text{T}\cdot\alpha_\text{l} = \frac{\text{N}(\uparrow)-\text{N}(\downarrow)}{\text{N}(\uparrow)+\text{N}(\downarrow)}, \tag{1.6.4}$$

where p_T is the transverse momentum of the top-quark, $\text{N}(\uparrow)/\text{N}(\downarrow)$ represents the number of charged leptons aligned or oppositely aligned with the direction of the spectator quark which is recoiling against the single-top-quark produced in an event and α_l represents the degree of correlation of its angular distribution with respect to the top-quark spin. The value of α_l is exactly equal to one in the standard model. The vector minus axial coupling produces angular correlations in the decay products. Figure 1.8 shows the differential distribution of $\cos(\theta^*)$ in the muon (electron) channel. The angle θ is the angle between the charged lepton, stemming from the decay of the top-quark, and the spin axis

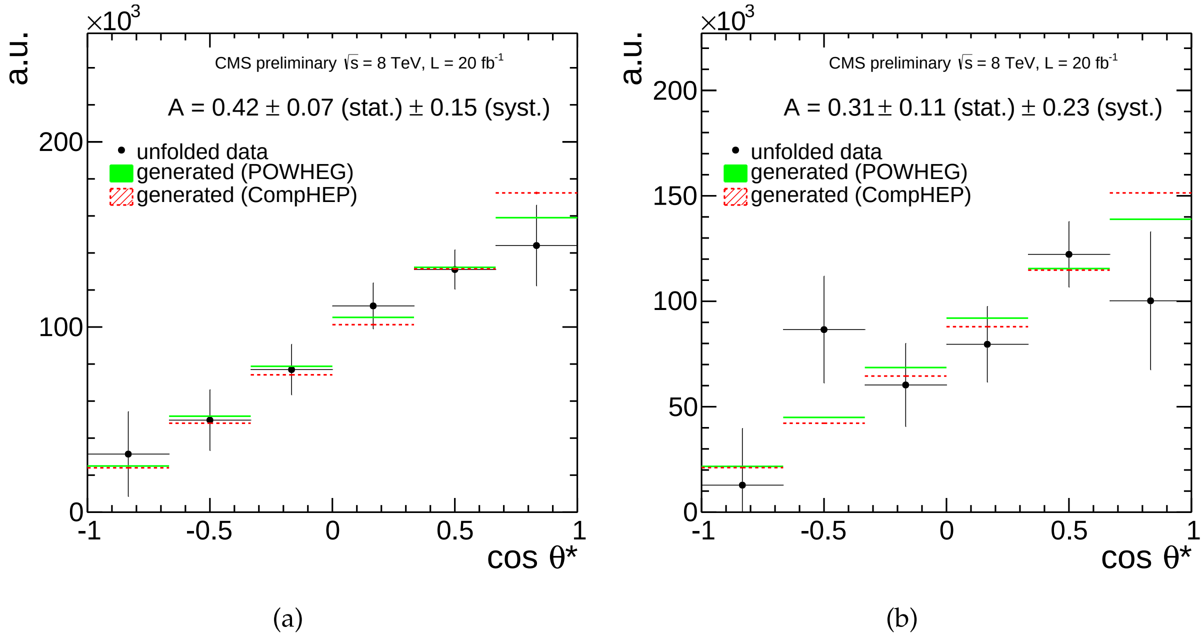

Figure 1.8: The single-top-quark polarization in t-channel in the muon (electron) channel [96].

of the top-quark in the top-quark rest frame. For all the contributing background processes to t-channel polarization the distribution of the $\cos(\theta^*)$ is almost flat. This plays a pivotal role to discriminate the signal and background. The measurement comes out to be in a good agreement with the standard model predictions.

Chapter 2

Introduction to Experiment

In the following, a general introduction to the LHC [97] and the CMS experiment [98] are presented. The LHC accelerator and the CMS detector located at French-Swiss border near Geneva. There are four major experiments which are operating at the LHC:

- ATLAS (**A** **T**oroidal LHC **A**pparatu**S**) [99]
- CMS (**C**ompact **M**uon **S**olenoid) [98]
- LHC-b (**L**arge **H**adron **C**ollider **b**eauty) [100]
- ALICE (**A** **L**arge **I**on **C**ollider **E**xperiment) [101]

There are two general purpose detectors, ATLAS and CMS, the other two experiments LHC-b and ALICE are dedicated detectors studying the b-physics and heavy ion physics respectively. Figure 2.1 shows the four experimental sites along the LHC ring. The CMS experiment is one of the major purpose detector being operated at the LHC ring near the village of Cessey, France which is taking data of both the proton-proton and the lead-lead collisions.

2.1 The Large Hadron Collider - LHC

The LHC accelerator was completed at CERN and first proton beam was injected in the beam pipe in September, 2008. The LHC ring uses the former Large Electron Positron Collider (LEP) tunnel with 27 km circumference. The main physics goal is the search for Higgs boson, the only missing piece of the standard model, and the testing of the standard model at the TeV energy scale. The LHC will be operating at a $\sqrt{s}$ = 14 TeV for proton-proton collision and $\sqrt{s}$ = 5.5 TeV for heavy ion collisions with an instantaneous luminosity of $10^{34}\,\mathrm{cm}^{2}\,\mathrm{s}^{-1}$ and $10^{28}\,\mathrm{cm}^{2}\,\mathrm{s}^{-1}$ respectively. Figure 2.1 shows the schematic view of the CERN accelerator complex. The protons, before they are pumped into the main LHC ring for the acceleration, are passed through a complex chain of accelerators. The protons are obtained from the ionization of a hydrogen gas with the help of duoplasmatron. The protons from the duoplasmatron are than accelerated by 100 kV and are passed to the radio frequency quadrupole RFQ. This RFQ than accelerates the protons beam up to 750 KeV before they are ready to be injected to Linear Ion Accelerator (LINAC2). From the LINAC2 the protons are than injected into the Proton Synchrotron Booster(PSB) which further accelerates the beam of protons to 1.4 GeV. PSB than shoots the accelerated beam to Proton Synchrotron (PS) which in turn further accelerates the

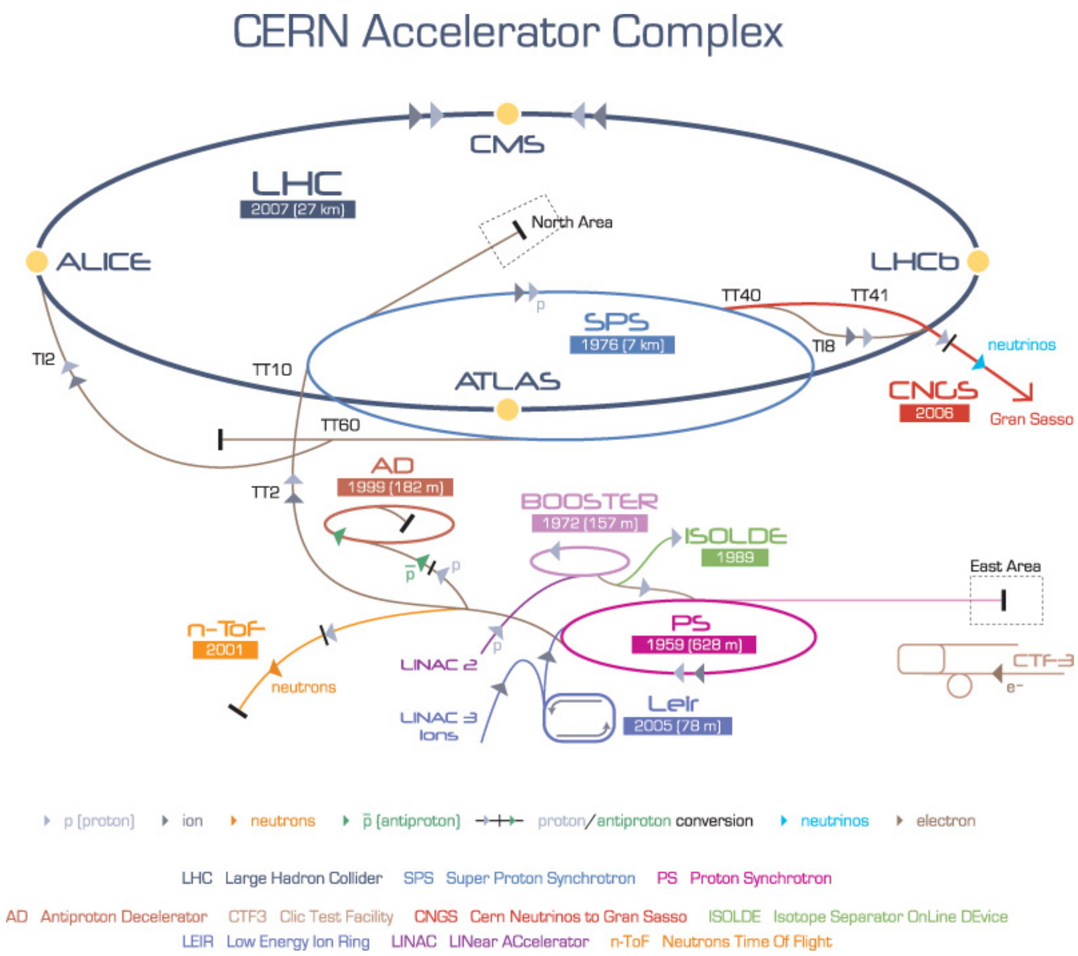

Figure 2.1: The CERN accelerator complex showing the various parts of the machine.

beam to 25 GeV. From PS the beam is than injected to Super Proton Synchrotron (SPS) which accelerates the particles to an energy of 450 GeV before it is injected to the main LHC ring where it is accelerated up a 6.5 TeV. To achieve the design luminosity for proton-proton collision two beams with 2800 bunches are injected into the beam pipe with 25 ns gap. To keep the particles in track 1232 Niobium-Titanium superconducting dipole magnets producing a field of 8.3 T are used. These super conducting magnets are cooled with the help of liquid helium at a temperature of about 1.9 K. At nominal luminosity the energy stored in each beam is more than 350 MJ and this is two orders of magnitude more than any other machine. In general the mathematical expression giving the number of collisions in each second at LHC is given by:

$$N_{\mathrm{event}} = L\sigma_{\mathrm{event}}, \tag{2.1.1}$$

where σ is the cross-section for the event and L gives the instantaneous luminosity delivered by the LHC accelerator. The luminosity of the machine depends of the beam parameters and is given by:

$$L = \frac{N_b^2 n_b f_{rev} \gamma_r}{4\pi\epsilon_n \beta^*} F, \tag{2.1.2}$$

where the parameters in the equation; N_b is the number of particles per bunch, n_b is the number of bunches per beam, f_{rev} is the frequency of revolution, γ_r is the relativistic gamma factor, ϵ_n is the normalized beam emittance, β^* is the beta function at the interaction point and F is the luminosity reduction factor due to the crossing angle at the interaction point, which mathematically can be written as:

$$F = \sqrt{(1 + (\frac{\theta_c \sigma_z}{2\sigma^*}^2))}. \tag{2.1.3}$$

Table 2.1: The designed parameters for the LHC accelerator [102].

Parameter	Designed value
Circumference	26.7 km
Beam energy at injection	0.45 TeV
Dipole field at 7 TeV	8.33 T
Beam energy at collision	7.04 TeV
Luminosity	10^{34} cm^2 s^{-1}
Beam current	0.56 A
Protons per bunch	1.1×10^{11}
Nominal bunch spacing	24.95 ns
Normalized emittance	3.75 μm
Total crossing angle	300 μrad
Energy Loss per Turn	6.7 KeV
Radiated power per beam	3.8 kW
Stored energy per beam	350 MJ
Operating temperature	1.9 K

2.2 Compact Muon Solenoid

One of the general purpose detector, the CMS, is located near the village of Cassey, France. One of major purpose of the CMS detector is the discovery of the Higgs boson and Super symmetric particles. The golden channel to be studied for the discovery of Higgs boson is its decay to four muons and two photons in the final state. The high luminosity and short bunch spacing of LHC beam demanded a sophisticated detector. The CMS detector is a very compact when compared to another general purpose detector ATLAS which has more than twice the volume of CMS. The CMS detector has an excellent muon system assisted by central tracking detector and solenoid produces a magnetic field twice large as used by ATLAS. This allows the accurate particle momentum measurement. Figure 2.3 below shows perspective view of the CMS detector.

The overall dimensions of the CMS detector are 22 m in length 15 m in diameter with a total mass of 12500 tons. The coordinate conventions are as follows: The interaction point which lies in the middle of barrel part of the CMS where the two beams collide is referred as the origin of the coordinate system. The *x*-axis points radially inward to the center of the LHC ring. The *z*-axis points along the direction of the beam pipe and the *y*-axis points

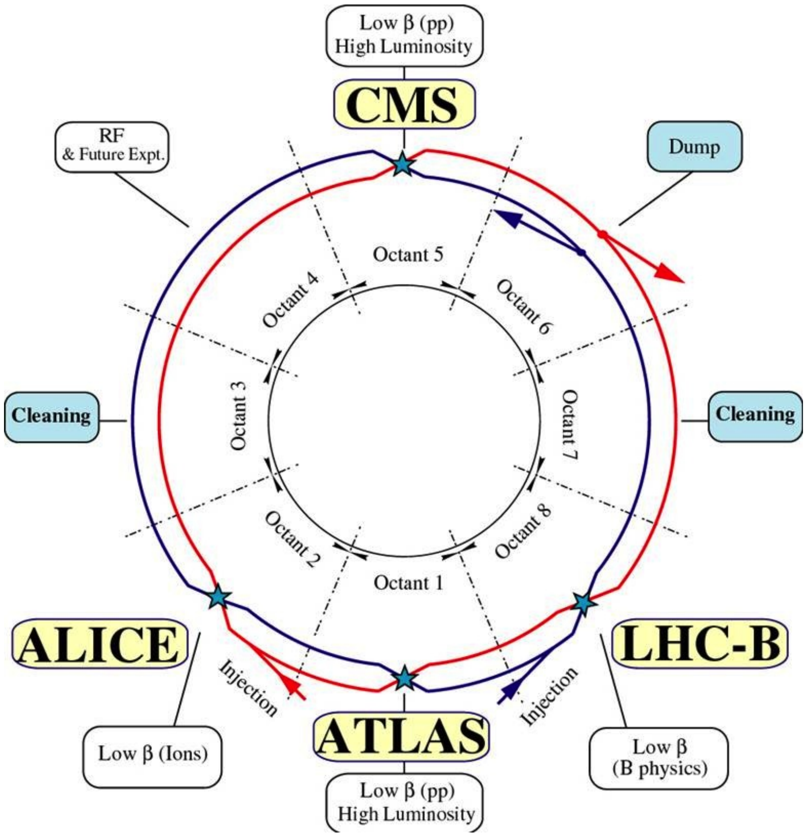

Figure 2.2: The schematic layout of the LHC tunnel which is the same tunnel which was used by the LEP experiment. There are eight sectors of the machine and 4 collision points. The ATLAS experiment is situated at point 1, CMS experiment is located at point 5, ALICE experiment is located at point 2 and LHC-b experiment is located at point 8. In between those points the radio frequency, collimation, beam dumping and momentum collimation systems are installed.

vertically to the surface. The azimuthal angle ϕ is measured in the x-y- plane from x-axis. In the y-z-plane the angle θ is measured from z-axis. The rapidity and pseudorapidity are the two additional quantities which are very useful in the describing an event in the experimental particle physics apart from cartesian and polar co-ordinates. The rapidity is defined as:

$$y = \frac{1}{2} \ln \left(\frac{E - p_z}{E + p_z} \right). \tag{2.2.1}$$

For a hadron collider the number of particles per unit area in a given rapidity interval is a constant quantity and rapidity is also a Lorentz variant quantity if the motion is considered along the beam directions. The pseudorapidity of a particle in detector can be mathematically like:

$$\eta = -\ln \left(\tan \frac{\theta}{2} \right). \tag{2.2.2}$$

In the high energy limit and the particle being massless the rapidity transforms into pseudorapidity, pseudorapidity has an advantage over the rapidity that only θ is needed to describe the pseudorapidity of a particle. More details of CMS experiment can be found in [103, 104].

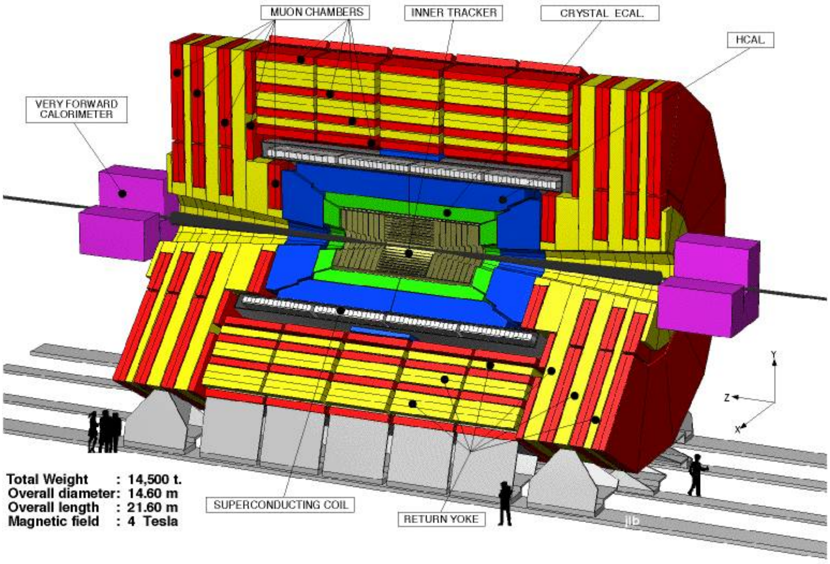

Figure 2.3: Longitudinal view of the CMS detector at CERN, very close to the beam pipe lies the tracking system of the experiment, than comes the electromagnetic and hadronic calorimeters which are built inside the superconducting solenoid. The muon system lies at the most outer part of the detector.

2.2.1 Tracking System

The tracking system is the heart of the CMS experiment, the state of the art tracker system is designed in such a way that it provides an efficient and precise measurement of trajectories of charged particles produced during a high energy collisions as well as the precise reconstruction of secondary vertices in the LHC collisions. The momentum of a charged particle can be calculated from the curvature of the track produced in the tracker. The resolution of the momentum measured from the track is given by:

$$\frac{\sigma_{p_\mathrm{T}}}{p_\mathrm{T}} = \frac{8 \times p_\mathrm{T}}{0.3 \times \mathrm{B} \times \mathrm{L}^2}\sigma_\mathrm{s}, \tag{2.2.3}$$

where B is the magnetic field, L is the path length and σ_s is the measure of uncertainty on the sagitta. Also the relative momentum of the particle is proportional to the σ_{p_T} times the σ_s, the sagitta uncertainty. Figure 2.5 shows the pictorial view of how the momentum is measured from the curvature of charged particle in the tracker. The whole tracking system is fully immersed in the solenoidal magnetic field with a total length of 5.8 m and a diameter of 2.5 m. The Tracking system is designed to take the huge particle flux coming for the LHC collisions. The CMS tracker consists of about 20000 silicon sensors with a total area of 210 m^2 having a diameter and length of about 2.4 m and 5.4 m respectively thus its acceptance is up to $\eta < 2.5$. Tracker is located directly around the interaction point therefore it receives a very high particle flux. At LHC, per bunch crossing around 1000 charged particles will hit the tracker at the radius of about 4 cm therefore at such a distance the tracker has to be radiation hard. The inner tracker mainly consist of silicon pixel detector and silicon strip sensors. The whole system is surrounded by 4 T homogeneous magnetic field [105].

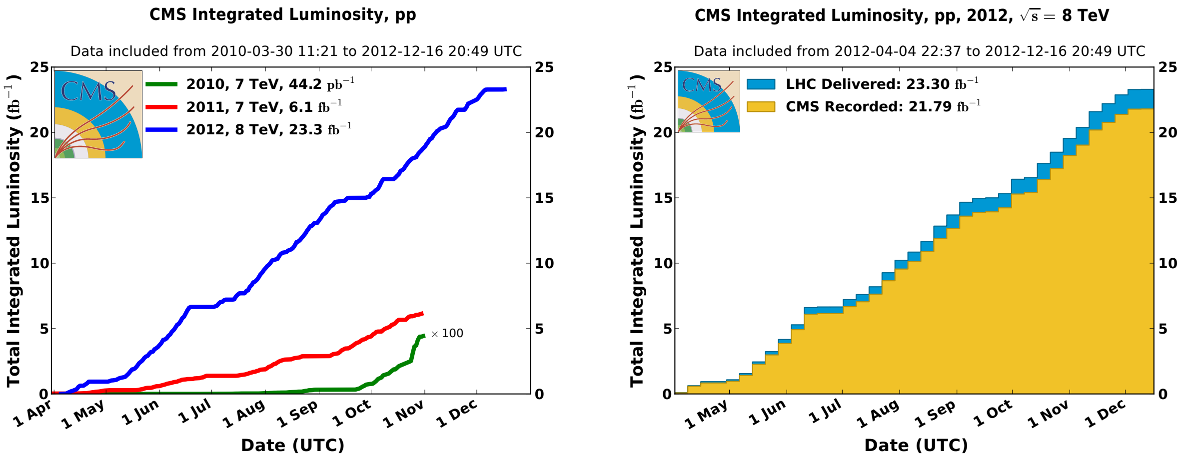

(a) (b)

Figure 2.4: (a) The total data recorded at CMS during the total running of LHC since 2008 (b) total luminosity delivered and recorded in the year 2012 at $\sqrt{s}$ = 8 TeV

The pixel tracker is subdivided into two parts: First, three cylindrical barrels located at radii of 4.4, 7.3 and 10.2 cm around the interaction point with a length of 53 cm. Second, on each side of the barrel two discs complement the tracker at $z = \pm$ 32.5 and $\pm$ 46.5 cm. Therefore, for every charged particle with $\eta < 2.5$ hitting the tracker, three high precision space points will be measured. The pixels have a cell size of 100$\times$150 μm ^{2}.

The silicon strip tracker surrounds the pixel tracker. Here the inner and outer part is different. The inner barrel (TIB) consists of four layers ranging from 20 cm to 55 cm and covering $|z| <$ 65 cm. Three tracker inner discs (TID) are located at each end in the region of 65 cm $< |z| <$110 cm. The inner strip tracker measures four spatial points for each trajectory. The resolution for a single point is 23 to 34 μm. The inner part is surrounded by the tracker outer barrel (TOB) comprising 6 layers, which extend from 55 to 116 cm in radius and $\pm$118 cm in z. The barrel part takes out 6 measurements with a single point resolution in between 35 and 53 μm. Finally the outer tracker is completed by 9 endcap discs (TEC) on each side ranging from 124 cm $< |z| <$ 282 cm and 22.5 cm $<$ r $<$ 113.5 cm.

2.2.2 Electromagnetic Calorimeter – ECAL

The electromagnetic calorimeter, ECAL, of the CMS detector is made up of a very dense lead tungstate $PbWO_4$ scintillating crystals. The material for the ECAL is chosen because of the fact that lead tungstate crystal has radiation hardness up to 10 M rad and has a very fast response time within 25 ns. There are about 61200 crystals installed in the barrel part and about 7342 crystals are installed in each of two end caps of the CMS detector. The scintillation light produced due to these crystal is very low, for the amplification of the light emitted by the crystal is done by using the photo diodes. For amplification in the barrel region, two silicon avalanche photodiodes (APDs) are used. For the endcap region due to the high radiation instead of APDs, vacuum phototriodes (VPTs) are used. One vacuum phototriode is attached at the back of each crystal. The energy resolution of ECAL is described by:

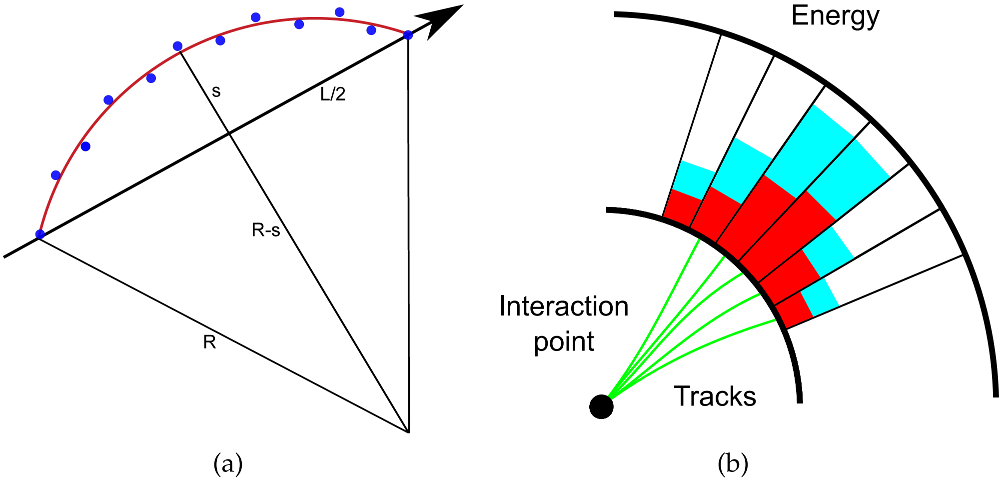

Figure 2.5: A pictorial view of momentum measurement from the tracks in magnetic field.

$$\left(\frac{\sigma_E^2}{E}\right) = \underbrace{\left(\frac{2.8\% \cdot \sqrt{E}}{\sqrt{E}}\right)^2}_{\text{Stochastic term, S}} + \underbrace{\left(\frac{0.12\,\text{GeV}}{E}\right)^2}_{\text{Noise term, N}} + \underbrace{(0.3\%)^2}_{\text{Constant term, C}} , \tag{2.2.4}$$

where S is the stochastic term, N is the noise term and C is the constant term [106]. The stochastic term is mainly stemming from lateral shower containment, photo-statistics and from the energy fluctuations are measured in the pre-shower detector. The noise term originates from the unavoidable electronic noise present in every detector. The constant term has its main origin from the non-uniform behavior of the longitudinal light collection. The calibration errors of the detectors and flow of energy from the crystals also contributes to the constant term. The Electromagnetic calorimeter of the CMS detector can be sub divided into two regions, the ECAL endcap and the barrel regions.

Endcap ECAL

The endcap ECAL is located 3.4 m away from the interaction point and is located on the either side of barrel and covers a pseudorapidity range $1.479 < |\eta| < 3.0$. The endcap crystals are larger in size as compared to the size of barrel ECAL crystals. The endcap ECAL crystal is $28.62 \times 28.62\,\text{mm}^2$ while the size of barrel ECAL crystal is $22 \times 22\,\text{mm}^2$. There are 7324 installed in each endcap and are grouped together in a unit of $5{\times}5$ crystals known as super clusters. The each endcap is made up of 276 standard super-clusters and 36 partial super-clusters.

Barrel ECAL

The barrel ECAL consists of 61200 crystals and each crystal has a cross-sectional area of 0.0174×0.0174 in the $\eta - \phi$ plane. The barrel ECAL covers up to a pseudorapidity range $|\eta| < 1.479$. There are 360 crystals along any circle in ϕ and 170 crystals along any length

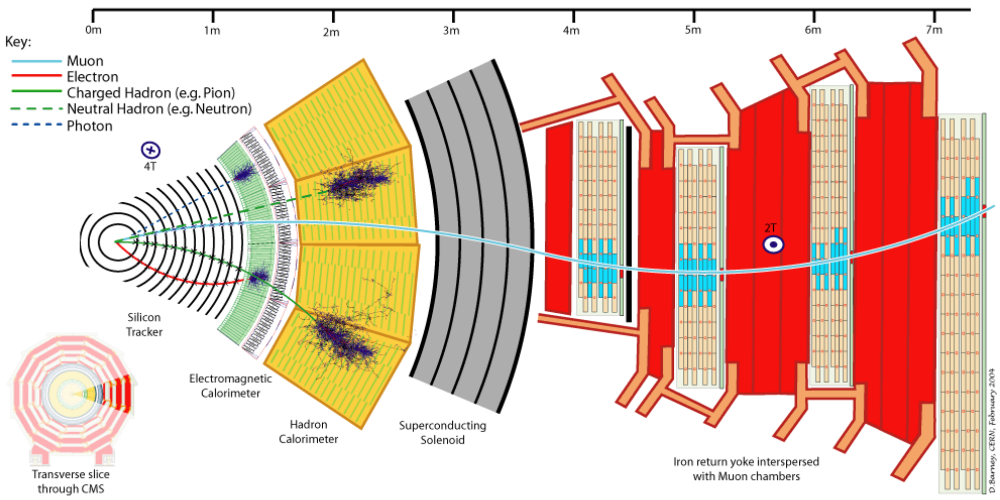

Figure 2.6: A slice of Compact Muon Solenoid experiment at LHC.

in the z direction. The crystals are joined together to form a submodules and than these submodules are joined together to form modules. Each module than contains 400 to 500 crystals depending on its position in η. These modules are further joined together into super-modules. Each super module then contains 1700 crystals.

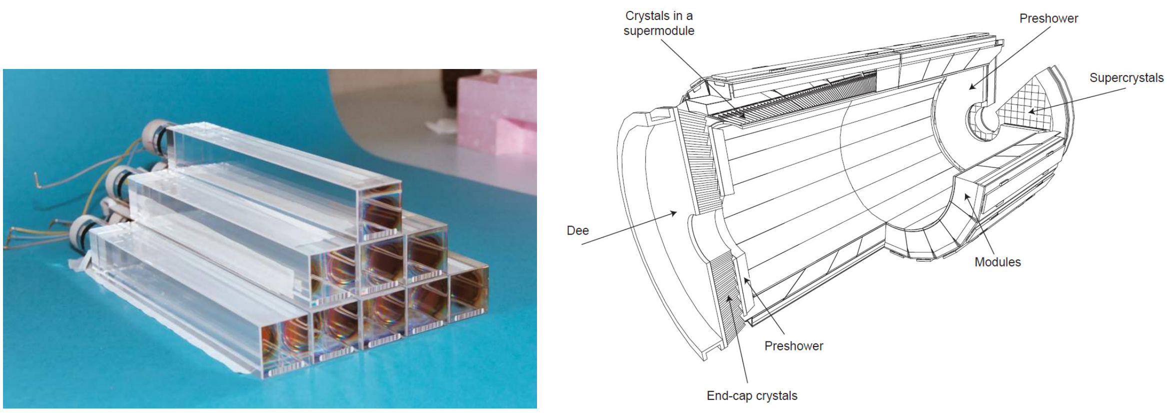

(a) (b)

Figure 2.7: (a) Crystals from ECAL endcap with vacuum photo triodes attached at their back (b) the geometrical layout of one quarter of the electromagnetic calorimeter of the Compact Muon Solenoid experiment presenting the arrangement of crystal modules, super-modules, endcap and the pre-shower [106].

ECAL Pre-shower

During the high energy collision large number of short lived particles are produced which decay into photons and those photons are in turn detected in the ECAL of the CMS detector. There are also neutral pions produced during the collisions which are likely to decay into two photons. These photons are very close to the beam pipe or in high eta region. The ECAL is not able to separate these two photons coming very close to each other as a result the two photons are treated as one entity. To solve this problem, a pre-shower detector is placed in front of ECAL to prevent such false signals. The pre-shower has much finer granularity than the ECAL where the detector strips are 2 mm wide as compared to the ECAL crystals where the separation is 3 cm. The pre-showers cover up to $1.653 < \eta < 2.6$. The pre-shower is made of two planes of lead followed by a silicon detectors. A high energy photon when strikes the lead layer it produces an electromagnetic shower containing the electron-positron pairs which can be easily detected by the silicon detector. The two pre-shower detectors installed at the both ends of the CMS detectors use 8 square meters of silicon for the detection of electron hole pairs. The dimensions of each silicon detectors are about 6.3 cm $\times$6.3 cm $\times$0.3 mm and divided into 32 strips and arranged to cover the whole ECAL crystals. The total circumference of the pre-shower detector is about 2.5 m with a 50 cm whole diameter for the beam pipe.

2.2.3 Hadron Calorimeter – HCAL

The hadron calorimeter of the CMS detector is built to measure the energies of the hadrons produced during the collisions. Additionally it provides indirect measurement of non interacting uncharged particles such as Neutrinos. Measuring these particles is important because they hint towards the existence of new particles such as Higgs boson or any super symmetric particles. Figure 2.8 shows the longitudinal view of the HCAL detector for CMS Experiment. The HCAL can be further subdivided into hadron barrel (HB) and hadron endcap (HE). The HCAL sits behind the tracker and electromagnetic calorimeter as seen from the interaction point. However a portion of Hadron Barrel is restricted between the outer radius of ECAL and inner radius of the magnetic coil. The outer radius to which the ECAL extends is 1.77 m and the inner radius of magnetic coil is 2.95 m when measured from the point of interaction. Thus the Hadron outer is placed after the solenoid and Hadron Forward HF is placed 11.2 m from the interaction point IP providing a coverage in η from 3 to 5.2.

The hadron barrel and endcap sampling calorimeters are made from several layers absorbers made from brass and tiles made of dense 3.7 mm thick Kuraray SCSN81 plastic scintillators. The absorber material which consists of brass, which has a short interaction length which is used effectively for the detection of missing transverse energy [107]. The hadron barrel (HB) being installed inside the magnetic coil, and covers the pseudorapidity range up to $\eta < 1.3$. The hadron outer (HO) is located at the outer vacuum tank of the magnetic coil and covers a range up to $|\eta| \leq 1.26$. The hadron endcap (HE) covers the pseudo-rapidity range up to $1.3 \leq |\eta| \leq 3.0$, hadron barrel covers up to $3.0 \leq |\eta| \leq 5.0$. The HB is further subdivided into HB+ and HB-. Each of HB+/HB- consists of 36 identical azimuthal wedges. The HCAL has a certain resolution which is given by the following equation:

$$\left(\frac{\sigma_{\mathrm{E}}^2}{\mathrm{E}}\right)^2 \approx \left(\frac{100\% \cdot \sqrt{\mathrm{E}}}{\sqrt{\mathrm{E}}}\right)^2 + (5\%)^2 . \tag{2.2.5}$$

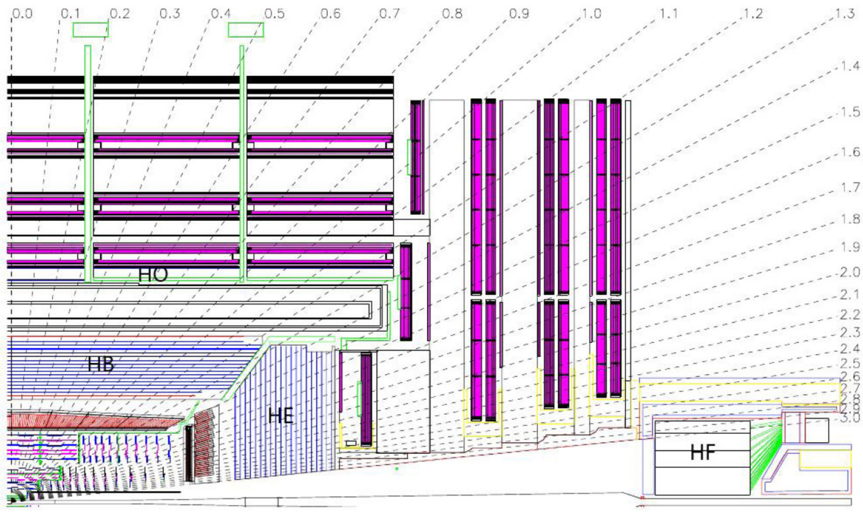

(a)

Figure 2.8: The Longitudinal view of one quarter of the detector in the $r\eta$ - plane, showing the positions of the HCAL parts: hadron barrel (HB) detector, hadron endcap (HE) detector, hadron outer (HO) detector, and hadron forward (HF) detector [106].

2.2.4 Superconducting Magnetic Coil

The Superconducting magnetic coil is one of the central part of the CMS detector which produces a magnetic field of 4 T which is 100,000 times stronger than the earth's magnetic field. The strong magnetic field is used to bend the charged particles and than the momentum is measured from the curvature of the track. More energetic the particle is, lesser it has the radius of curvature hence large momentum. The geometry of the magnet used is solenoidal and produces a uniform magnetic field around the interaction point when a current of 19.5 kA flows through it, the momentum resolution is given by [108]:

$$\frac{\delta p}{p} \approx 10\% \qquad \text{at } p = 1\,\text{TeV}. \tag{2.2.6}$$

2.2.5 Muon System

The muon detection is one of the most important task which the CMS detector performs. The muons, charged particles like electrons but having more mass as compared to electrons, are expected to be produced in decay of particles which are not known to the physics world. One of such examples is the decay of standard model Higgs boson to 4 leptons and leptons in this case being muons. The muon being least interacting particle, therefore the muons detectors are stationed at the outer most layer of the CMS detector. The muon system of the CMS experiment plays an important role in the muon identification and triggering. Muon system consists of the three different types of sub-detectors, Cathode Strip Chambers (CSC), Drift Tubes (DT) and Resistive Plate Chambers (RPC). The Resistive Plate Chambers along with the Drift Tubes (DT) detectors are installed in the barrel region to give the space and timing information. The CSC detectors are installed along with the RPC in the endcap region to give the timing information. The CMS muon system is shown in the Fig. 2.9.

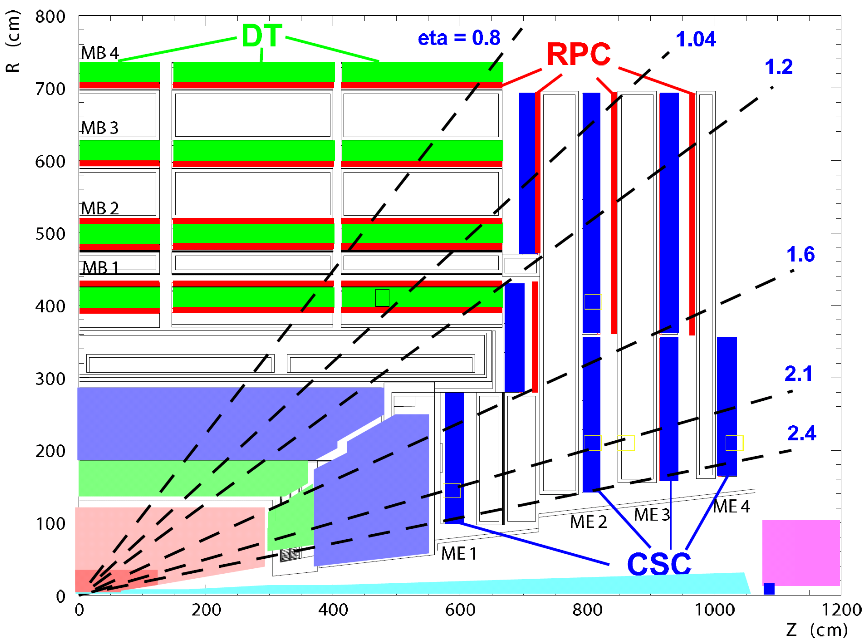

Figure 2.9: The layout of one quadrant of CMS experiment with four DT stations in Barrel region shown in green (MB1 - MB4) and four CSC shown in blue (ME1 - ME4) stations in the endcap region and RPC shown in red in the Barrel and endcap region.

Drift Tube System

The drift tube system consists of 172000 delicate wires arranged in 4 stations in a cylindrical geometry along the beam pipe in the barrel region. The drift tube chambers cover a pseudorapidity region up to $|\eta| \leq 1.2$. This is the region where the neutron flux is very small. The DT with rectangular drift cells are arranged in such a way that each DT chamber is offset by half a cell in order to decrease dead area of the detector. The DT chambers are filled with 85% Ar and 15% CO_2. The ratio of the gas mixture is adjusted such that the maximum path and time is 21 mm and 380 ns. There are five wheels of the CMS detector and each wheel of the CMS detector is than divided into 12 sectors. Each sector making an angle of 30° as shown in Fig. 2.10. In each sector of the wheel, there are four muon chambers installed which are labelled as MB1, MB2, MB3 and MB4.

The drift tube is made of 3 or 2 super layers (SL) and each super layer is made of 4 layers of drift cells. The whole structure is housed inside the honey comb panel which separates the outer super layers(s) from the inner ones. In the super layers the wires are arranged in such a way that one wires in one layer are perpendicular to the beam pipe and other has wires being parallel to the beam pipe. A charged particle coming from the interaction point first enters into ϕ measuring super layer and than enters the z-measuring super layer and finally passes through the second ϕ measuring super layer.

Cathode Strip Chambers – CSC

The CMS endcap muon system consists of the CSCs and the RPCs and covering the pseudorapidity range 0.9 $|\eta| \leq 2.4$. The CSC like the DT measures the position of the charged particle. The RPC and the CSC are installed in the endcap where the magnetic

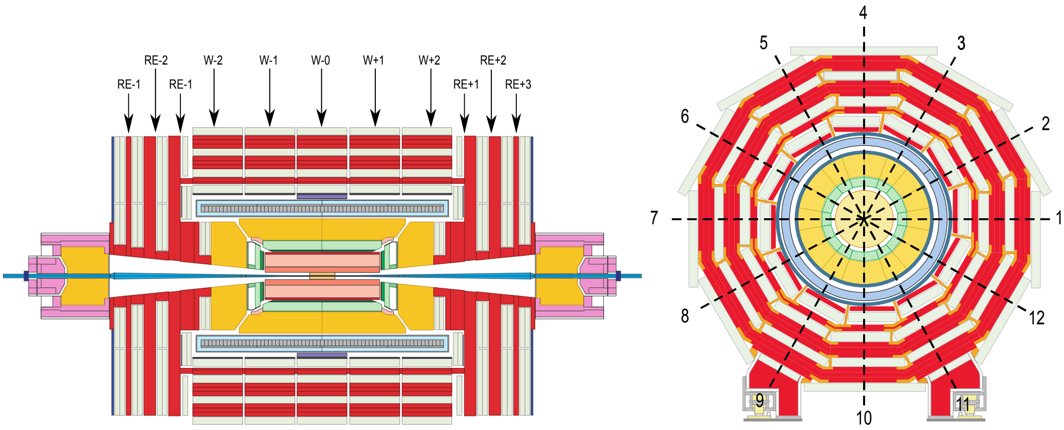

(a) (b)

Figure 2.10: The five wheels of the CMS detector labeled as W0, W $\pm$ 1, and W $\pm$ 2, 3 (a) the endcap rings on each side of the interaction point labeled as RE $\pm$ 1, RE $\pm$ 2 and RE $\pm$ 3. (b) The transverse view of the one of the five wheels of CMS detector.

field is not uniform and the flux of the particle is large. The CSCs are gaseous detectors with a total area of about $5000\,\mathrm{m}^2$, a total volume of gas being $\geq 50\,\mathrm{m}^3$ and the total number of wires is about 2 Million. CSC work in the avalanche mode and characterized by the short drift length. The gas mixture of Ar, CO_2 and CF_4 are used to fill the chambers are in a ratio of 30%, 50% and 20% respectively. These multi wire proportional chambers consists of 6 anode wire planes interleaved among 7 cathode panels running in radial direction with reference to beam pipes. The position of the incoming particle is collected both in the anode wire and in the cathode strips. The anode helps in trigger purposes while the cathode strips helps to perform center of gravity measurements ensuring the high resolution in position.

Resistive Plate Chambers – RPC

The RPCs are used in both barrel and endcap regions. In the barrel region the RPCs are used together with the DT. The DT detectors gives the spatial resolution while the RPCs give the timing information. Similarly in the endcap region the RPCs are combined with CSC to get the timing and spatial information. The RPCs are gaseous detectors with excellent timing resolution and beecause of its timing resolution they used to ensure the precise bunch crossing identification in the muon trigger system. The RPC also play an important role in global trigger. Figure 2.12 shows a cross-section of RPC detector. It is a double gap gaseous ionizing detector made from high resistive material such as bakelite with the bulk resistivity of 10^9 - $10^{10}\Omega\,\mathrm{cm}$. The two sheets of Bakelite are separated with a gas gap of 2 mm. The bakelite sheets are coated with graphite paint which acts as an electrode that are set at 9.5 kV. A gas mixture of freon ($C_2H_2F_4$), isobutane (C_4H_{10}) and SF_6 in the ratio of 95.5%, 3.8% and 0.3% respectively. The SF_6 gas is used as an quenching agent for the excess amount of charge produced. The readout if performed by means of copper strips separated from the graphite coating by an insulating Polyethylene (PET) film. The dead time of the RPC detector is around 3 ns, the time resolution is 3 ns and efficiency is about 97% [109].

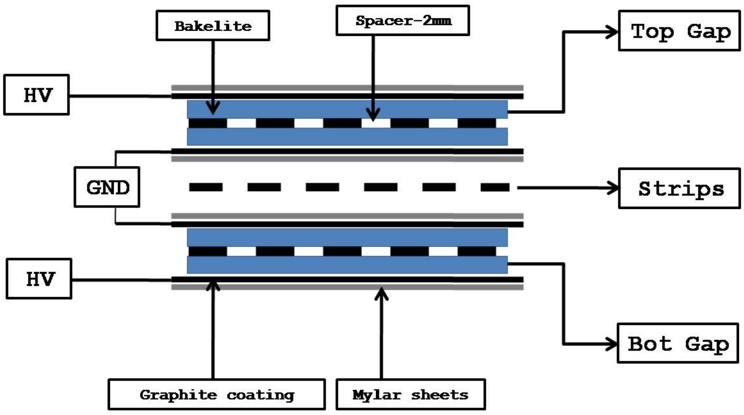

Figure 2.11: The RPC detectors built for CMS experiment for the detection of muon. A cross-section of the RPC detector is shown here.

2.2.6 Trigger and Data Acquisition System

The designed luminosity of the LHC experiment is $10^{34}\,\mathrm{cm}^{2}\,\mathrm{s}^{-1}$. At this luminosity the total number of expected proton-proton collisions are 20 per bunch crossing. The bunch crossing interval for the proton in the LHC beam pipe is 25 ns and this corresponds to a bunch crossing frequency of 40 MHz. The typical size of an event is about 1 MB and at this rate it would be impossible to record the data and manage at this frequency. The final storage system can only handle data up to 100 Hz. So the system has to be developed which can reduce the event frequency from 40 MHz to 100 Hz. The total reduction rate is roughly of the order 10^5. In order to reduce this rate a trigger system is developed such that it selects only those events which are relevant for the physics analysis. The trigger system can be divided into two main categories hardware level triggers, L1T [110] and software level triggers, HLT [111].

The Level-1 triggers are hardware level trigger which take information from calorimeters and muon stations on every bunch crossing, and take a fast decision whether the event is to be accepted or rejected and reduce the event rate to less than 100 kHz. In contrast to L1 triggers, the HLT are software level triggers running on large number of computers which can reduce the event rate, which as a result is easily written on the storage tapes. The architecture of the CMS data acquisition system is shown in Fig. 2.13. The information coming from a detector is buffered in a pipeline. The Detector information is forwarded to the readout system after receiving a Level-1 trigger acceptance. The event manager is responsible for the data flow. The builder network splits the information and than passes on to the Higher Level Trigger. The schematic architecture of the CMS DAQ system is shown in the Fig. 2.13

The CMS computing infrastructure follows the hierarchical distribution [113]. The first copy of the data, i.e., the raw data coming out of the detector readouts is stored at CERN which is named as Tier-0. The initial processing is performed at CERN before it is transfered to other Tier-1 centers around the world. There are 7 Tier-1 centers in total. The data from Tier-0 is reprocessed again to improve the quality of the physics objects used in the analysis. This improved quality data is transfered to another layer of Tier-2 is added which stores the copies of Monte Carlo simulation and data. There are a total 40 Tier-2

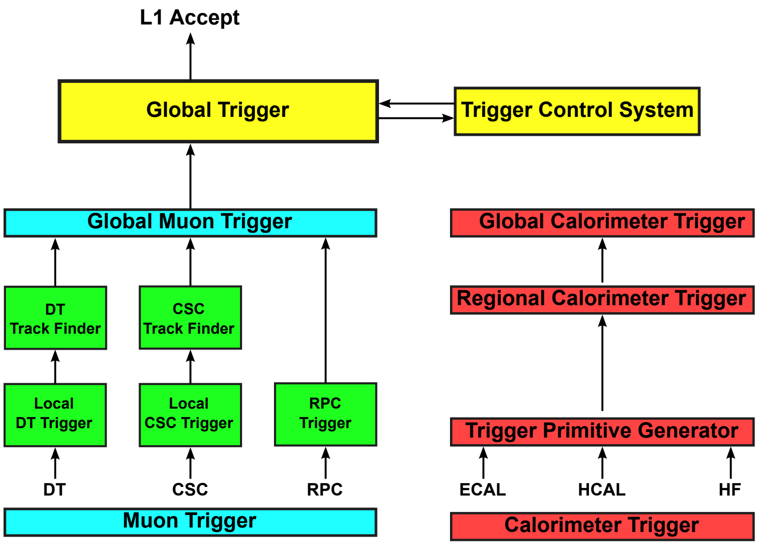

Figure 2.12: The CMS Level-1 trigger divided into three main categories, the muon trigger, the calorimeter trigger and the global trigger. The first two triggers do not accept or reject any thing, the candidates are passed to the global trigger to accept/reject.

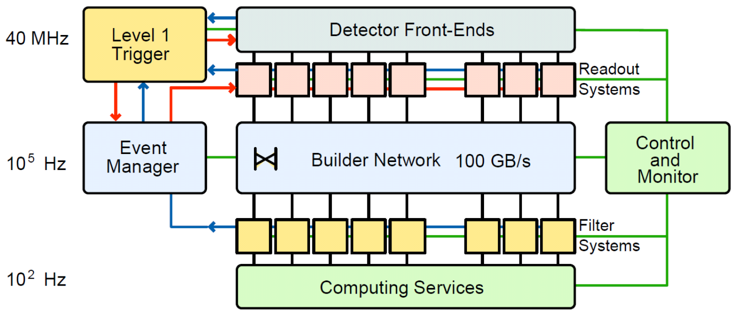

Figure 2.13: A schematic architecture of the CMS DAQ system [112].

centers around the world.

Chapter 3

Event Generation, Simulation and Reconstruction

In the following, a general introduction to the various event generators and comparison among them are presented. In the next section, a discussion of various physics objects which includes jets, missing transverse energy, leptons and the photons are presented. The various algorithms used in the reconstruction of these physics objects are also described, than various tools used in the physics analysis are presented at the end.

3.1 Event Generators

The event generators are the tools used in experimental high energy physics for the simulation of collision process. The Monte Carlo generators are used to simulate the real experimental conditions. These simulated events are used to calibrate and optimize the selection cuts used in the physics analysis. The Monte Carlo generators are based on principle of random number generators to simulate the real life collision of two particles. The whole chain from the generation of particles to the detection of particles can be categorized in the three major steps.

The hard process generation is in fact the simulation of interaction of proton-proton and also the simulation of newly created particles. The hard process generation is based on the information obtained from the parton distribution functions and the theoretical predicted probability densities using the Feynman rules for the process under observation. The processes mentioned above are well understood when we are simulating a particle interaction with high momentum transfer Q but when we have a small momentum transfer for the massless particles the calculations do not converge. We have ultra-violet and infrared divergences. We need to take into account these radiations and confinement in the process of hadron formation or a process known as Showering and Hadronization. Within showering the initial state and final state radiations are also approximated to higher corrections. In parton showering the partons are modeled down to the scale $\alpha_s \approx 1$ using the DGLAP equations, this is the scale at which non-perturbative hadronization starts [114–116]. During the process of hard process generation and showering if two different tools are used one should apply the matching procedure so that the double counting of the parton emission in the common phase space can be avoided.

After the showering and hadronization the interaction of particles produced in the second

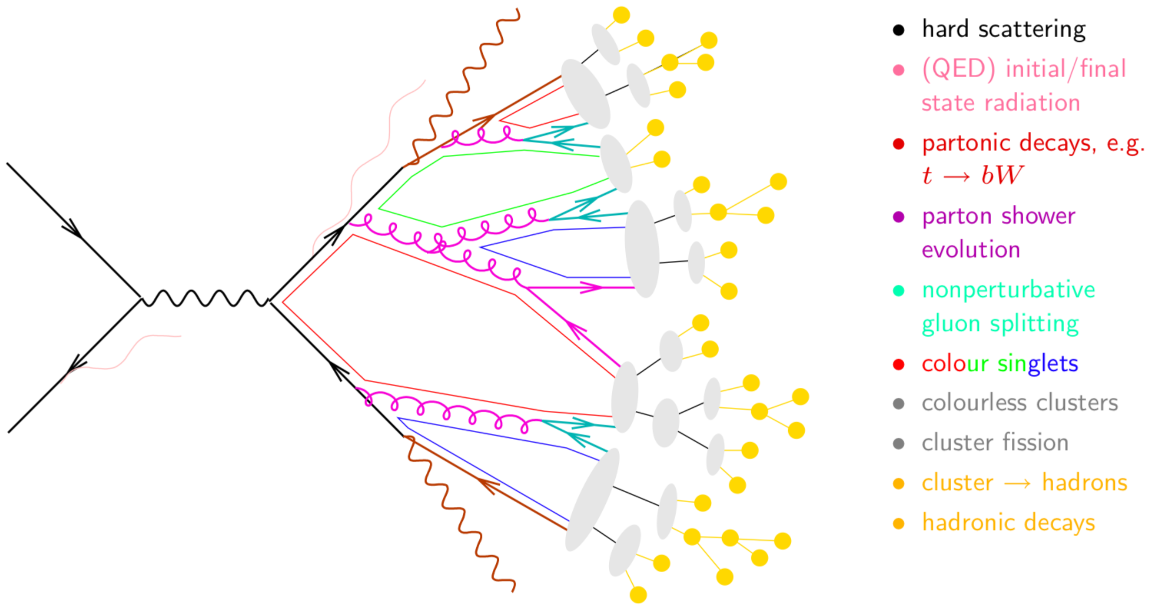

Figure 3.1: The diagram representing an electron and positron annihilating into a Z-boson and its subsequent decay into a top anti-top pair. The brown lines also show the subsequent decay of each top into a Wand (anti-)bottom quark adapted from [117]

step, the detector effects are now simulated. The detector geometry and all other parameters are added to the simulation of generated particles. The final out come of all these process should be comparable to real data obtained from the detector. In the following few most important Monte Carlo generators used will be discussed briefly. However the complete and detailed overview can be found at [118].

Underlying Events – UE

During the process of collisions there are more than just two partons. These partons interact with each other, hadronize and produce other particles. At the CMS experiment these effects are summarized in underlying event description, using Z*2 tunes.

Pileup Events – PU

Due to the high instantaneous luminosities multiple interaction can happen when the two proton bunches cross each other at the LHC. There is a non-negligible probability that in each bunch crossing there are several separate events which are produced. These events are called the pileup events and are described by PYTHIA in simulation. In order to calculate the number of pile-up events one needs to know the luminosity per bunch crossing, at the end all of the monte carlo simulation's pile-up distribution has to be re weighted with distribution obtained from data.
Since the detector is not able to distinguish between a signal-like event and an additionally produced pile-up event, therefore the data coming from a detector is a combination of both signal-like event and an additional pile-up event. Therefore one needs to take the correct modeling of underlying pile-up events in monte carlo simulation before they can be compared from the LHC data. For a $\sqrt{s}$ = 8 TeV, around 20 pile-up interactions are

seen per event in the LHC data, and for $\sqrt{s} = 13\,\text{TeV}$ expected number of PU interaction per event are around 135.

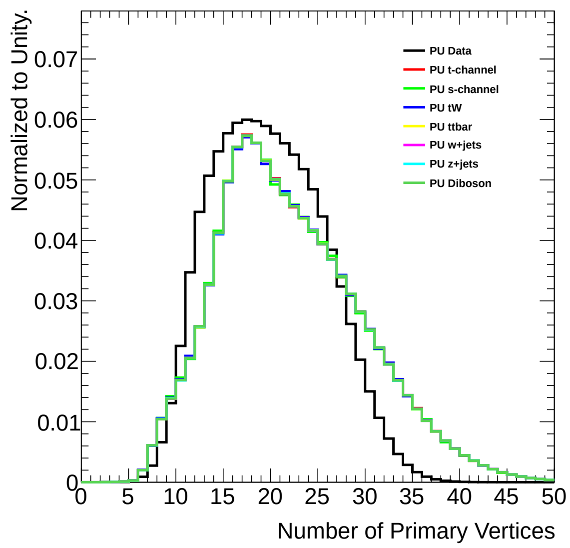

Figure 3.2: The pileup distribution for data and monte carlo simulation at $\sqrt{s} = 8$ TeV. The PU distribution in monte carlo simulation is re-weighted to the distribution obtained from data. All the monte carlo simulations used in the analysis follows the same pile-up distribution.

3.1.1 PowHEG

The PowHEG is a technique in which a hard physical process is interfaced with NLO parton showering calculations [119–121]. As explained earlier the general problem which one may face is the double counting of partons when interfacing the NLO hard scattering process with leading order showering. The Positive Weight Hardest Emission Generator method abbreviated as PowHEG deals with the problem very efficiently using the positive event weight technique.

3.1.2 MadGraph

It is a matrix element generator [122], which can be interfaced and used with multipurpose event generator MadEvent [123]. The physical process under observation is given to MadGraph which automatically calculates the amplitudes for different processes and than mapping is performed for the integration over the phase space. The MadGraph does not do any hadronization or showering. This can can be done with Pythia [124] or the Herwig++ [125]. The generated events with all the information is than stored in Les Houches Event Files (LHEF) format [126] before they are passed for the showering and hadronization in the dedicated packages.

3.1.3 CompHEP

The CompHEP [127] is based on the idea of calculating the cross-sections and various distributions from the Lagrangian directly. Unlike other generators CompHEP does not include recalculated matrix elements library but the matrix elements for the defined process are calculated symbolically using the Feynman rules.

3.1.4 Pythia

The Pythia is one of the most widely used event generator tool to simulate the real condition during high energy collision process which results in a production and decay of various particles [124]. It can be used as a standalone package for the generation of physics process and it can also be interfaced with other packages for the showering and hadronization.

3.1.5 Detector Simulation and Data Set

The events generated with a generator are now passed to detector simulation using the package GEANT [128]. Before the simulated data can be compared with real data the, the interaction of generated particles with the detector material, the magnetic field and the response of the detector subsystems have to be simulated. The multiple scattering, hadronic interactions, bremsstrahlung and electromagnetic interactions are taken into account during the process of detector simulation.

Table 3.1: List of simulated datasets. The value of different subprocess cross sections, taken from [129] at NNLO calculations except for diboson production which is calculated at NLO precision. The name for the data set is given in the firt column, second gives the official data set name, third gives the number of simulated events and the fouth gives the cross section multipled with corresponding leptonic branching ratio.

Sample	Official Dataset Name	# No. of Events	$\sigma\cdot$ BR[pb]
t-channel(t)	/TToLeptons_t-channel_8TeV-powheg-tauola/Summer12_DR53X-PU_S10_START53_V7A-v1/AODSIM	3914913	56.4×0.324
t-channel($\bar{t}$)	/TBarToLeptons_t-channel_8TeV-powheg-tauola/Summer12_DR53X-PU_S10_START53_V7A-v1/AODSIM	1711095	30.7×0.324
s-channel(t)	/T_s-channel_TuneZ2star_8TeV-powheg-tauola/Summer12_DR53X-PU_S10_START53_V7A-v1/AODSIM	3932002	3.79×0.324
s-channel($\bar{t}$)	/Tbar_s-channel_TuneZ2star_8TeV-powheg-tauola/Summer12_DR53X-PU_S10_START53_V7A-v1/AODSIM	1999326	1.76×0.324
tW(t)	/T_tW-channel-DR_TuneZ2star_8TeV-powheg-tauola/Summer12_DR53X-PU_S10_START53_V7A-v1/AODSIM	497569	11.1
tW($\bar{t}$)	/Tbar_tW-channel-DR_TuneZ2star_8TeV-powheg-tauola/Summer12_DR53X-PU_S10_START53_V7A-v1/AODSIM	493382	11.1
$t\bar{t}$ semileptonic	/TTJets_SemiLeptMGDecays_8TeV-madgraph/Summer12_DR53X-PU_S10_START53_V7A_ext-v1/AODSIM	86798454	245.8×0.438
$t\bar{t}$ fully leptonic	/TTJets_FullLeptMGDecays_8TeV-madgraph/Summer12_DR53X-PU_S10_START53_V7A-v2/AODSIM	12009320	245.8×0.104
$t\bar{t}$ hadronic	/TTJets_HadronicMGDecays_8TeV-madgraph/Summer12_DR53X-PU_S10_START53_V7A-v1/AODSIM	10515175	245.8×0.456
W+2jets	/W2JetsToLNu_TuneZ2Star_8TeV-madgraph/Summer12_DR53X-PU_S10_START53_V7A-v1/AODSIM	34040035	2159.20
W+3jets	/W2JetsToLNu_TuneZ2Star_8TeV-madgraph/Summer12_DR53X-PU_S10_START53_V7A-v1/AODSIM	15537065	640.40
W+4jets	/W2JetsToLNu_TuneZ2Star_8TeV-madgraph/Summer12_DR53X-PU_S10_START53_V7A-v1/AODSIM	13380573	264.00
Z+jets	/DYJetsToLL_M-50_TuneZ2Star_8TeV-madgraph-tarball/Summer12_DR53X-PU_S10_START53_V7A-v1/AODSIM	30455398	3503.71
diboson (ww)	/WW_TuneZ2star_8TeV_pythia6_tauola/Summer12_DR53X-PU_S10_START53_V7A-v1/AODSIM	9998866	54.83
diboson (wz)	/WZ_TuneZ2star_8TeV_pythia6_tauola/Summer12_DR53X-PU_S10_START53_V7A-v1/AODSIM	9998663	33.21
diboson (zz)	/ZZ_TuneZ2star_8TeV_pythia6_tauola/Summer12_DR53X-PU_S10_START53_V7A-v1/AODSIM	9798339	8.05

For the analysis described in this thesis, the full 8 TeV dataset is used. Only those runs are considered in this analysis in which the CMS detector has been fully operational. Therefore a certified JSON file, listing all runs of the given datasets that are considered good, has to be applied to the dataset, depending on all those lumi-sections marked bad by the detector performance group (DPG) are excluded from this JSON file [130].
The total integrated luminosity corresponding to this JSON file is 19.7 fb^{-1}. Table 3.1 gives the list of simulated data sets used for the differential and inclusive cross-section measurements. The simulated samples used are taken from the `Summer12` cycle of CMS Monte Carlo production and are produced using the 5_3_11 release of the CMS software CMSSW.

3.1.6 Signal Modeling

The single-top-quark samples used for analysis are generated using the POWHEG and it give very good results for the electroweak single-top-quark production at present. MADGRAPH is used for the generation of $t\bar{t}$, W+jets and Z+jets. PYTHIA is used for the generation of diboson (WW, WZ, ZZ) samples.

A comparison of different kinematic variables is presented in the following using a Monte Carlo samples generated from POWHEG and COMPHEP after applying the selection cuts at the parton level. The mass of the top-quark used is $m_{\mathrm{top}} = 172.5\,\mathrm{GeV}$ and the parton distribution function PDF used in POWHEG is NLO CTEQ6M [131], for COMPHEP PDF used is CTEQ5M. The Figures 3.3 to Figures 3.8 represents the shape comparison of POWHEG and COMPHEP of various important kinematic variables in the t-channel single-top-quark production in the electron and the muon channel.

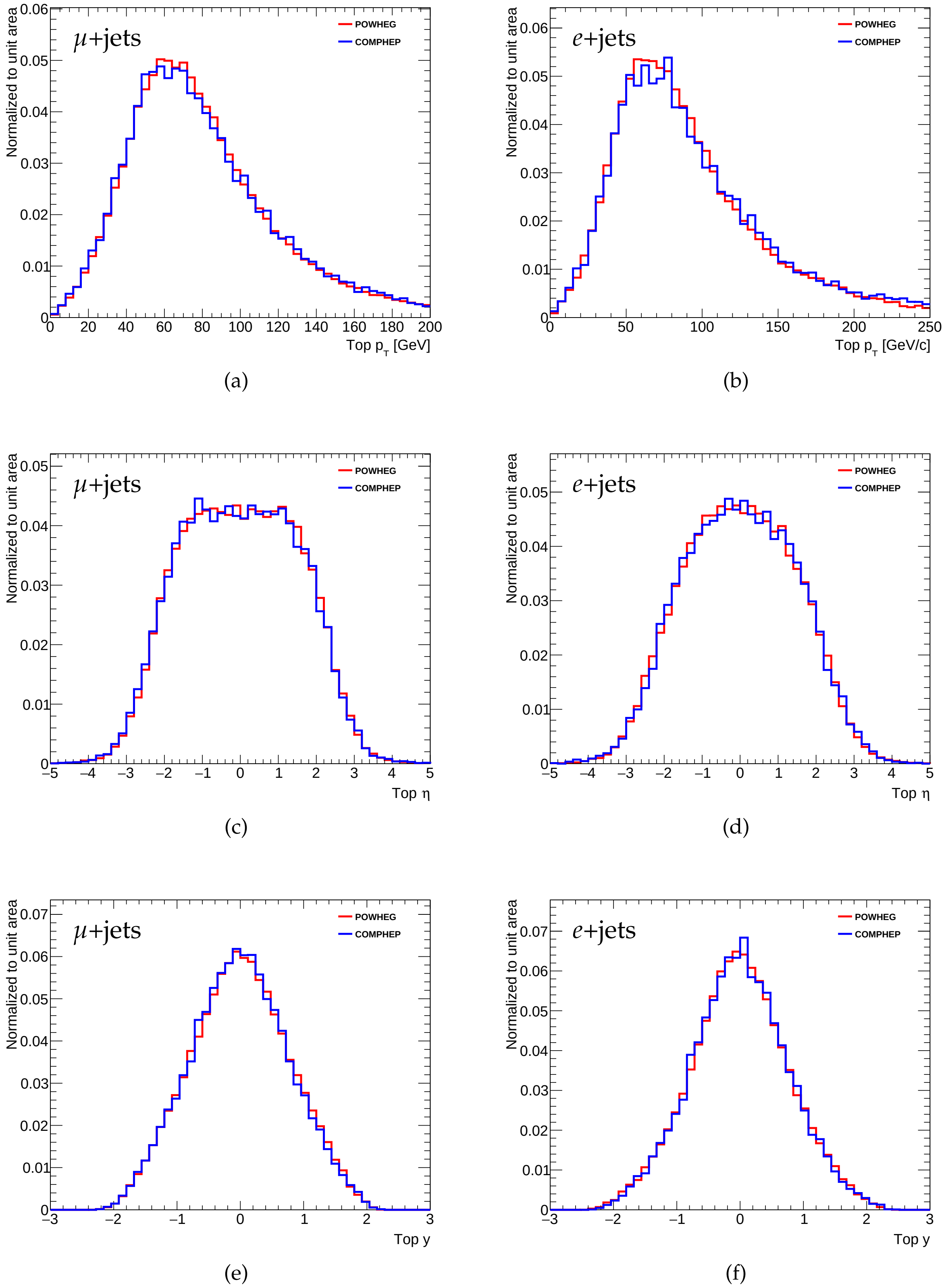

Figure 3.3: (a) - (f) top-quark p_{T}, η and y in the muon(electron) channel for PowHEG and CompHEP at generator level.

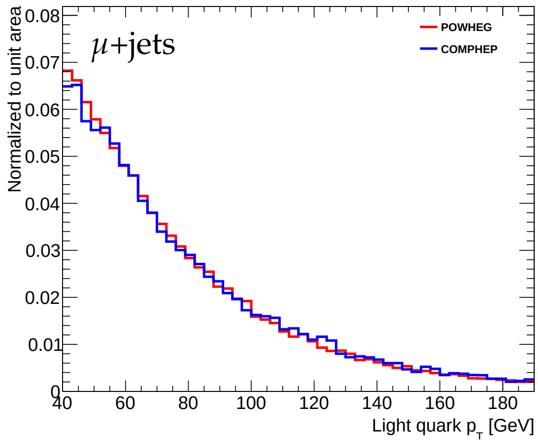

(a)

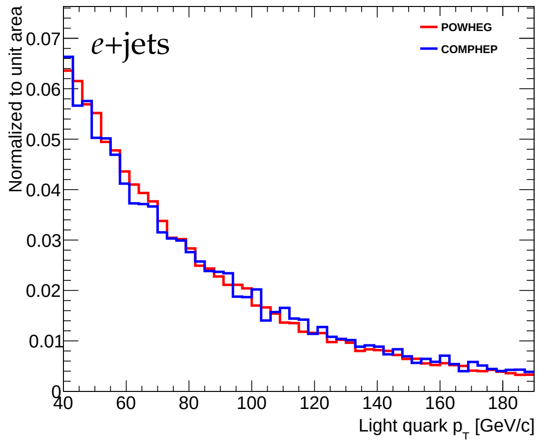

(b)

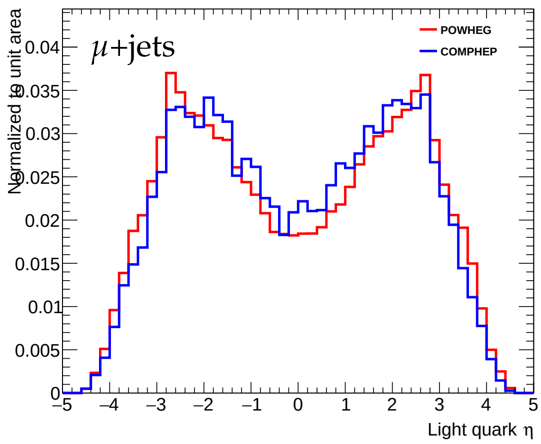

(c)

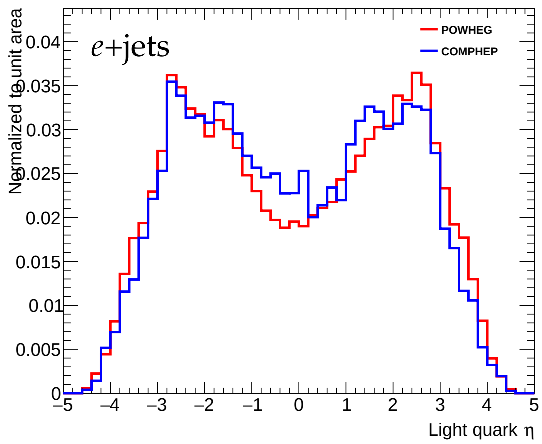

(d)

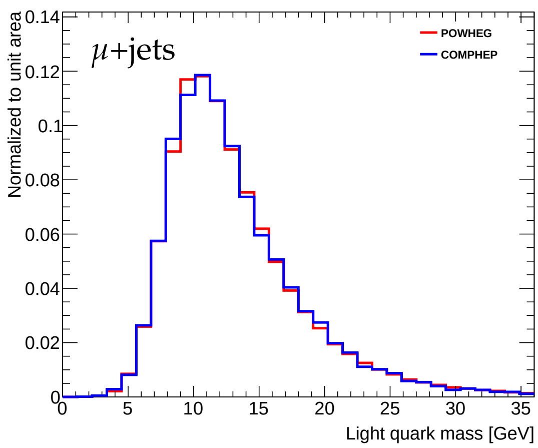

(e)

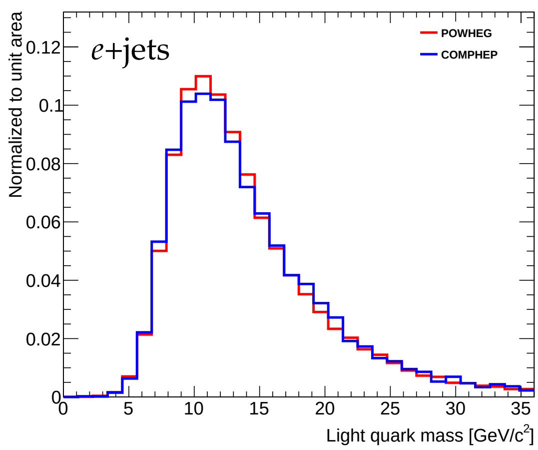

(f)

Figure 3.4: (a) - (f) Light quark p_{T}, η and mass in the muon (electron) channel for PowHEG and CompHEP at generator level.

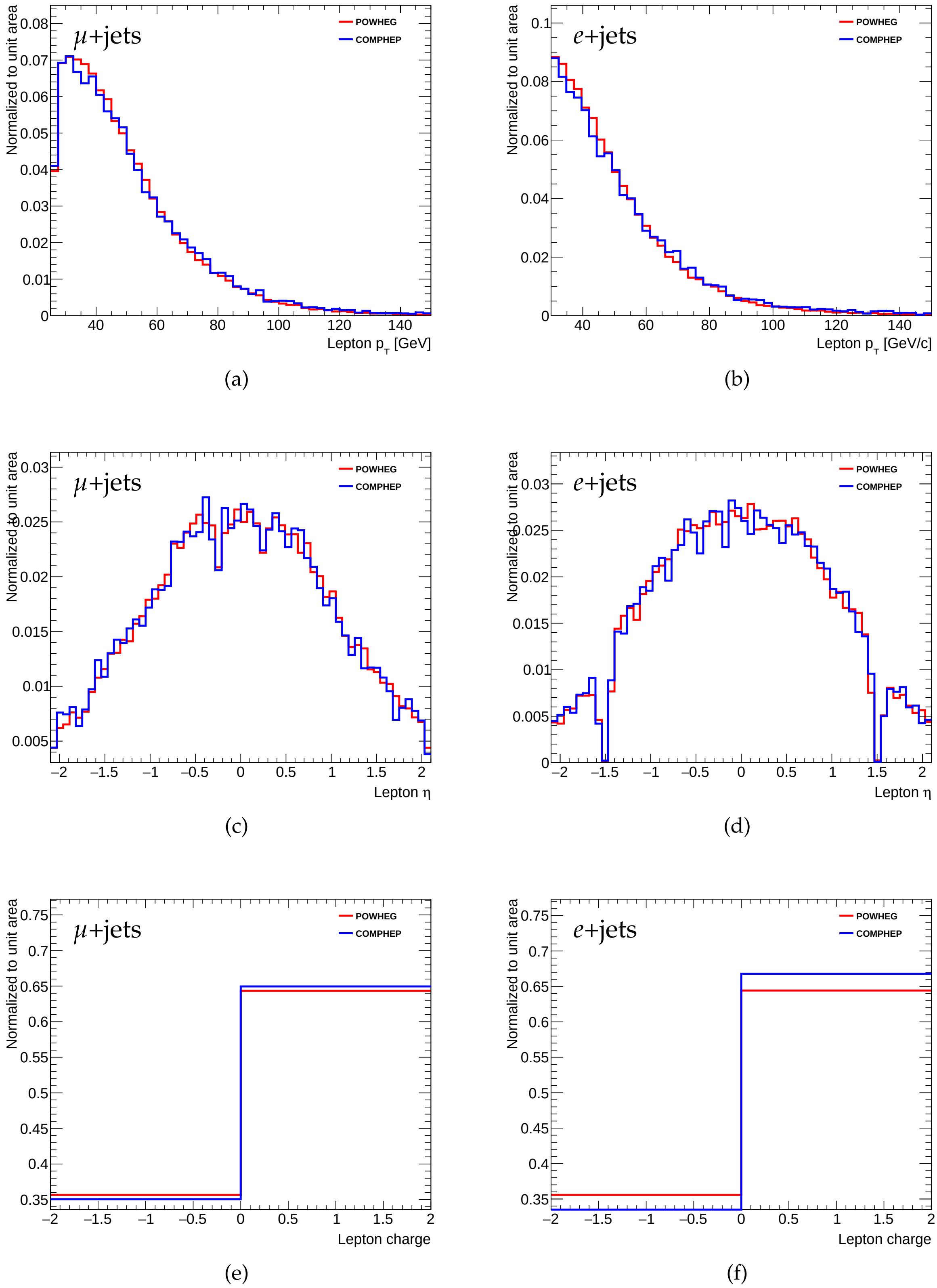

Figure 3.5: (a) - (f) Lepton p_{T}, η and lepton charge Q_l in the muon (electron) channel for PowHEG and CompHEP at generator level.

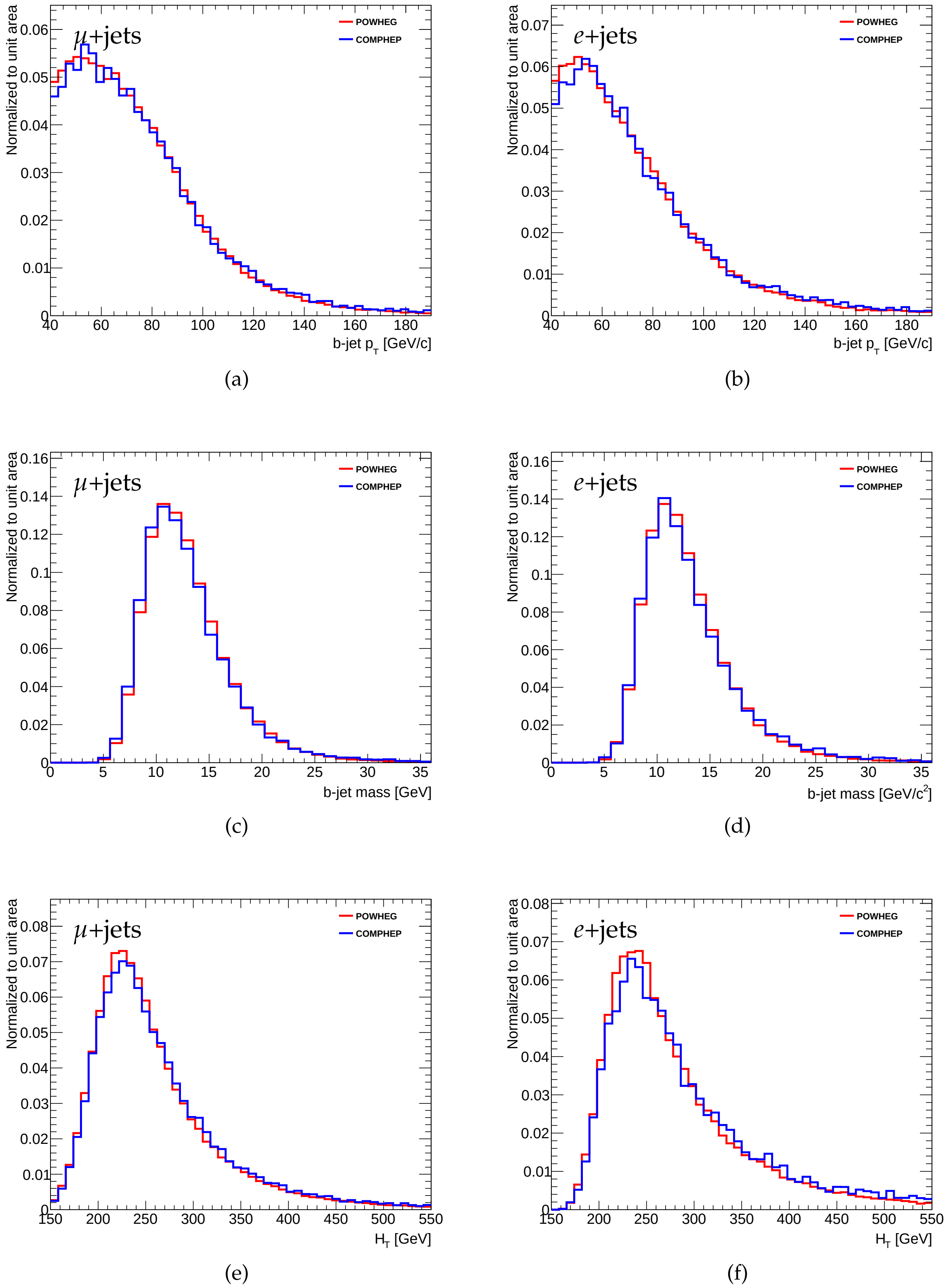

Figure 3.6: (a) - (f) b-quarks p_T, η and H_T in the muon(electron) channel for PowHEG and CompHEP at generator level.

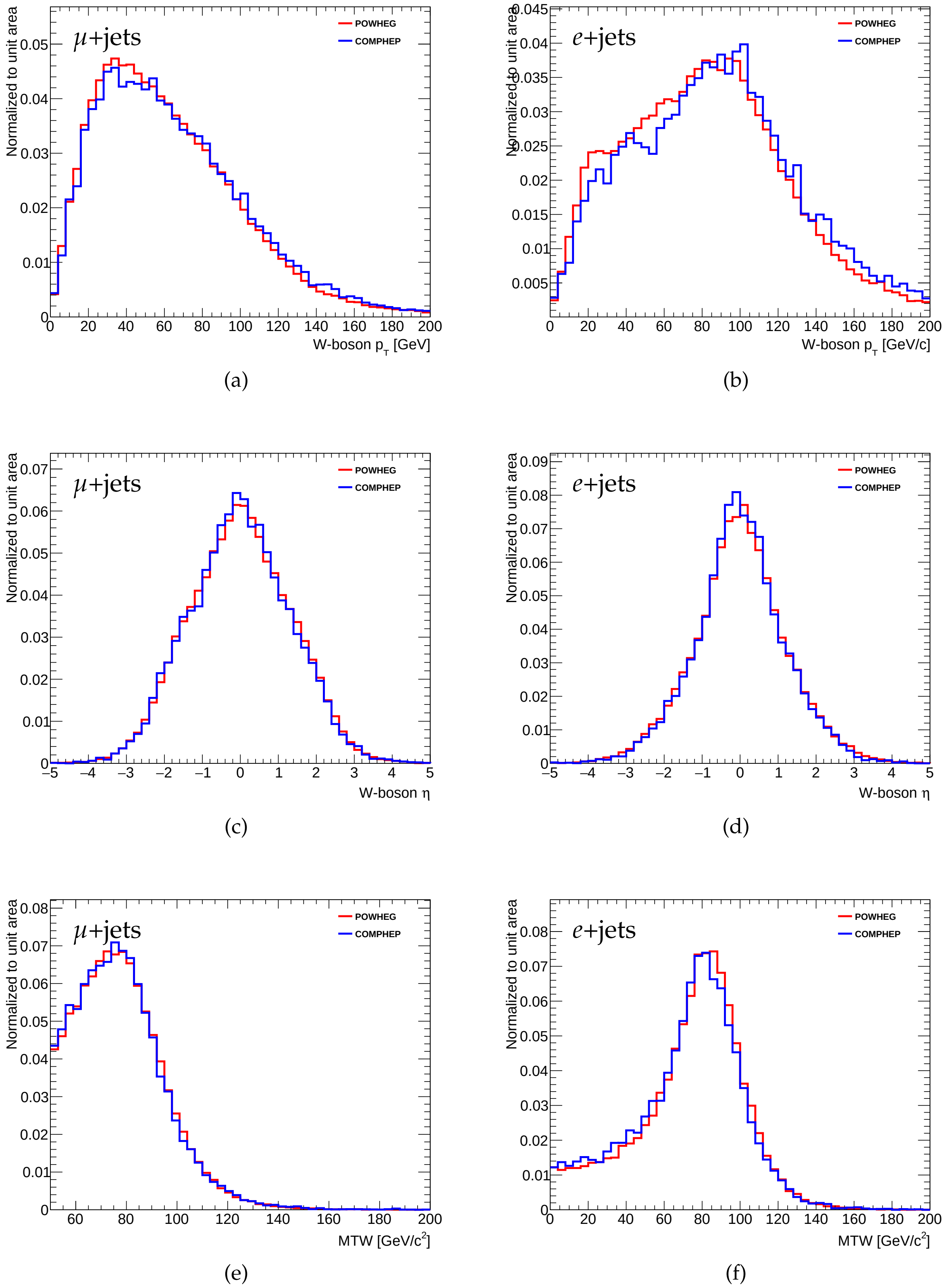

Figure 3.7: (a) - (f) W-boson p_T, η and m_T in the muon(electron) channel for PowHEG and CompHEP at generator level.

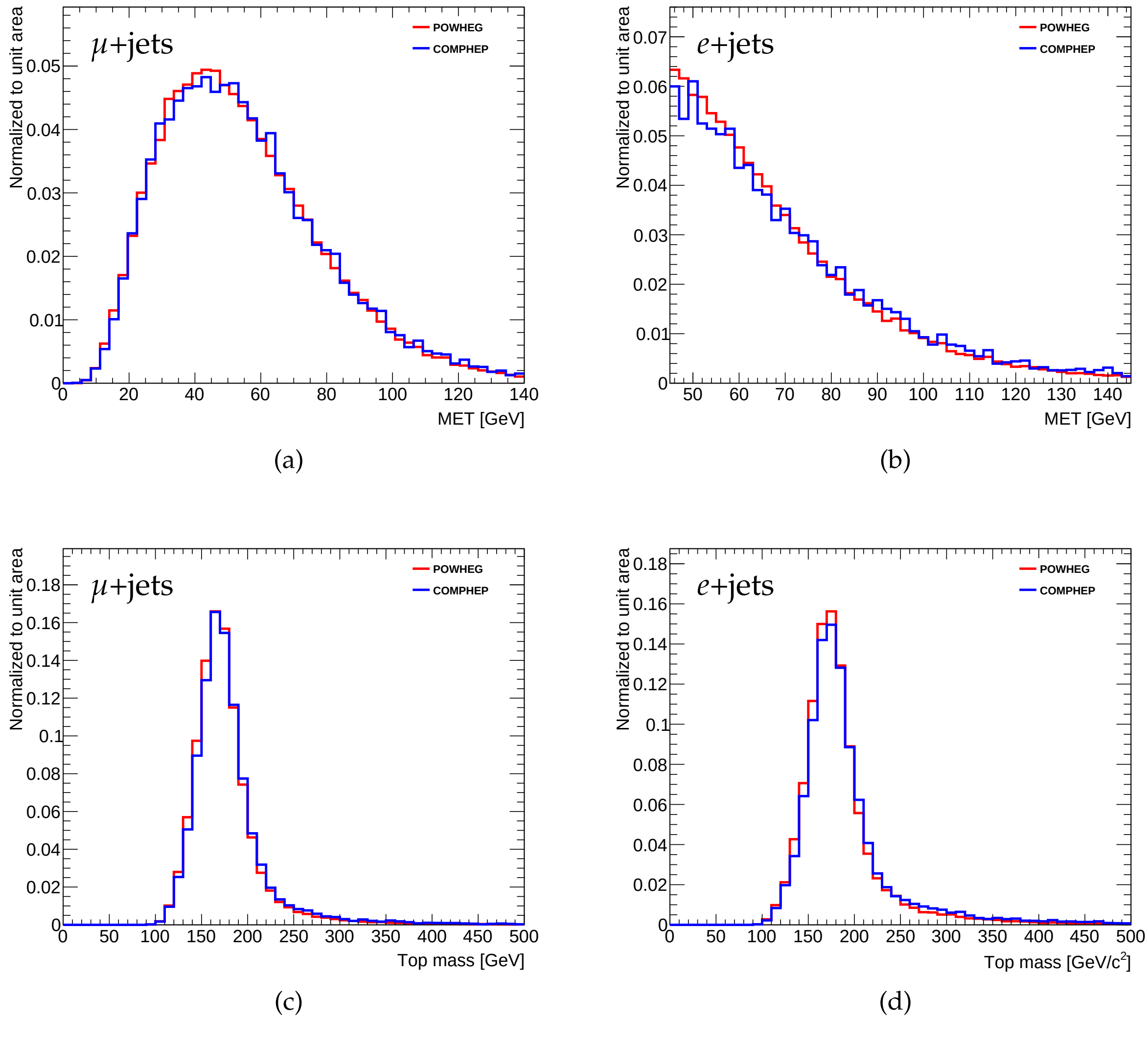

Figure 3.8: (a) - (d) $\not{E}_{\mathrm{T}}$ and $m_{\ell\nu b}$ in the muon(electron) channel for PowHEG and CompHEP at generator level.

3.2 Physics Objects

The information collected by the sub-detectors installed at the CMS experiment is used to reconstruct the physics objects with an off-line software. These software allow the identification of particles traversing through the CMS detectors by measuring its momentum, energy, charge and other parameters which are helpful during the physics analysis. The main physics objects reconstructed using the off-line softwares are muons, electrons, Taus, Jets, MET, Photons. In the following, we describe the structure in which an event is stored and the reconstruction of these physics objects in CMS experiment before they are used for a specific physics analysis.

Event Data Model – EDM

The Event Data Model (EDM) is the general structure in which all the data recorded in a CMS experiment is written. The EDM basically provides access to all the information written to it, e.g., one can access all the physics analysis objects simulated or real. It also contains all the information about the raw data and the provenance of all derived data products. This provenance information gives a probe to a user so that at any stage the complete information regarding the origin of an event can be traced out. With EDM model all the physics modules can read data from it or add new data to it with complete history of an event written automatically. All the information stored in this format is written to the ROOT files. There are several types of modules written and each module performs a specific task whether it is the event selection, event reconstruction or physics analysis.

There are several event formats with differing levels of detail and precision, allowing to achieve the necessary level of data reduction for each analysis. One can add or remove different level of data layers which results to read and write data very quickly. The three main data tiers used in the CMS simulated data production:

RAW i.e. the data which comes directly from the detector, it contains information regarding the detector objects, trigger bits. The typical size of single event of a RAW data is about 1.5 MB where as the typical size of the simulated data event is about 2 MB. The size of simulated event is larger since it contains other information like MC truth information.

RECO data is a short hand for the Reconstructed data. The input of the RECO is the RAW data which after the application of several pattern recognition like track finding, primary and secondary vertex reconstruction, clustering and compression algorithms results in the RECO data format. The typical size of a RECO event is about 0.5 MB.

AOD which stands for Analysis Object Data is a data tier which contains physics objects which can be used for the specific study. It also contains sufficient information which can be used to perform kinematic fitting if needed. The typical size of the AOD event is about 100 KB, which orders of magnitude small when compared to the RECO.

3.3 Tracks

During high energy collisions large number of charged particles are produced. These charged particles are detected at the inner tracker of the CMS experiment. Due to the presence of a strong magnetic field and to initial projection angle of a charged particle these charged particle follow a helical path due to the Lorentz force. The transverse momentum of a charged particle is directly proportional to the magnetic field B and radius of curvature $r_{\text{curv.}}$. Mathematically it can be written naively as:

$$p_{\text{T}} \propto B \times r_{\text{curv.}} \tag{3.3.1}$$

The charged particles when passing through the inner tracker produce hits. These hits are recorded and then fitted with track reconstruction algorithm. The set of these three dimensional coordinates are fitted using these algorithms. The two track recognition algorithms which the CMS experiment uses are the Kalman-Filter (KF) [132, 133] and the Gaussian Sum Filter (GSF) [134].

Kalman-Filter

The Kalman-Filter algorithms fit the track through a set of three dimensional points. The starting point of the algorithms is a seed which is found by looking at all the hits in the tracker. These hits are used to get the direction of trajectory of the particle. The Kalman-Filter progresses iteratively to the next layers on the calculated path and than looks for other hits in the tracker without producing any conflict with the current track and satisfies the initial threshold for hit to be a valid hit. The algorithm now reaches the next layer with the help of curvature of the track and energy loss in the material. As there are more than one hits the Filter iterates through the complete list of all the valid hits and the position of each hit is re-evaluated using the new values of different parameters. As a second step towards the track reconstruction the other algorithms is initialized which runs in backward direction towards the primary vertex. These two steps help to evaluate the parameters related to each hits with high accuracy with emphasis on the first and the last hit.

The Kalman-Filter has one major draw back. Although its a draw back in Kalman-Filter but it helped towards the development of other filters. The Kalman-Filter undertakes the energy loss (radiative) and than re-corrects the momentum of the track with mean of energy loss in each forward step, at the same time the variance in the momentum is also increased by the energy loss distribution variance. As a result the Kalman-Filter gives the best result when the probability distributions are taken to be Gaussian.

Gaussian Sum Filter

The electrons lose their energy via bremsstrahlung radiation. The energy loss is a complicated process and cannot be described by single Gaussian but can be very well modelled by a weighted sum of Gaussian probability distributions as compared to the Kalman-Filter where it is modelled by a single Gaussian distribution. Using the GSF one can find the position of tracker hits with high accuracy in the subsequent layers which leads to more precise and accurate electron track reconstruction.

For the reconstruction of tracks, the hits produced by the charged particles in the tracker are combined using the combinatorial track finder [135]. The combinatorial track finder is based on the Kalman-Filter, which produces a collection of reconstructed tracks which in than can be used for the reconstruction of primary vertices. The primary vertex (PV) is a region of space or point where the hard scattering process takes place. The reconstruction of primary vertex is primarily based on the common origin of tracks. Minimum four tracks are required within the longitudinal distance of $\mid z \mid < 24\,\text{cm}$ along the beam direction and a distance of $\rho < 2\,\text{cm}$ in a direction perpendicular to beam direction. The proton in the two colliding beams tend to spread and diverge, this results in the fact that beam spot and primary vertex are not same. In this case there are several vertices which are reconstructed but the primary vertex is chosen from these vertices by taking the highest transverse momentum square of all the tracks. The tracks which are not coming from PV or its associated secondary vertices are considered as pile-up events and are thrown away from the events selected for the analysis. This is known as Charged Hadron Subtraction (CHS).

For the reconstruction of electron, photons, muon, taus, jets and missing transverse energy an algorithm known as Particle-Flow (PF) is used [136]. This algorithm takes information from all the sub detectors, e.g., energy deposits from electromagnetic calorimeter, hits from tracker or hits in the muon system and than reconstructs the stable particle individually. Figure 3.9 shows the pictorial view of PF algorithm as used for the reconstruction of PF candidates. The particle flow algorithm consists of the following steps [137]:

- Fundamental ingredients/inputs:
  - Calorimeter clustering
  - Tracking (with the tracker POG) and extrapolation to the calorimeters
  - Muon identification (from the muon POG)
  - electron pre-identification (with the e/gamma POG)
- Linking topologically connected elements
- Particle identification and reconstruction

It may sometime happens that there is an overlap of a lepton and jet. This overlap is removed by using the so-called the top projections.

3.4 Muons

The muons being charged particles are reconstructed best in the tracker. The muons mainly interact with the silicon detector but they loss almost negligible amount of energy during interaction. As a result the muons traverse through the whole volume of tracker by producing hits on different tracker layers. The muon reconstructed tracks are classified in three categories.

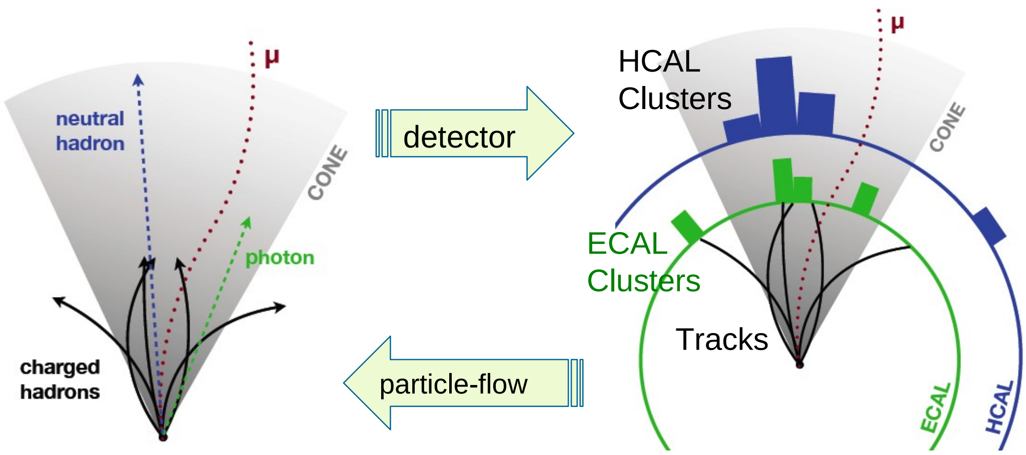

Figure 3.9: Illustration of the particle-flow concept to reconstruct every individual muon, electron, photon, charged and neutral hadron from a maximum of detector information. Taken from [138]

- **Standalone Muons:** If the muons are reconstructed using only the information from the muon system than the reconstructed muon is termed as Standalone Muons.

- **Tracker Muons:** The tracker muons are reconstructed using the tracker information. The inner tracker information is matched to the segments either in DT in case of Barrel region and with CSC if the reconstructed muon is in the end-cap region.

- **Global Muons:** The information from the tracker and the muon system is used for the reconstruction of muon candidate which can be termed as Global Muon. The inner tracks in the tracker are matched to the tracks in the muon system by considering the energy loss and multiple scattering in the calorimeter depending on some predefined threshold values. The parameters of the muons are estimated by applying the Kalman-Filter to the hits produced in the tracker and muon system [139].

The objects reconstructed from the information obtained from the tracker and the muon system are only muon candidates and they are further refined before they can be used for physics analysis. The baseline selection of the tight muon used in physics analysis for the 2012 data is described in detail in [140]:

3.5 Photons and Electrons

The electromagnetic calorimeter of the CMS detector is designed by giving an immense importance to the identification and measurements of photons and electrons. The main goals of the experiment were the discovery of Higgs boson and identification of some super-symmetric particles. Most promising channel for the Higgs discovery are H$\rightarrow \gamma\gamma$ and H$\rightarrow l^+l^-e^+e^-$ where $l = \mu, e$. As a result, an excellent resolution of the photon energy is required to separate a Higgs signal from background. Thus, the ECAL of CMS experiment is designed to measure photons with high precision and than information from the tracking detectors are combined for the identification and reconstruction of electrons. About 97% of the shower produced by the unconverted photons is contained in 5×5 matrix of crystals in η, ϕ plane. Nearly, half of the photons produced during the collision are converted into electron position pair in the tracker material. In case of electron the measurement is a bit more difficult because of the bremsstrahlung. The electron energy shower also spreads in ϕ direction due to the presence of strong magnetic field.

The photons in the ECAL of the CMS experiment can be identified and reconstructed with excellent resolution. The energy deposited by photons in 5×5 crystal matrix is recovered with high accuracy by using different algorithms. Also several other quality cuts tracker isolation, ECAL isolation, hadron calorimeter isolation, hadronic to electromagnetic ratio and R_9 is defined as the ratio of energy deposited in 3×3 crystal matrix ($E_{3\times3}$) and the total energy deposited in super cluster, are imposed to identify the true photons. Also R_9 is the quantity which is used to determine whether if the photon is converted or unconverted. If the ratio, R_9, of the possible candidate is above 0.94 (0.95) in the barrel (endcap) respectively, the energy of the 5×5 crystals matrix ($E_{5\times5}$) around the highest energy crystal is used. Otherwise, the super-cluster energy is used. It is important to note that R_9 threshold in case of endcap is a bit higher as compared to the barrel region. This is due to the large size of the ECAL crystal in the end-cap region.

The electrons and photons deposit their energy in the form of small or basic clusters. These basic clusters are than added together to form a super cluster. These super cluster after applying the energy corrections are used for the reconstruction of photons, electrons and for the track reconstruction of electrons. Further details on the matching of tracks to the super clusters are found in [141]. The candidates found are marked as electron candidate when a super-cluster can be associated with a track found in the silicon tracker. The electron reconstruction uses two additional complementary algorithms at seeding stage, namely, tracker driven and ECAL driven. The tracker driven seeding works much better for the low p_T electrons and also for the reconstruction of electron which are present inside a jet. While the former starts the reconstructions of ECAL super clusters of energy $E_T > 4\,\text{GeV}$. Since the photos do not produce any tracks therefore photons are reconstructed using the energy corrected super clusters.

3.6 Jets

The Quantum Chromodynamics (QCD) has two very important properties, namely 'confinement' and 'asymptotic freedom'. The confinement is a property which states that no isolated coloured charge can exist as a free particle but only colour singlet particles can be isolated. They form hadron (Baryon or Meson) which are color neutral particles. Confinement is due to the fact that the potential between two colour charges, for example a quark and an anti-quark, is a linear combination of Coulombic like part and a linearly rising term. The linearly rising term in the potential makes it energetically impossible to separate the two colour charges.

The asymptotic freedom is the property that the QCD coupling becomes weak at high energies, due to quantum corrections, so that the theory becomes perturbative in this regime. Purturbative in the sense that the theoretical predictions can be expressed in powers of the coupling constant, limited to the first few terms. During the high energy collision large number of particles and gluons are produced, these initially produced particles when grouped together in a collimated bunch in a certain direction is known as a "Jet". The reconstruction of these spray of particles in a certain direction is not an easy task especially in the LHC environment when in the interaction rate is very high. Dedicated algorithms are used for the reconstruction of these jets. The algorithms used should be fast, intelligent enough to understand the structure of hadronic shower, able to differentiate between signal event and pile-up event. The algorithms should be able to handle MC truth information and the detector objects form HCAL/ECAL and tracker. Jets reconstructed from the calorimeter are known as "Calo Jets". Jets reconstruction when it takes in the information from the inner tracker the reconstructed jet is known as "Jet Plus Track". Similarly when the information is taken from all the sub detectors for the reconstruction of jet the resulting object is known as "Particle-Flow Jet". Figure 3.10 shows an illustration of the jet reconstruction process in CMS.

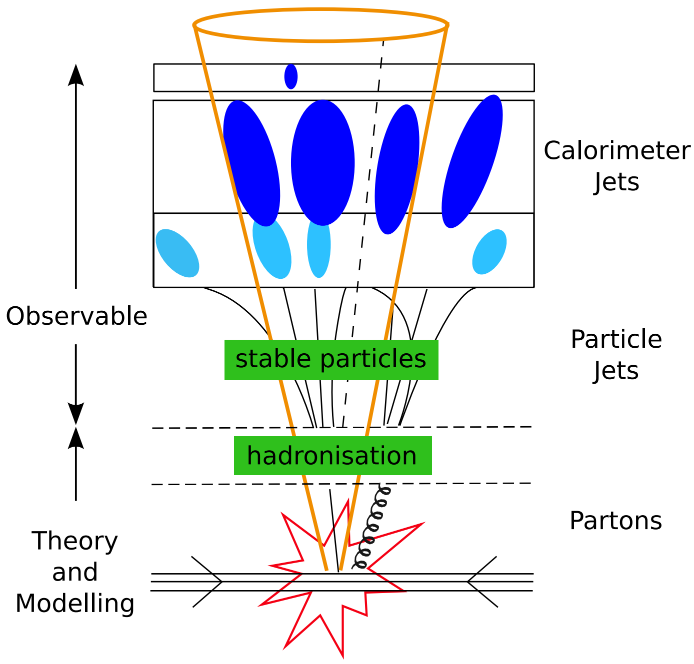

Figure 3.10: The figure shows how the evolution of jet takes place in a high energy proton proton or proton anti-proton collision process, taken from [142]. Energy deposits are marked as blue ellipses in the ECAL (bright) and HCAL (dark). They are used as input for jet reconstruction algorithms.

The energy and momentum of the jet should be reconstructed with high precision and accuracy. This helps to compare the measured distribution to the MC truth information and than one can draw a conclusion about the various theoretical predictions. There are two important pitfalls that have to be considered by jet algorithm.

Infrared Safe: The additional soft radiation present in an event, originating from soft gluon radiation in a hadron shower or detector noise or any soft radiation coming from an underlying event should not in any way effect the number of jets present in an event.

Collinearly Safe: The jet reconstruction algorithm should be collinearly safe, i.e., any particle splitting into two having the same momentum and energy in total should not change the algorithms output. The clustering of jets is basically done with two types of algorithms.

Iterative Cone Algorithms

As the name suggests works by clustering all the particles in given radius of the cone in the $(\eta - \phi)$ plane [141]. The algorithm takes in a list of particles or calorimetric entries which satisfies selection criterion ordered by transverse energy E_{T}. A proto-jet is built up from a particle with the highest transverse energy E_{T}. The current proto-jet is used as a seed for algorithm. The iteration stops when a certain criterion is reached. The criterion could be the direction of jet axis, energy or the maximum number of iteration steps. The object containing all this information is than stored as a stable object or interesting object. The object and its constituent are than removed from the list of calorimetric entries or particles, the algorithm repeats itself for all other objects in the list.

The cone algorithms are not infrared and collinearly safe since particles are included which are above certain threshold. Removing the threshold would be an alternate solution but this would require lot of computing power because there are huge number of particles produced in the LHC environment. A more advanced version of cone algorithm known as SISCone Algorithm, "Seed Less infrared Safe Cone Algorithm", is used, which is infrared and collinearly safe [143].

Sequential Clustering Algorithms

Sequential clustering algorithms when compared to the cone algorithm do not consider the shape of reconstructed jet. Rather it takes the distance between two objects under observation. Mathematically the sequential clustering algorithm can be written as:

$$\mathrm{d}_{i,j} = \min(p_{\mathrm{T_i}}^{2\mathrm{N}}, p_{\mathrm{T_j}}^{2\mathrm{N}}) \times \frac{(\Delta \mathrm{R})^2}{\mathrm{R}^2}, \tag{3.6.1}$$

where $\mathrm{d}_{i,j} = (\eta_i - \eta_j)^2 + (\phi_i - \phi_j)^2$ is the distance between two objects in the $\eta - \phi$ plane, $p_{\mathrm{T_{i,j}}}$ is the transverse momentum of the object $i,\ j$ and R is the resolution parameter which determines the size of the jet cone, ΔR is the distance between two jet objects in the $\eta - \phi$ and N is the free parameter for different methods of the distance calculation. The distance of the object k to the beam axis is given by:

$$\mathrm{d}_{\mathrm{beam,\ k}} = p_{\mathrm{T,\ k}}^{2\mathrm{N}}. \tag{3.6.2}$$

The clustering algorithm works in three steps. In the first step it calculates $\mathrm{d}_{i,\ j}$ and $\mathrm{d}_{\mathrm{beam,\ k}}$ while in the second step it computes all $\mathrm{D} = \min(\mathrm{d}_{i,\ j}, \mathrm{d}_{\mathrm{beam,\ k}})$.

If $\mathrm{D} = \mathrm{d}_{i,\ j}$ Combine Jet$_i$ with Jet$_j$,

If $\mathrm{D} = \mathrm{d}_{\mathrm{beam,\ k}}$ Define Jet$_k$ as final Jet.

In the last step the process is repeated and all the other jets are exhausted. The value of free parameter N when changed to 1, 0, and -1 the algorithm gets a different meaning but the main logic behind all the three algorithms remains the same

- N = 1 k_{T} Algorithm [144]
- N = 0 The Cambridge-Aachen Algorithm [145, 146]
- N = -1 Anti-k_{T} algorithm [147]

At present the Anti-k_{T} algorithm is used for the reconstruction of jets, and all those jets which have a cone of radius R = 0.5 are taken into account while those jets, which have a cone of radius greater than the selected radius, are not taken into account. Three different approaches being adopted by the CMS for the reconstruction of jet, CaloJet, Jet Plus Track (JPT) and Particle-Flow Jet (PF). The measured energy and momentum of the reconstructed jets does not correspond to the true parton-level energy and momentum obtained from gen jets clustered from stable particles at the generator level. The main reasons contributing to this discrepancy are the loss of energy due to the particles which are outside jet cone area, undetected neutrinos, additional particles coming from the pile-up events and the nonlinear behavior of the calorimeter. These effects are corrected by applying the Jet Energy Corrections after the reconstruction of jets. The correction process can be divided into seven steps, namely Level-1 to Level-7 [148]. First three corrections (Jet Energy Corrections – JEC) handle the hardware and instrumental effects and the next four corrections are used for the improvement of estimation of energy and momentum of the partons. However at the moment within the CMS experiment only first corrections are being used.

The JECs are derived centrally by the CMS JetMET Physics Analysis Group using the MC predictions as well as data [149–151]. The factorized approach to jet energy correction is used as shown in the Fig. 3.11.

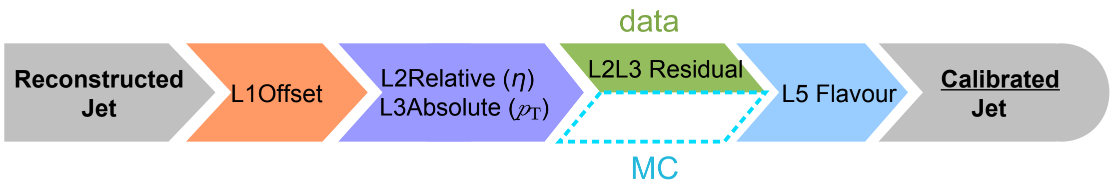

Figure 3.11: The factorised approach of jet energy calibration implement in the jet reconstruction at the CMS [151].

L1: Due to the electronic noise in the detector and the pile-up events, the over all energy of the jet increases. The jet energy is corrected by applying the p_{T} and η dependent corrections using the concept of jet areas [152, 153]. The energy density ρ per unit area for jet in each event is calculated and the median of ρ is subtracted from the jet energy.

L2L3: Due to the nonlinear and non-uniform behavior of the electromagnetic calorimeter, p_{T} and η depend correction factors derived from MC are applied to data [154].

L2L3Residuals: In order to correct the remaining data-MC differences the absolute/residual corrections are applied to the data. These corrections are derived from MC to data ratio [154].

b-Jets

During the proton-proton collision there is a high probability that the event will contain jets, where as the probability of b-quark present in an event is very small. Therefore an event which contains a b-quark can be used to separate from other events which does not contain b-quark, e.g., separation of $t\bar{t}$ from other backgrounds. A jet stemming from the hadronization of the quarks coming from the b-quark is known as "b-jet". The b-jets usually contain B-hadrons which possess several characteristics used to discriminate the b-jet from other jets coming from the hadronization of light quarks or light jets. The typical life time of B-hadrons is of the order $\mathcal{O}$(ps), therefore travelling a distance of $c\tau \approx 450$ μm before decaying into at least 5 charged particles. The tracks associated with these charged particles are extrapolated backwards at a point which can be called as "Secondary Vertex". The perpendicular distance from primary vertex to the point where it touches the track is called "Impact Parameter (IP)". The impact parameter in CMS is measured with a precision of few hundred μm. An interesting quantity in this regard would be ratio of impact parameter to the error on impact parameter. This new quantity is known as "Significance of Impact Parameter" $\mathrm{S_{IP}}$, given by:

$$\mathrm{S_{IP}} = \frac{\mathrm{IP}}{\sigma_{\mathrm{IP}}}. \tag{3.6.3}$$

The $\mathrm{S_{IP}}$ can be positive or negative depending on the angle between the jet axis and the IP segment. It is positive for the tracks coming from the decay of particles traveling in the same direction i.e., the cosine of the angle between the jet axis and impact parameter segment is positive and negative for those travelling in opposite direction. Another quantity derived from the $\mathrm{S_{IP}}$ known as "discriminator", it is the signed value of impact parameter significance. As the value of jet discriminator increases the probability that a jet is b-jet increases. So if a jet has a large number of tracks and impact parameter or discriminator of these jets is smaller then the jet is most likely to be coming from the hadronization of other quarks. The b-jets have large $\mathrm{S_{IP}}$ which explains the fact that B-hadrons are displaced from primary vertex before they decay, thus producing a secondary vertex.
b-tagging algorithms can be divided into the following categories [156]:

- Life Time Taggers: These taggers work on finding the tracks which have large impact parameters or finding the jets which have secondary vertex. For the Track Counting (TC), a jet is counted as a b-jet if there are N number of tracks each having an impact parameter significance $\mathrm{S_{IP}}$ larger than certain threshold. Depending on the number of tracks chosen $N = 2$, 3 the TC tagger can be named as "Track Counting High Efficiency (TCHE)" and "Track Counting High Purity (TCHP)" respectively. These taggers have three working points Loose, Medium, and Tight (L, M, T), with a misidentification probability for light-parton jets of close to 10%, 1%, and 0.1% respectively, at an average jet p_{T} of about 80 GeV. The operating point value for the "Track Counting High Purity Tight (TCHPT)" tagging criterion is set to 3.41 for the inclusive cross-section measurement.

  Instead of looking at first N tracks coming from a jet, another way to identity a b-jet is to estimate the likelihood that all tracks associated to the jet come from the primary vertex, known as "Jet Probability Tagger (JP)". It combines the impact-parameter information of several tracks instead of one. Another version is "Jet B Probability JBP" gives more weight to the tracks with the highest impact parameter

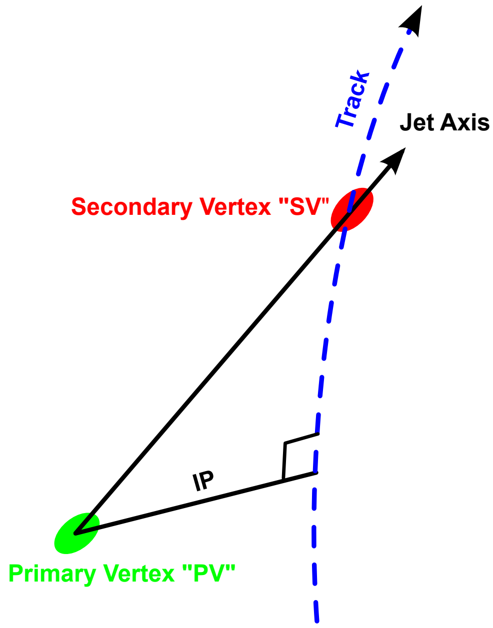

Figure 3.12: The green spot shows the primary vertex and red spot shows the secondary vertex. The blue dashed line represents the track belonging to a jet. The impact parameter is the perpendicular distance from primary vertex to the point where it touches the track. The impact parameter segment always makes right angle to the track and there is only one impact parameter segment per track. Adapted from [155].

significance, up to a maximum of four such tracks which match the average number of reconstructed charged particles from B-hadron decays. The likelihood is defined as [156]:

$$\mathrm{P_{jet}} = \prod \cdot \sum_{i=0}^{\mathrm{N}-1} \frac{(-\ln \prod)^i}{i!} \qquad \text{with} \qquad \prod = \prod_{i=1}^{\mathrm{N}} \max(\mathrm{P}_i, 0.005), \tag{3.6.4}$$

where N gives the number of tracks, P_i is the estimated probability for track i to come from the primary vertex [157, 158]. The operating working point values for the JP Loose, JP Medium, JP Tight tagging criteria are set to 0.275, 0.545, 0.790, respectively.

The Simple Secondary Vertex (SSV) tagger is based on reconstruction of at least one secondary vertex, which usually comes from the decay of B-Hadron. A SSV discriminator is calculated from three dimensional decay length L_{3D} which is IP measured in three dimensions, i.e., $\mathrm{D} = \log(1 + \frac{|\mathrm{L_{3D}}|)}{\sigma_{\mathrm{L_{3D}}}})$ [156]. Like the track corrected discriminator, the number of tracks associated with the vertex is larger than 2 (3), a simple secondary tagger can be than named as “high efficiency” and “high purity” respectively.

- Soft Lepton Based Taggers: These taggers are based on the presence of a lepton, which originates from the decay of B-hadron, near to jet axis. The discriminator values of soft lepton taggers are based on the relative p_{T} distribution of lepton, impact parameters significance and few other variables of interest. There are two

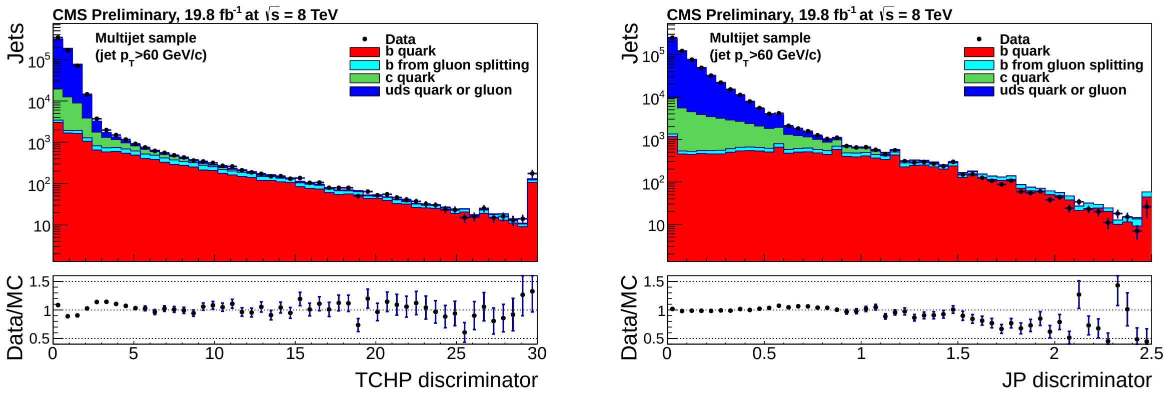

(a) (b)

Figure 3.13: (a) Discriminator values for TCHP and (b) JP taggers. The small discontinuities in the JP distribution are due the single track probabilities which are required to be greater that 0.5% [156].

versions available, one is based on cutting the p_{T} of lepton and the other is based on cutting the multi-variate-analysis output.

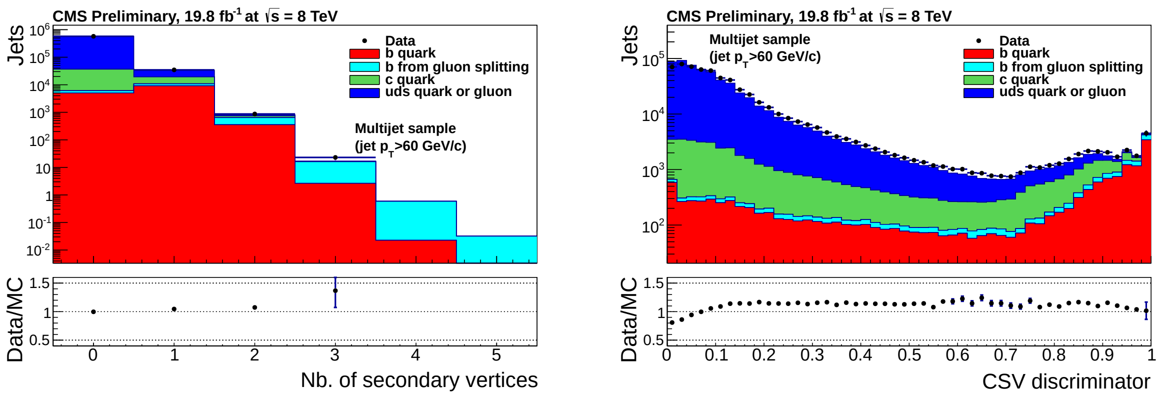

(a) (b)

Figure 3.14: (a) The of primary vertices and the discriminator distribution for the light and heavy quarks of CSV tagger [156].

- Combined Taggers: These taggers use a complex approach which makes use of secondary vertices along with track based life time of the B-hadron. With the additional information taken as an input, Combined Secondary Vertex (CSV) provides the better separation as compared to Simple Secondary Vertex (SSV) tagger even when there is no secondary vertex found. When there is no vertex found, tracks are combined together to form a "pseudo-vertex". It also happens that it is not possible to form a pseudo-vertex, a "no vertex" category, then the track based variables, the number of tracks in the jet and the 3D IP significances for each track in the jet are combined in similar way like JP algorithm.

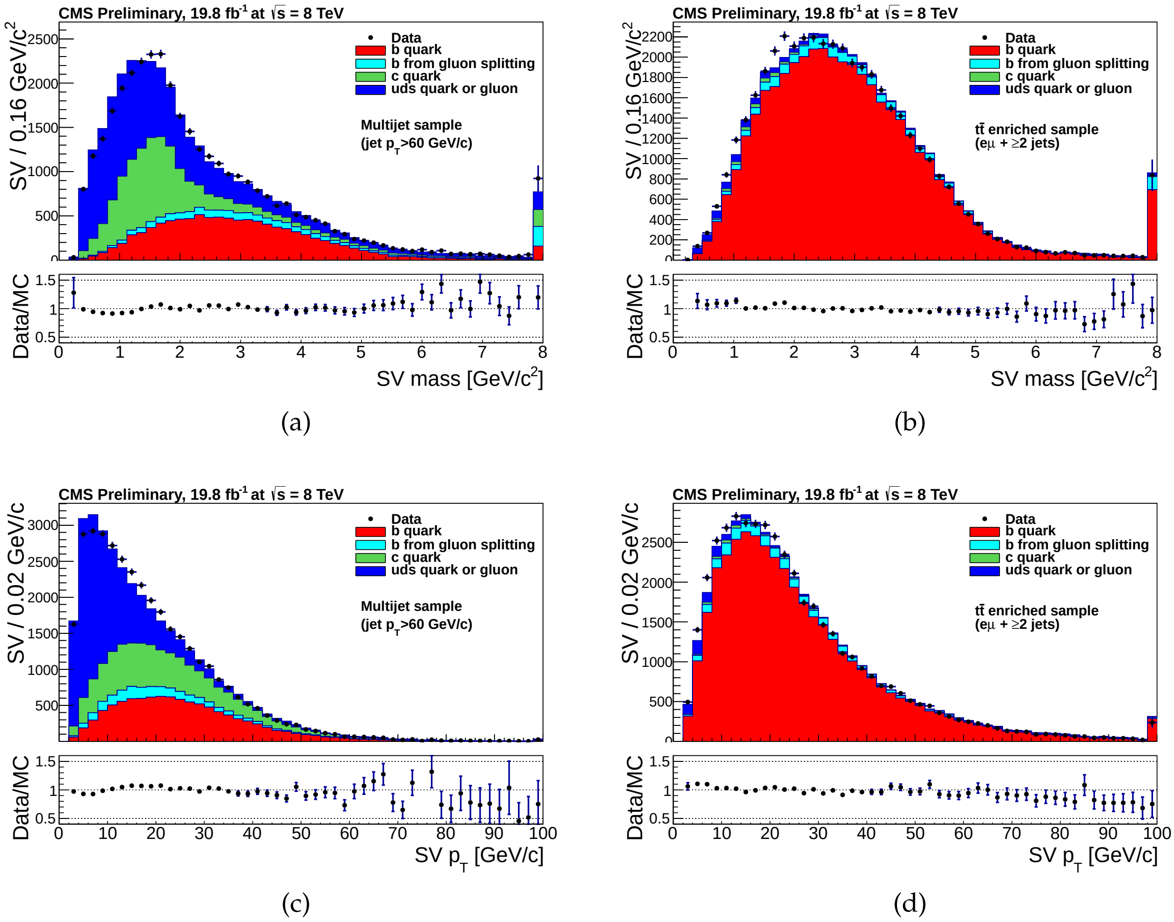

Figure 3.15: (a)-(b) The SV mass which is defined as the invariant mass of tracks associated to the secondary vertex, (c)-(d) the "SV p_T" defined as the sum of transverse momenta of tracks associated to the secondary vertex [156].

Differences between data and simulation are corrected, using per jet SFs, which is defined as: $\mathrm{SF_b} = \epsilon_\mathrm{b}^{\mathrm{Data}}/\epsilon_\mathrm{b}^{\mathrm{MC}}$, for the b–tag and mis-tag efficiencies. These identification and mis-identification efficiencies are estimated by the CMS B-tagging and Vertexing Physics Object Group (BTV POG) [159]. There are several methods available for the determination of these identification efficiencies, e.g., PtRel, IP3d, LT, LT$J/\psi$, System8. Further details on these methods can be found at [156]. Figure 3.16 (left) shows the number of b-tagged jets in data and MC for different processes and $\mathrm{SF_b}-$ for CSV discriminator per event normalized to the fit result using the Flavour Tag Consistency (FTC) method, right-upper panel shows the b-jet efficiency as a function of CSV discriminator threshold and right-lower panel shows the $\mathrm{SF_b}-$ scale factors for heavy flavour. The blue dotted lines forming a band around the data points is the sum of statistical and systematic uncertainties. The different working points, loose-medium-tight, for CSV algorithm are marked with arrows.

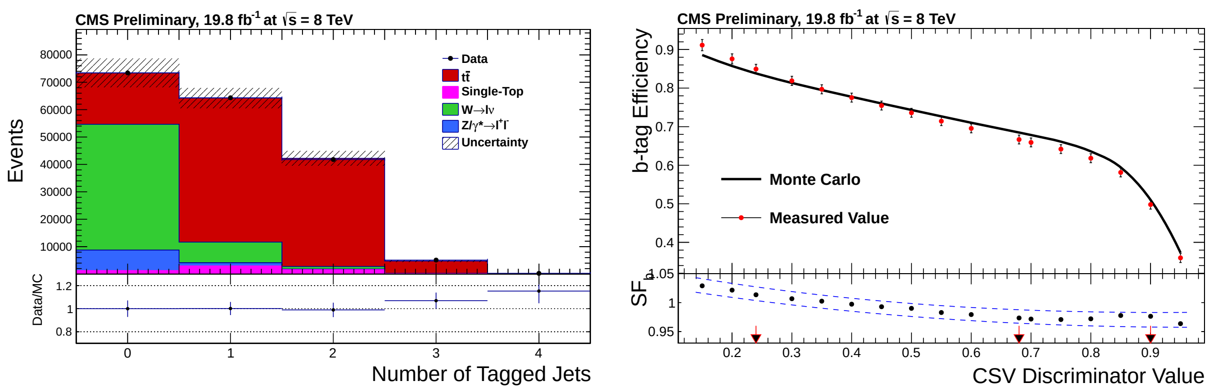

(a) (b)

Figure 3.16: (a) Number of tagged jets per event with the CSVM operating point in data and MC. (b) b-jet tagging efficiency as a function of the discriminator threshold for the CSV algorithm [156].

3.7 Missing Transverse Energy

The undetectable neutrino present in the final state leads to imbalance of momentum in the transverse plane. Due to the conservation of momentum, negative vectorial sum of the momenta of all particle-flow candidates in the transverse plane of incoming particles is measured as missing transverse momentum. Since neutrinos are being mass less magnitude of the momentum is stored as missing transverse energy $\not\!\!E_{\mathrm{T}}$. Mathematically it can written as:

$$\vec{E}_{\mathrm{T}}^{\mathrm{miss}} = \sum_{\text{all the PF } i} \vec{P}_{\mathrm{T}}^{i}, \tag{3.7.1}$$

$$E_{\mathrm{T}}^{\mathrm{miss}} = \mid \vec{E}_{\mathrm{T}}^{\mathrm{miss}} \mid . \tag{3.7.2}$$

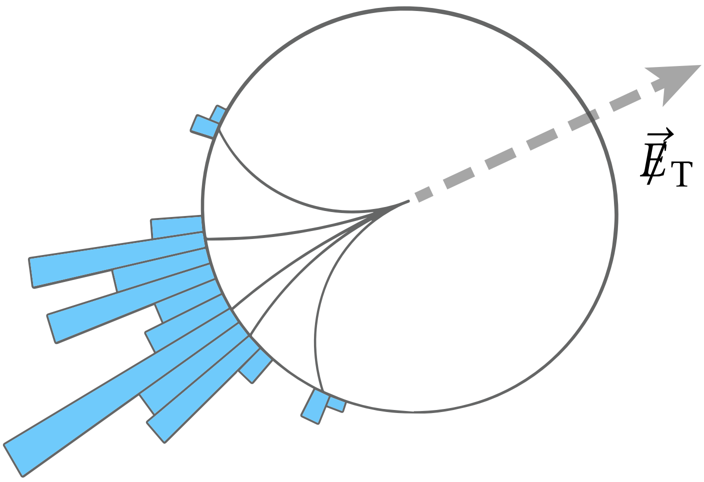

Figure 3.17: Schematic diagram of missing transverse energy. Taken from [160].

The reconstruction of missing transverse energy is sensitive to the detector noise and object mis-measurements, therefore several types of corrections, e.g., Type-0, Type-I, type-II xy-shift corrections are applied during the computation of $\not\!\!E_{\mathrm{T}}$.

Type-0 Corrections: The Type-0 correction is a mitigation for the degradation of the MET reconstruction due to the pile-up interactions. This correction is developed for pfMET and cannot be sensibly defined for CaloMET.

Type-I Corrections: The Type-I correction is the most popular MET correction in CMS. This correction is a propagation of the jet energy corrections (JEC) to MET. The Type-I correction replaces the vector sum of transverse momenta of particles which can be clustered as jets with the vector sum of the transverse momenta of the jets to which JEC is applied.

Type-II Corrections: The Type-II correction was originally developed for the CaloMET and is not recommended to use for pfMET.

xy-Shift: The xy-shift correction reduces the MET ϕ modulation and it also helps to mitigate the pile-up effects. The distribution of MET is independent of ϕ because of the rotational symmetry of the collision around the beam axis, but depends on ϕ is seen in the reconstructed MET. The ϕ_{MET} has roughly a sinusoidal curve with the period of 2π. The possible cause for this modulation mainly comes from the anisotropic detector response, inactive calorimeter cells, misalignment of detector and the displacement of beam spot around the hypothetical point of collision. It has been observed that the amplitude of modulation increases roughly linearly with number of the pile-up interactions.

3.8 Tools

In the following we describe the various tools which are used extensively during the t-channel single top quark inclusive and differential cross-section measurements. In the first subsection the general introduction about the `CMSSW` "Compact Muon Solenoid Software" is presented [161] then the concept of multivariate analysis (MVA) is presented. The NeuroBayes package [162, 163] is used as MVA tool in the differential cross-section measurements. The NeuroBayes combines many kinematic variables to one discriminator which is used to separate the signal from background events. Finally the statistical inference package `ROOT` [164] and `theta` [165], used for fitting and plotting the signal and background.

CMSSW

The **C**ompact **M**uon **S**olenoid **S**oft**W**are, referred as CMSSW [161] is generic name given to the overall collection of various modules, plug-in, services needed by the simulation, calibration and alignment that are used to process the event data. The CMSSW event processing model consists of one executable called **cmsRun**, and many plug-in modules which are managed by the Framework. The necessary geometry needed in the event processing (calibration, reconstruction algorithms, etc.) is available in the dedicated modules. The same executable is used for both real and simulated Monte Carlo data. The CMSSW executable, cmsRun, is configured at the run time by the user's job-specific configuration file. The configuration file, which is highly optimized, in terms of computing resources loads only those modules which are required at the beginning of the job, tells **cmsRun**:

- which data to use
- which modules to execute
- which parameter settings to use for each module
- what is the order or the executions of modules, called path
- how the events are filtered within each path, and
- how the paths are connected to the output files

Multivariate Analysis

Generally deals with the idea of combining many variables in one discriminant and that discriminant is than used to make decision about the unknown variable. A typical examples would be to make a decision whether the event is a t-channel or a $t\bar{t}$ event, or if a jet is stemming from a light quark or from b-quark. Mathematically MVA can be visualized as a function which transforms a vector to a number:

$$f(\vec{x} \in \mathbb{R}^n) \to y \in \mathbb{R}. \tag{3.8.1}$$

There are several multivariate analysis algorithms available, Boosted Decision Trees (BDT), Support Vector Mechanics (SVM) and Neural Networks. All these algorithms work mostly on the same principle in which a decision is made based on several kinematic variables as input and then each event is marked as signal event or background event. Multivariate analysis tools like `BSAURUS` [166], are being used in experimental high energy physics since decades. These packages take lot of computing power as well as learning insignificant fluctuations, known as "over training", from the input training sample. A more advanced package like NeuroBayes [162,163] automatically takes care for these two problems. For the differential cross-section NeuroBayes is used to classify the signal and background events.

Artificial Neural Networks – ANN

Artificial neural networks is an analogue of biological networks of neurons present in a human brain. A feed forward artificial neural network consists of set of nodes, like neuron, which are arranged in different layers. The first layer is known as input layer and the outer most layer is known as output layer. The nodes present in the first layer are termed as input nodes. Every input node of the i^{th} layer has a one direction connection (feed-forward) to the nodes of the $(i+1)^{th}$ layer. Pictorially 3 layers feed forward artificial neural network is shown in the Fig. 3.18. Every line connecting the two layers has a specific weight which is determined during the training of artificial neural network. If the weight between two nodes becomes too small the training process prunes the connection. The training of artificial neural network is done using the monte carlo simulation and than the properly trained artificial neural network can be used to classify the unknown data.

There can be any number of layers in between these two layers and are called hidden layers. The values in the output layer are proportional to the input values which are summed together. These values usually are not linearly dependent on each other but every input value is weighted accordingly and the sum of the these input values. The activation function shown in the Fig. 3.19.

A typical sigmoid function, shown in the Fig. 3.20, is symmetric around zero is applied as transfer function S(x), in order to regularize the output from $]-\infty, \infty[$ to the interval [1, 1]. Mathematically, sigmoid function can be written as:

$$\mathrm{S(x)} = \frac{2}{1+\exp^{-\alpha\cdot \mathrm{x}}} - 1. \tag{3.8.2}$$

Another feature of sigmoid function is that it is twice continously differentiable. It plays an important role in the training process using the back propagation technique. The free

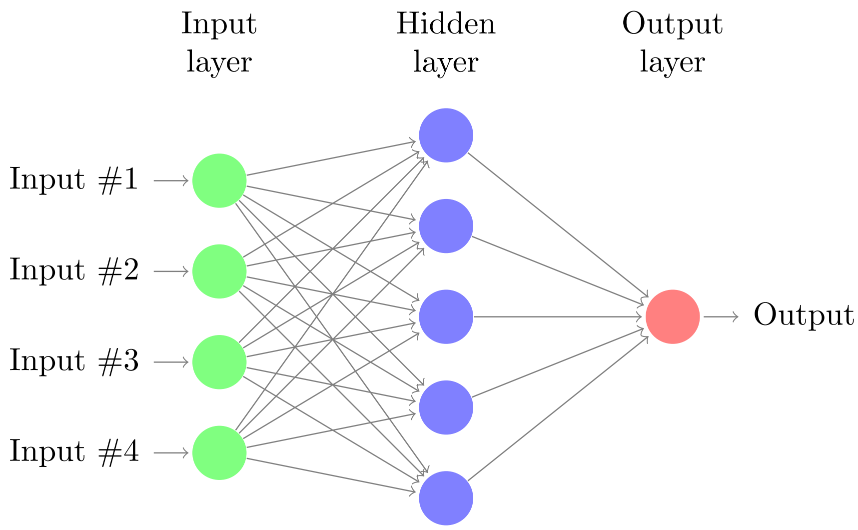

Figure 3.18: The pictorial view of feed-forward artificial neural network [167].

parameters in the training of neural network are the weights between the input layer and the hidden layer, the thickness of line between the input layer and the hidden layer can be seen as the weight. These weights are optimized during the training of artificial neural network to get the desired output.

The artificial neural network and many other Multi-Variate Analysis (MVA) methods work on a principle of parametrising a function which uses a complex method for the weighting which is used for the transformation of input variables. A network has to be trained before it can be used to classify the data. A network is trained using a simulated set of data in which a signal and background type of the event is already known. The accuracy of an artificial neural network output can be estimated by a parameteric loss function given by "E" which compares the value of variable y_i to the values t_i integrated over all events. Mathematically loss fuction can be written as:

$$err(y) = \sum_i E(y_i, t_i), \tag{3.8.3}$$

where $E(y_i, t_i)$ is either a quadratic or entropic loss fuction.

$$E(y_i, t_i) = (y - t)^2, \quad \text{Quadratic loss function.} \tag{3.8.4}$$

$$E(y_i, t_i) = \log\left(\frac{1 + y.t}{2}\right), \quad \text{Entropic loss function.} \tag{3.8.5}$$

One can think err(y) as hyperplane in a higher dimensional space and finding the minimum can be difficult. One can use any minimization algorithms to solve the problem. The artificial neural network are normally trained by making use of the back propagation algorithm [169]. The algorithm works by propagating the network result backwards so that the connection weight between the layers are adjusted. In every iteration, the input weights are modified accordingly to the value specified in the parametric loss function. NeuroBayes algorithm provides an additional algorithm BroydenFletcherGoldfarbShannon (BFGS) [170] which is used for optimizing the network's weights. In general this

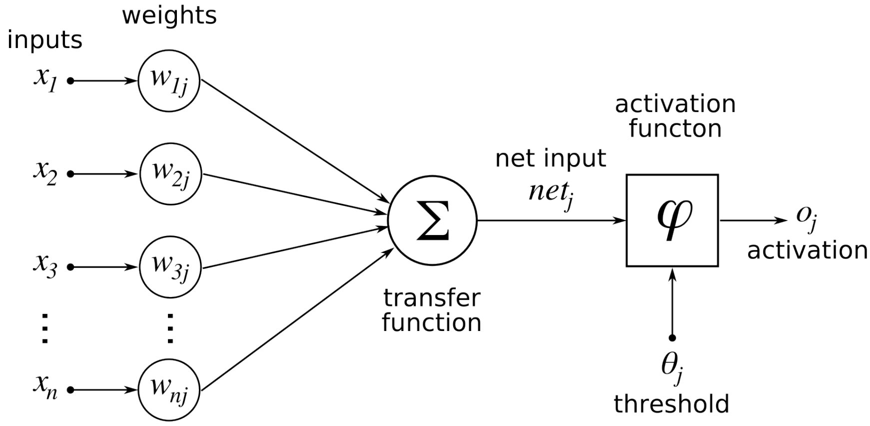

Figure 3.19: A pictorial view of an artificial neural network. The input values which are first weighted and than summed together are than operated with a activation function which results in neural network output. Taken from [168].

algorithm works best when solving the non linear complex problems and works on the same principle on which the Newton algorithm works. The neurobayes algorithm requires the error function should be twice differentiable, this condition is fully satisfied in our case since the loss function and sigmoid functions both are two times differentiable.

A major advantage of NeuroBayes is the preprocessing of the input variables. It automatically takes care for the correlation between the input variables. It avoids the risk of over training of NN thus making the training robust against the statistical fluctuations. The input variables are flattened and scaled to the interval [-1, 1]. The variables are transformed into Gaussian with a mean of zero and a width of one standard deviation which ensures the output of input and hidden nodes are not saturated. The artificial neural network takes care for the decorrelation of transformed variables in such a way that the covariance matrix of input variables can be given by a unit matrix. For this, the total correlation and the correlation matrix of all training variables to the target variables is calculated. For the next iteration the variable with least correlation to the target is removed and the loss of correlation is calculated until the correlation of all variables to target is known. The significance of every variable is calculated by dividing the loss of correlation to the target by the square root of the sample size. The variables which have significance less than 3σ are excluded from the classification. The modelling of input variables and data to Monte Carlo simulation comparison is discussed in Section 6.2.

ROOT

ROOT [164] is an object oriented High Energy Physics analysis frame work. ROOT package entirely depends on C++ . It is an open source software used in various fields of research, it can handle large scale of data very efficiently. It provides a very fast access to data. It can be used for advanced statistical analysis which includes multidimensional histogramming, fitting etc. The user interacts with ROOT via graphical user interface, the command line or scripts. The command and scripting language is C++, thanks to the embedded CINT C++ interpreter, and large scripts can be compiled and dynamically loaded.

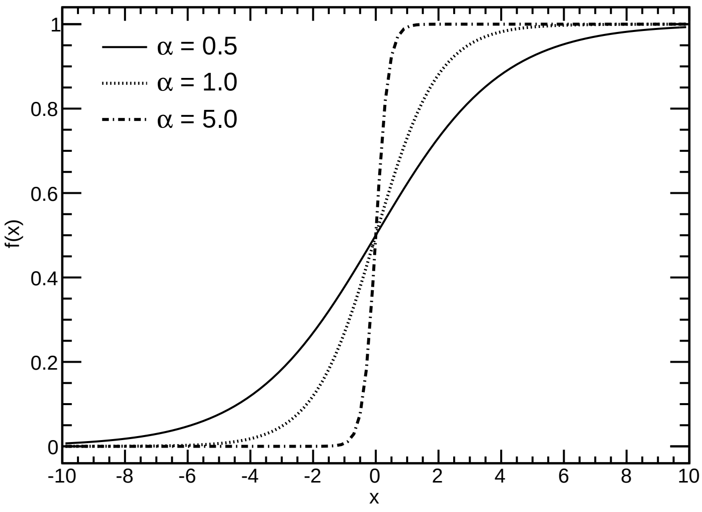

Figure 3.20: A typical Sigmoid Function for different values of α.

theta

The "`theta`" is a framework which is used for statistical modeling and inference in high-energy physics [165]. The `theta` framework provides the possibility for the user to express a model, i.e., the expected data distribution, as function of physical parameters. This model can be used to make statistical inference about the physical parameter of interest. The statistical models are built using the templates of the parameter of the interest, e.g., m_{T}. The template used in the theta framework should be properly normalized and for each data distribution a corresponding Monte Carlo template is needed to fit it to the data distribution.

Chapter 4

Event Selection

In the following, the single-top-quark t-channel selection is performed on physics object reconstruction done with the CMS dedicated softwares is presented. The single-top-quark t-channel production cross-section is orders of magnitude smaller than the total inelastic proton-proton cross-section. The production cross-section of various processes at the LHC energy are shown in Fig. 4.1. One can see from the figure that the total production cross-section of the top-quark is way lower than the vector boson production cross-section. Similarly for the Higgs boson the production cross-section is even more smaller than the top-quark. The processes which have higher production cross-section as compared to the single-top-quark t-channel will serve as a background to the signal, hence the proper selection steps are to be applied on the data as well as on monte carlo simulation so as to get better signal to background ratio.

The single-top-quark t-channel events and the various backgrounds are simulated for the comparison with the data. The event topology of t-channel production is such that it has a leptonically decaying Wboson, two jets one of which is required to be b-jet, one isolated lepton (μ/e) and missing transverse energy, $\not{E}_{\mathrm{T}}$, associated with escaping neutrino. Figure 4.2 shows the NLO Feynman diagram for the production of the single-top-quark via t-channel. However, it is pertinent to note that there is a second b-jet present in the event signature, but this second b-jet most of the time has a very soft p_{T} spectrum, i.e., it lies along the direction of beam pipe thus escaping the detector acceptance. The other jet present in the event is termed as "light jet" or "spectator jet", which is most of the time stemming for u, d or s-quarks.

In the following, the quality cuts as recommended by various physics objects groups (JET/ MET POG, Muon POG, Electron POG,) imposed on the reconstructed objects, as discussed in Chapter 3, and the top-quark and W-boson reconstruction will be described in detail.

4.1 Major Background Processes

In the following, a short introduction to major background to the single-top-quark t-channel will be presented. The s-channel, associated production (tW) and $\mathrm{t\bar{t}}$ processes can be grouped together which are named as top-quark like. Other includes the W+jets, Z+jets, diboson and QCD multijet processes. Among these background processes $\mathrm{t\bar{t}}$ and W+jets serve as major backgrounds.

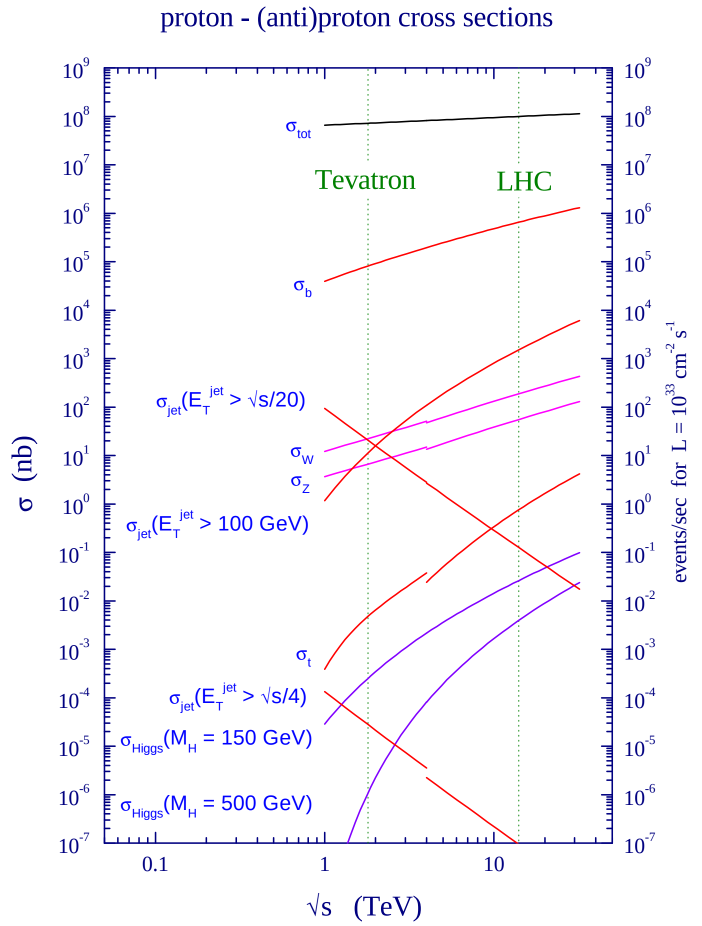

Figure 4.1: The various NLO cross-sections plotted as a function of center-of-mass energy for the Tevatron and the LHC experiments [171]. The step in the curves at $\sqrt{s} = 4\,\mathrm{TeV}$ is due to transition from $p\bar{p}$ collisions at Tevatron to pp at LHC and the σ_t represents the production cross-section of $t\bar{t}$.

Top-quark Like Backgrounds

At the LHC, top-quarks can be produced via strong interaction and via electroweak interaction. The strong interaction produces the top-quark in pairs while electroweak interaction produces the single-top-quark via *s*-channel and tW (associated production). Figure 4.3 shows the leading order Feynman diagrams for $t\bar{t}$ pair production. Similarly Fig. 4.4 shows the leading order Feynman diagrams of *s*-channel and associated production of the single-top-quark.

W/Z+jets Background

The W+jet is one of the largest contributing background for the *t*-channel production of the single-top-quarks. In the final state these vector bosons are produced together with light and heavy quarks along with the gluons. Figure 4.5 show the Feynman diagrams for W+jets and Z+jets. Most of the jets which are coming from W/Z+jets processes are not b-jets. As a result, the presence of exactly one b-jet in the signal final state significantly

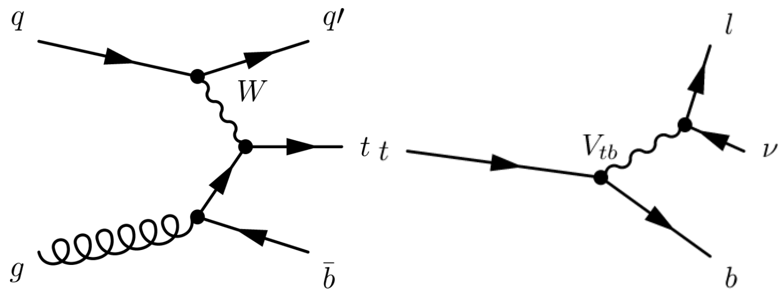

Figure 4.2: The t-channel single top-quark production Feynman diagrams, at next to the leading order (b) shows the of top-quark decaying into W-boson and a b-quark.

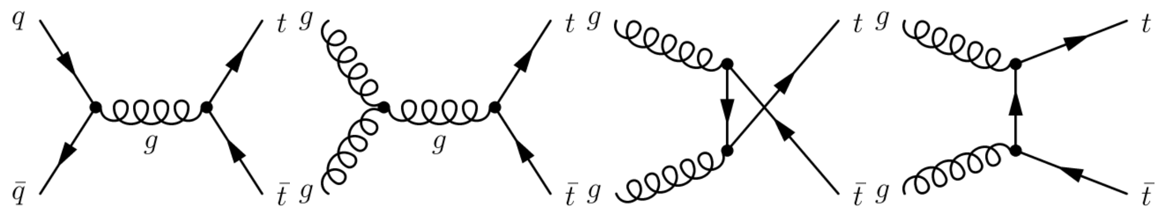

Figure 4.3: The leading order Feynman diagrams for the top anti-top-quark production at hadron colliders (a) represents the top quark pair production via quark anti quark annihilation and (b) - (d) represents the top pair production via gluon fusion.

reduces the contribution from these backgrounds due to their large production cross-section. The W+jets samples are further divided into W+light $(u,\ d,\ s,\ g)$ and W+heavy $(c,\ b)$ and fitted separately to get their contribution towards the final number.

Diboson Background

The diboson background consists of WW, WZ, ZZ. These three processes are produced with Pythia. In the final state they have a charged lepton, a neutrino and heavy quarks in the final state. The diboson has a very small contribution towards the background in both the inclusive and differential cross-section measurements. The ZZ production can contribute to the background when one lepton is not detected and increases the amount of missing transverse energy. Figure 4.6 shows the diboson production modes at the LHC.

QCD Multijet Background

The largest contributing background to the t-channel single-top-quark events comes from QCD multijet. The QCD multijet events mostly contains the muons which originated from heavy flavor decay or from the decay of kaons and pions. For the inclusive cross-section measurement, QCD multijet background is estimated from the data which is discussed in Section 5.1.1, similarly for the differential cross-section measurement QCD multijet background is also estimated from the data described in detail in Section 6.1.1. Table 3.1

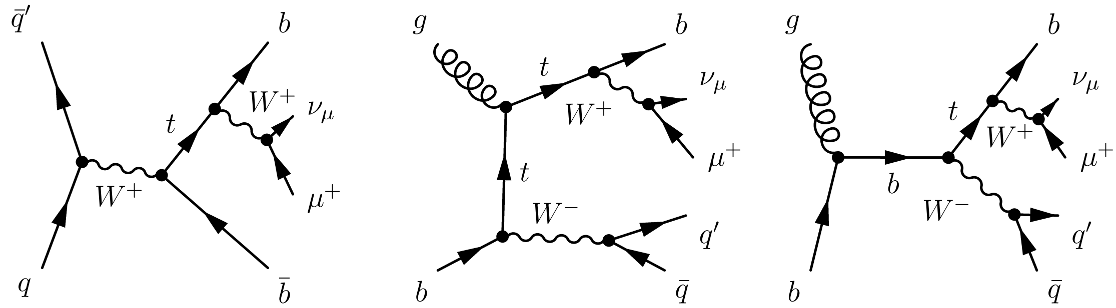

Figure 4.4: The tree level Feynman diagrams for the production of the single-top-quark via s-channel and associated production of the single-top-quark with W-boson. In each of these process the top-quark decays almost 100% into a W-boson and a b-quark, where as the W-boson can decay into a $\bar{q}q'$ hadronically or $l\nu_l$ leptonically . These process have the similar final state topology as the single-top-quark in t-channel.

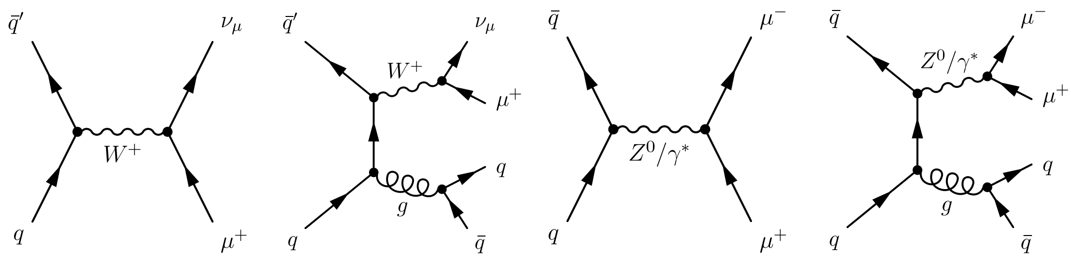

Figure 4.5: The Feynman diagrams for Wand Z-boson production. The LO order and NLO order production of W/Z-boson are shown. With the presence of additional jet and lepton in the final state they the similar event topology as in the single-top-quark t-channel.

gives overview of the simulated samples and their predicted cross-sections used for the differential measurements.

4.2 Primary Vertex, Noise Cleaning and Trigger

At least one primary vertex is required to be reconstructed from at least four tracks, requiring the track fit to have $n_{\mathrm{dof}} \geq 5$, with $|z_{\mathrm{PV}}| < 24\,\mathrm{cm}$ and $\rho_{\mathrm{PV}} < 2\,\mathrm{cm}$, where $|z_{\mathrm{PV}}|$ and ρ_{PV} are the vertex distance with respect to the nominal interaction point along the z axis and in the transverse plane, i.e., the plane perpendicular to the direction of the incoming proton beam respectively.

Events with very high energy noise in the HCAL barrel or end caps are rejected, using pulse shape, hit multiplicity, and timing criteria (`HBHENoiseFilter`). The details about the rejection of events can be found at [172]. The events have to pass the trigger selection. Separate trigger selection is used in the electron and muon channels. The muon events are

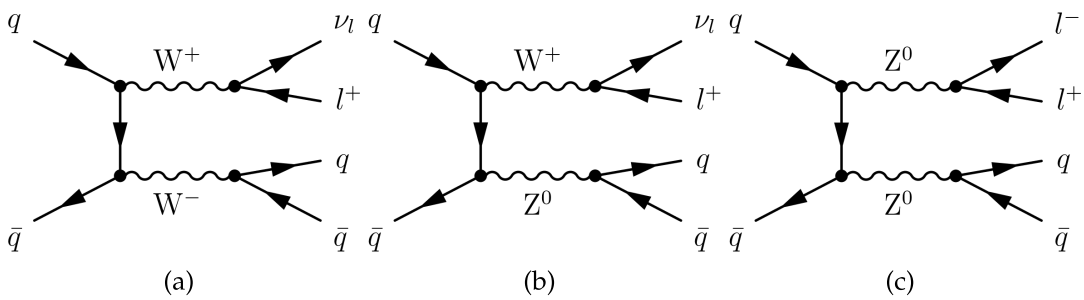

Figure 4.6: The LO Feynman diagrams for the diboson production.

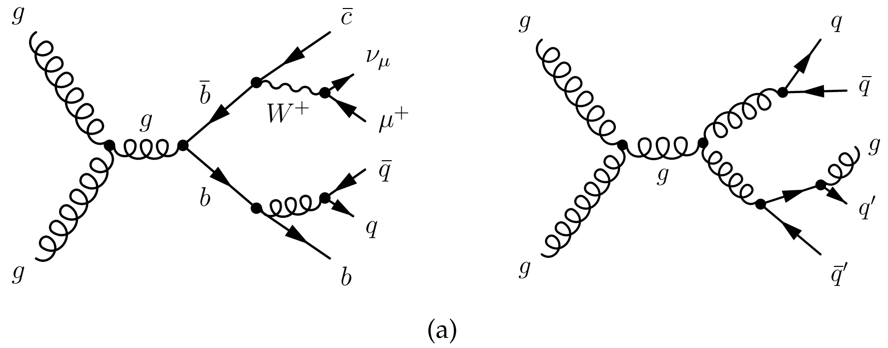

Figure 4.7: The Feynman diagrams for QCD multijet production processes. The first diagram shows the production of $b\bar{b}$ where the b-quark decays hadronically and the $\overline{\mathrm{b}-}$ decays via weak interaction into a $\bar{c}$-quark, a muon and a corresponding neutrino. In the second diagram a possible QCD multijet production process is shown which leads to 4 quarks and a gluon.

selected using the High Level Trigger (HLT) path `HLT_IsoMu24_eta2p1` [173, 174], which requires muon candidates with p_{T} >24 GeV and $|\eta| < 2.1$ during the on line reconstruction. On Monte Carlo we use the η-dependent efficiencies derived from [174] to scale the event yield. The electron events are selected with the HLT path `HLT_Ele27_WP80` which requires electron candidates with $E_{\mathrm{T}} > 27$ GeV and tracking identification criteria yielding an electron selection efficiency of 80%.

4.3 Muon Selection

The presence of one isolated muon in the t-channel is the key signature which discriminates the signal from the background. However, the selected muon has to pass the following quality criteria: The selected muons must have a transverse momentum $p_{\mathrm{T}} > 26$ GeV, must be within the trigger acceptance range ($|\eta| < 2.1$) and they have to pass the muon ID. The quality of the selected muon candidates has to meet the requirements of a "global muon". Furthermore, the quality of the global fit has to be better than $\chi^2/\mathrm{ndof} < 10$ and at least one valid hit in the muon chambers has to be present. The muon candidates are required to have more than 5 valid hits in the silicon tracker, out of which at least one must lie in the pixel detector. At least two segments must match the global muon object in the muon chambers.

The absolute 2D impact parameter must be smaller than 0.2 cm with respect to the primary vertex position for the suppression of the background contribution coming from the cosmic-ray muons.

The distance between the z coordinates of the leading primary vertex[1] and of the muon track at the point of closest approach must be less than 0.5 cm. We define the "particle-flow relative isolation" ($I_{\rm rel}^{\delta\beta-\rm corr.}$) with so-called "Delta Beta" corrections as

$$I_{\rm rel}^{\delta\beta-\rm corr.} = \frac{I^{\rm ch.\,h} + \max((I^{\gamma} + I^{\rm n.\,h} - I^{\rm PU}), 0)}{p_{\rm T}}, \tag{4.3.1}$$

where $I^{\rm ch.\,h}$, I^{γ}, and $I^{\rm n.\,h}$ are the sums of the transverse energies deposited by stable charged hadrons, photons, and neutral hadrons in a cone of size $\Delta R = \sqrt{(\Delta\eta)^2 + (\Delta\phi)^2} = 0.4$ around the muon direction. $I^{\rm PU} \equiv 0.5 \times \sum p_T^{PU}$ is the sum of transverse momenta of tracks associated to non-leading vertices, used to estimate the contribution of neutral particles from pileup events by applying a multiplicative factor 0.5 that takes into account the neutral-to-charged particles ratio expected from iso-spin invariance. The tight muons are selected by the requirement $I_{\rm rel}^{\delta\beta-\rm corr.} < 0.12$. Similarly the loose muons are selected by a transverse momentum cut of $p_{\rm T} > 10\,\rm GeV$, a pseudorapidity requirement of $|\eta| < 2.5$, and a relaxed requirement on the isolation of $I_{\rm rel}^{\delta\beta-\rm corr.} < 0.2$. The loose muons candidates selected are required to be a global muon or a "tracker muon".

4.4 Electron Selection

Similarly as for the definition of muons, also for the electron candidates two categories exist, i.e., "Tight Electrons" and "Loose Electrons". The reconstructed electron candidates are selected by applying a cut on the transverse energy of $E_{\rm T} > 30\,\rm GeV$, requiring $|\eta| < 2.5$, and if they pass the electron identification criterion of MVA ID > 0.9. For the calculation of the relative isolation in the electron channel we make use of the effective area corrections:

$$I_{\rm rel}^{\rho-\rm corr.} = \frac{I^{\rm ch.\,h} + \max((I^{\gamma} + I^{\rm n.\,h} - \rho \times A), 0)}{p_{\rm T}}, \tag{4.4.1}$$

where ρ is the average energy of the particles not used to reconstruct jets and A is the area of the jet cone in the $\eta - \phi$ plane. The values of ρ are calculated using the jets built with the $k_{\rm T}$ algorithm and a distance parameter of 0.6. An isolation cone of $\Delta R = \sqrt{(\Delta\eta)^2 + (\Delta\phi)^2} = 0.3$ is chosen for the reconstruction of electrons. The tight electrons are selected by the requirement $I_{\rm rel}^{\rho-\rm corr.} < 0.1$.

The loose electron candidate selection requires an electron with $E_{\rm T} > 20\,\rm GeV$, $|\eta| < 2.5$, $I_{\rm rel}^{\delta\beta-\rm corr.} < 0.2$ and it has to pass a selection based on a simple cut based identification variable described in Ref. [175]. The effective area corrections $I_{\rm rel}^{\rho-\rm corr.}$ are also applied for the loose electron selection.

[1]If more than one primary vertex is identified, the one with the largest sum of the squared transverse momenta of associated tracks is taken.

There is a different criteria for the selection of lepton by Top Physics Analysis Group (Top PAG) Reference selection and by particle-flow default definitions used for the top-quark projections known as "Hermetic Top projections". However there can be several possibilities in an event.

1. All particle-flow isolated muons(electrons) are Reference muons(electrons).
2. Some particle-flow isolated muon(electron) is not a Reference muon(electron).
3. Some Reference muon(electron) is not a pfIsolated muon(electron).
4. More complicated combinations of (2) and (3).

   In the case of (2), top projection removes the muon(electron) from further consideration as electron(jet) but it is not included in the Reference muon(electron) collection: it is missing from the analysis level objects.

   In the case of (3), the candidate is passed on for further consideration instead of possibly triggering a (di-lepton) veto.

   Analyses may wish to limit the possibilities to (1) by configuring the particle-flow lepton collections used for top projection to match the Top PAG Reference Selection lepton criteria.

4.5 Jet Selection

Jets used in this analysis are so-called particle-flow jets and are reconstructed using the anti-k_T algorithm [147]. The distance parameter of a jet is 0.5. The jet energy is scaled by a factor that describes the detector response depending on the transverse energy and the pseudorapidity of the jet [154]. The selected jet has to pass the following quality cuts, so called `JetId`, recommended by JetMET POG [176].

- Minimal selection for any analysis: Jets with corrected $p_T > 10\,\text{GeV}$ and $\eta < 5.2$
- Charged Hadron Subtraction (CHS): Recommended for 2012 data
- Jet Energy Corrections: L1FastJet+L2L3(+L2L3Residuals for data) [177].
- Jet ID:
  - Number of Jet constituents > 1
  - Neutral Hadron Energy Fraction: NHF < 0.99
  - Neutral Electro-Magnetic Energy Fraction: NEF < 0.99
  - if $\mid \eta \mid < 2.4$, Charged Electromagnetic Energy Fraction CEF < 0.99
  - if $\mid \eta \mid < 2.4$, Charged Hadron Energy Fraction CHF > 0
  - if $\mid \eta \mid < 2.4$, Neutral Hadron Energy Fraction NHF > 0

In this analysis, we consider only those jets with $p_T > 40\,\text{GeV}$ and $|\eta| < 4.5$ and they have to pass the quality cuts which are specific to the algorithm used. The final state event topology of the t-channel features a spectator b-quark, coming from the initial gluon splitting. As this second b-quark has on average a very soft transverse momentum distribution, in most events the corresponding b-jet fails the transverse momentum requirement and is therefore not selected. Another special feature of the *t*-channel is that the light quark in the final state is more likely to be found in the forward region. This feature can be used to suppress the major background contributions coming from $t\bar{t}$ and W+jets production. For that reason we apply the extended pseudorapidity requirement in the jet selection.

After passing all the selection criteria for a jet, we further categorize jets into b tagged jets and jets which are not b-tagged by using a b-tagging discriminator variable. For the inclusive cross section measurement the "Track Counting High Purity Tight (TCHPT)" tagger is used with a working point 3.41 and for differential cross-section measurement "Combined Secondary Vertex (CSVM)" tagger is used with working point 0.898.

Lepton & b-Jet Counting

Figure 4.2 shows that the final state of *t*-channel consists of a light quark recoiling against the W-boson, b-quark stemming from the decay of top-quark, 2^{nd} b-quark coming form the gluon splitting, $\not\!\!E_{\mathrm{T}}$ and one isolated tight lepton which is used to reduce the background contribution coming from two lepton events which can originate from $t\bar{t}$ or Drell-Yan. The events with additional loose muon or electron are vetoed.

The naming convention used is "x-jets y-tags", e.g., 2j1t which refers to a region where we have 2jets out which exactly one is b-tagged. This 2jets 1-tag region is marked as our signal region. The "2j0t" refers to a region in which we have exactly two jets, out of which none is b-tagged, this region 2jets 0-tag is marked as W+jets control region. Similarly "3j2t or 3j1t" is $t\bar{t}$ enriched region. These two (W+jets, $t\bar{t}$ and QCD) are the main backgrounds which are estimated from data in inclusive cross-section measurements. The extraction of these backgrounds is described in detail in the section 5.1.1. Jet RMS cut is used for the jets failing to pass the b-tagging criteria of inclusive cross-section measurement, this reduces the contribution coming from pileup events. The distance in the $\eta - \phi$plane between the momenta of the particles constituting the jet and the jet axis is evaluated and its root-mean-square over all the jet constituents required to be smaller than 0.025. For differential cross-section measurement only QCD is estimated from data which is described in Section 6.1.1.

4.6 Missing Transverse Energy

The $\not\!\!E_{\mathrm{T}}$, which is defined as the negative of the vectorial sum of the transverse momenta of the identified PF particles. The particle-flow algorithm is used to reconstruct $\not\!\!E_{\mathrm{T}}$ and the $\not\!\!E_{\mathrm{T}}$ is corrected by applying Type-0, Type-I and MET-Φ corrections. This means that the difference between the L1 and L3 correction levels of the jets is propagated to MET. In the electron channel the events are required to have $\not\!\!E_{\mathrm{T}} > 45\,\mathrm{GeV}$ in order to suppress events from QCD multijet production.

4.7 Transverse Mass of W-boson

The transverse mass of the W-boson m_{T} is defined as

$$m_{\mathrm{T}} = \sqrt{(p_{\mathrm{T},l} + p_{\mathrm{T},\nu})^2 - (p_{x,l} + p_{x,\nu})^2 - (p_{y,l} + p_{y,\nu})^2} \,, \tag{4.7.1}$$

and reconstructed from the four-vector of the charged lepton and the $\not{E}_{\mathrm{T}}$ vector. In the muon channel the QCD contribution in the signal region is rejected by requiring $m_{\mathrm{T}} > 50\,\mathrm{GeV}$.

4.8 Top-quark Reconstruction

The top-quark is the heaviest quark and due to its large mass it decays before it can form bound states. The decay of the top-quark to W-boson and a b-quark ($t \rightarrow$Wb) is almost 100%. The W-boson also decays via leptonically or hadronically. In this analysis we consider the leptonic decay of the W-boson. For that reason we have a charged lepton (muon or electron) along with the corresponding neutrino. The transverse components of the neutrino momentum are taken from the missing transverse energy vector. The missing z component of the neutrino momentum is determined by applying a constraint on the W-boson mass. Mathematically it can be written as:

$$M_W^2 = (E_{lep} + \sqrt{\not{E}_{\mathrm{T}}^2 + P_{z,\nu}^2})^2 - (\mathbf{P}_{\mathrm{T},lep} + \not{E}_{\mathrm{T}})^2 - (P_{z,lep} + P_{z,\nu})^2 \,. \tag{4.8.1}$$

Solving this equation for $P_{z,\nu}$ gives in general two solutions:

$$P_{z,\nu}^{A,B} = \frac{\mu \cdot P_{z,lep}}{P_{\mathrm{T},lep}^2} \pm \sqrt{\frac{\mu^2 \cdot P_{z,lep}^2}{P_{\mathrm{T},lep}^4} - \frac{E_{lep}^2 \cdot \not{E}_{\mathrm{T}}^2 - \mu^2}{P_{\mathrm{T},lep}^2}} \,, \tag{4.8.2}$$

With

$$\mu = \frac{M_W^2}{2} + \mathbf{P}_{\mathrm{T},lep} \cdot \not{E}_{\mathrm{T}} \,. \tag{4.8.3}$$

For a positive discriminant in (4.8.2) we have two real solutions which happens in 72% of the cases and the solution of the equation with the smallest value of $|P_{z,\nu}|$ is chosen. For the case when m_{T} is greater than the pole mass of W-boson (80.4 GeV), the discriminant in equation (4.8.2) becomes negative. This happens in 28% of the cases, primarily due to the finite resolution of $\not{E}_{\mathrm{T}}$. In order to get a real solution, one can either just take the real part of (4.8.2) or increase the W-boson mass so that the square root becomes zero. However, these methods lead to a wrong W-boson mass. The method used in this analysis eliminates the imaginary part by modifying the components of the missing transverse energy so that $m_{\mathrm{T}} = m_{\mathrm{W}}$ while satisfying equation (4.8.1).
We have a quadratic equation in $P_{x,\nu}$ and $P_{y,\nu}$ when we set the square root of equation (4.8.2) to zero. By setting the transverse W-boson $m_{\mathrm{T}} = 80.4\,\mathrm{GeV}$, the missing transverse energy ($\not{E}_{\mathrm{T}}$) can be modified. Under the assumption that the missing transverse energy measurement is approximately correct, the distance δ between the transverse momentum of the neutrino and missing transverse energy is minimized with respect to the solutions $P_{y_{1,2},\nu}$:

$$\delta_{1,2}(P_{x,\nu}) = \sqrt{(P_{x,\nu} - (\not{E}_{\mathrm{T}})_x)^2 + (P_{y_{1,2},\nu}(P_{x,\nu}) - (\not{E}_{\mathrm{T}})_y)^2}. \tag{4.8.4}$$

In order to keep the transverse energy of the neutrino close to the measured $\not{E}_{\mathrm{T}}$, the solution with smaller $\delta_{1,2}$ is chosen. The new values $P'_{x,\nu}$, $P'_{y,\nu}$ obtained from the minimization are used to calculate the new real value of $P_{z,\nu}$.

There are several ways to assign the selected jets to the final state quarks of the event. Depending on the analysis bin "*x*jets *y*tag", different strategies are applied in order to get this assignment done. For the signal region with two jets and one of them tagged as b-jet (2j1t) the assignment of the selected jets to the final state quarks is straight forward: the tagged jet is assigned to b-quark stemming from top-quark decay and the other jet can be assigned to the light quark in the final state.

In the W+jets control region with two jets and no b-tag (2j0t) the jet-quark assignment is done based on the pseudorapidity of the two jets. The forward jet is assigned to the light quark in the final state and the other jet is assigned to the b-quark stemming from the decay of top-quark.

In the $\mathrm{t\bar{t}}$ control region with three or more jets and two b-tags (3j2t and 4j2t) the jet-quark assignment is done in the following way: The jet with the lowest b-tagger value is assigned to the light quark and for the remaining jets the invariant masses of the reconstructed top-quarks using each jet candidate are calculated and the jet yielding the mass value that is closest to the true top-quark mass of 172.5 GeV is assigned to the b-quark stemming from the decay of top-quark. From the remaining jets the one with the largest value of the b tagger output is assigned to the second b-quark in the event, assuming the single-top-quark event topology in the *t*-channel, where an additional b-jet is coming from the initial gluon which splits into a $\mathrm{t\bar{t}}$ pair.

To verify if this assignment is correct, we use the signal Monte Carlo to check if the reconstructed jets are matched to the corresponding final state partons. A matching criterion of $\Delta R < 0.3$ between the jet and parton leads to the fractions in Table 4.1 for "2j1t" and "3j1t". The choice of the b-tagged jet as the jet from the b-quark of the top-quark decay is correct in 84.04% of the cases in 2j1t region and 64.69% in 3j1t region. The untagged jet can be matched to the recoiling light quark in 81.2% of the cases in 2j1t region and 62.48% in 3j1t.

Table 4.1: Matching of the reconstructed b-tagged and untagged jets to the underlying final state parton in selected signal events in the muon channel. For the matching, the jet and parton must have a distance $\Delta R < 0.3$.

Assignment	Fraction	2j1t	3j1t
b-tagged jet is b-quark jet from top-quark		84.04%	64.69%
b-tagged jet is spectator b-quark jet		10.58%	21.92%
b-tagged jet is the recoiling light quark jet		3.36%	5.65%
b-tagged jet is none of the above		2.01%	11.45%
untagged jet is b-quark jet from top-quark		7.59%	6.67%
untagged jet is spectator b-quark jet		5.07%	9.94%
untagged jet is the recoiling light quark jet		81.2%	62.48%
untagged jet is none of the above		6.18%	21.49%

Chapter 5

Inclusive Cross-section Measurement

In the following, the inclusive cross-section measurements based on the event selection criteria described in Chapter 4 are presented. For inclusive cross-section measurement the b-tagger used to identify the b-jets is "Track Counting High Purity Tight (TCHPT)" (see Section 3.6) where as for the differential cross-section measurement (see Section 6) "Combined Secondary Vertex Tight (CSVT)" is used. The W+jets and $t\bar{t}$ are the two major backgrounds in *t*-channel production, in the inclusive measurements the QCD, W+jets and $t\bar{t}$ are derived from data. The estimation of these backgrounds from data is discussed in section 5.1.1, 5.1.2 and 5.1.3 respectively, where as for the differential cross-section measurements only QCD multijet is extracted from data which is described in section 6.1.1.

5.1 Background Estimation

The main contributing backgrounds in *t*-channel the single-top-quark production are $t\bar{t}$, W+jets and QCD multijet. These main backgrounds together with the constraints on their production rates are derived from data in the different control regions. The discussion on the other contributing backgrounds can be found in Chapter 4.1.

5.1.1 QCD Multijet Background

Due to the higher center-of-mass energy of the LHC accelerator, there is a large amount of gluon radiation present which contributes as a jet in the final state. The large amount of QCD multijet events are rejected by applying event selection discussed in Chapter 4. The presence of exactly one isolated lepton reduces the QCD multijet background a lot. Therefore the QCD multijet contribution towards the signal is estimated from data in the signal region (2-jet 1-tag) and other side band region. The QCD multijet contribution is extracted from a maximum-likelihood fit to the full distribution of transverse of the W-boson stemming from top-quark decay in the muon channel and the missing transverse energy distribution, the undetected neutrino, in the electron channel. In case of the differential cross-section measurement as described in Section 6.1, the maximum-likelihood is not performed to the full distribution but up to certain value in order to avoid the double counting of QCD events when the fit is performed to the neural network distribution (see Section 6.4). The data can be parameterised as:

$$\mathrm{F_l}(x) = a_l \cdot \mathrm{S_l}(x) + (1 - a_\mathrm{l}) \cdot \mathrm{B_l}(x); \qquad \mathrm{l} = \mu, e, \tag{5.1.1}$$

where the variable x is transverse mass (m_T) in muon channel and is missing transverse energy ($\not{E}_\mathrm{T}$) in the electron channel. The choice of transverse mass for the muon channel and missing transverse energy for the electron channel is purely conventional. One can use the transverse mass for muon (electron) channel or missing transverse energy for muon(electron) channel. The $\mathrm{S_l}(x)$ and $\mathrm{B_l}(x)$ are the expected distributions by summing over all processes including W-boson in the final state and QCD multijet events respectively. The signal distribution $\mathrm{S_l}(x)$ is derived from simulation and it includes the contribution from signal, where as $\mathrm{B_l}(x)$ is extracted from data by defining a orthogonal phase space in which the tight lepton is required to fail a isolation cut $I_\mathrm{rel}^{\delta\beta-\mathrm{corr.}} > 0.2$ or > 0.15 for muon or electron respectively.

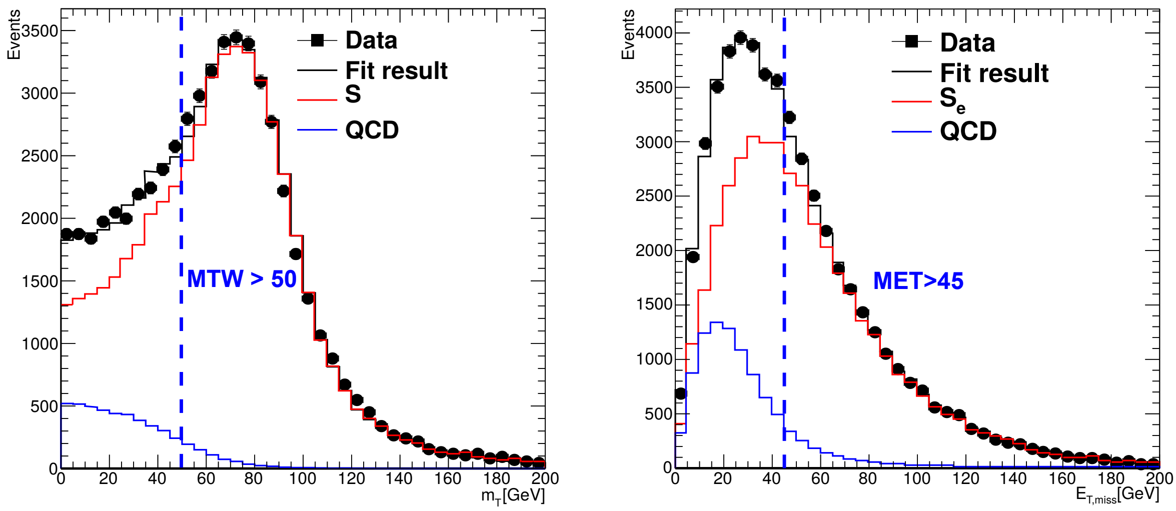

(a) (b)

Figure 5.1: The QCD extraction in muon (electron) channel. (a) m_T template for the extraction of QCD, to further reduce the QCD contribution a $m_\mathrm{T} > 50\,\mathrm{GeV}$ cut is applied (b) shows the $\not{E}_\mathrm{T}$ template where a $\not{E}_\mathrm{T} > 45\,\mathrm{GeV}$ is applied to further reduce the QCD contribution.

The data obtained by defining an orthogonal phase space in this way may contain a fraction of events coming from the QCD multijet processes. The selection is than run over the QCD monte carlo samples and the number of events coming from this MC QCD are subtracted from the data driven QCD template to get the purity of these templates in muon and electron channel. In case of muon channel the purity comes out to be 98% and in case of electron channel it comes out to be 99%. However the kinematic bias on the transverse mass and missing energy distribution due to the data driven estimation is covered by the systematic uncertainty quoted in Section 5.3.

5.1.2 $\mathrm{t\bar{t}}$ Background Estimation

The final state topology of $\mathrm{t\bar{t}}$ process is such that it has exactly two top-quarks in a single event and if the hadronic decay of W-boson is considered than at-least there are 6 jets in an event. Therefore $\mathrm{t\bar{t}}$ processes are higher in jet and b-tag multiplicities as compared to the 2j1t region. The $\mathrm{t\bar{t}}$ is estimated from data by defining two control regions 3j2t and 3j1t.

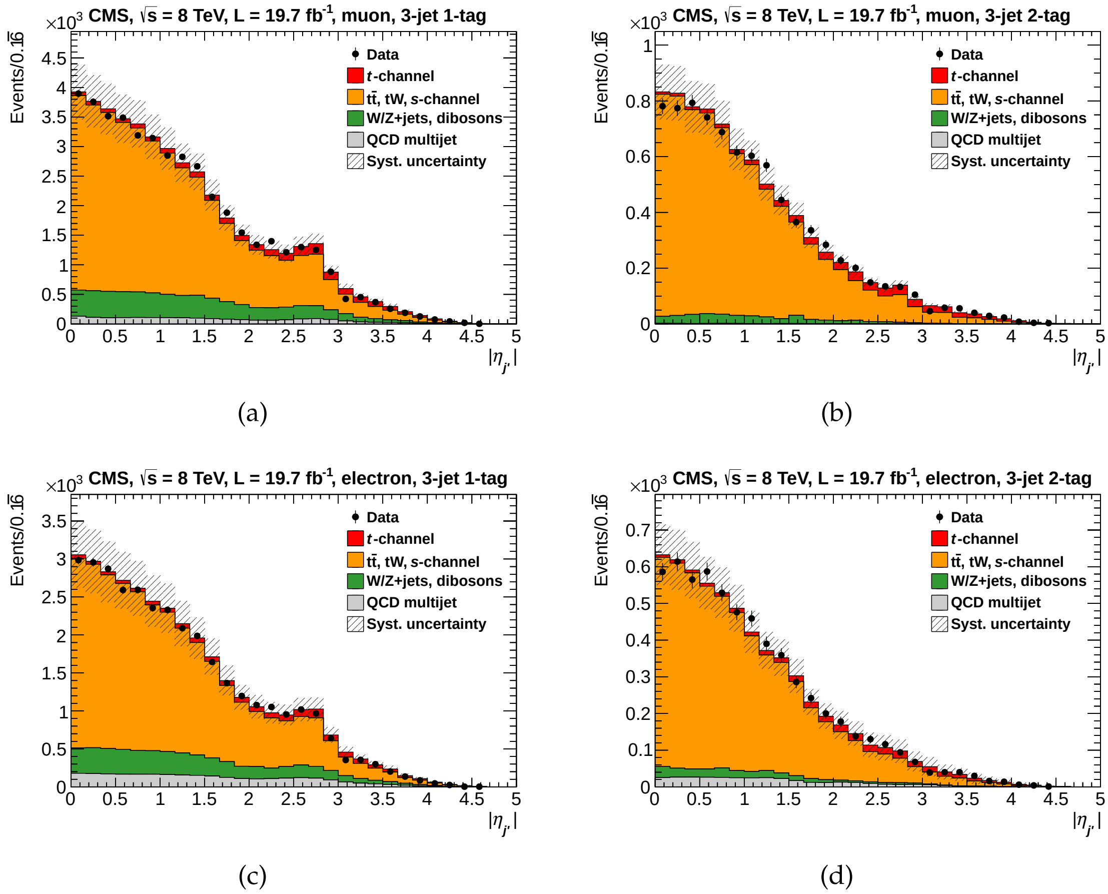

Figure 5.2: The $|\eta_{j'}|$ distribution for $t\bar{t}$ enriched regions (3-jet 2-tag, 3-jet 1-tag) for the muon (electron) channel. The histograms are normalized to the fit result.

The pseudorapidity of the jets is a crucial variable for the strategy in this analysis. The variable $|\eta_{j'}|$ is defined as the pseudorapidity of light-quark jet recoiling against the W-boson. The $|\eta_{j'}|$ remain at the lower values for the signal events where as it extends to value larger than for the background processes. Figure 5.2(a), 5.2(b) show the distributions of $|\eta_{j'}|$ of the jet with the lowest values of the b-tag discriminator in 3j2t and 3j1t region for the muon channel and the Fig. 5.2(c), 5.2(d) show the distribution of $|\eta_{j'}|$ of the jet with the lowest values of the b-tag discriminator in 3j2t and 3j1t region for the electron channel.

The top-quarks and anti top-quarks produced in the $t\bar{t}$ process are identified using the charge of the lepton in the final state. Figures 5.3(a), Fig. 5.3(b) (Fig. 5.3(c), Fig. 5.3(d)) show the number of positive and negative muon (electron) channel produced in 3j2t and 3j1t. The ratio of positive to negative charged lepton for the 3j2t and 3j1t can be seen in the Fig. 5.4. The ratio in the two $t\bar{t}$ enriched regions is close to unity as expected.

Furthermore, the dependence of the measurements on the modelling of $t\bar{t}$ enriched regions is also modified using the information of non b-tagged jets in 3j2t samples. By using the $|\eta_{j'}|$ distribution, the contribution of all the other contributing processes except for $t\bar{t}$ in 3j2t region is subtracted from the $|\eta_{j'}|$ distribution of non b-tagged jets taken from

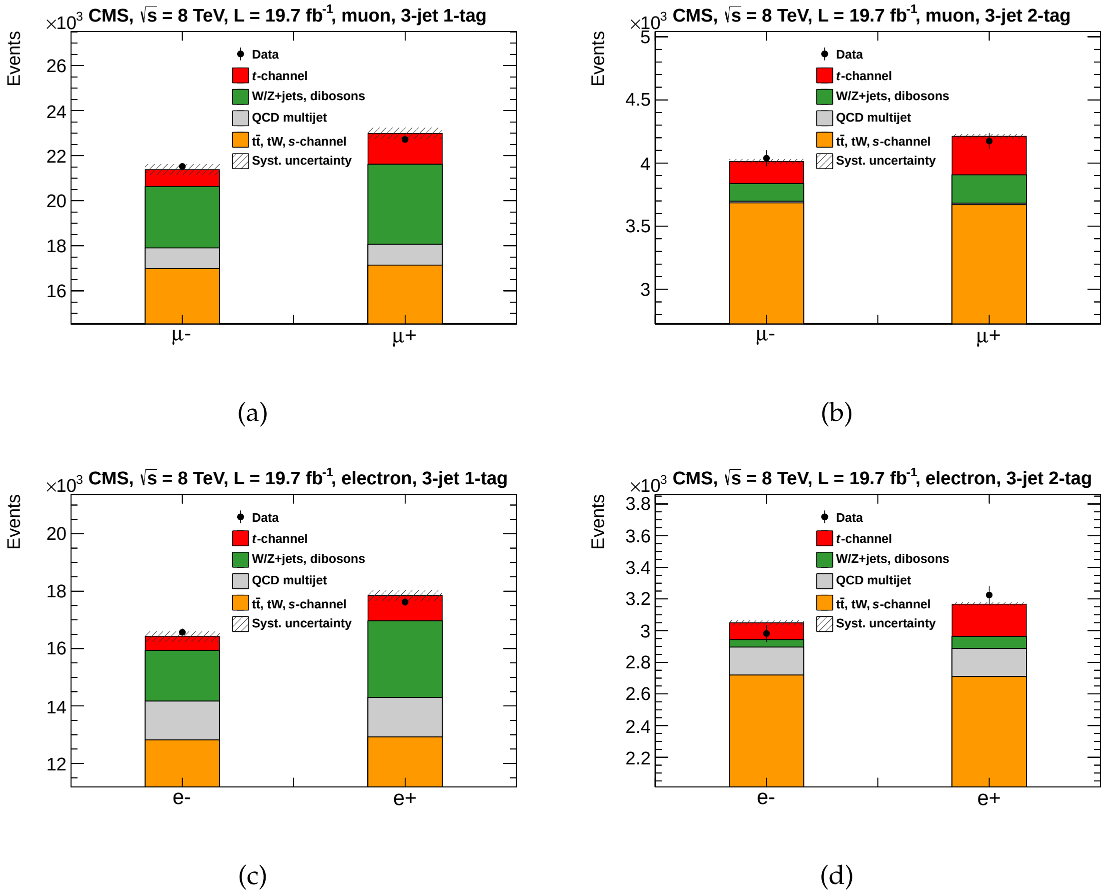

Figure 5.3: The lepton charge in 3-jet 2-tag, 3-jet 1-tag region for the muon (electron) channel. The sum of all the Monte Carlo predictions is normalized to the data yield and the systematic uncertainty band include all the possible sources of uncertainty.

data. The bin by bin ratio of this template and the template from $t\bar{t}$ process is taken as $|\eta_{j'}|$ dependent correction factor for the $t\bar{t}$ in the 2j1t region. This ratio is than used in the signal and side band region for the $|\eta_{j'}|$ distribution.

5.1.3 W/Z+jets Background

In the W/Z+jets samples the probability of finding the b-jets is very small almost negligible. Therefore the 2-jet 0-tag sample is used for the estimation of W/Z+jets background. The 2j0t tag sample is used for the comparison of data to Monte Carlo simulation. The $|\eta_{j'}|$ distribution in W/Z+jets is shown in the Fig. 5.5 and fairly good data to MC comparison is attained. Similarly like the $t\bar{t}$ enriched region the corresponding lepton (muon/electron) charge in 2-jet 0-tag region is shown in the Fig. 5.7.

Looking closely at the Fig. 5.6 and Fig. 5.7 the characteristic asymmetry in the production of positively and negatively charged leptons in W+jets can be seen in data and is fairly complemented by MC comparison to data.

The jets present in the 2-jet 0-tag samples are mostly coming from the light quarks (u, d,

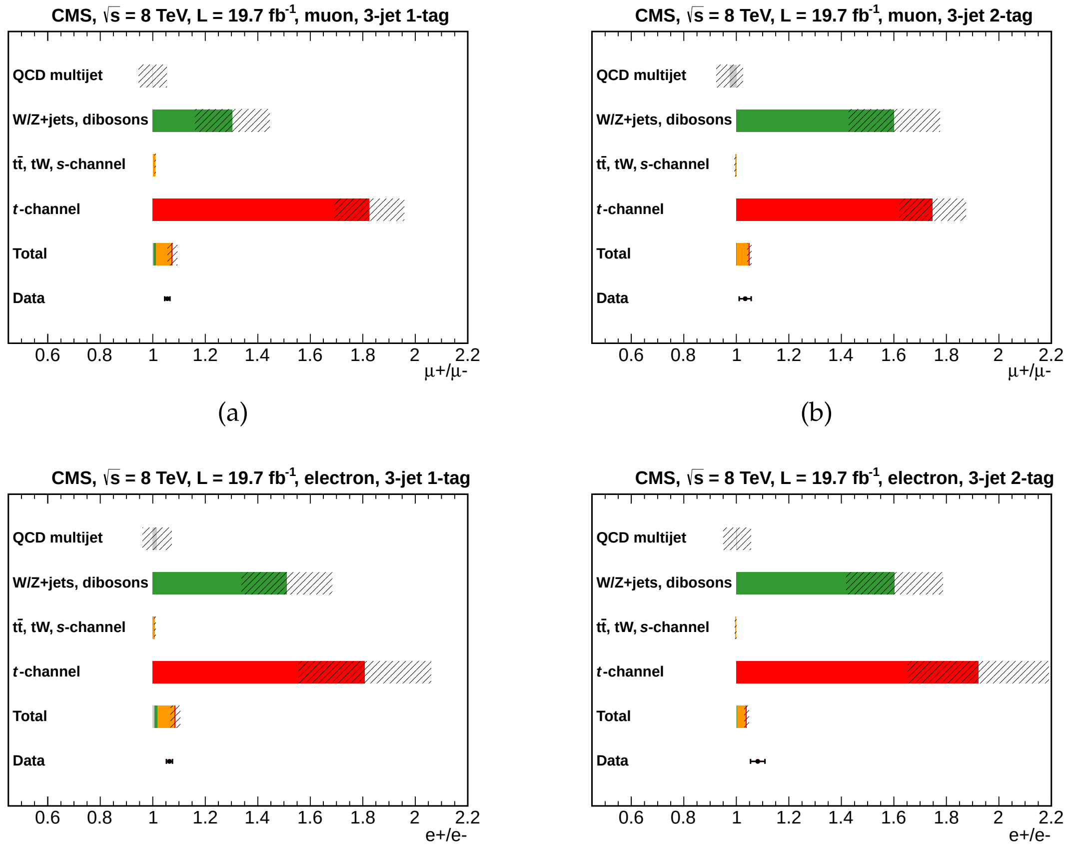

(a) (b) (c) (d)

Figure 5.4: The ratio of lepton charge in 3-jet 2-tag, 3-jet 1-tag region for the muon (electron) channel. The sum of all the Monte Carlo predictions is normalized to the data yield and the systematic uncertainty band include all the possible sources of uncertainty.

s) and gluons. The behavior of these light quark and gluon jets are quite different from the heavy flavour jets which originate from c or b quarks. For this reason the W+jets charge ratio in the final state is derived from data. The side band region SB which is defined as the region in which the reconstructed mass "$m_{\ell\nu b}$" of the top-quark lies outside the mass window $130 < m_{\ell\nu b} < 220\,\mathrm{GeV}$ and signal region SB is defined as the region in which the reconstructed mass "$m_{\ell\nu b}$" of the top-quark lies inside the mass window $130 < m_{\ell\nu b} < 220\,\mathrm{GeV}$.

The side band region in the 2j1t sample is used for the estimation of the W/Z+jets in a region that is expected to have a similar contribution in terms of W/Z+heavy flavours with respect to the sample that is used for the cross-section extraction, i.e., the 2j1t signal region. The $|\eta_{j'}|$ for the W/Z+jets is extracted from the sideband region by subtraction all other processes bin by bin. The $t\bar{t}$ and QCD used here are derived from data while the rest of the processes are taken from simulation. The scale factors are derived from simulation for the signal region and the side band region. The similar process is performed for the inclusive and exclusive distribution when separated on the basis of lepton charge. The bias in the two regions is estimated on simulation and removed from the samples derived from data . The uncertainty on the W+c-jets and W+b-jets events is taken into account,

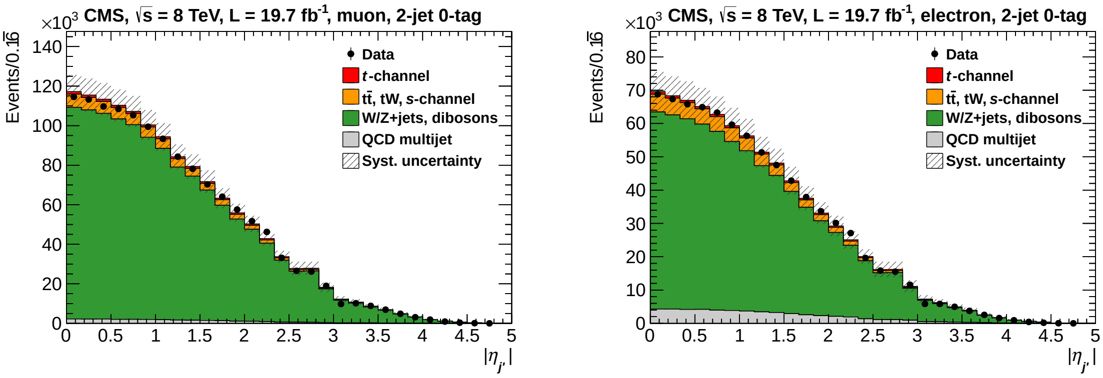

(a) (b)

Figure 5.5: $|\eta_{j'}|$ distribution for W/Z+jets enriched regions 2-jets 0-tag for the muon (electron) channel. The systematic uncertainty, the shaded bands, include pre-fit uncertainties on the normalisation and on the shape of the distributions.

described in section 5.3.

5.2 Signal Extraction

The signal is extracted by performing a two binned maximum likelihood fit to $|\eta_{j'}|$ distribution in 2-jet 1-tag signal region. The fit performed to the distribution in which the events are not separated on the basis of their charge gives the inclusive cross-section while the fit performed to those distribution in which events are separated on the basis of their charge gives the cross-section of t and $\bar{\mathrm{t}}$. The expected contribution of every process in each bin of $|\eta_{j'}|$ can be modelled with the following likelihood function:

$$\mathrm{n}(|\eta_{j'}|) = \mathrm{N_s P_s}(|\eta_{j'}|) + \mathrm{N_t P_t}(|\eta_{j'}|) + \mathrm{N_{EW} P_{EW}}(|\eta_{j'}|) + \mathrm{N_{MJ} P_{MJ}}(|\eta_{j'}|), \tag{5.2.1}$$

where in the equation 5.2.1 the subscript "s" represents the signal, "EW" represents the electroweak component composed of W/Z+jets and WW, WZ, ZZ. Similarly the subscript "t" represents the top-quark component consisting of $\mathrm{t\bar{t}}$, *s*-channel and tW. The subscript "MJ" represents the QCD multijet component. The $\mathrm{N_s}$, $\mathrm{N_t}$, $\mathrm{N_{EW}}$ and $\mathrm{N_{MJ}}$ are the yields of the signal and backgrounds components. The $\mathrm{P_s}$, $\mathrm{P_t}$, $\mathrm{P_{EW}}$ and $\mathrm{P_{MJ}}$ are the binned probability distribution functions for the signal and backgrounds components. The *t*-channel single-top-quark inclusive cross-section is extracted from events with positively or negatively charged leptons, defining one likelihood function per lepton flavour, as described in Eq. 5.2.1. The two distributions for electron and muon are than fitted together. For the extraction of cross-section of t and $\bar{\mathrm{t}}$ the events are further divided on the basis of charge of muon or electron. One likelihood function per lepton flavour and per charge as described in the Eq. 5.2.1 is used for fitting the four distribution together.

The binned probability distribution $\mathrm{P_s}$ for both the fits are taken from $|\eta_{j'}|$ simulation. For the inclusive cross-section fit, the total signal yield $\mathrm{N_s}$ is fitted unconstrained, where as for the signal t and $\bar{\mathrm{t}}$ cross-section fit two parameters are introduced for the positively

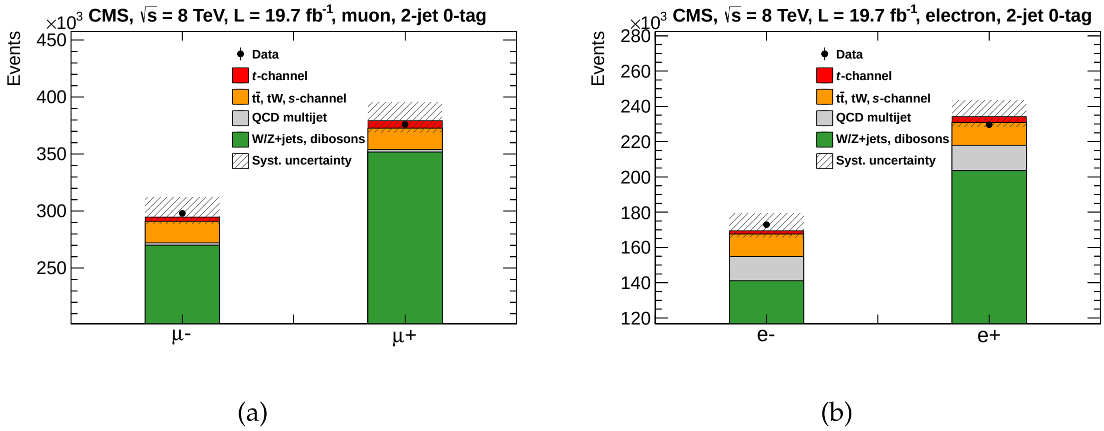

Figure 5.6: The ratio of lepton charge in 2jet 0-tag region for the muon (electron) channel. The sum of all the Monte Carlo predictions is normalized to the data yield and the systematic uncertainty band include all the possible sources of uncertainty.

and negatively charged lepton signal yield.

The binned probability distribution P_{EW} is the sum of the contribution of diboson and W/Z+jets processes. The W/Z+jets are estimated from the side band region of $m_{\ell\nu b}$ distribution. This estimation is applied to both electron and muon with respect to the charge of the lepton in case of the inclusive top-quark cross-section fit. Similarly for t and $\bar{t}$ cross-section extraction the estimation is applied separately to the positively and negatively charged leptons. The diboson contribution is taken from simulation. The two resulting distributions are summed together and the resulting total event yield N_{EW} is derived from the fit. The prior knowledge of the normalisation is obtained from the side-band and a Gaussian constraint is applied to N_{EW} in the fit. The mean value is taken from the simulation and the standard deviation taken is equal to the difference between the data driven yield of W/Z+jets and the expectation from simulation in the sideband region. For the single t and $\bar{t}$ cross-section ratio fit, the electroweak component N_{EW} are fitted separately for positively and negatively charged electrons and muons.

The binned probability distribution P_t of the top-quark processes consists of $t\bar{t}$, tW and *s*-channel. The $t\bar{t}$ contribution is determined from data and the contribution of tW and *s*-channel is added to it with the normalization factor determined from the simulation. Because of the charge symmetry of $t\bar{t}$ and tW the contribution is also separated by lepton flavour and charge, where as *s*-channel charge ratio is fixed in standard model of particle physics. However the yield N_t is fitted with the Gaussian constraint with a standard deviation of $\pm 10\%$ and the mean value of Gaussian is centered at the value obtained from simulation. The $\pm 10\%$ variation is chosen to cover both experimental and theoretical uncertainties on $t\bar{t}$ cross-section. The binned probability distribution P_{MJ} for multijet QCD is determined from data and the yield fixed to the results of m_T and $\not{E}_T$ fit described in Section 5.1.1.

The fit strategy driving this parametrisation is mainly focused on constraining W/Z+jets and $t\bar{t}$ backgrounds which are derived from data. In case of the single t and $\bar{t}$ cross-section

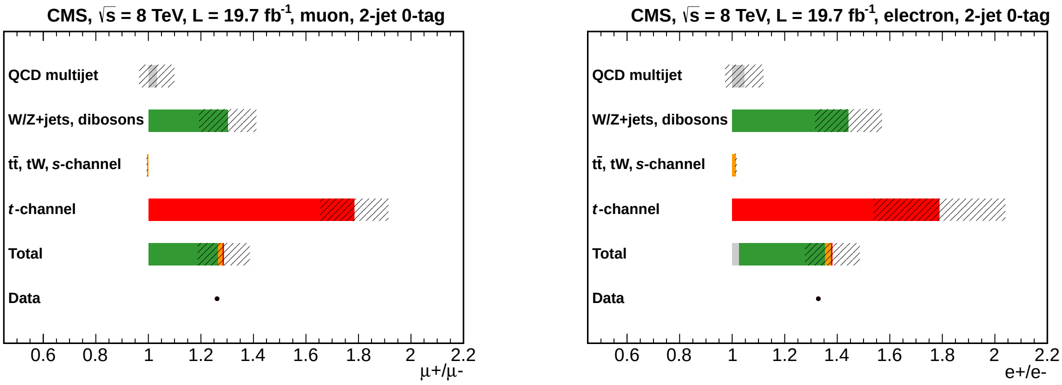

(a) (b)

Figure 5.7: The ratio of lepton charge in 2-jet 0-tag region for the muon (electron) channel. The sum of all the Monte Carlo predictions is normalized to the data yield and the systematic uncertainty band include all the possible sources of uncertainty.

fit, the event ratio of positively and negatively charged W-bosons is constrained as well. The total cross-section measurement from the inclusive analysis is more precise than the one inferred from the separate-by-charge fit, due to the additional uncertainty from the W-boson charged ratio.
Figure 5.8 shows the $|\eta_{j'}|$ distribution in muon (electron) channel for 2j1t region. The distributions of each process is normalized to the value of the inclusive cross-section. Similarly the Fig. 5.9 shows the $|\eta_{j'}|$ distributions for positively and negatively charged leptons in 2j1t region which are normalized to t and $\bar{\mathrm{t}}$ cross-section ratio fit. Figure 5.10 shows the reconstructed top-quark mass distribution in 2j1t region with $|\eta_{j'}| > 2.5$. The distributions are normalised by scaling with the fit result. The 2j1t region is a signal enriched phase space, hence a characteristic peak can be seen around the top-quark pole mass for the muon and electron channel.

5.3 Systematic Uncertainties

In the following section, the various sources of systematic uncertainties present on the signal are discussed. The uncertainties on the background and samples are not taken into account. The pseudo experiments are thrown using each process distributions and the yields generated considering the each up and down variation. A fit is performed to the $|\eta_{j'}|$ distribution for each pseudo experiment with the nominal setup. The difference of fit result for the up and down systematic with respect to the nominal result is taken as the corresponding uncertainty.

- **Jet Energy Scale/Resolution and Missing Transverse Energy:** The four-momenta of all the reconstructed jets in the Monte Carlo simulated events are smeared according to η and p_{T} dependent uncertainties in the Jet energy scale and resolution. This variation in the jet momentum is propagated to $\not{E}_{\mathrm{T}}$. The energy contribution from all jets with $p_{\mathrm{T}} < 10\,\mathrm{GeV}$ and PFCandidates not clustered to jets is called "unclustered energy". This energy contribution is varied $\pm 10\%$ [178] and the resulting uncertainty is propagated to the calculation of the missing transverse energy.

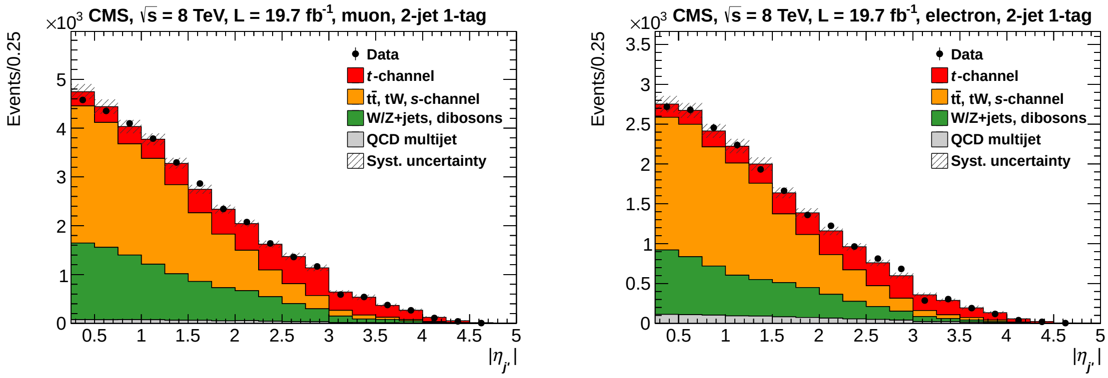

(a) (b)

Figure 5.8: The fitted $|\eta_{j'}|$ distributions for muon (electron) channels. The distribution is normalised to the yields obtained from the combined total cross-section fit. The systematic uncertainty bands include the shape uncertainties on the distributions.

- **Pileup Modelling (PU)**: The uncertainty which arises due to the average expected number of additional interactions per bunch crossing ($\pm5\%$) is propagated as a systematic uncertainty.

- b**-Tagging:** The b-tagging rate and misidentification rates are estimated from the control samples [179]. The simulated samples are than scaled to reproduce the efficiencies in data and the corresponding uncertainties are propagated as systematic uncertainties.

- **Muon/Electron Trigger and Reconstruction:** The lepton trigger efficiencies and the reconstruction efficiency as function of lepton p_T and η are estimated using tag and probe method using the Drell-Yan data [180]. The effect of incorrect determination of the lepton charge has been taken into account for muon and electron. In case of muon the effect is negligible while in case of electron the uncertainty on the determination of charge has already been measured [181].

- $\mathrm{t\bar{t}}$**,** W**+jets and QCD Estimation:** The normalization and distribution of $\mathrm{t\bar{t}}$, W+jets and QCD are derived from data. The uncertainty on the $\mathrm{t\bar{t}}$ is estimated by dicing the pseudo experiments in the side band region and 3j2t tag samples and the background estimation is repeated. The $|\eta_{j'}|$ distribution is fitted and the root mean square of the fit result gives the uncertainty on the $\mathrm{t\bar{t}}$ background. There is an additional uncertainty on the $\mathrm{t\bar{t}}$ estimation which is determined by performing a signal extraction from the $\mathrm{t\bar{t}}$ distribution in whole $m_{\ell\nu\mathrm{b}}$ range, the two different distributions are used for the signal and background regions. The uncertainty on W+jets is determined from different $|\eta_{j'}|$ shapes which are derived from Monte Carlo simulations by varying the heavy flavour content, W+heavy (b,c), independently by $\pm30\%$ in the signal and side band regions. The QCD normalization is varied by $\pm50\%$ independently in the electron and muon channel. The variation range is obtained by estimating the QCD background under different assumptions and conditions. The maximum difference with respect to the nominal estimation procedure is taken as an uncertainty on the QCD normalization, while all other systematic uncertainty are coherently propagated in the estimation procedure.

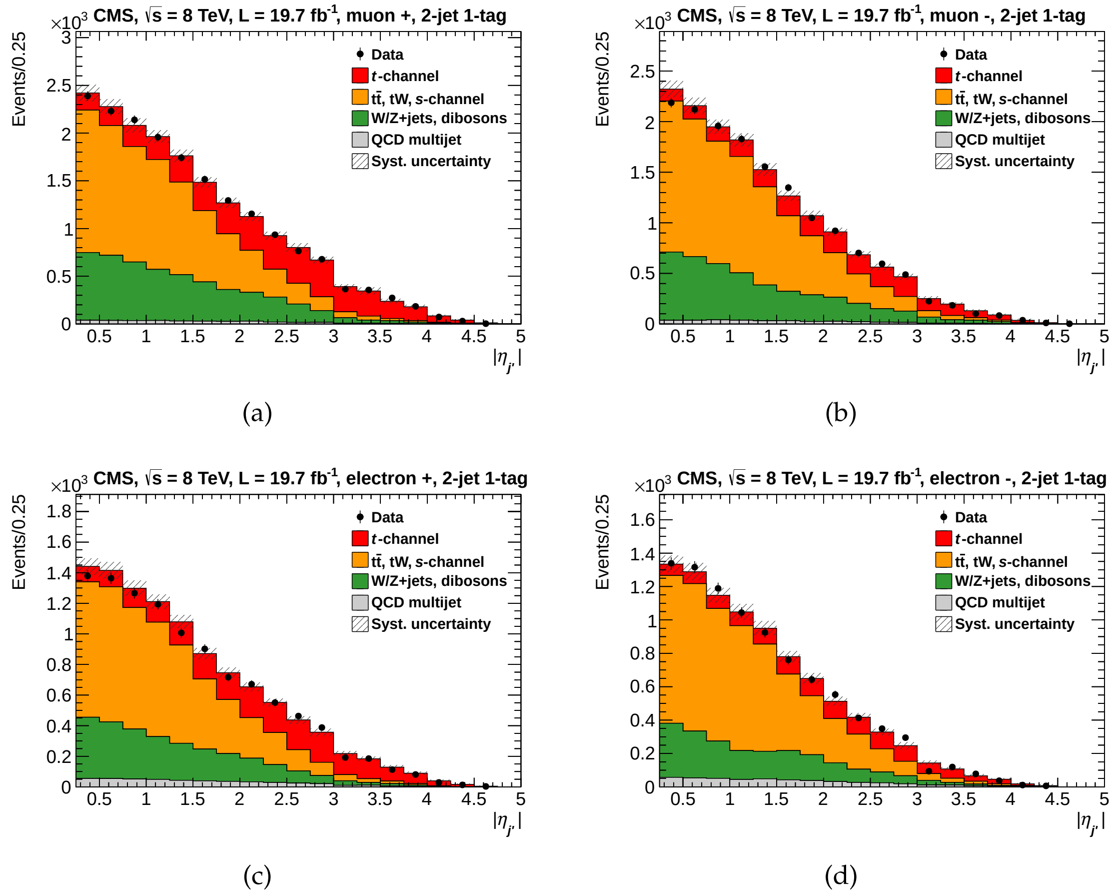

Figure 5.9: The fitted $|\eta_{j'}|$ distributions for muon (electron) channels. The distribution is normalised to the yields obtained from the combined t and $\bar{\text{t}}$ cross-section fit. The systematic uncertainty bands include the shape uncertainties on the distributions.

- **Background Normalization:** The uncertainty on the normalization of $\text{t}\bar{\text{t}}$ is taken to be $\pm 10\%$ which covers the theoretical differences [85, 182, 183]. The normalization on the diboson, tW, s-channel is taken to be $\pm 30\%$ [85, 182, 184].

- **Signal Modelling:** The uncertainty on the renormalization and factorization scale is determined by multiplying or dividing by a factor of 2 up and down. The corresponding variation is than taken as the scale uncertainty. The uncertainty due to the signal generator is obtained by comparing the nominal generated samples with POWHEG with CompHEP. Half of the difference is taken as the systematic uncertainty arising due to the signal modelling.

- **Parton Distribution Function:** The uncertainty due to the choice of PDFs is determined by reweighing the simulated events and repeating the signal extraction. The envelope of CT10 [185], MSTW [81], and NNPDF [186] PDF set is taken as the systematic uncertainty according to the PDF4LHC recommendations.

- **Simulation Sample Size:** The statistical uncertainty arising due to the limited size of the Monte Carlo simulation is estimated by dicing the pseudo experiments to reproduce the statistical fluctuation in the model. The fitting procedure is repeated

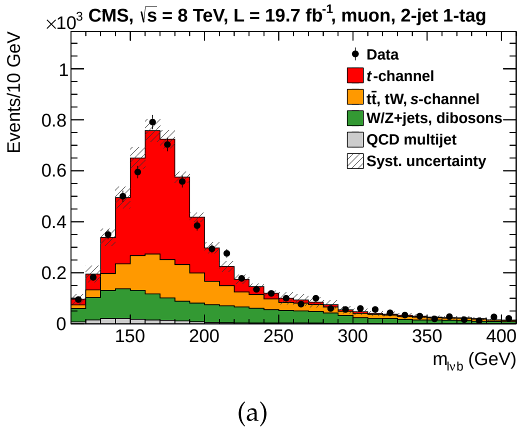

Figure 5.10: The fitted $m_{\ell\nu\mathrm{b}}$ distributions for muon (electron) channels in 2j1t region. The distribution is normalised to the yields obtained from the combined cross-section fit. Systematic uncertainty bands include the shape uncertainties on the distributions.

for each pseudo experiment and the uncertainty is evaluated as the RMS of the distribution of fit results.

- **Luminosity:** The total integrated luminosity is known with a relative uncertainty of $\pm 2.6\%$ [187].

Tables 7.1 and 7.2 give the relative impact of each uncertainty on the inclusive cross-section and on the ratio measurements in the lepton+jets final state respectively. The uncertainties arising due to the limited size of Monte Carlo simulation and on the data driven background estimation do not cancel each other, as a result they have a large impact on the ratio of cross-section measurement than on the inclusive cross-section measurement. The uncertainty due to luminosity have an impact on the total cross-section measurement but tends to cancel out in the ratio measurement. Similarly the uncertainty sources like b-tagging, lepton trigger and reconstruction efficiency which affect the signal events in a same way for t and $\bar{\mathrm{t}}$ have an impact in total cross-section but have a small effect on the ratio measurement. Uncertainties that can affect the background processes and are independent from the lepton charges, $\mathrm{t\bar{t}}$ or QCD, they have a much larger impact on the single t production cross-section, this is the reason they do not cancel out in the ratios of cross-sections. The production cross-section of t and $\bar{\mathrm{t}}$ depends largely on the PDFs of the contribution quarks, the corresponding PDF uncertainties are anti correlated as a result the corresponding uncertainty on the ratio measurement is enhanced. Since the momentum and pseudorapidity of quarks and leptons for t and $\bar{\mathrm{t}}$ are different, modelling uncertainties and uncertainties due to the missing transverse energy and jet energy scale do not cancel out totally in the ratio measurement. As a result the event yield obtained after fitting for total cross-section and for t and $\bar{\mathrm{t}}$ are not identical. The uncertainty in the heavy flavour component in total cross-section and cross-section obtained for t and $\bar{\mathrm{t}}$ are anti correlated, also the theoretical uncertainties are effecting the exclusive measurements more than the inclusive cross-section measurement.

Table 5.1: The Event yield for the signal and background processes in the 2j1t signal and the side band region for the muon and electron channel. The yield is obtained from simulation and the corresponding uncertainty quoted is due to the finite monte carlo size except for QCD and W/Z+jets whose yields and uncertainties are taken as the statistical component of the uncertainty in estimation from data.

Process	Muon		Electron	
	SR	SB	SR	SB
$t\bar{t}$	17214 ± 49	8238 ± 35	11162 ± 38	8036 ± 33
W/Z+jets	10760 ± 104	9442 ± 97	4821 ± 69	6512 ± 81
QCD	765 ± 5	271 ± 4	1050 ± 6	1350 ± 6
Diboson	179 ± 4	161 ± 4	95 ± 3	134 ± 3
tW	1914 ± 28	969 ± 20	1060 ± 28	858 ± 18
s-channel	343 ± 1	118 ± 1	180 ± 1	96 ± 1
t-channel	6792 ± 25	944 ± 9	3616 ± 17	753 ± 8
Total expected	37967 ± 121	20143 ± 106	21984 ± 85	17740 ± 90
Data	38202	20237	22597	17700

Table 5.2: The event yield for the signal and background processes in the 2j1t signal and side band region for the positively and negatively charged muon and electron. The yield is obtained from simulation and the corresponding uncertainty quoted is due to the finite monte carlo size except for QCD and W/Z+jets whose yields and uncertainties are taken as the statistical component of the uncertainty in estimation from data.

Process	Muon		Electron	
	+	−	+	−
$t\bar{t}$	8620 ± 35	8594 ± 35	5574 ± 27	5588 ± 27
W/Z+jets	5581 ± 75	4989 ± 71	2618 ± 52	2121 ± 46
QCD	361 ± 1	366 ± 1	697 ± 2	679 ± 2
Diboson	106 ± 3	73 ± 2	58 ± 2	39 ± 2
tW	964 ± 20	951 ± 20	535 ± 14	525 ± 14
s-channel	225 ± 1	118 ± 1	118 ± 1	62 ± 1
t-channel	4325 ± 19	2467 ± 16	2320 ± 13	1295 ± 11
Total expected	20181 ± 87	17557 ± 83	11920 ± 61	10310 ± 56
Data	20514	17688	12035	10562

Chapter 6

Differential Cross-section Measurement

In the following, the differential cross-section measurements of the single-top-quark t-channel production as function of top-quark p_{T} and $|y|$ are presented. First the QCD multijet background estimation is discussed, than the modelling of various input variables for the training of neural network in the W+jet control region (2j0t), $t\bar{t}$ enriched region (3j2t) and than in the signal region (2j1t) are discussed. The well trained neural network is used for the classification of unknown data is presented. Finally, we use the unfolding to get the true distribution of top-quark p_{T} and $|y|$ to extract the differential cross-section in the bins of p_{T} and $|y|$.

6.1 Background Estimation

Applying the described event selection criteria, the amount of QCD background events can be reduced a lot. Nevertheless, a significant contribution from the different sources of background events passes those requirements. Based on monte carlo simulation studies, we estimate the fraction of background events after applying the described selection criteria to be 86% (87%) in the muon (electron) channel respectively.

To further reduce the background contribution, a trained neural net is used to separate signal from background processes. For all processes except for QCD multijet production the distributions of the input variables are modeled using monte carlo simulations. The cross-section of QCD multijet production is so large that it can be modeled directly from data. For that purpose the selection criteria are altered to enrich the selected dataset in QCD events. This QCD enriched sample is not only used to model the distributions of all the kinematic variables used for the neural network training, but also to estimate the amount of QCD events in the signal region as no reliable prediction from monte carlo simulation is available for the QCD contribution.

As explained later in section 6.5, not only the signal region (2j1t) is used to fit the signal and background fractions, but also the $t\bar{t}$ enriched 3j2t control region. In the 2j1t region there is a significant contribution from QCD-multijet processes, while the fraction of this background is only small in the 3j2t region. In the data driven estimation of the QCD multijet contribution we make use of the transverse mass m_{T} of the W-boson as a discriminating variable in the muon channel and missing transverse energy $\not{E}_{\mathrm{T}}$ in the electron channel. The next two sections describe in detail how the QCD enriched sideband selection is defined and how the data-driven estimation of the QCD contribution in the signal region works.

6.1.1 Data Driven QCD Templates

The QCD multijet templates are obtained from data in QCD enriched sidebands of the 2j1t signal region and the 3j2t control region. These sideband regions are defined by inverting the isolation condition for the electron or muon candidate. Instead of requiring $I_{\mathrm{rel}}^{\delta\beta-\mathrm{corr.}}$ <0.12 for the muon and $I_{\mathrm{rel}}^{\delta\beta-\mathrm{corr.}}$ <0.1 for the electron candidate, for the definition of the QCD enriched sideband regions the isolation of the lepton has to be between 0.3 and 0.5. To ensure, that despite this inversion of the relative isolation the jets and leptons are well separated, a special requirement on the angular separation of jets and leptons is introduced. Only jets with a distance ΔR (jet,l) >0.3 from the selected charged lepton are considered for the analysis.

The events from these sideband are than used to model the QCD contribution in the various kinematic distributions used in the analysis. For the estimation of the amount of QCD events in the selected samples two sensitive variables, the transverse mass m_{T} distribution of the W-boson in case of the muon channel and $\not{E}_{\mathrm{T}}$ distribution in case of the electron channel, are used and for that purpose dedicated QCD templates are needed, which are from the same sideband regions as described above, with the obvious addition that the cut on m_{T} or MET is not applied. Using the Monte Carlo simulated samples the contamination from non-QCD events in the anti-isolated regions is estimated to be below 1.5% in the 2j1t region in both channels before the cut on m_{T} or $\not{E}_{\mathrm{T}}$, see Fig. 6.1 (a) and (b). The non-QCD contributions are normalized to their predicted cross-section and the assumed luminosity and are subtracted from the measured data distributions, see Fig. 6.1(c) and (d). Figure 6.1 (e) and (f) compare the distributions for m_{T} and $\not{E}_{\mathrm{T}}$ for the QCD templates from data, corrected for non-QCD contributions, with the distributions from QCD Monte Carlo samples in the QCD enriched sideband region.

The contamination from non-QCD processes in the 3j2t region is higher, but QCD plays only a negligible role here and therefore no dedicated correction of the data-driven template is done in this case.

Estimation of QCD Multijet Background

In general, the distribution F of any kinematic variable x measured in data can be parameterized as:

$$\mathrm{F(x)=a \cdot S(x)+b \cdot B_1(x)+c \cdot B_2(x).} \tag{6.1.1}$$

For the differential cross-section measurement, we make use of two variables: x is the transverse mass (m_{T})of the W-boson in case of the muon channel and missing transverse energy (MET) in case of the electron channel. S(X), B_i(x) are the expected distributions for signal and background events, respectively. In our case, B_i(x) refers to all non-QCD events (derived from the monte carlo simulation of all non-QCD processes) and S(x) refers to the amount of QCD events (derived from data as described above). All non-QCD processes are added up to two background templates B_1(x) and B_2(x), according to their relative contribution as calculated from the MC prediction. Backgrounds containing a real W-boson in the process are added together to B_1(x), while Z+jets events are represented by

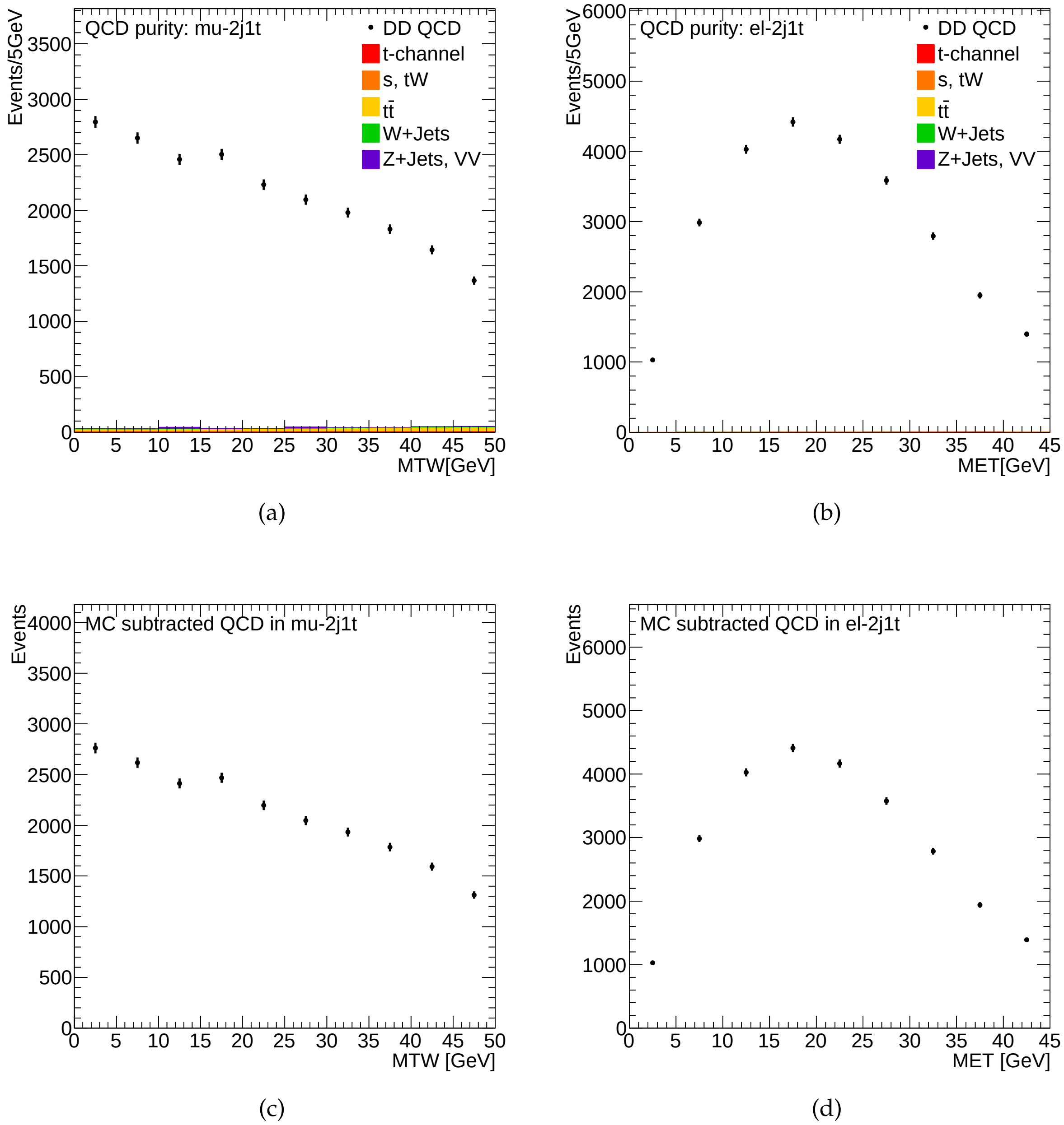

Figure 6.1: Distributions of MTW for the muon channel and MET distribution for the electron channel in the QCD enriched sideband of the 2j1t region. The non-QCD processes are simulated from MC and are normalized to their predicted cross-section and the assumed luminosity (a) and (b). The non-QCD processes have been subtracted from the data distributions (c) and (d).

$B_2(x)$. The normalization constants a, b and c are determined by a fit of F(x).

We fit the m_T ($\not{E}_T$) distribution in the low-m_T (low-$\not{E}_T$) region defined by $m_T < 50$ GeV ($\not{E}_T < 45$ GeV) and extrapolate the result into the region with $m_T > 50$ GeV in the muon channel and $\not{E}_T > 45$ GeV in the electron channel. Figure 6.2 and 6.3 show the m_T and $\not{E}_T$ distributions with the data-driven QCD template and the MC templates for the non-QCD events for the 2j1t and 3j2t regions. Table 6.1 gives the numbers of QCD events obtained for the muon and the electron channels in the two regions.

Table 6.1: The QCD estimation in the side band and the signal region for the muon (electron) channel. The uncertainties quoted are statistical uncertainties.

Muon Channel	Events	Electron channel	Events
2j1t region			
$m_T < 50$ GeV	21554±614	$\not{E}_T < 45$ GeV	26359±551
$m_T > 50$ GeV	5448±173	$\not{E}_T > 45$ GeV	2793±93
3j2t region			
$m_T < 50$ GeV	133±228	$\not{E}_T < 45$ GeV	580±14
$m_T > 50$ GeV	160±273	$\not{E}_T > 45$ GeV	117±41

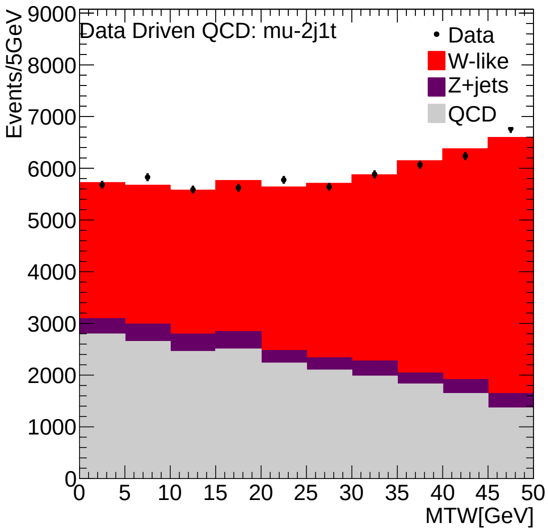

(a)

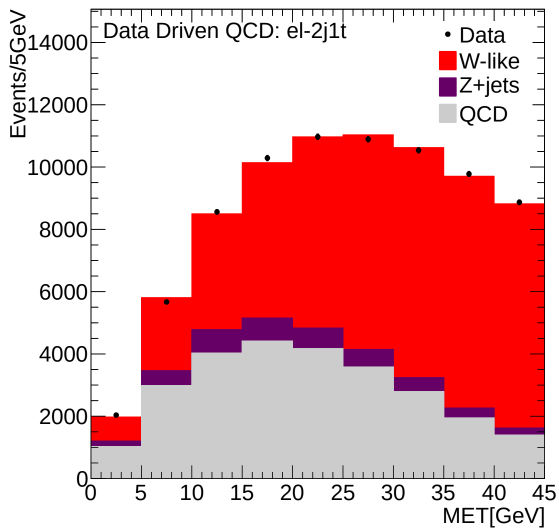

(b)

Figure 6.2: The transverse mass distribution of the W-boson (left) and missing transverse energy distribution (right) with the templates for QCD and non-QCD processes normalized to the fit results.

6.2 Variable Modeling

In the following, the modeling of various variables are presented. Since W+jets and $t\bar{t}$ are the two major backgrounds and proper modeling of different kinematic variables in

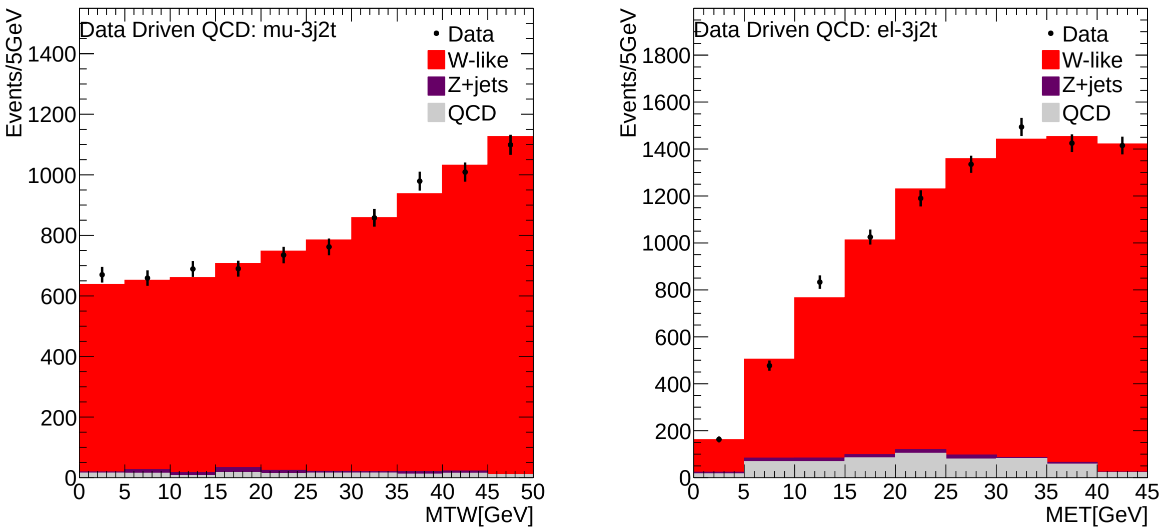

(a) (b)

Figure 6.3: The transverse mass (left) and missing transverse energy (right) distributions with the templates for QCD and non-QCD processes normalized to the fit results in the $t\bar{t}$ control region 3j2t.

the region enriched with these two backgrounds is very important. The W+jets control region is defined by the 2j0t region, where as the $t\bar{t}$ region is defined by 3j2t region.

6.2.1 Variable Modeling in 2j0t Region

The default signal region for the described analysis is the 2j1t region. Keeping all selection requirements but reverting the b-tag criterion by requiring that none of the two selected jets is identified as b-jet, defines the 2j0t region. This orthogonal sideband region is dominated by W+jets background events, with a fraction of 86% (81%) in the muon (electron) channel, and is therefore suited to compare the distributions of the used kinematic variables from simulated W+jets events with data events in order to validate the W+jets modelling. In the following figures this comparison between simulation and data is shown for all used input variables. The relative contributions of the different background processes are normalized to their predicted cross-sections, except for the contribution from QCD multijet events, which is normalized according to the results of the QCD fit described in Section 6.1. To allow for a better comparison of the shapes of the kinematic distributions, the sum of the modelled signal and background templates is scaled to yield the same integral as the data distribution.

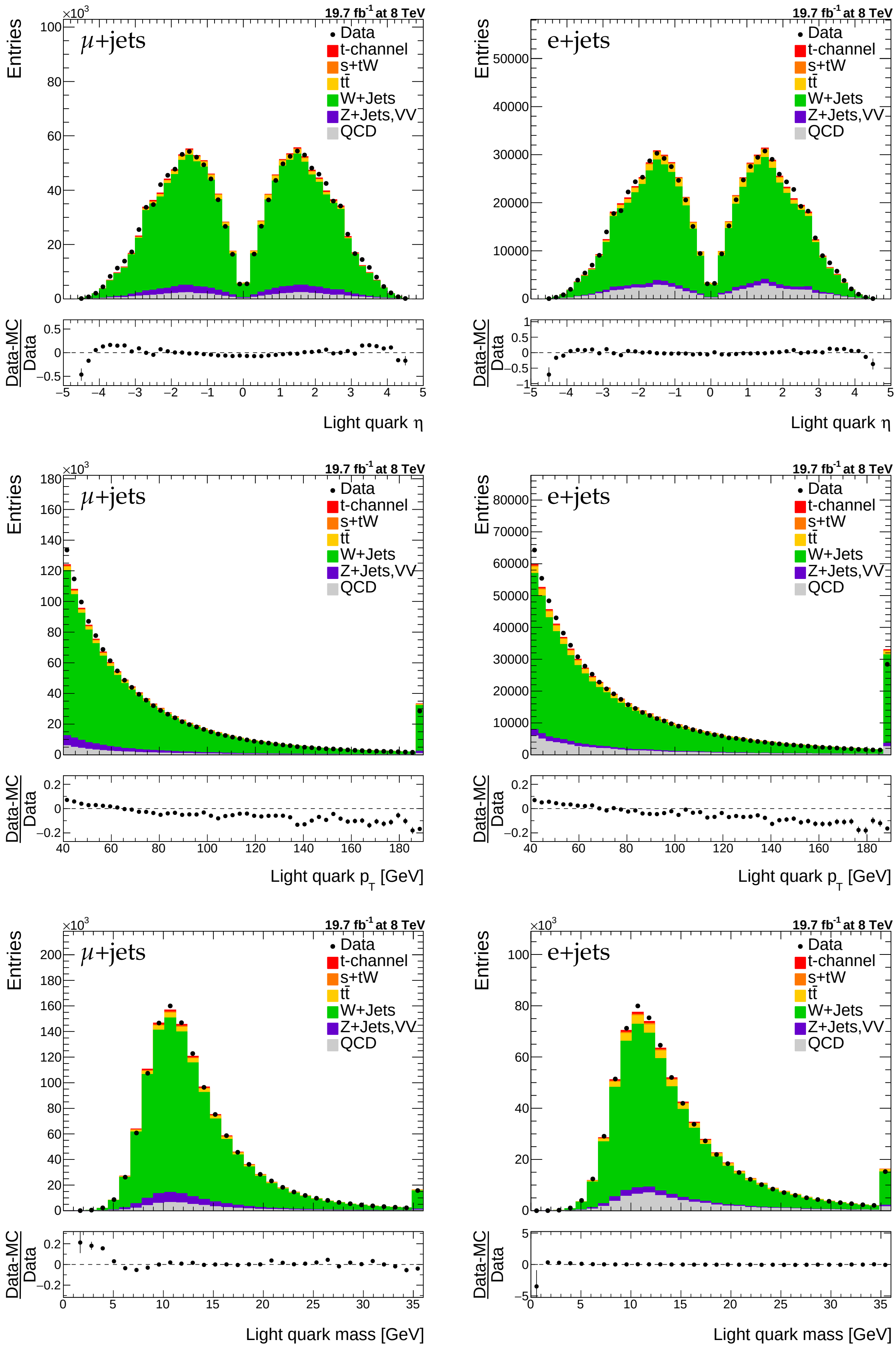

Figure 6.4: The pseudorapidity, transverse momentum, and mass of the jet assigned to the light quark in the W+jets control region (2j0t). The simulation is scaled to match the integral of the data distribution.

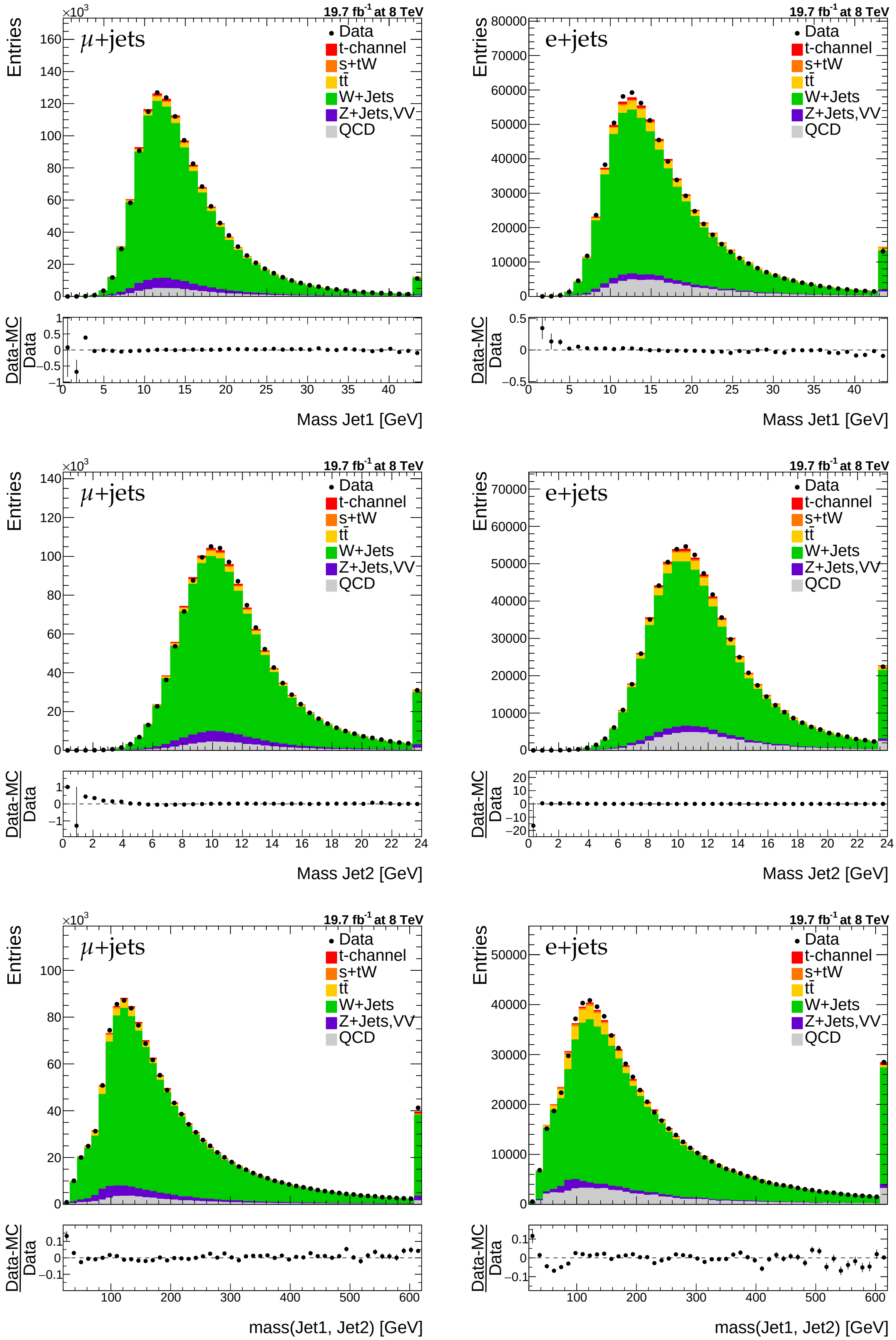

Figure 6.5: The invariant-mass of the leading jet, of the second leading jet, and of the dijet system in the W+jets control region (2j0t). The simulation is scaled to match the integral of the data distribution.

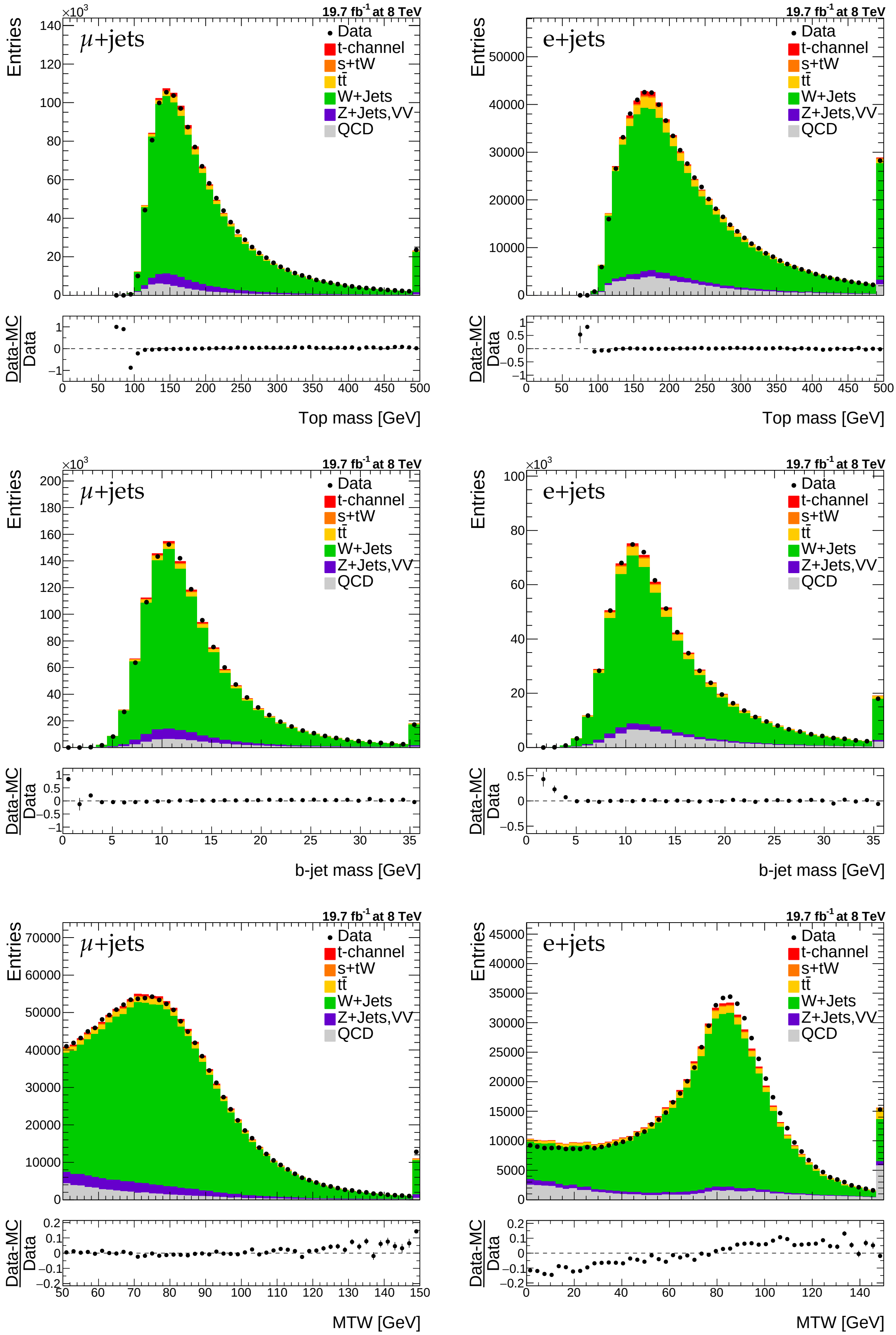

Figure 6.6: The reconstructed mass of the top-quark, of the jet assigned to the b-quark stemming from the decay of top-quark, and the transverse mass of the W-boson in W+jets control region (2j0t). The simulation is scaled to match the integral of the data distribution.

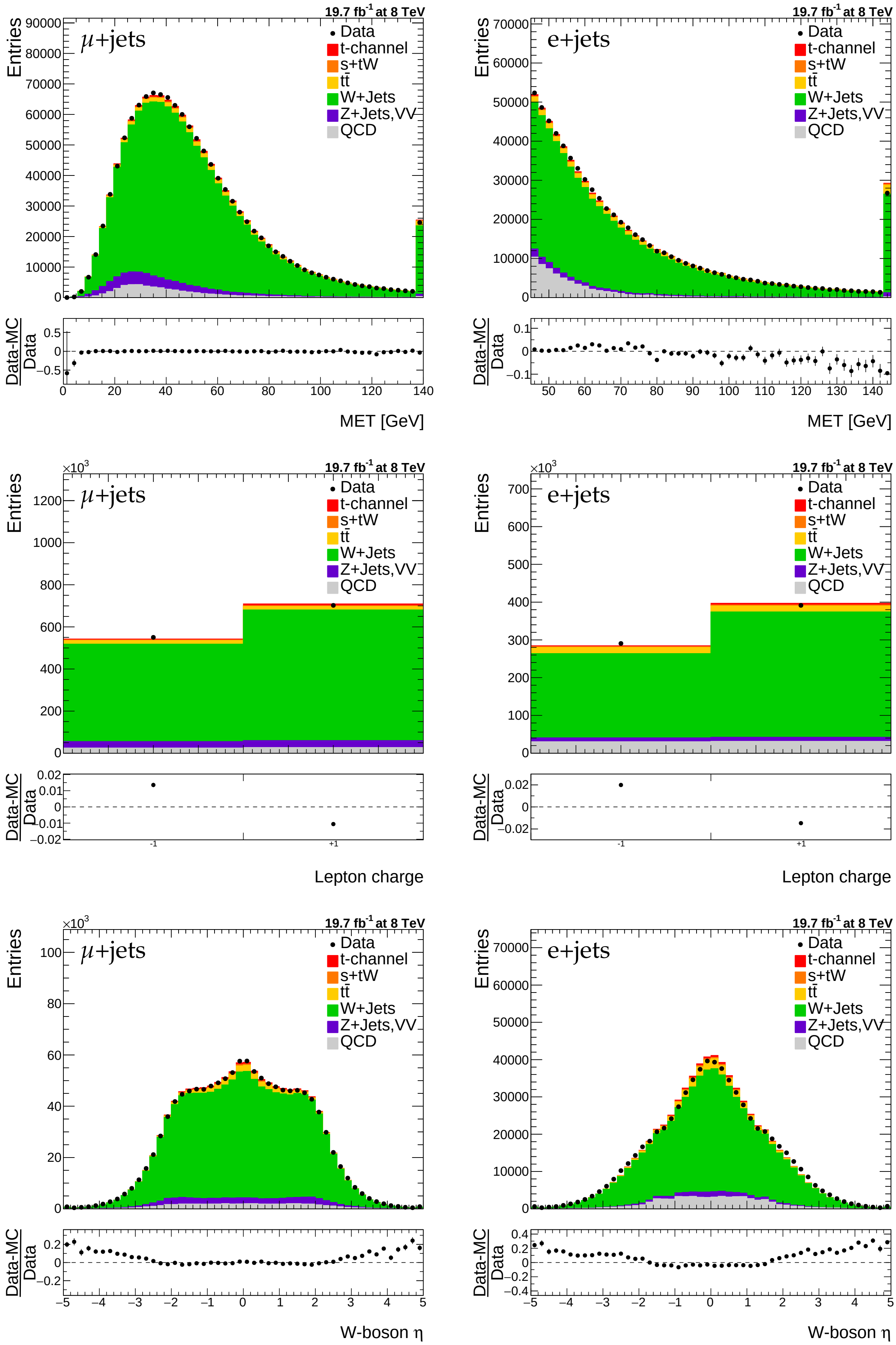

Figure 6.7: The missing transverse energy, the charge of the lepton, and the pseudorapidity of the W-boson in the W+jets control region (2j0t). The simulation is scaled to match the integral of the data distribution.

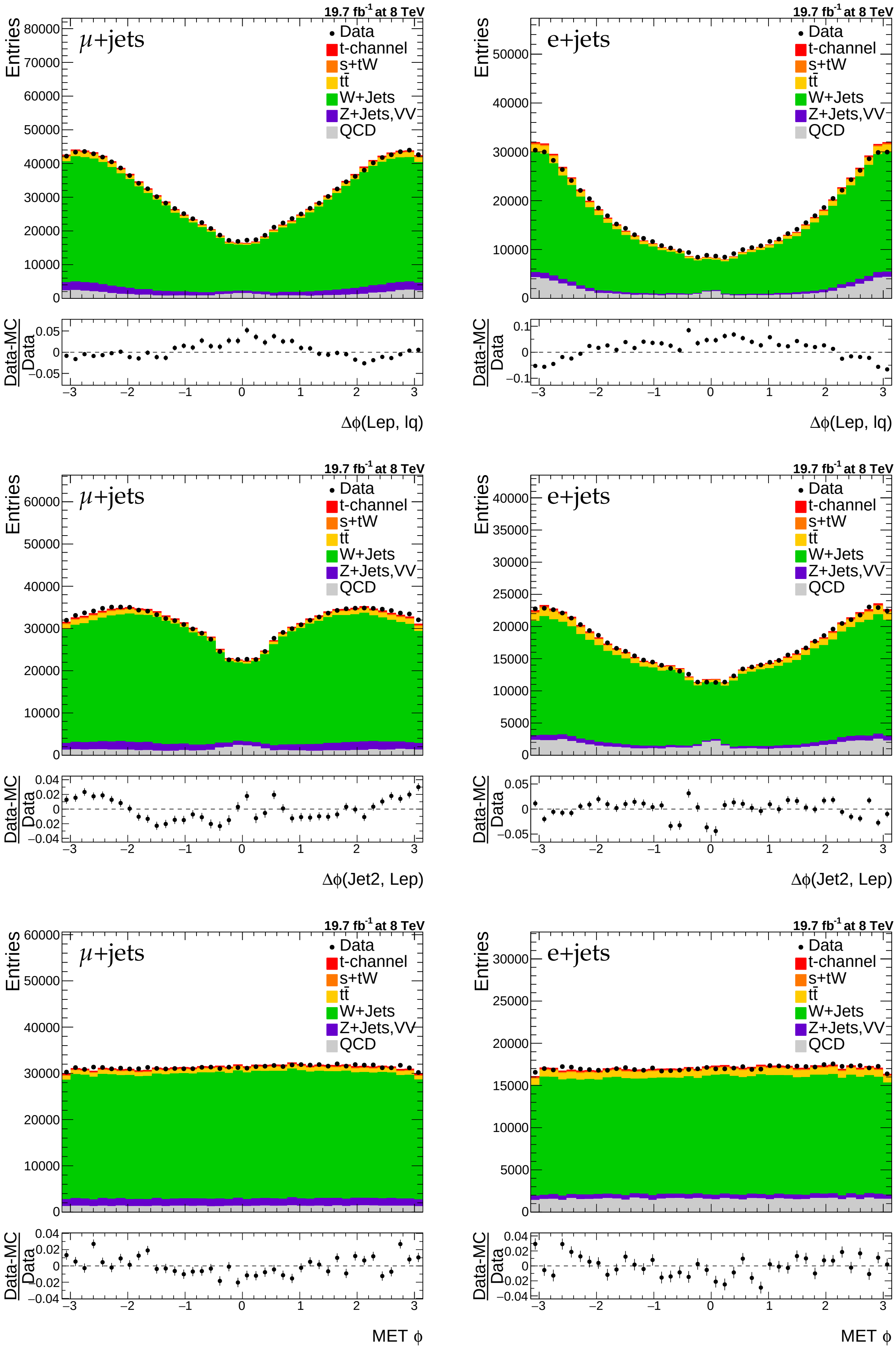

Figure 6.8: The $\Delta\phi$ between the lepton and jet stemming from light quark, $\Delta\phi$ of the second leading jet and the lepton, and ϕ of $\not{E}_T$ in the W+jets control region (2j0t). The simulation is scaled to match the integral of the data distribution.

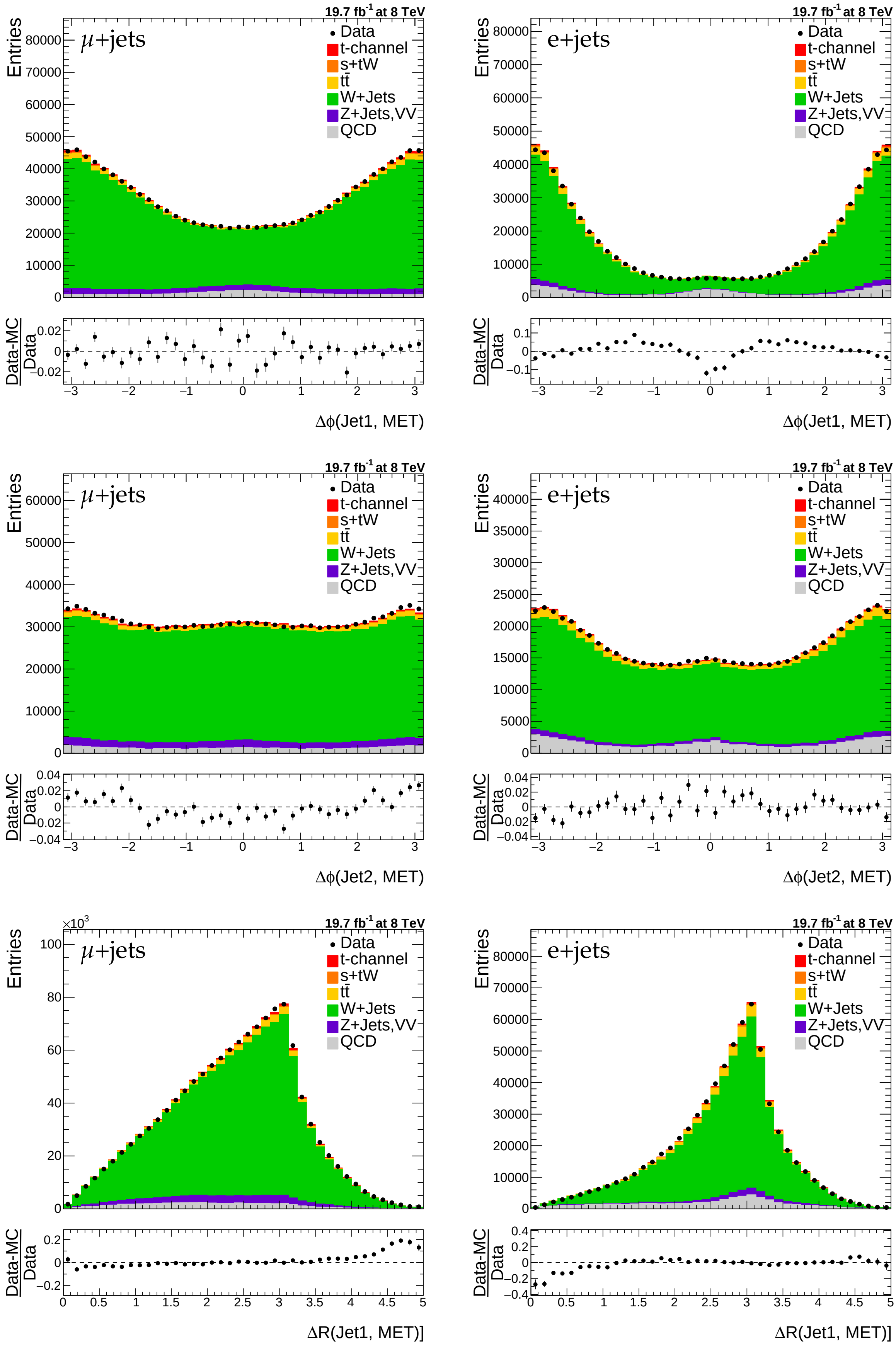

Figure 6.9: The $\Delta\phi$ between the leading jet and $\not{E}_T$, $\Delta\phi$ of the second leading jet and $\not{E}_T$, and the angular separation between the leading jet and $\not{E}_T$ in W+jets control region (2j0t). The simulation is scaled to match the integral of the data distribution.

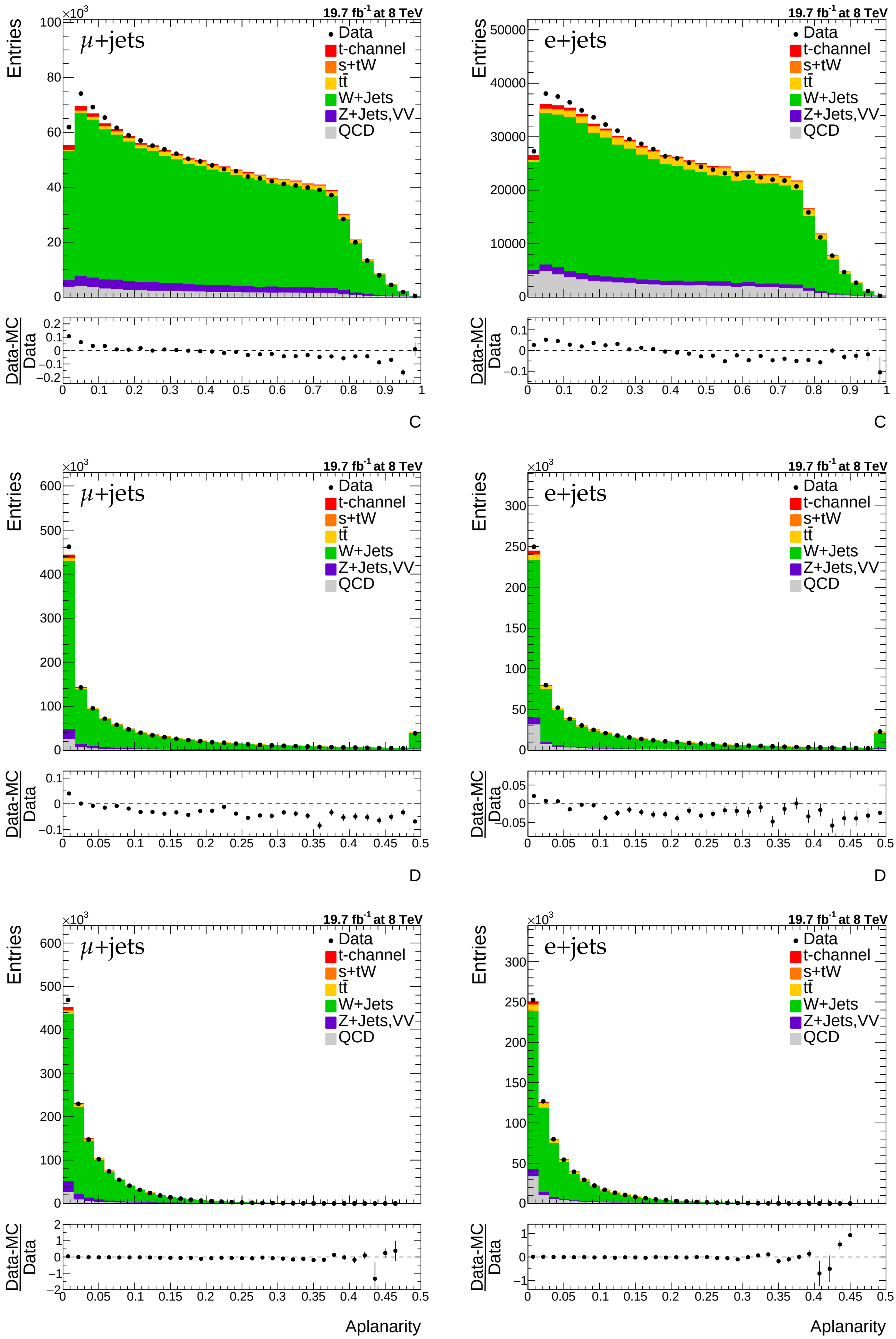

Figure 6.10: The C-parameter, D-parameter and Aplanarity in W+jets control region (2j0t). The simulation is scaled to match the integral of the data distribution.

6.2.2 Variable Modeling in 2j1t Region

For the signal selection, we required exactly two jets with one of them being tagged as b-jet. In this section, we check the modeling of those variables in our signal region (2j1t) which are used in the training of the neural network. The relative contributions of the different background processes are normalized to their predicted cross-sections, except for the contribution from QCD multijet events, which is normalized according to the results of the QCD fit described in Section 6.1. To allow for a better comparison of the shapes of the kinematic distributions, the sum of the modelled signal and background templates is scaled to yield the same integral as the data distribution.

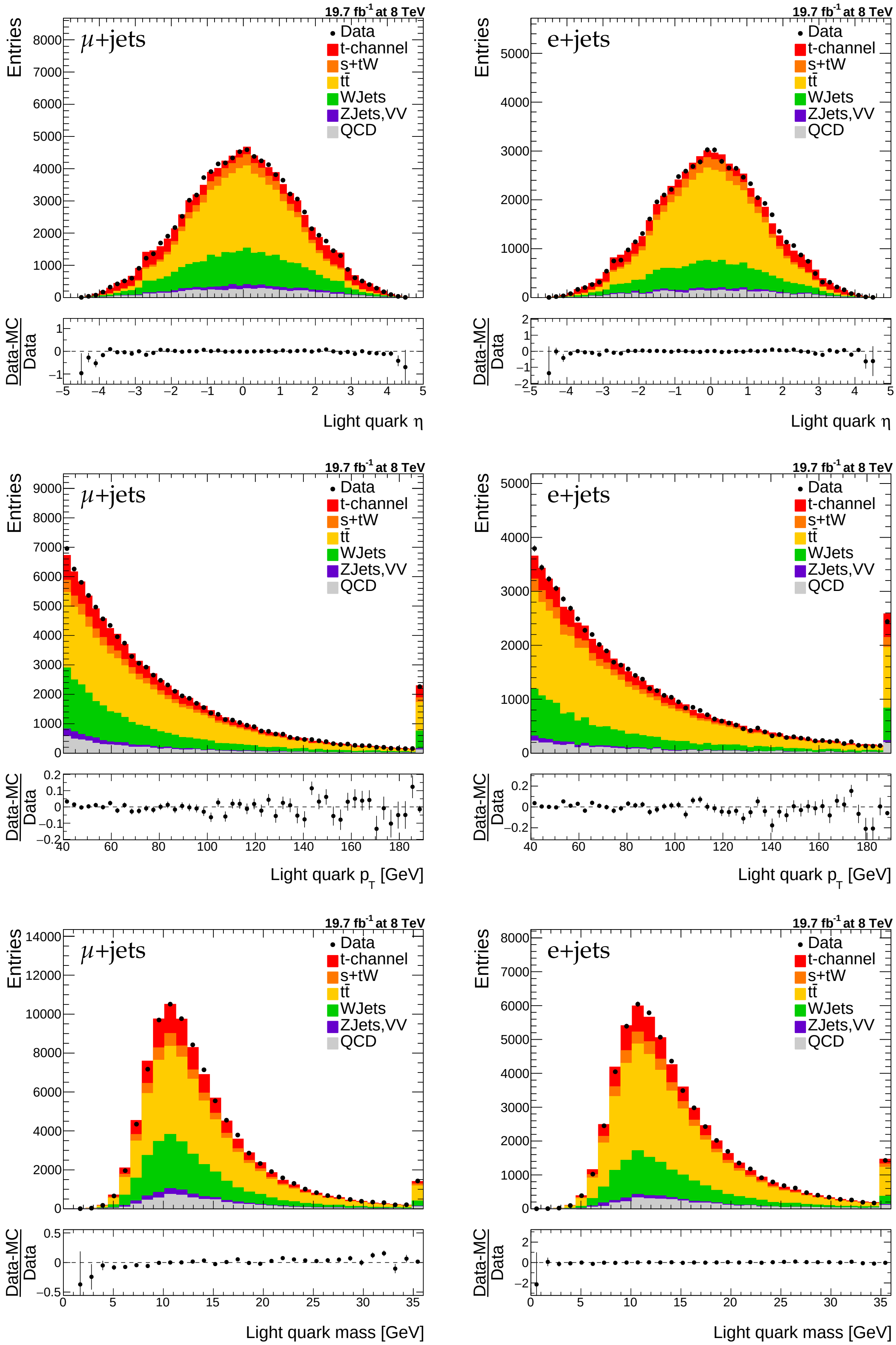

Figure 6.11: The pseudorapidity, transverse momentum, and mass of the jet assigned to the light quark in the signal region (2j1t). The simulation is scaled to match the integral of the data distribution.

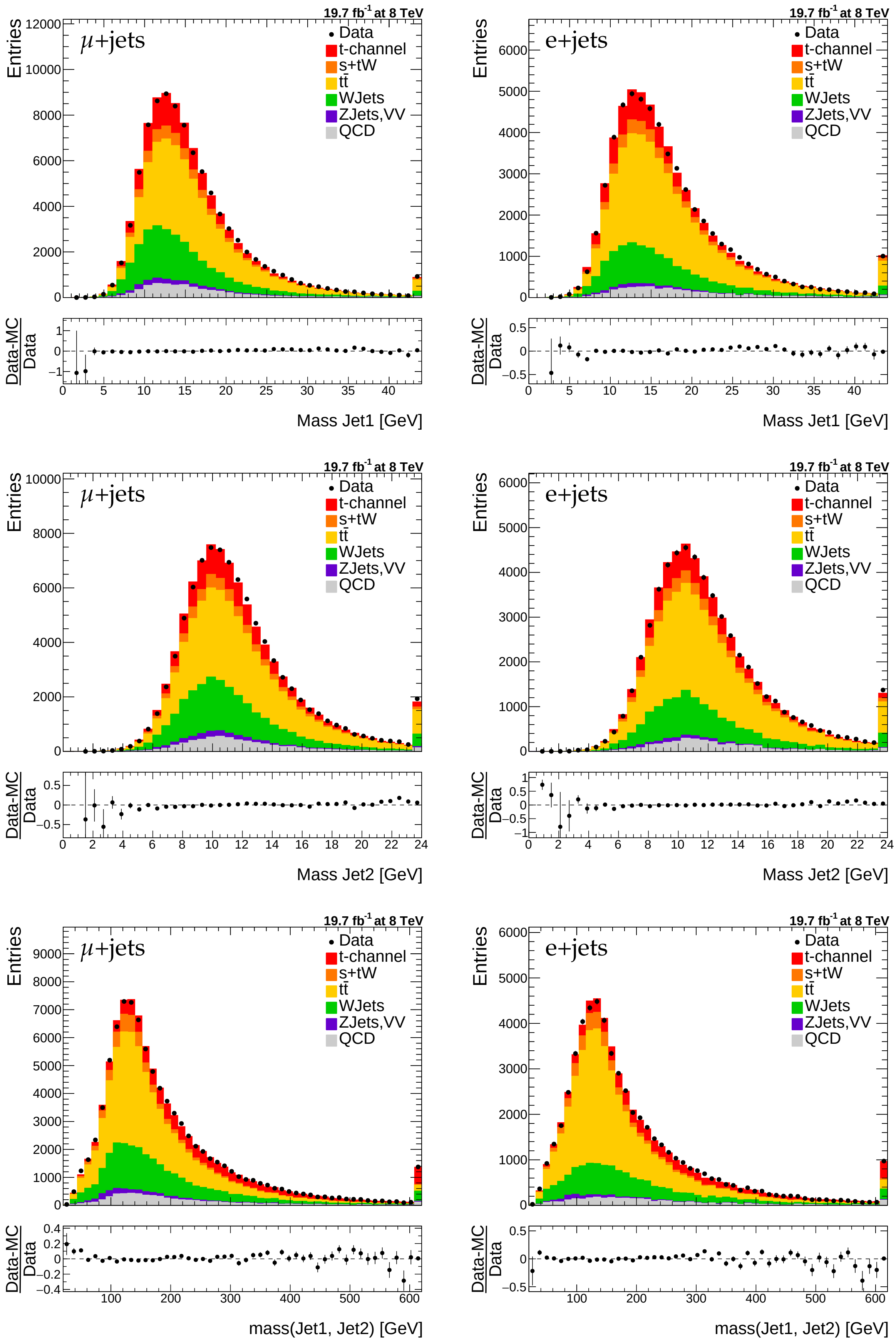

Figure 6.12: The invariant-mass of the leading jet, of the second leading jet, and of the dijet system in the signal region (2j1t). The simulation is scaled to match the integral of the data distribution.

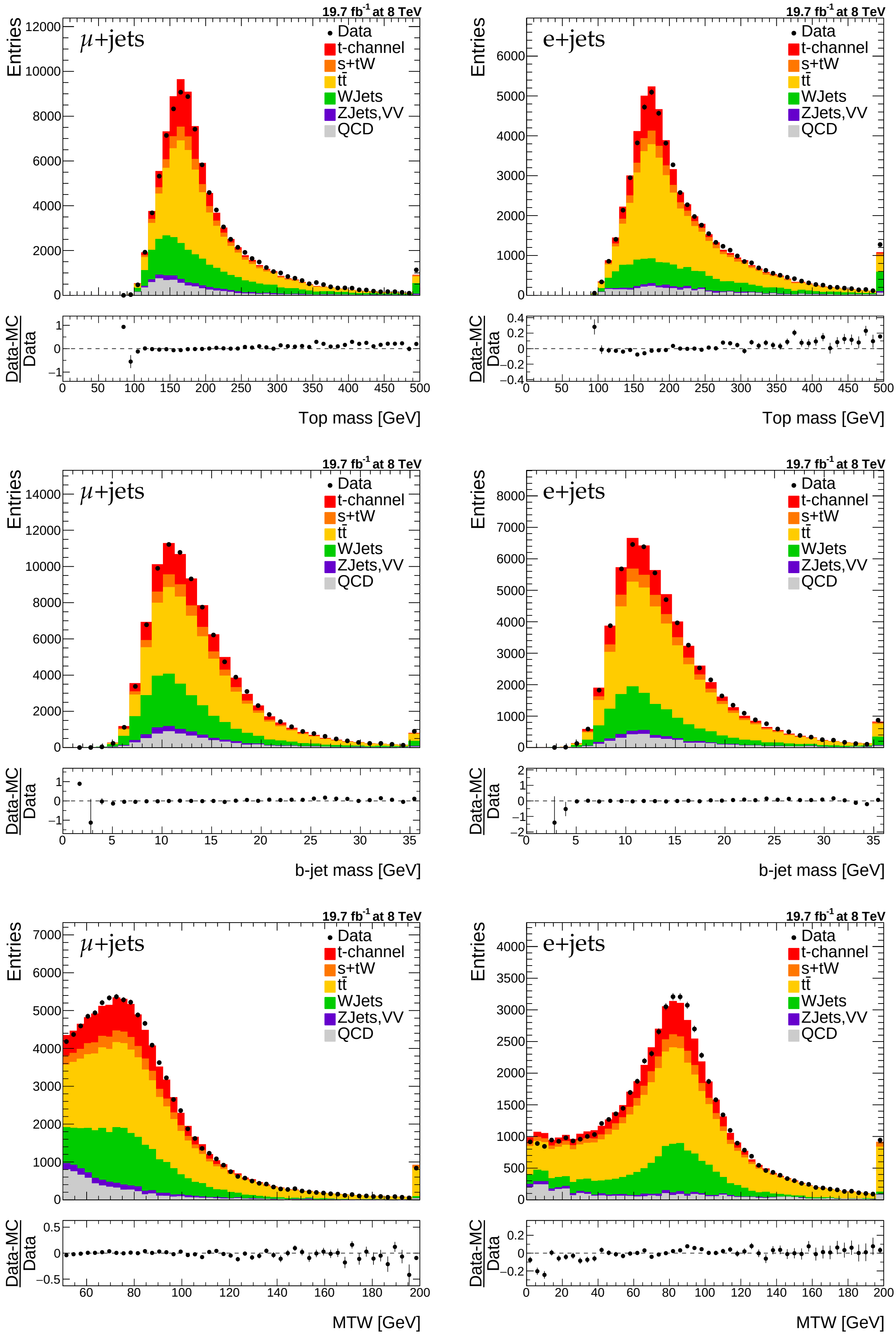

Figure 6.13: The reconstructed mass of the top-quark, of the jet assigned to the b-quark stemming from the decay of top-quark, and the transverse mass of the W-boson in signal region (2j1t). The simulation is scaled to match the integral of the data distribution.

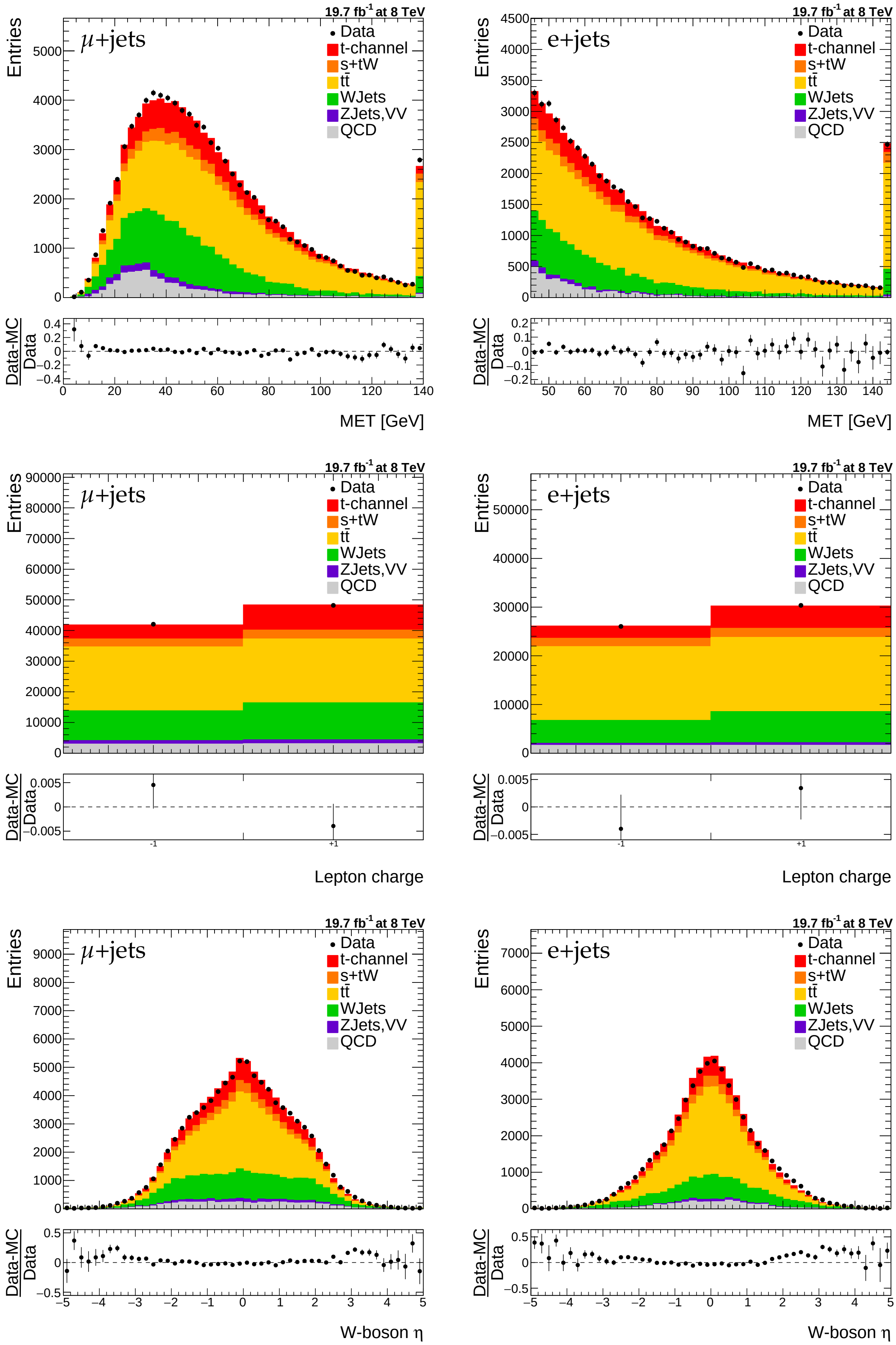

Figure 6.14: The missing transverse energy, the charge of the lepton, and the pseudorapidity of the W-boson in the signal region (2j1t). The simulation is scaled to match the integral of the data distribution.

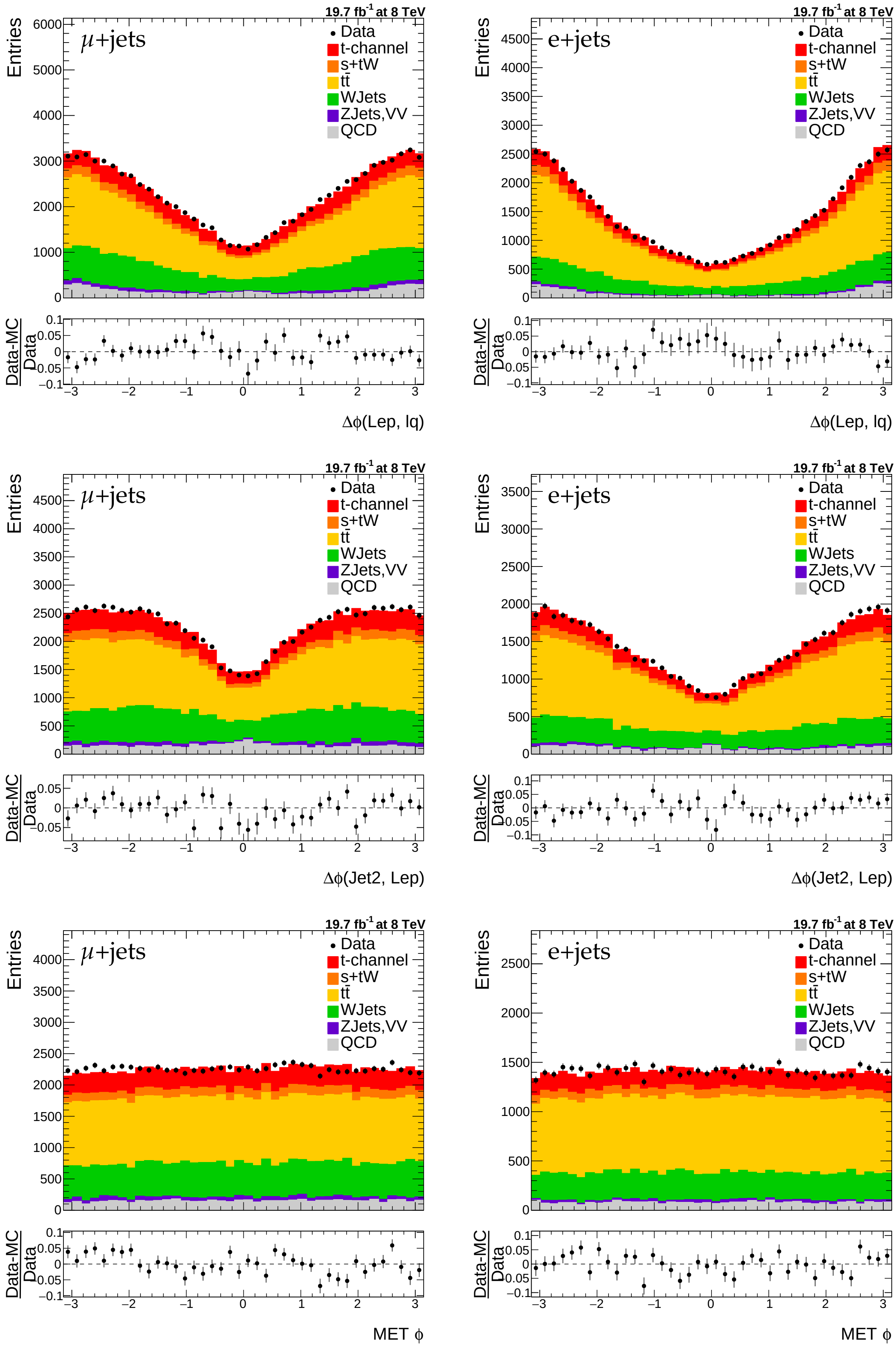

Figure 6.15: The $\Delta\phi$ between the lepton and jet stemming from light quark, $\Delta\phi$ of the second leading jet and the lepton, and ϕ of $\not{E}_T$ in the signal region (2j1t). The simulation is scaled to match the integral of the data distribution.

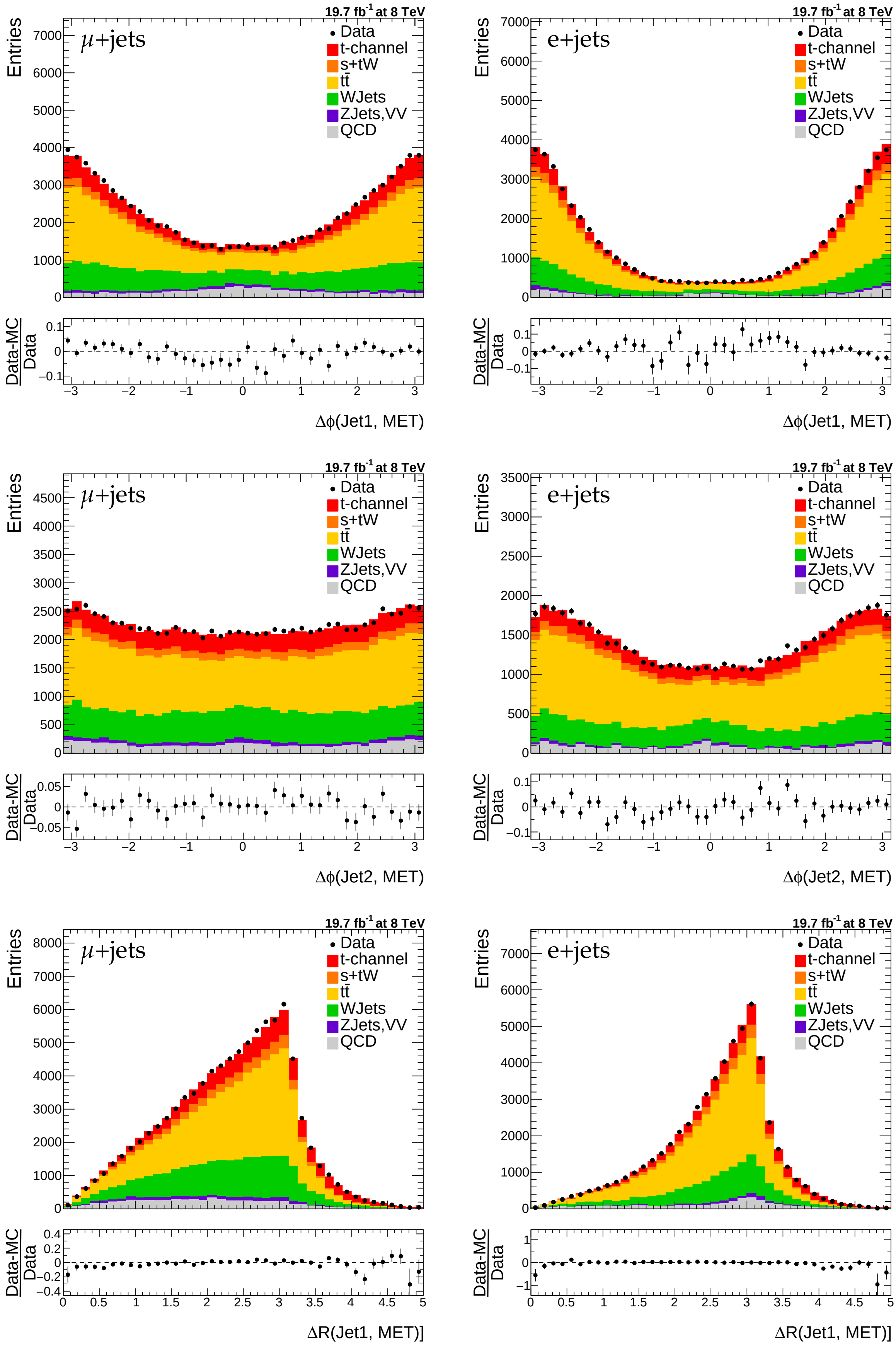

Figure 6.16: The $\Delta\phi$ between the leading jet and $\not\!\!E_{\mathrm{T}}$, $\Delta\phi$ of the second leading jet and $\not\!\!E_{\mathrm{T}}$, and the angular separation between the leading jet and $\not\!\!E_{\mathrm{T}}$ in signal region (2j1t). The simulation is scaled to match the integral of the data distribution.

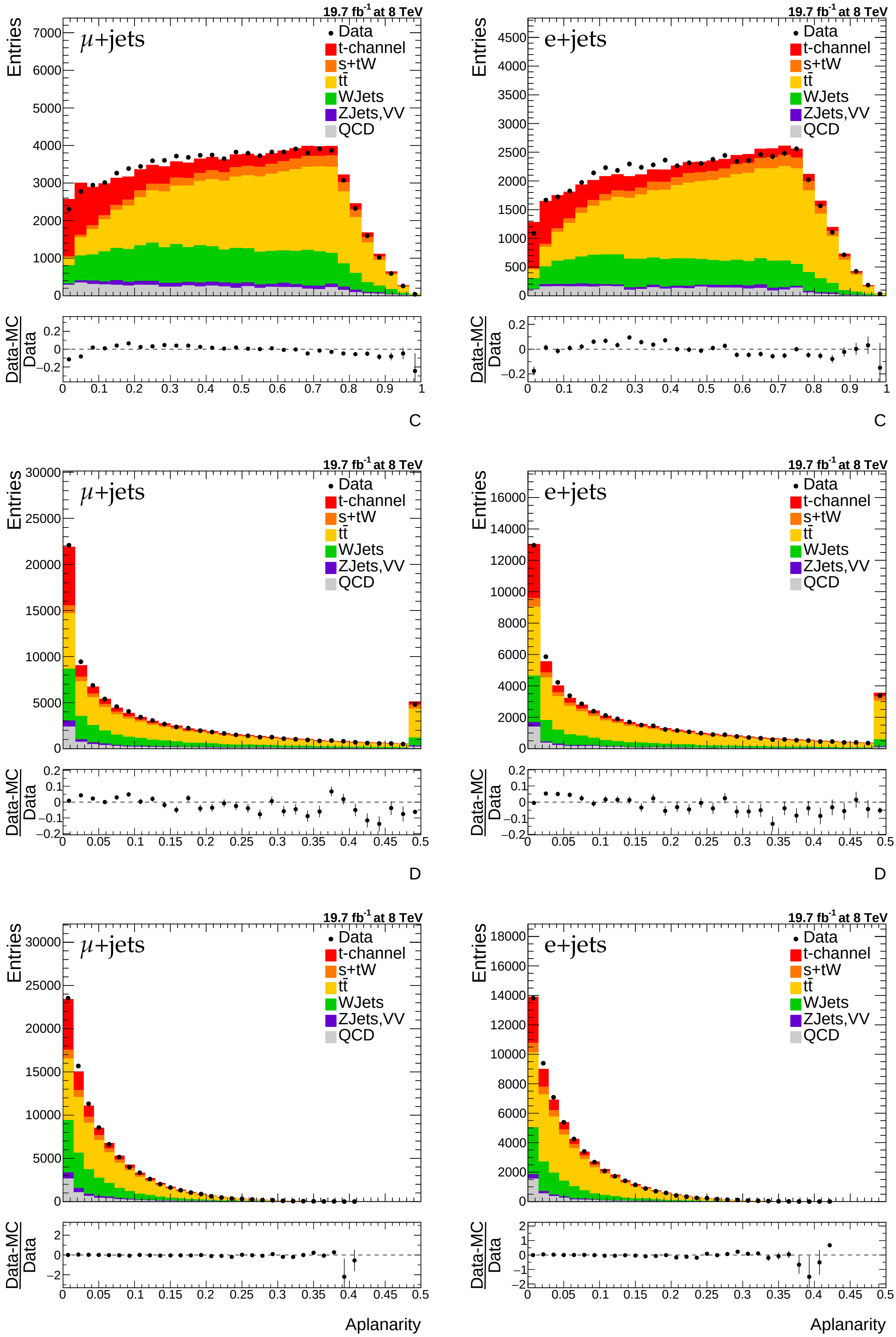

Figure 6.17: The C-parameter, D-parameter and Aplanarity in signal region (2j1t). The simulation is scaled to match the integral of the data distribution.

6.2.3 Variable Modeling in 3j2t Region

Requiring one or two jet more than for the signal region and requiring two b-tagged jets which defines the 3j2t or 4j2t control regions. For simplicity we show here only the 3j2t region. This region is dominated by the $t\bar{t}$ background contribution, with a fraction of about 94% (95%) of all events in the muon (electron) channel. Therefore we use this region for the validation of the $t\bar{t}$ modeling of the various kinematic variables used in the training of the neural network. In the following figures this comparison between simulation and data is shown for all used input variables. The relative contributions of the different backgrounds is normalized to the prediction, except for the contribution from QCD multijet events, which is normalized according to the results of the QCD fit described in Section 6.1. To allow for a better comparison of the shapes of the kinematic distributions, the sum of the modelled signal and background templates is scaled to yield the same integral as the data distribution.

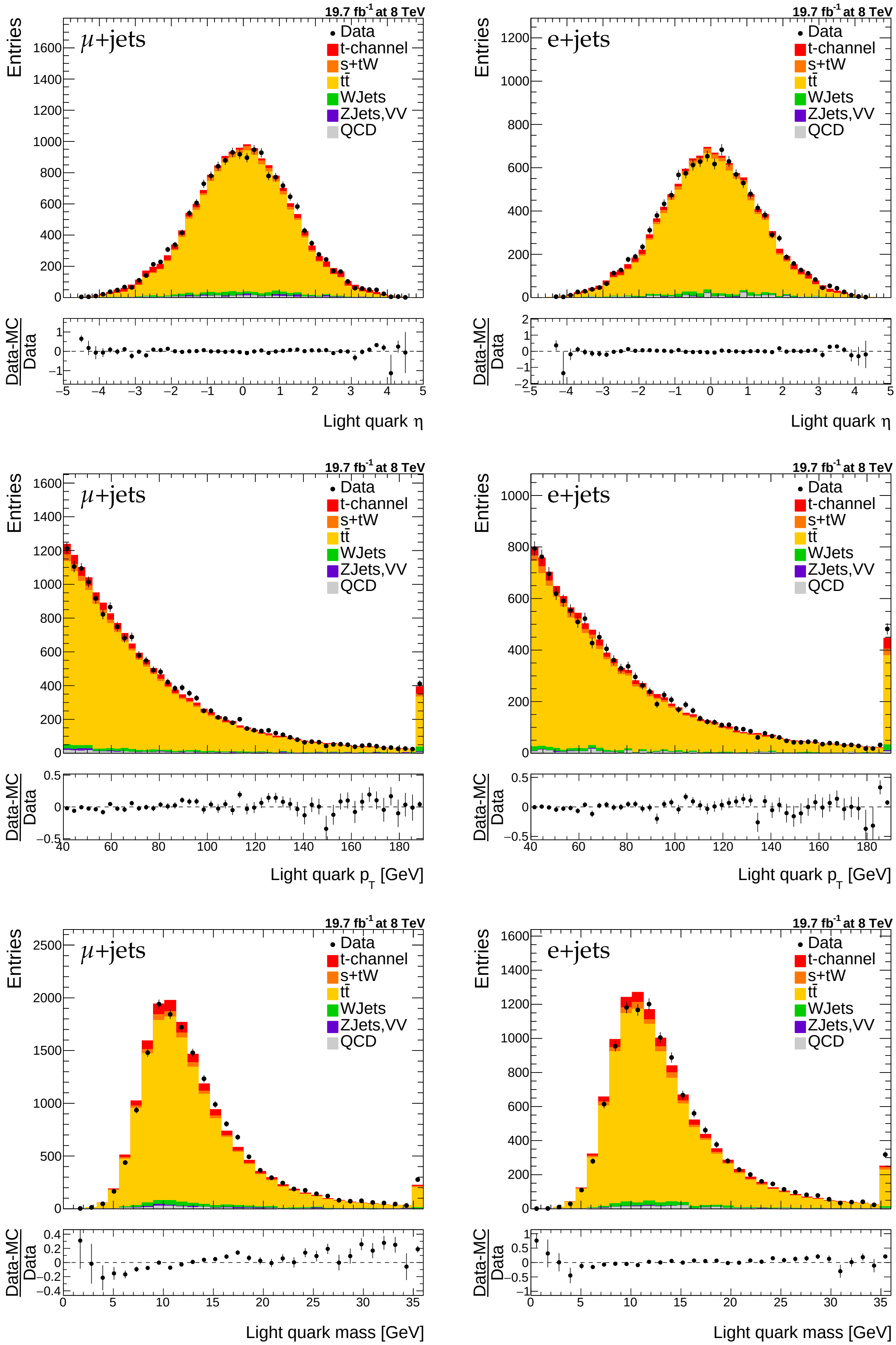

Figure 6.18: The pseudorapidity, transverse momentum, and mass of the jet assigned to the light quark in the $t\bar{t}$ control region (3j2t). The simulation is scaled to match the integral of the data distribution.

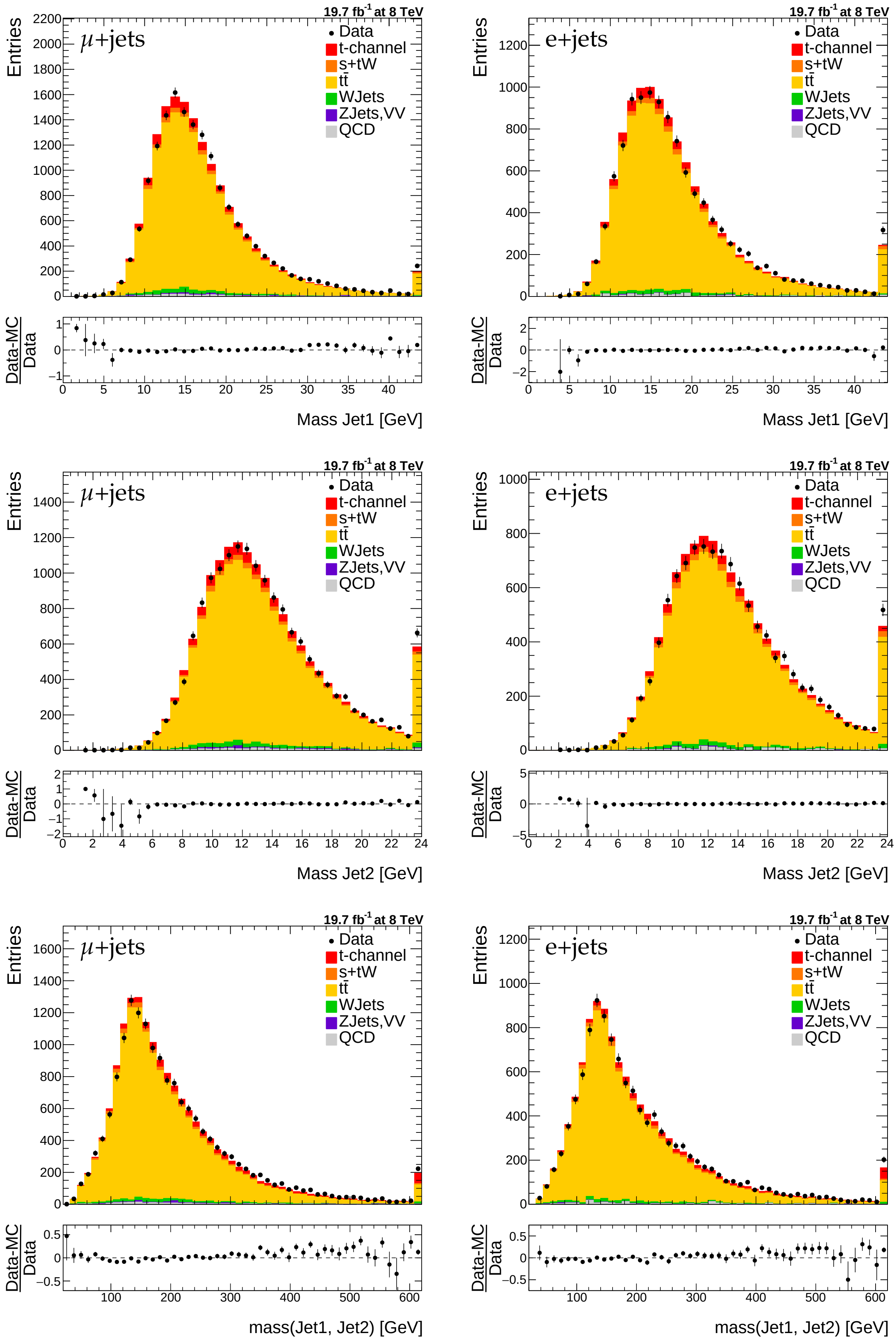

Figure 6.19: The invariant-mass of the leading jet, of the second leading jet, and of the dijet system in the $t\bar{t}$ control region (3j2t). The simulation is scaled to match the integral of the data distribution.

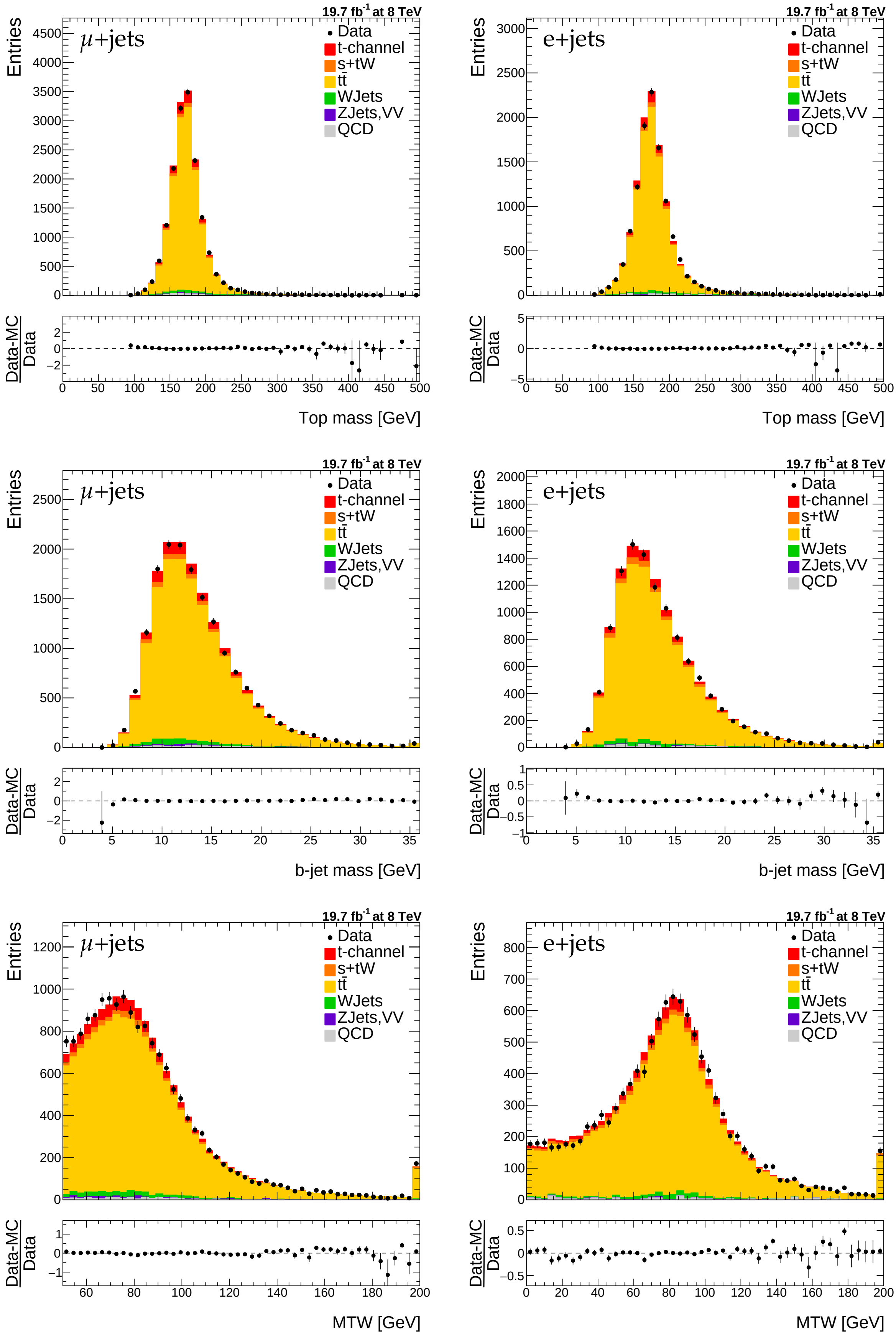

Figure 6.20: The reconstructed mass of the top-quark, of the jet assigned to the b-quark stemming from the decay of top-quark, and the transverse mass of the W-boson in $t\bar{t}$ control region (3j2t). The simulation is scaled to match the integral of the data distribution.

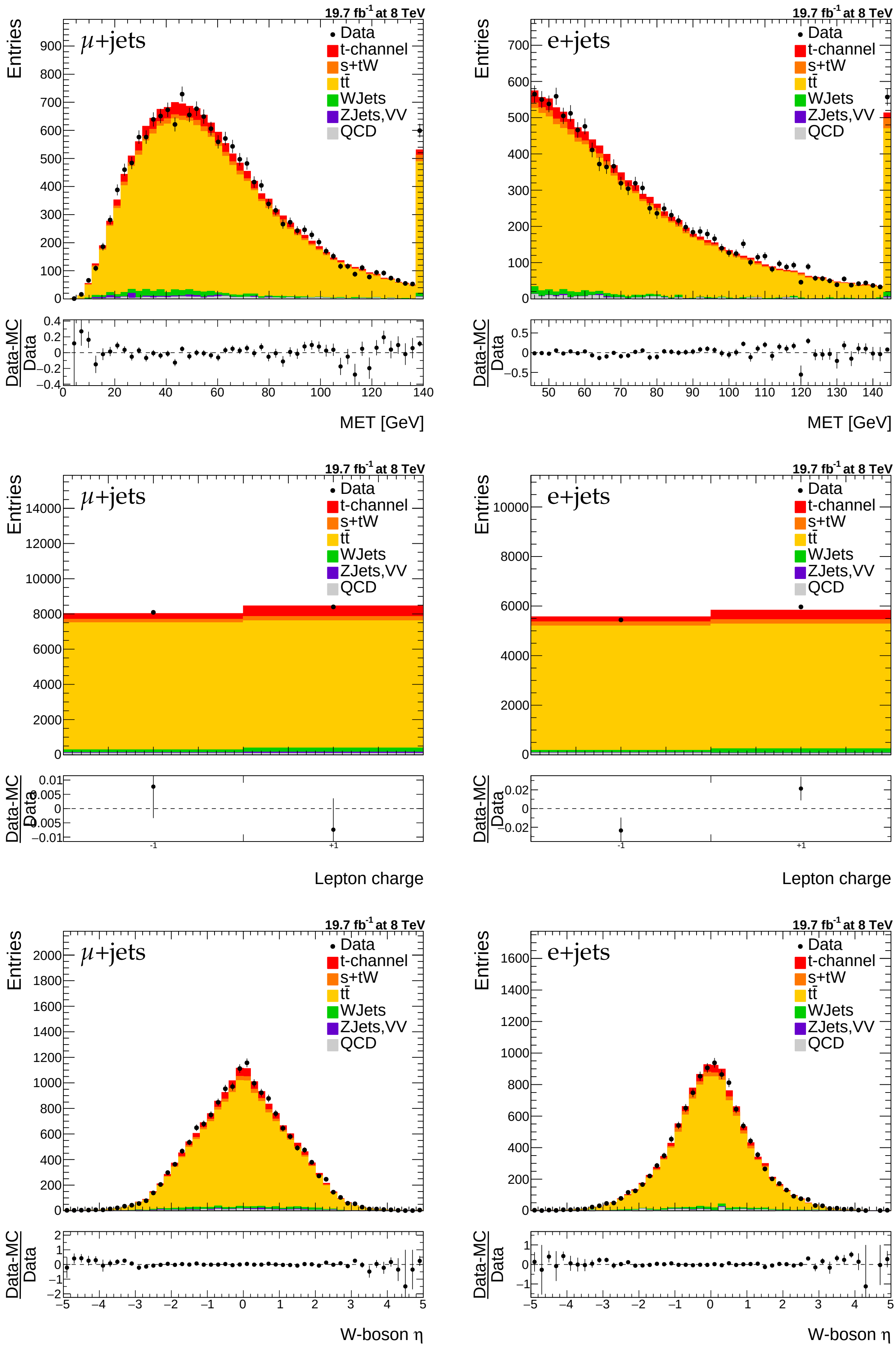

Figure 6.21: The missing transverse energy, the charge of the lepton, and the pseudorapidity of the W-boson in the $t\bar{t}$ control region (3j2t). The simulation is scaled to match the integral of the data distribution.

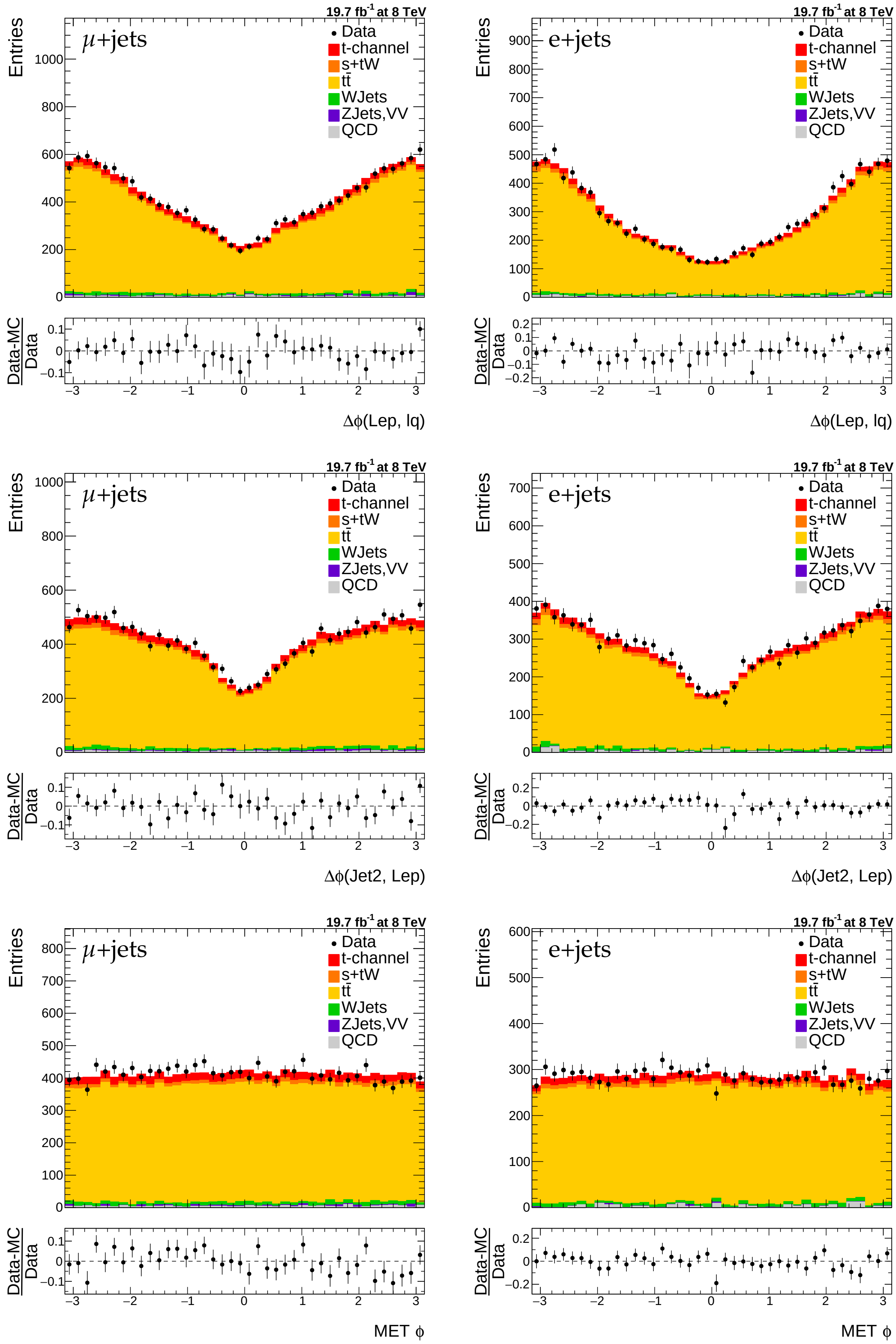

Figure 6.22: The $\Delta\phi$ between the lepton and jet stemming from light quark, $\Delta\phi$ of the second leading jet and the lepton, and ϕ of $\not\!\!E_{\mathrm{T}}$ in the $t\bar{t}$ control region (3j2t). The simulation is scaled to match the integral of the data distribution.

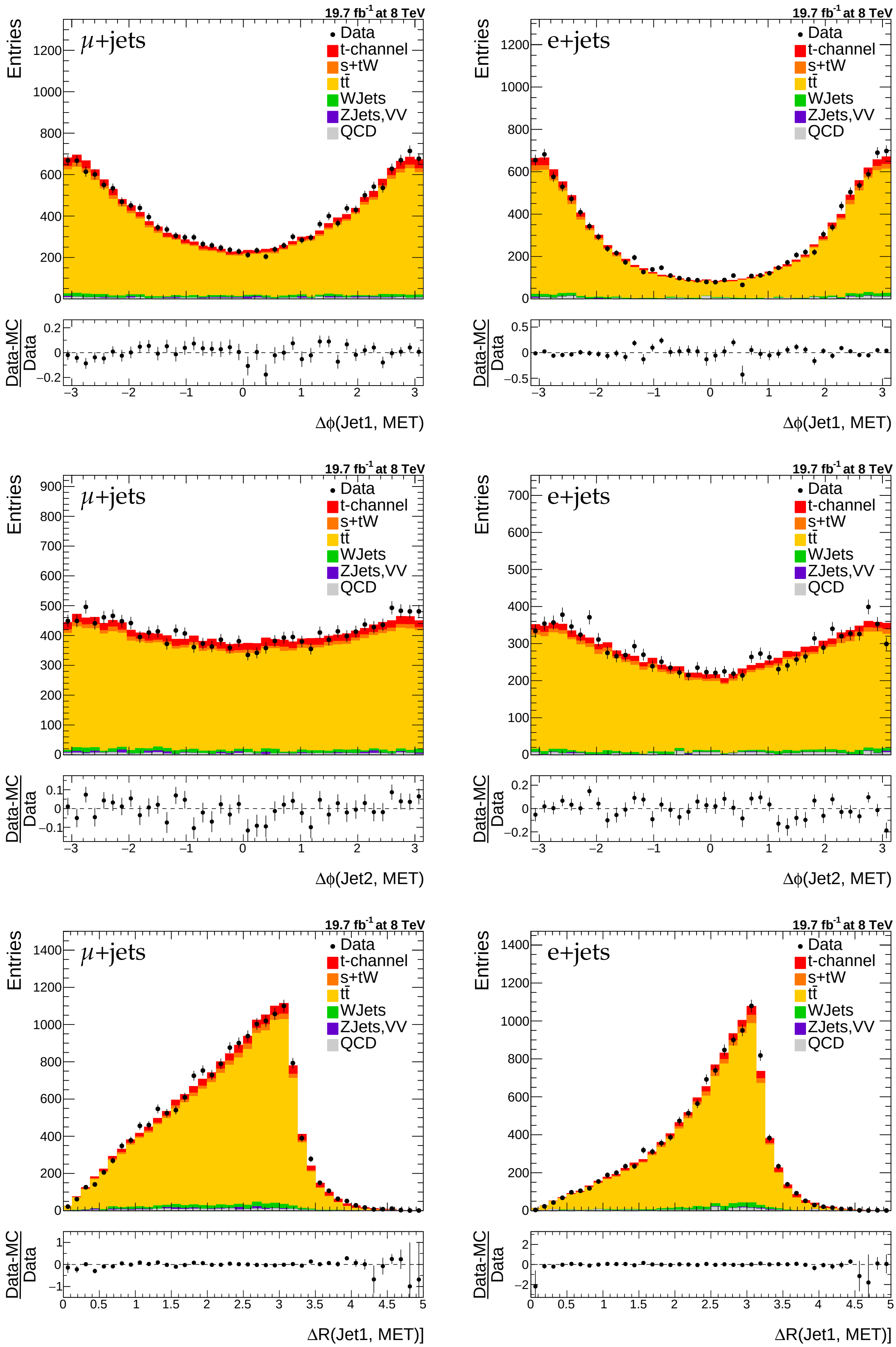

Figure 6.23: The $\Delta\phi$ between the leading jet and $\not{E}_T$, $\Delta\phi$ of the second leading jet and $\not{E}_T$, and the angular separation between the leading jet and $\not{E}_T$ in $t\bar{t}$ control region (3j2t). The simulation is scaled to match the integral of the data distribution.

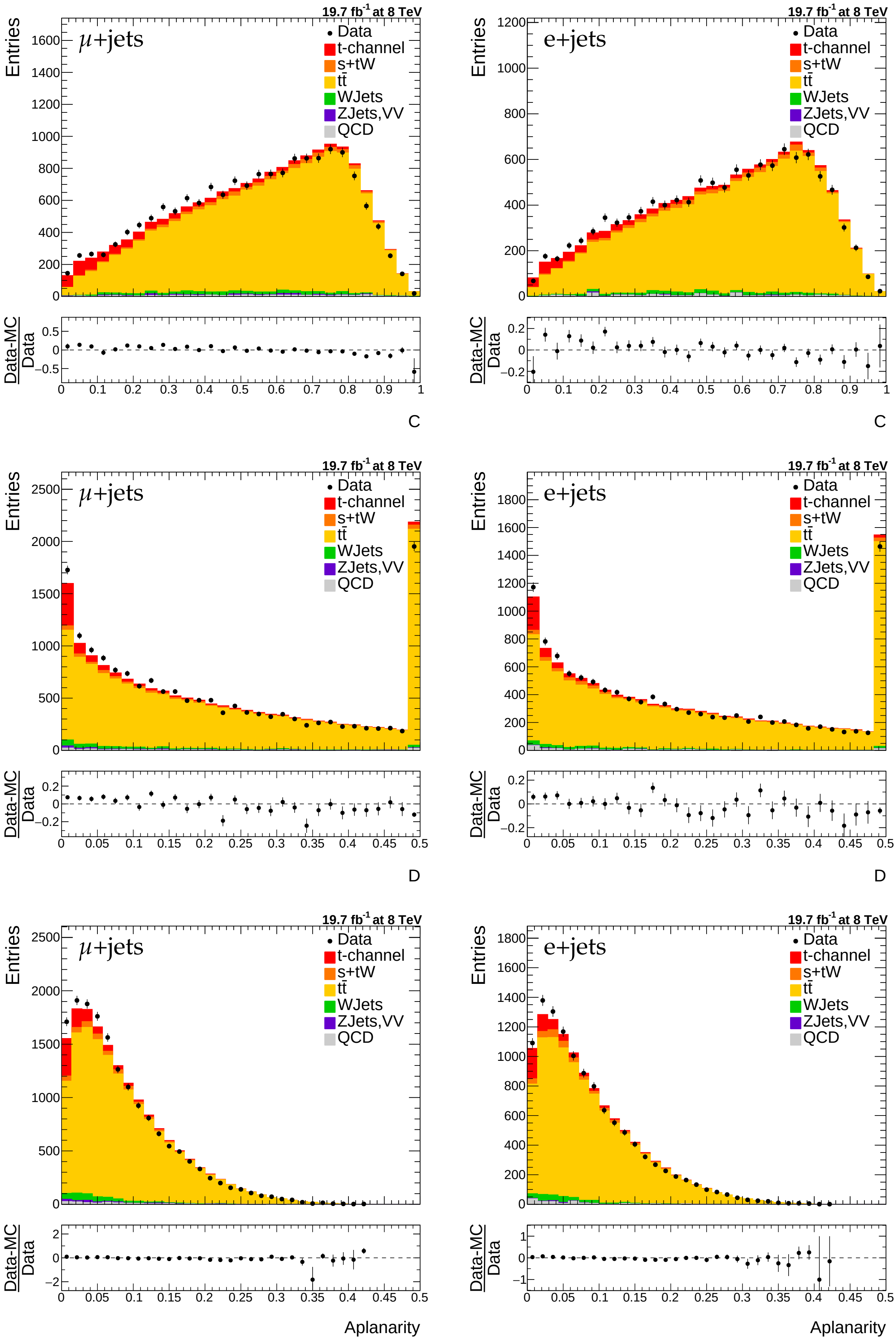

Figure 6.24: The C-parameter, D-parameter and Aplanarity in $t\bar{t}$ control region (3j2t). The simulation is scaled to match the integral of the data distribution.

6.3 Input Variables to Neural Network

A large number of input variables, some of which had been successfully employed for the neural network training at the CDF single-top-quark observation [188], have been tested for their separation power. Among these, 21 variables were found to be suitable for the training. The training of neural network is done for the muon and electron channel separately

Table 6.2: The list of input variables for the training of neural network, ranked by relevance in the two channels.

variable	rank in channel μ+jets	rank in channel e+jets	variable	rank in channel μ+jets	rank in channel e+jets
η_{lq}	1	1	C	11	12
$m_{\ell,\nu,b}$	2	2	$p_{T,lq}$	12	9
$m_{\mathrm{jet1,jet2}}$	3	3	D	13	17
$m_{\mathrm{T,W}}$	4	4	m_{jet1}	14	5
Q_ℓ	5	6	$E_{\mathrm{T}}^{\mathrm{miss}}$	15	14
m_{lq}	6	13	$\Delta\phi[jet2, \not{E}_{\mathrm{T}}]$	16	16
η_{W}	7	7	m_{jet2}	17	8
$\Delta\phi[\ell, lq]$	8	11	$\Delta R[jet1, \not{E}_{\mathrm{T}}]$	18	15
$m_{b_{top}}$	9	–	$\Delta\phi[jet2, \ell]$	–	10
$\Delta\phi[jet1, \not{E}_{\mathrm{T}}]$	10	–	Aplanarity	–	18

The neural network is configured to only use variables for the training with an additional significance greater than 3σ. The variables with additional significance less than 3σ do not have any effect on the training of the neural network.

Pseudorapidity of the light quark, η_{lq}

The pseudorapidity η of the light quark is the most discriminating variable in the training. The jet is mostly detected in the forward region for the signal, while for all background processes it is detected in the central region of the detector. Figure 6.25(a) and 6.25(b) show the pseudorapididty of the light quark for the data, t-channel, $t\bar{t}$ and W+jets for the muon and election channel respectively.

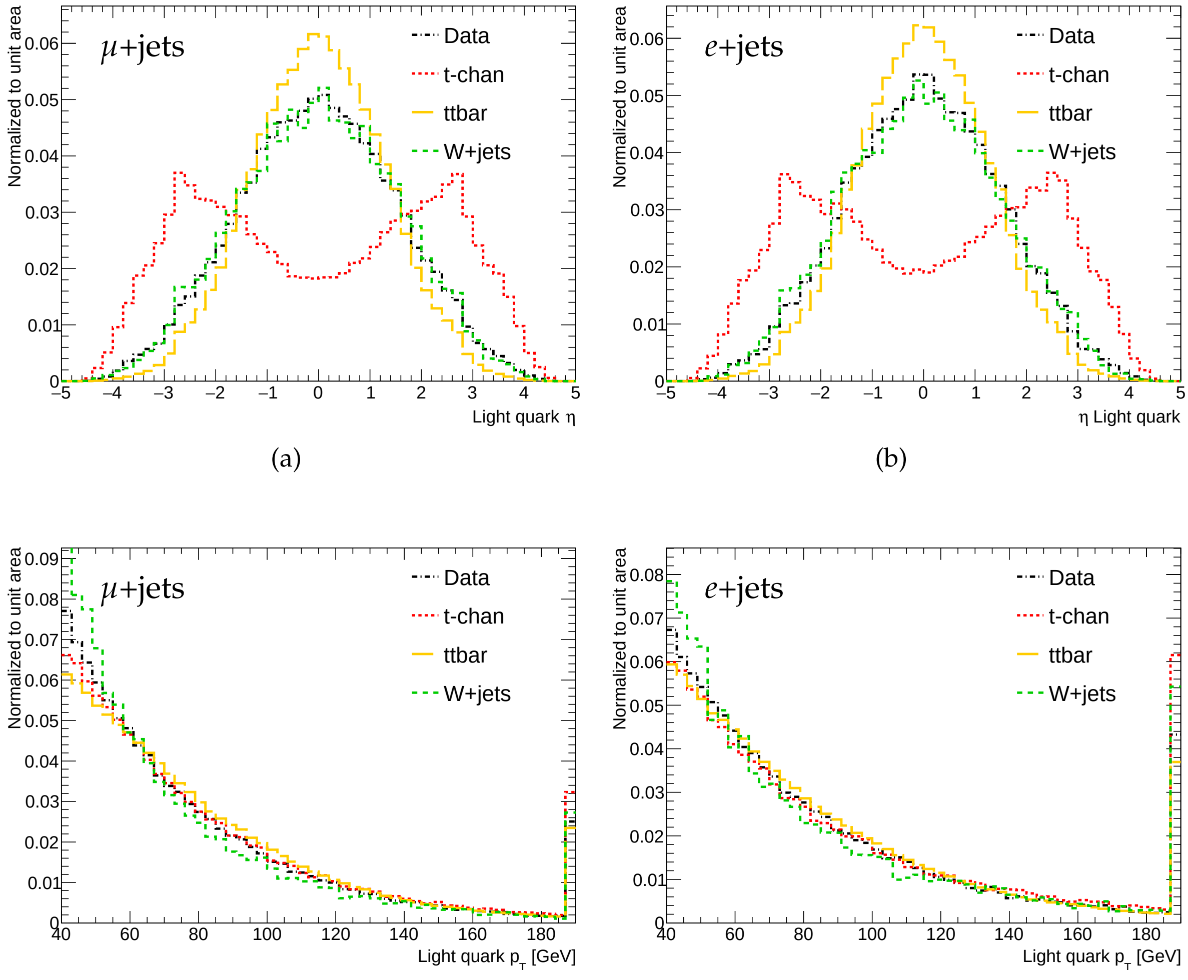

Figure 6.25: The pseudorapidity and p_{T} distribution of the light quark in muon (electron) channel for signal region. The simulation is normalized to unity.

Transverse momentum distribution of light quark

The transverse momentum distribution of the jet assigned to the light quark. Figure 6.25(c) and 6.25(d) show the pseudorapididty of the light quark for the data, t-channel, $t\bar{t}$ and W+jets for the muon and election channel respectively.

Mass of light quark, m_{lq}

It is the invariant mass of the jet assigned to the quark recoiling against the intermediate W-boson produced in the t-channel. Figure 6.26(a) and 6.26(b) show the mass of the light quark for the data, t-channel, $\mathrm{t\bar{t}}$ and W+jets for the muon and election channel respectively.

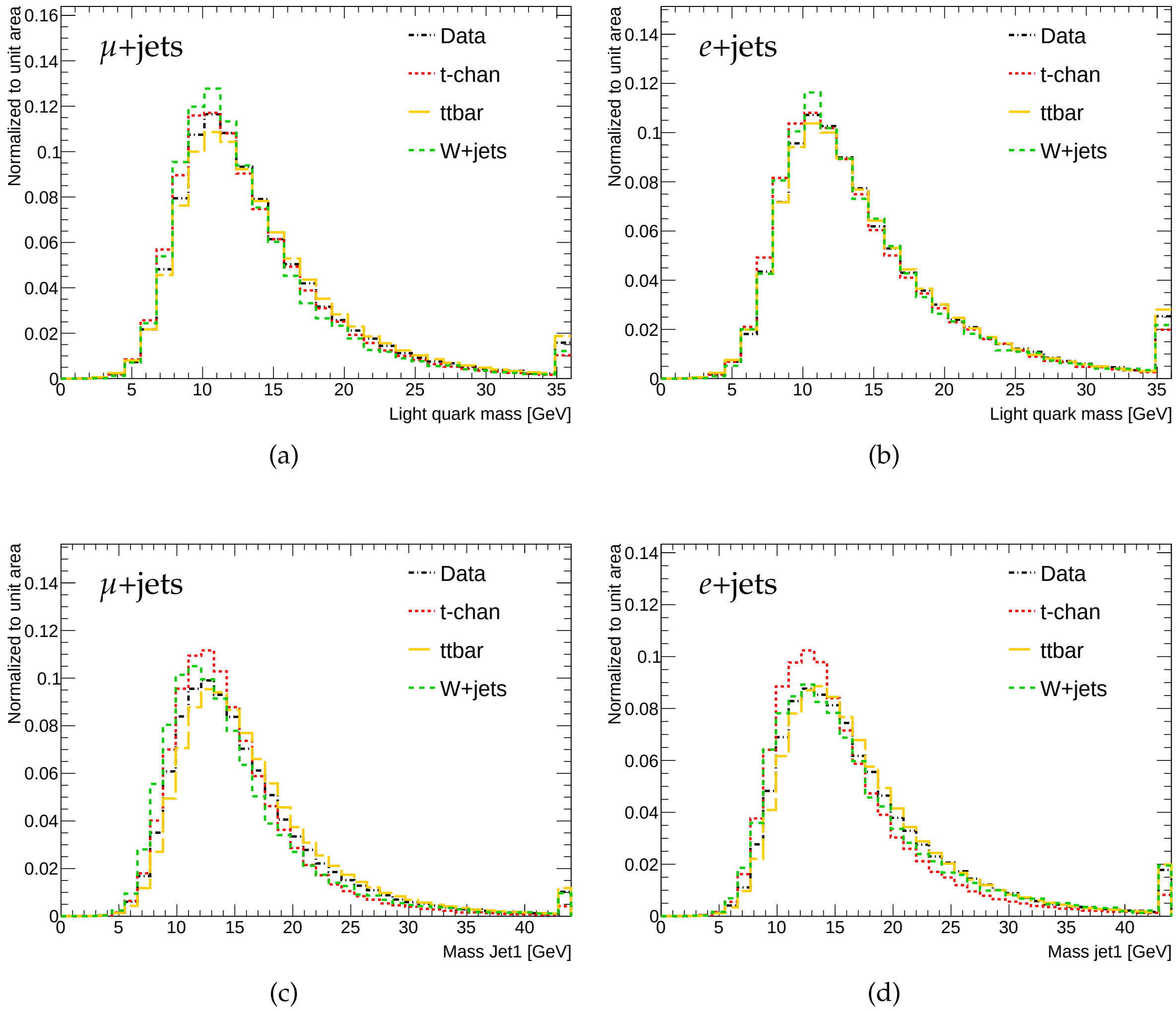

Figure 6.26: The mass of the light quark jet and mass of first leading jet in signal region. The simulation is normalized to unity.

Mass of first leading jet, m_{jet1}

The invariant mass of the jet with the highest transverse momentum p_{T}. Figure 6.26(c) and 6.26(d) show the mass of the first leading jet for the data, t-channel, $\mathrm{t\bar{t}}$ and W+jets for the muon and election channel respectively.

Mass of second leading jet, m_{jet2}

Mass of the second leading (ordered in terms of decreasing transverse momentum) jet present in the event. Figure 6.26(c) and 6.26(d) show the mass of the second leading jet for the data, t-channel, $t\bar{t}$ and W+jets for the muon and election channel respectively.

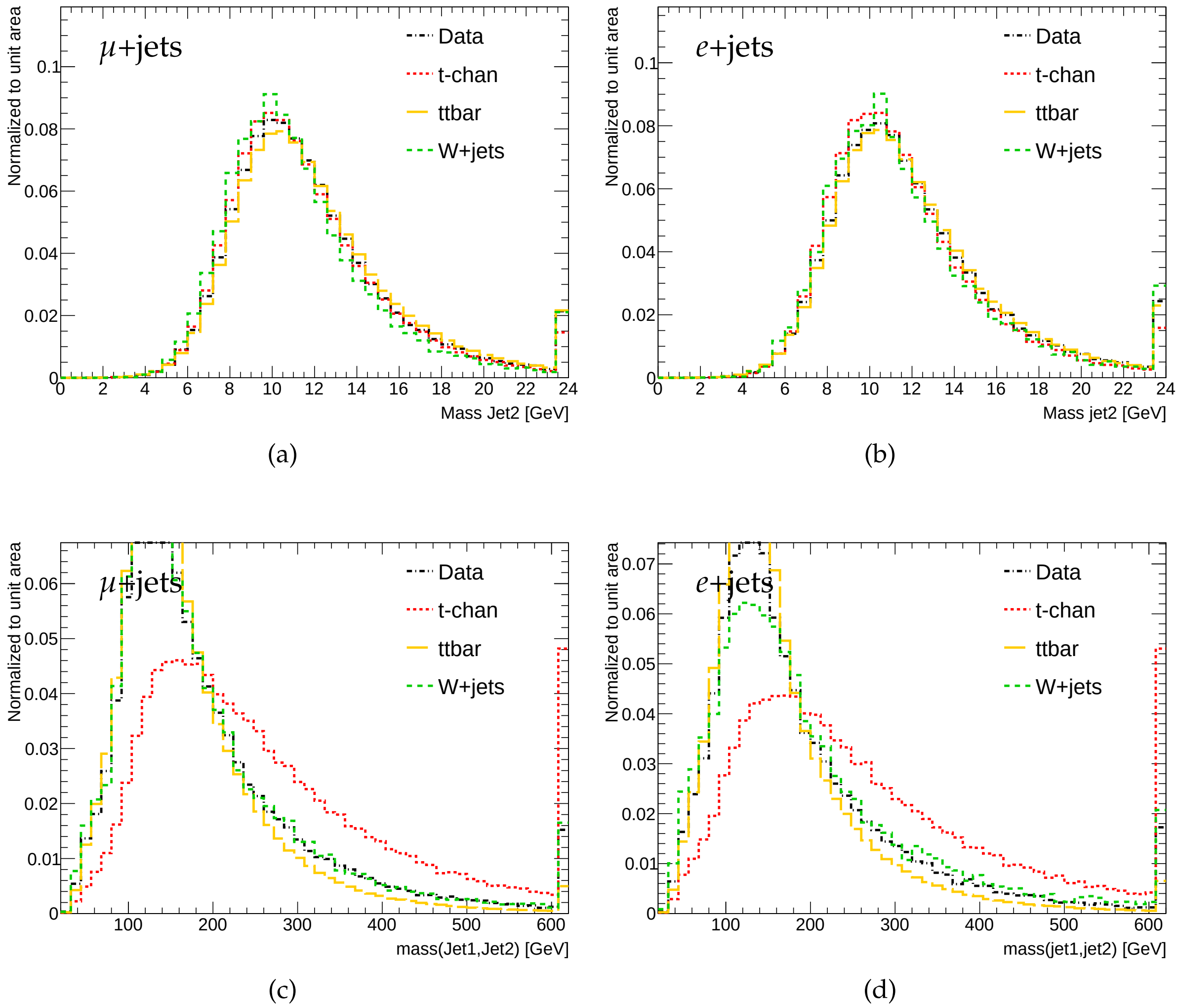

Figure 6.27: The mass of the second leading jet and invariant di-jet mass shape in the signal region. The simulation is normalized to unity.

Invariant di-jet mass, $m_{\text{jet1,jet2}}$

The invariant mass of the two selected jets can discriminate between signal and background due to the longer tail of the signal. In case of more than two jets, the two leading jets, ordered in decreasing jet-p_{T}, are used for the calculation of this variable. Figure 6.26(c) and 6.26(d) show the di-jet invariant mass for the data, t-channel, $t\bar{t}$ and W+jets for the muon and election channel respectively.

Reconstructed top-quark mass, $m_{\ell\nu\mathrm{b}}$

The invariant mass of the top-quark reconstructed from the four vectors of the of the neutrino, charged lepton, and the jet assigned to the b-quark stemming from the decay of top-quark. The peak around 173 GeV is a clear indication for the precise reconstruction of top-quark candidates. The peak is broadened for $\mathrm{t\bar{t}}$ production compared to single top t-channel production. The reason for this is, that in half of the cases, the selected b-quark is not coming from the same top-quark as the selected muon. Also, if the two W-bosons decay leptonically, there are two neutrinos which contribute to the missing transverse energy. Contributions from W-bosons and light or heavy flavor jets do not peak at the top-quark mass and have a longer tail. Figure 6.28(a) and 6.28(b) show the reconstructed top-quark mass for the data, t-channel, $\mathrm{t\bar{t}}$ and W+jets for the muon and election channel respectively.

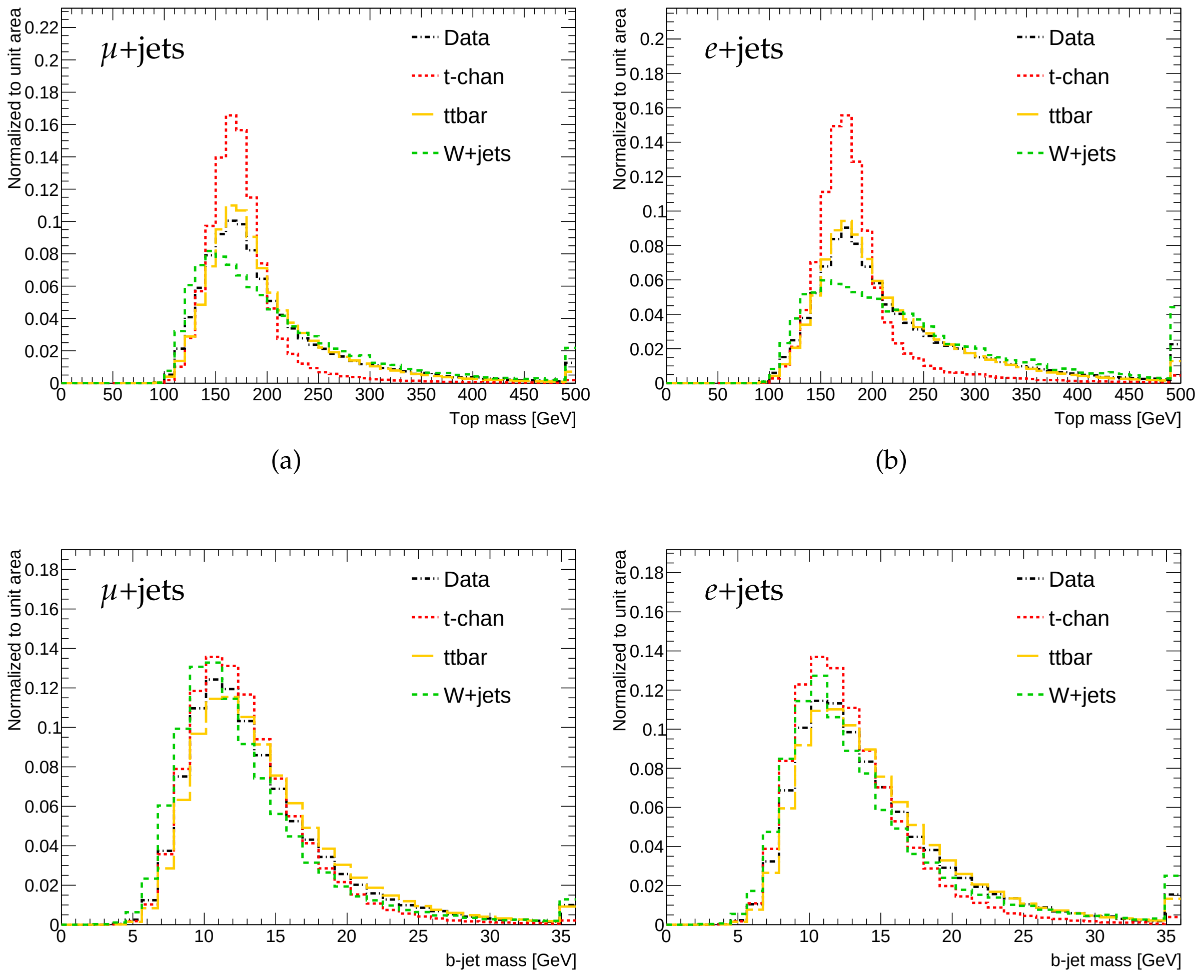

(a) (b) (c) (d)

Figure 6.28: The reconstructed top-quark mass b-quark mass stemming from the decay of top-quark in signal region. The simulation is normalized to unity.

Mass of the b-quark stemming from the decay of top-quark, $m_{b_{top}}$

The invariant mass of the jet assigned to the b-quark stemming from the decay of top-quark. Figure 6.28(c) and 6.28(d) show the mass of b-quark for the data, t-channel, $t\bar{t}$ and W+jets for the muon and election channel respectively.

Transverse mass of the W-boson, $m_{\mathrm{T,W}}$

The transverse mass distribution m_{T} of the W-boson obtained from the isolated charged lepton and the missing transverse energy. Figure 6.29(a) and 6.29(b) show the transverse mass of the W-boson for the data, t-channel, $t\bar{t}$ and W+jets for the muon and election channel respectively.

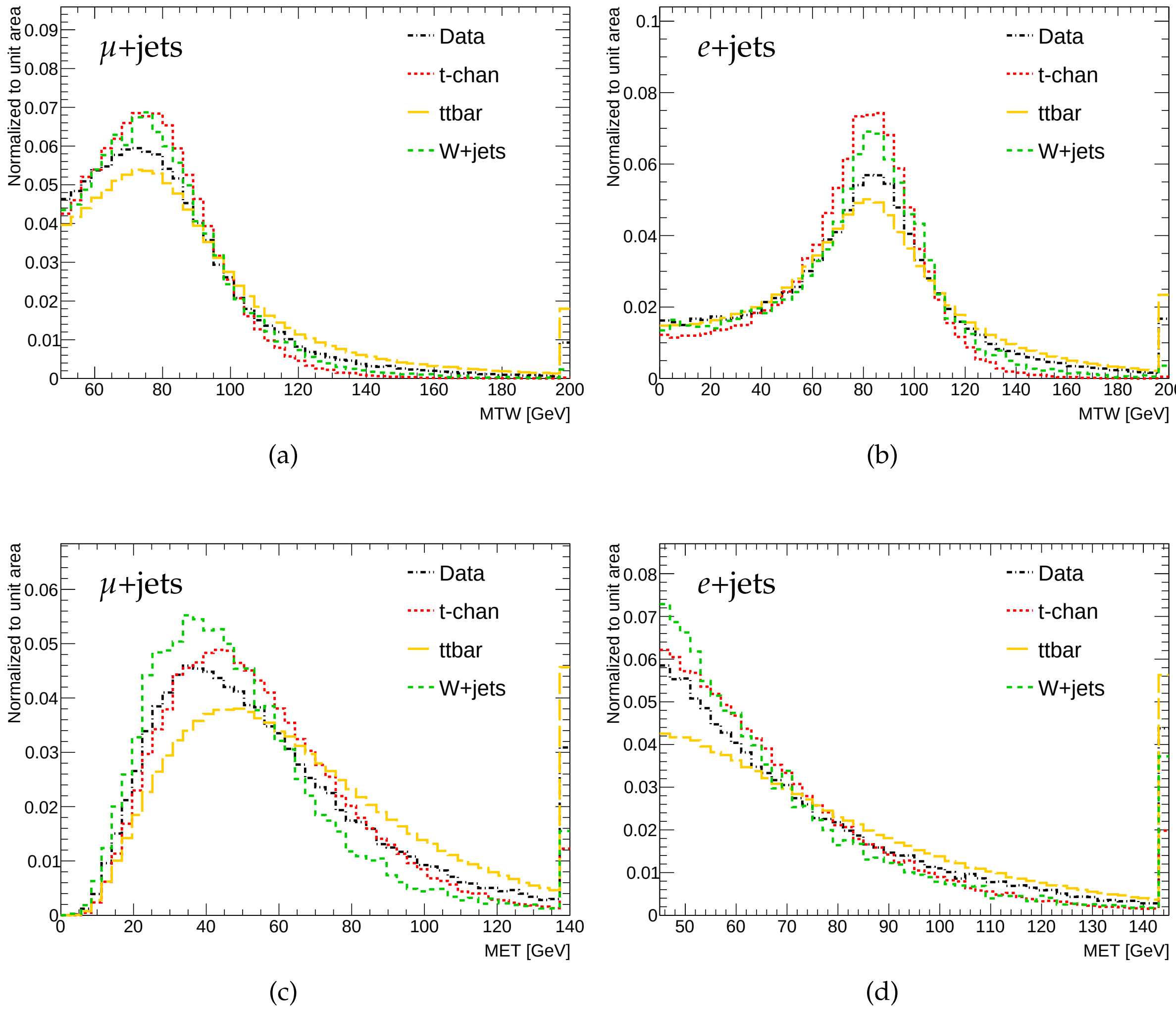

Figure 6.29: The transverse mass and missing energy distribution of the W-boson in muon (electron) channel for signal region. The simulation is normalized to unity.

Missing transverse energy, $\not{E}_{\mathrm{T}}$

Missing transverse energy is the energy associated to the neutrino present in final state. Figure 6.29(c) and 6.29(d) show the missing transverse energy for the data, t-channel, $\mathrm{t\bar{t}}$ and W+jets for the muon and election channel respectively.

Lepton charge, Q_{ℓ}

The charge of the selected isolated lepton in the event. Figure 6.30(a) and 6.30(b) show the leptonic charge for the data, t-channel, $\mathrm{t\bar{t}}$ and W+jets for the muon and election channel respectively.

Pseudorapidity of the W-boson, η_{W}

The pseudorapidity of the W-boson coming from the decay of the top-quark. Figure 6.30(c) and 6.30(d) show the psedudorapidity of the W-boson for the data, t-channel, $\mathrm{t\bar{t}}$ and W+jets for the muon and election channel respectively.

Delta ϕ of the lepton and the light jet, $\Delta\phi[\ell, lq]$

$\Delta\phi[l, lq]$ is defined as the difference of the azimuthal angle of the four-vector of the isolated lepton and the four-vector of the light quark jet is shown in Fig 6.30(e) and 6.30(e) the data, t-channel, $\mathrm{t\bar{t}}$ and W+jets for the muon and election channel respectively.

Delta ϕ of the second leading jet and the charged lepton, $\Delta\phi[jet2, \ell]$

Difference of the azimuthal angle of the four-vector of the second leading jet and the four-vector of the lepton is shown in Fig 6.31(c) and 6.31(c) the data, t-channel, $\mathrm{t\bar{t}}$ and W+jets for the muon and election channel respectively.

Azimuthal angle of $\not{E}_{\mathrm{T}}$, $\phi_{\not{E}_{\mathrm{T}}}$

The azimuthal angle of the $\not{E}_{\mathrm{T}}$ vector is shown in Fig 6.31(a) and 6.31(b) the data, t-channel, $\mathrm{t\bar{t}}$ and W+jets for the muon and election channel respectively.

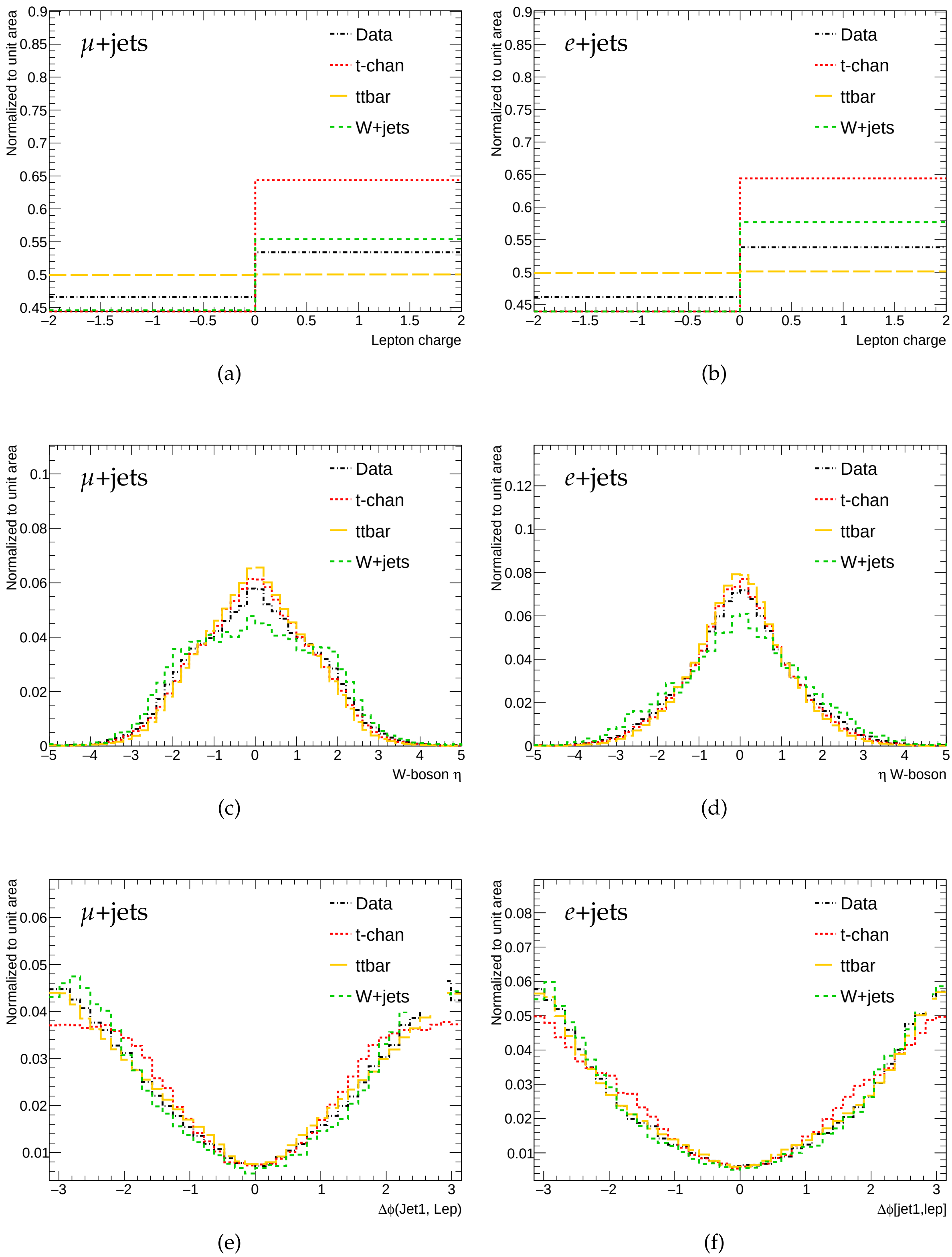

Figure 6.30: The lepton charge, η of W-boson and delta ϕ between the lepton and the first jet in the signal region. The simulation is normalized to unity.

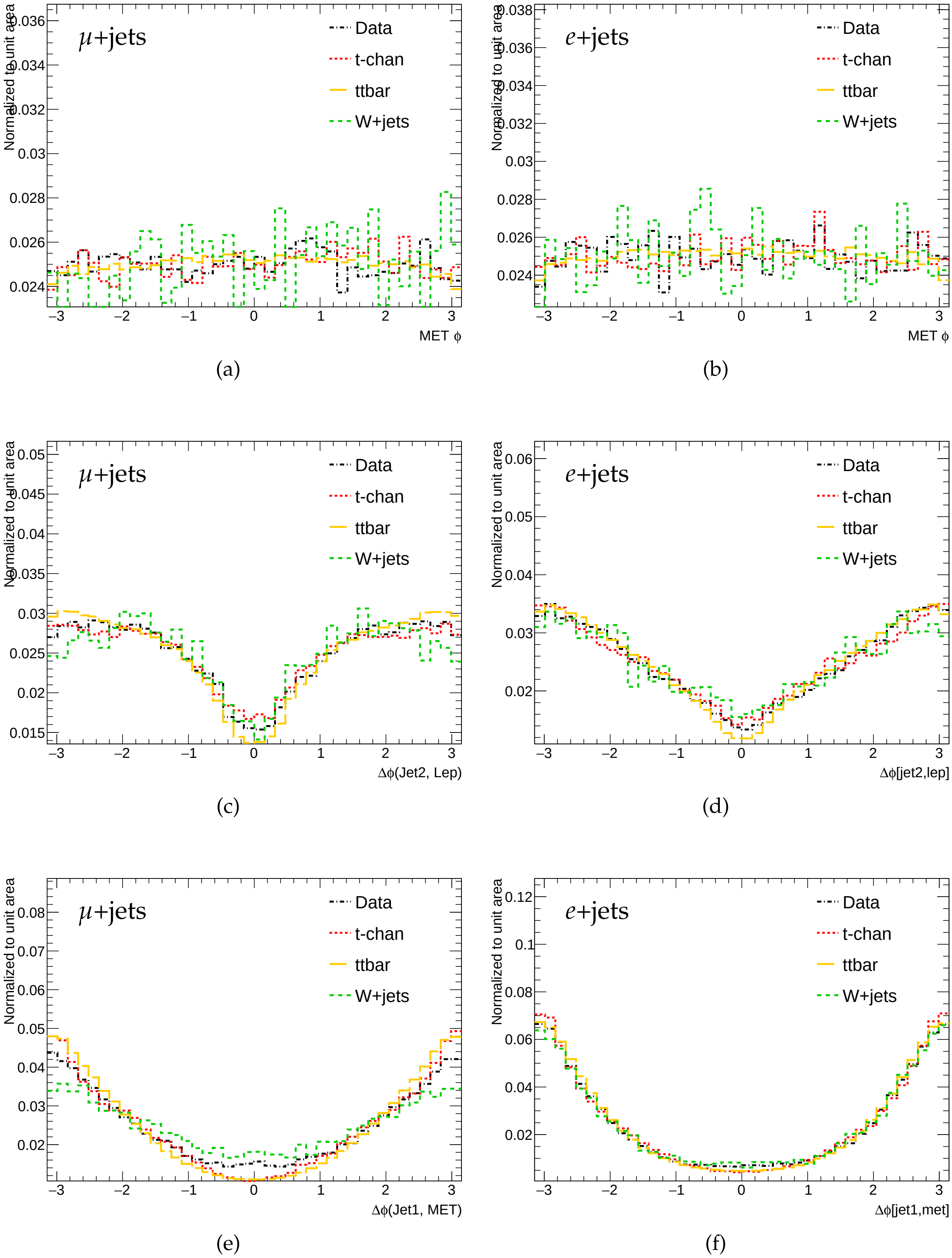

Figure 6.31: The Azimuthal angle of $\not{E}_{\mathrm{T}}$, $\delta\phi$ between the second jet and lepton and $\delta\phi$ between first jet and $\not{E}_{\mathrm{T}}$ in muon (electron) channel for signal region. The simulation is normalized to unity.

Delta ϕ between the leading jet and $\not{E}_{\mathrm{T}}$, $\Delta\phi[jet1, \not{E}_{\mathrm{T}}]$

The difference in the azimuthal angle between the four-vector of the leading jet and MET shown in Fig 6.32(a) and 6.32(b) the data, t-channel, $\mathrm{t\bar{t}}$ and W+jets for the muon and election channel respectively.

Delta ϕ of the second leading jet and $\not{E}_{\mathrm{T}}$, $\Delta\phi[jet2, \not{E}_{\mathrm{T}}]$

Azimuthal angle distribution of second leading jet and $\not{E}_{\mathrm{T}}$ is measured, the difference of these two angles comes out to be an important variable for the training of the neural network. Figure 6.32(c) and 6.32(d) the data, t-channel, $\mathrm{t\bar{t}}$ and W+jets for the muon and election channel respectively.

Angular separation of first jet and $\not{E}_{\mathrm{T}}$, $\Delta R[jet1, \not{E}_{\mathrm{T}}]$

The angular separation between the four-vector of the first jet and $\not{E}_{\mathrm{T}}$. Figure 6.32(f) and **??** the data, t-channel, $\mathrm{t\bar{t}}$ and W+jets for the muon and election channel respectively.

Event Shape Variable, C

The C-parameter is derived from the eigenvalues λ_i of the momentum tensor:

$$C = 3 \times (\lambda_1\lambda_2 + \lambda_2\lambda_3 + \lambda_3\lambda_1),$$

is shown in Fig. 6.33(a) and 6.33(b) the data, t-channel, $\mathrm{t\bar{t}}$ and W+jets for the muon and election channel respectively.

Event Shape Variable, D

The D-parameter is defined by the eigenvalues λ_i of the momentum tensor:

$$D = 27(\lambda_1\lambda_2\lambda_3),$$

is shown in Fig. 6.33(c) and 6.33(d) the data, t-channel, $\mathrm{t\bar{t}}$ and W+jets for the muon and election channel respectively.

Event Shape Variable, Aplanarity

Aplanarity is calculated from the third largest eigenvalue of the momentum tensor:

$$A = \tfrac{3}{2}(\lambda_3),$$

is shown in Fig. 6.33(e) and 6.33(f) the data, t-channel, $\mathrm{t\bar{t}}$ and W+jets for the muon and election channel respectively.

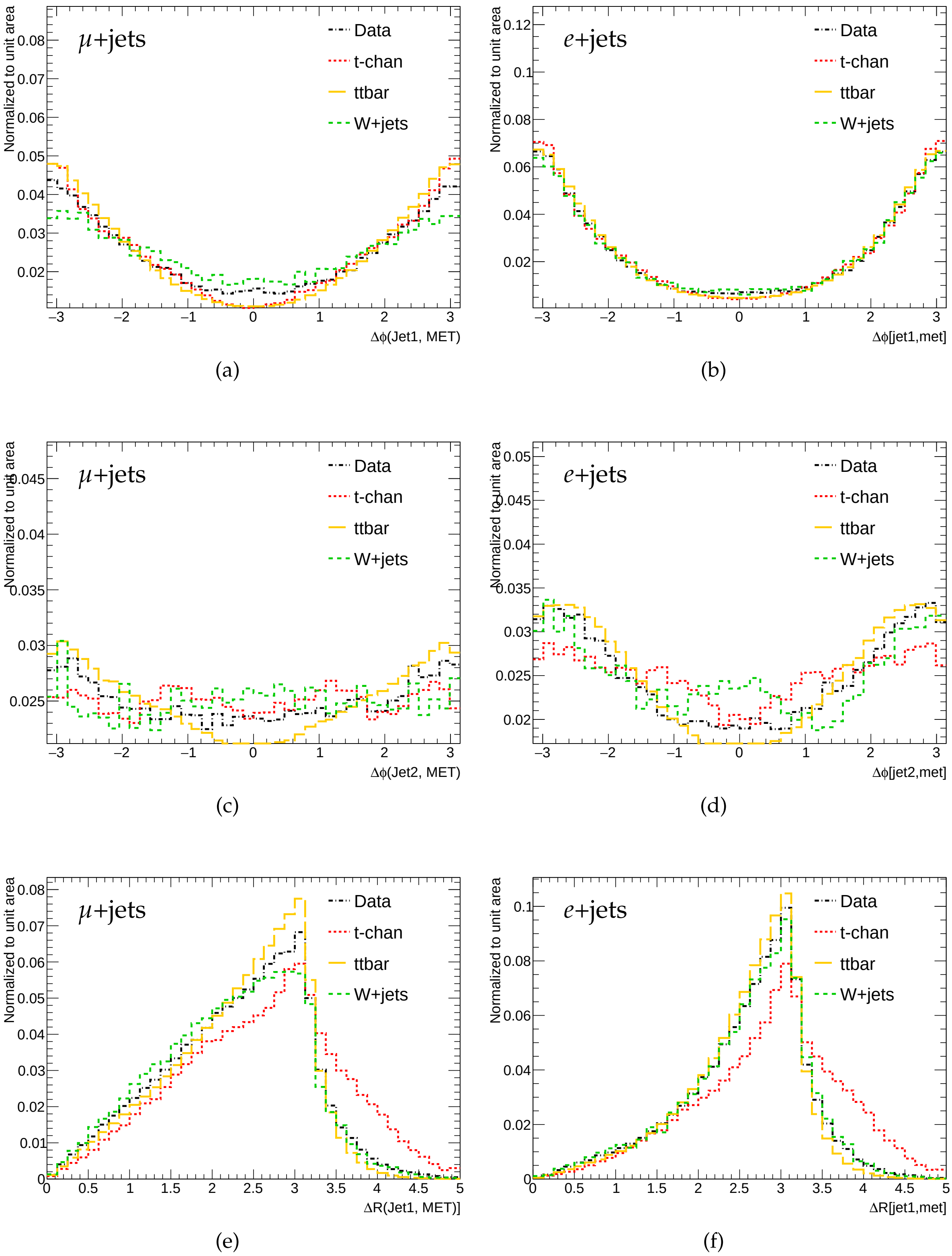

Figure 6.32: The $\Delta\phi$ between the 1^{st} and $\not{E}_{\mathrm{T}}$, 2^{nd} jet and $\not{E}_{\mathrm{T}}$, angular separation $\Delta R(1^{st}$ jet, $\not{E}_{\mathrm{T}})$ in muon (electron) channel for signal region. The simulation is normalized to unity.

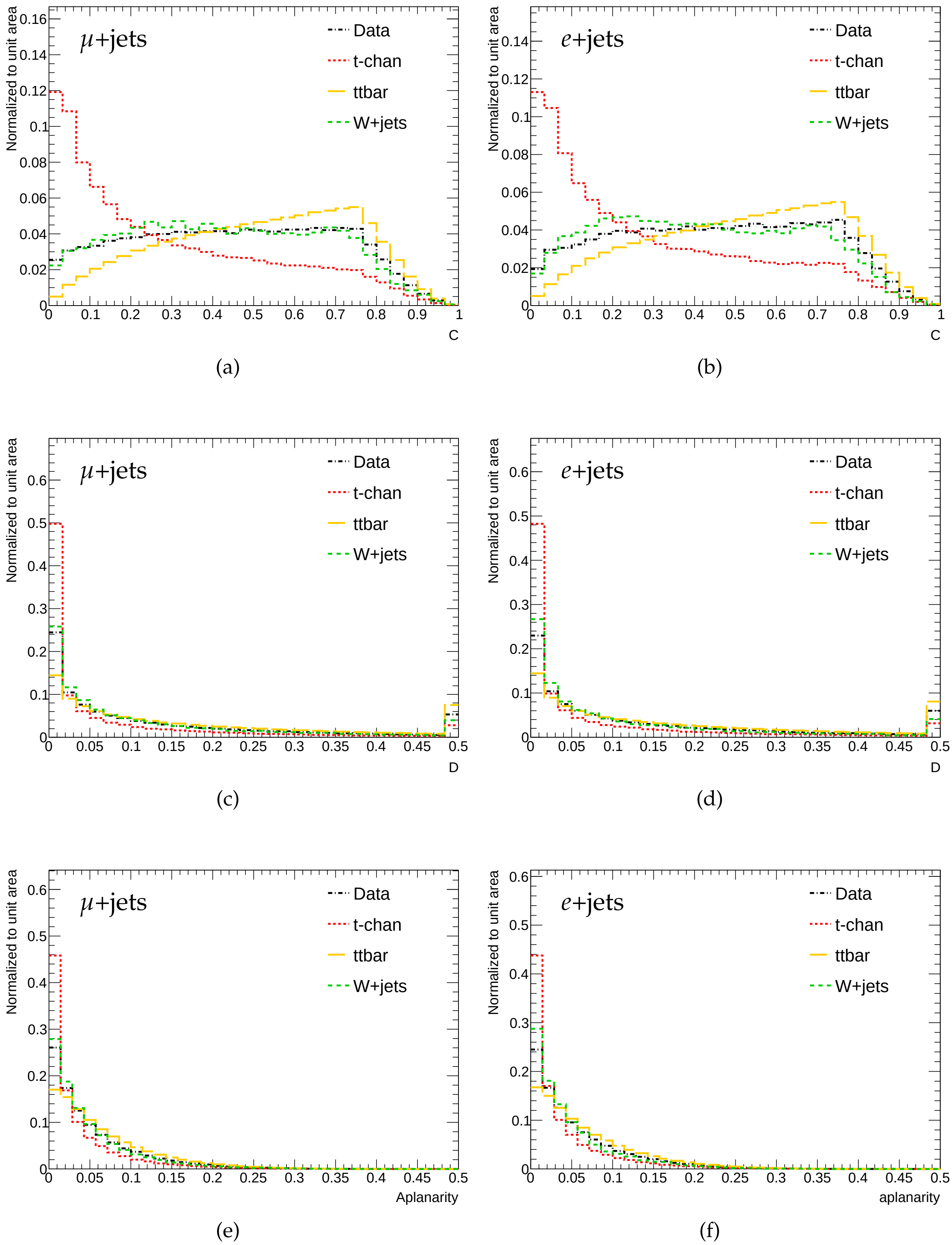

Figure 6.33: The event shape variable C-parameter, D-parameter and Aplanarity in muon (electron) channel for signal region. The simulation is normalized to unity.

6.4 Neural Network Discriminator

The variables described above are used in the training of a neural network which combines the separation power of the various input variables into one single NN output distribution. The training is done in the 2j1t signal region and the trained NN is applied to events in both the signal region and the $t\bar{t}$ control region. Figure 6.34 shows the resulting shapes of the NN discriminator distributions for the signal and background processes in the electron and muon channel in the signal region and in the $t\bar{t}$ control region. Figure 6.35 shows the NN discriminator distributions for the NN trained in the 2j1t region and applied to all three regions (2j0t, 2j1t, and 3j2t) for data and the signal and background models, which have been normalized to the number of selected data events.

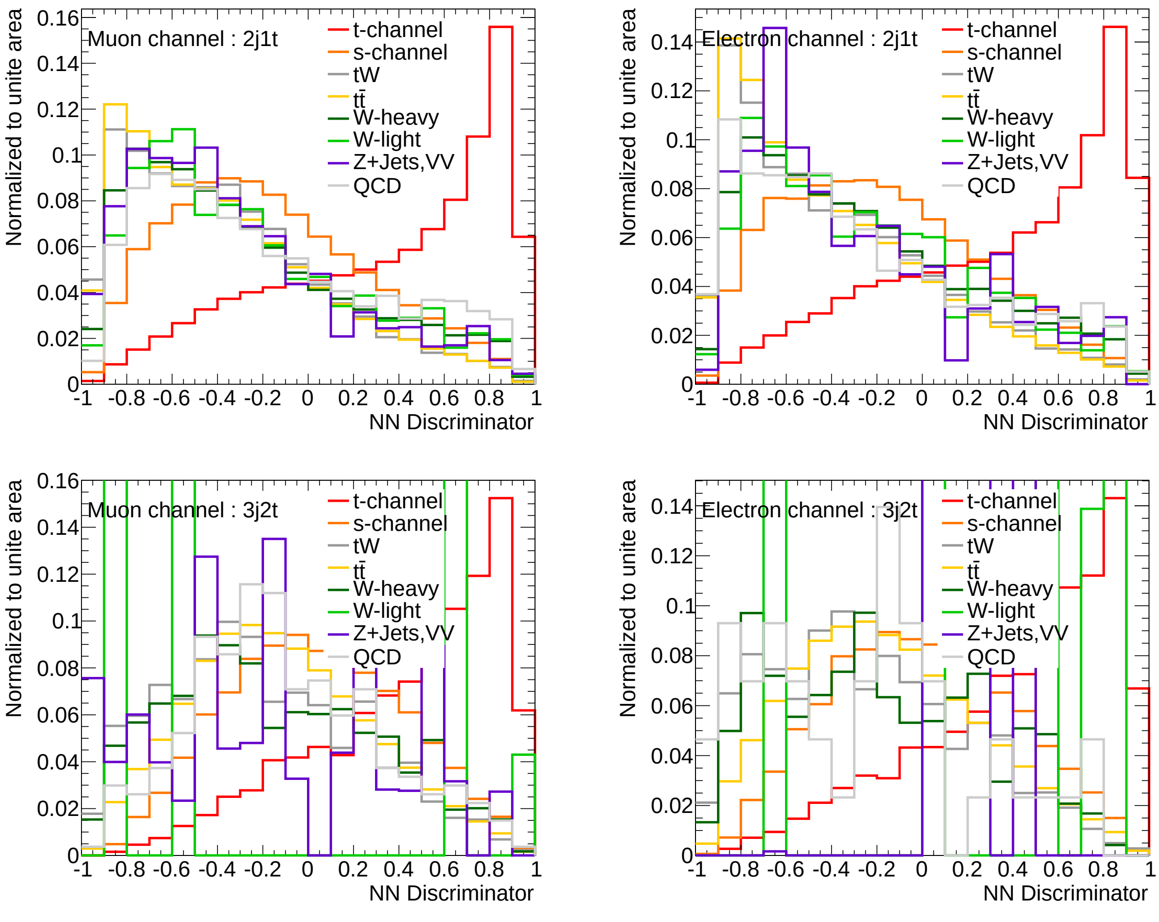

Figure 6.34: The NN discriminator shape shown for the 2j1t region (upper row) and in the 3j2t region (lower row) for the signal and background.

6.5 Fitting the NN Discriminator

We performed a binned maximum likelihood fit of the neural network templates in the electron and muon channel using the `theta` package to get a scale factor for each process. The fit is done simultaneously in the signal region and the $t\bar{t}$ control region in order to gain more power on constraining the fraction of $t\bar{t}$ events. The range of the maximum likelihood fit is from -1 to 1 for each discriminator distribution. The scale factors are defined as $\beta_i = \frac{\sigma_{\text{measured}}}{\sigma_{\text{SM}}}$, where i is the index for each fitted process, σ_{measured} is the measured cross-section and σ_{SM} is the cross-section as predicted by standard model calculations. These predictions are taken from theory and simulation. Background processes are constrained using Gaussian prior uncertainties. The prior uncertainty on $t\bar{t}$ is 20%, prior uncertainties on other backgrounds are 30%. The QCD background contribution is not fitted, but is kept fixed for the results from the dedicated QCD estimation described in Section 6.1 during the fit.

Table 6.3: The scale factors for neural network discriminator fit in the muon channel. The uncertainty quoted on the scale factor is the statistical uncertainty for the signal and background.

	Combined (3j2t-2j1t)	2j1t
Process	Scale Factor	Scale Factor
β_{signal}	0.98±0.02	1.00±0.02
s-channel	0.73±0.29	0.80±0.21
tW	1.38±0.24	0.78±0.28
$t\bar{t}$	1.08±0.01	1.25±0.05
W+jets(heavy)	1.32±0.07	1.10±0.11
W+jets(light)	0.82±0.29	0.91±0.28
Z+jets	0.98±0.28	0.88±0.28
VV	1.18±0.29	1.07±0.29

Table 6.4: The scale factors for neural network discriminator fit in the electron channel. The uncertainty quoted on the scale factor is the statistical uncertainty for the signal and background.

	Combined (3j2t-2j1t)	2j1t
Process	Scale Factor	Scale Factor
β_{signal}	0.99±0.03	1.00±0.03
s-channel	0.93±0.29	0.98±0.29
tW	1.36±0.25	0.96±0.29
$t\bar{t}$	1.14±0.01	1.22±0.04
W+jets(heavy)	1.34±0.09	1.23±0.13
W+jets(light)	1.02±0.29	1.02±0.29
Z+jets	1.03±0.29	1.03±0.29
VV	1.08±0.29	1.02±0.29

The fitted scale factors with the corresponding statistical uncertainties on each process are given in the Table 6.3 and Table 6.4 for muon and electron channel respectively. For comparison reasons we also display the fit results when using only the 2j1t region. It can clearly be seen that the precision of the fit results, especially for the main background, $t\bar{t}$, increases when fitting in the signal and $t\bar{t}$ control region simultaneously. In the following the results of this simultaneous fit are used. Figure 6.37 shows the NN discriminator distributions in the two channels and two regions (2j1t and 3j2t) as measured in data and for comparison the signal and background templates normalized to the fit results.
As a cross check we estimate the t–channel cross-section from the discriminator templates using a Bayesian method. The posterior of the signal strength is extracted by marginalizing all nuisance parameters via a Markov Chain Monte Carlo (MCMC) integration. The

50% quantile of the posterior is taken as best estimate for the signal strength β_{signal}. The cross-section is calculated with

$$\sigma_{\text{measured}} = \beta_{\text{signal}} \times \sigma_{\text{SM}}, \tag{6.5.1}$$

where σ_{SM} is the predicted t-channel cross-section at 8 TeV. The quoted uncertainties are statistical uncertainties which are extracted from the 84% and 16% upper and lower quantile limits of the signal strength posterior. The measured inclusive cross-section and statistical uncertainties in both channels are given in Table 6.5.

Table 6.5: The measured inclusive cross-sections and statistical uncertainties in muon and electron channel.

	Muon channel	Electron channel
Cross-section [pb]	87.25 ± 2.05	87.48 ± 2.70

In order to enrich the selected sample in signal events a proper value for the cut on the NN discriminator has to be found. As a figure of merit the significance $\frac{\text{S}}{\sqrt{\text{S+B}}}$ is used to find the optimal cut value. For that purpose the NN discriminator is scanned from -1 to 1 for both the channels and the resulting significances are compared, see Fig. 6.38. In muon(electron) channel a value of Discriminator $>$ 0.3 (0.4) was found to yield the best significance. Tables 6.6 and 6.7 list the number of events for each process in the signal region with the additional requirement of Discriminator $>$ 0.3 (0.4) is applied for muon(electron) channel. The numbers are determined based on the templates in the 2j1t region and the fitted scale factors for each process.

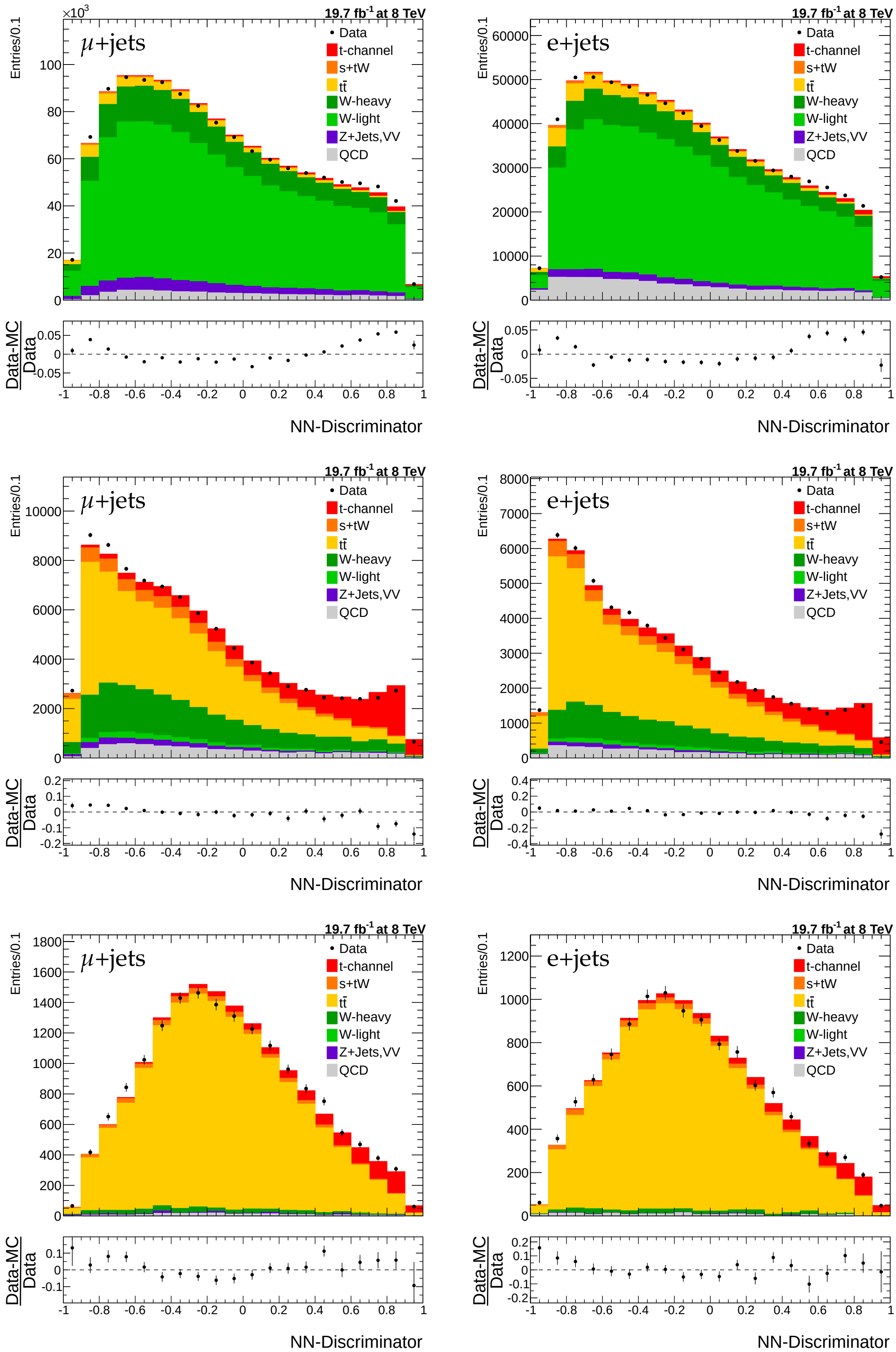

Figure 6.35: The NN discriminator output shown for the 2j0t, 2j1t and 3j2t region. The templates are normalized to the data.

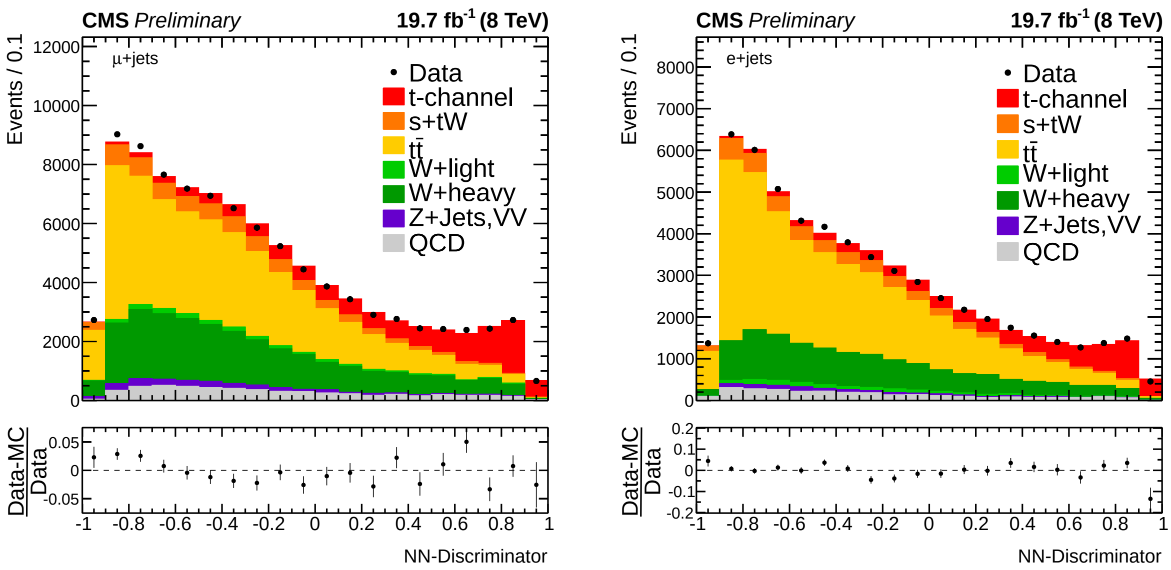

Figure 6.36: The NN discriminator output for the muon (electron) channel in the 2j1t region. The templates are normalized to the fit results.

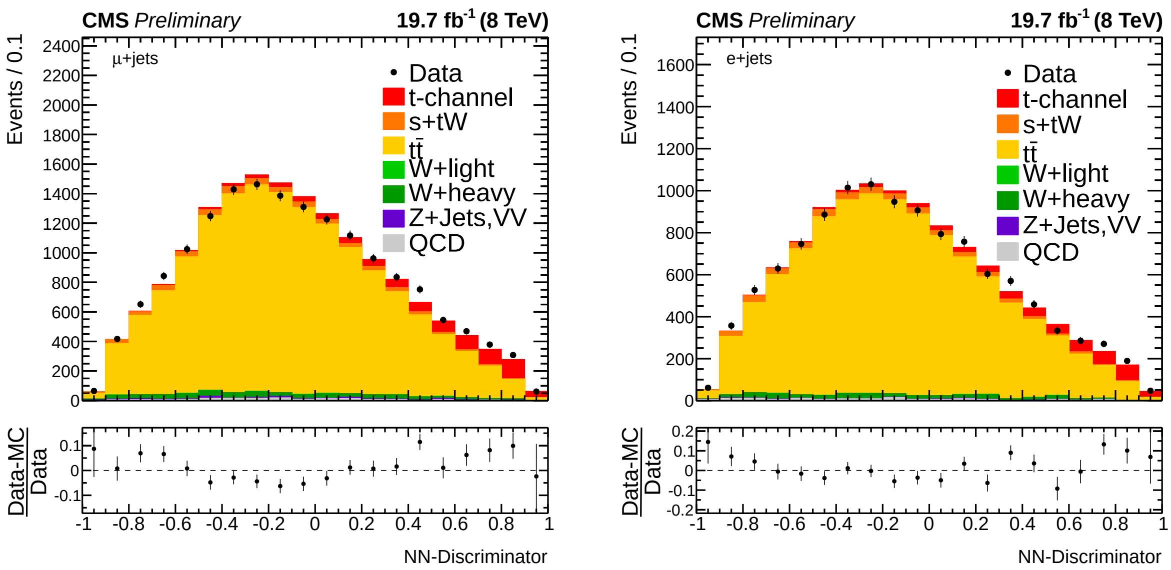

Figure 6.37: The NN discriminator output in the muon and electron channel in 3j2t region. The templates are normalized to the fit results.

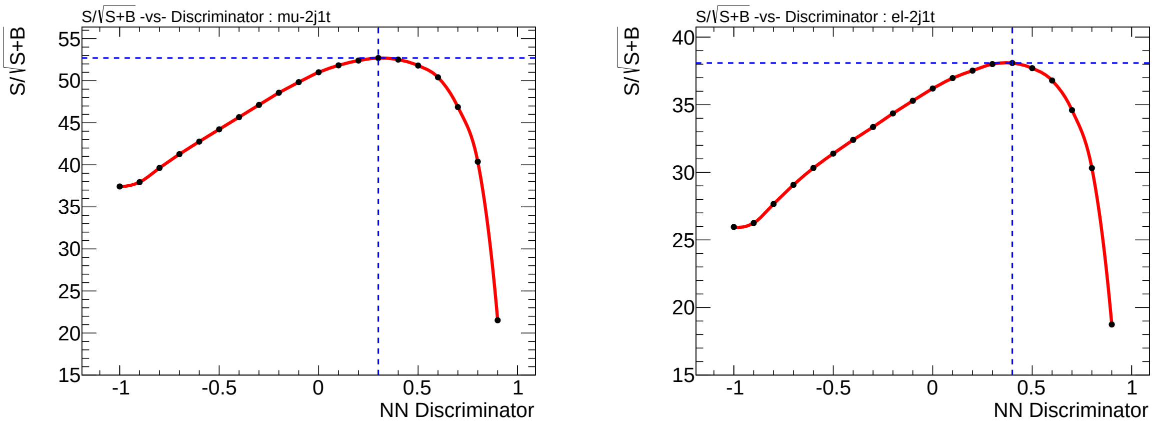

Figure 6.38: The NN discriminator scan in the muon and electron channel in 2j1t bin. The normalized NN template is scanned from minimum to maximum range to find the cut value for electron and muon channel.

Table 6.6: The event yield in the muon channel after cutting the scaled neural network templates at Discriminator>0.3. The quoted uncertainties are the statistical uncertainties from the fit.

Muon Channel	Process	Events		Unc.
	t-channel	6618	±	135
	s-channel	75	±	31
	tW	508	±	95
	$t\bar{t}$	3638	±	76
	W+jets(heavy)	3366	±	200
	W+jets(light)	253	±	90
	Z+jets	172	±	51
	VV	58	±	17
	Multijet QCD	1083	±	55
	Total MC	15772	±	297
	Data	15843		

Table 6.7: The event yield in the electron channel after cutting the scaled neural network templates at Discriminator >0.4. The quoted uncertainties are the statistical uncertainties from the fit.

Electron Channel	Process	Events		Unc.
	t-channel	3307	±	92
	s-channel	43	±	15
	tW	260	±	53
	$t\bar{t}$	1985	±	57
	W+jets(heavy)	1360	±	104
	W+jets(light)	129	±	39
	Z+jets	57	±	18
	VV	26	±	9
	Multijet QCD	375	±	40
	Total MC	7540	±	170
	Data	7548		

6.5.1 Top-quark-p_{T} for Different NN Cut Values

The possible impact of the cut value on the NN discriminator on the distribution of the transverse momentum of the top-quark is studied in both channels by comparing the shapes of this distribution for various cut values (see Fig. 6.39, 6.40). Within the uncertainties no shape differences could be observed.

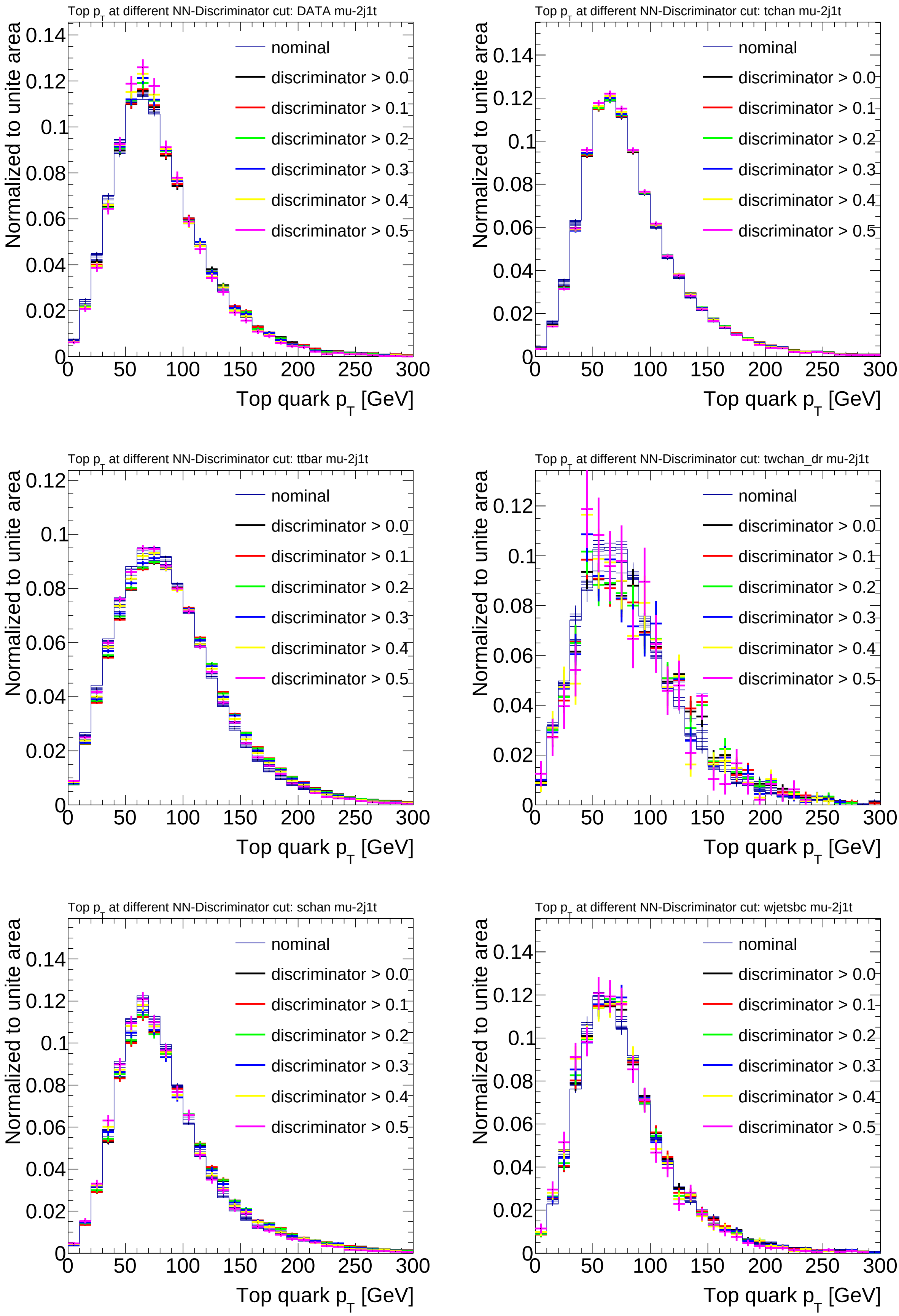

Figure 6.39: Muon channel: The top-quark p_T shape in the 2j1t region for various cut values of the discriminator. The comparison is shown for data (top left), signal MC (top right), and background monte carlo simulation.

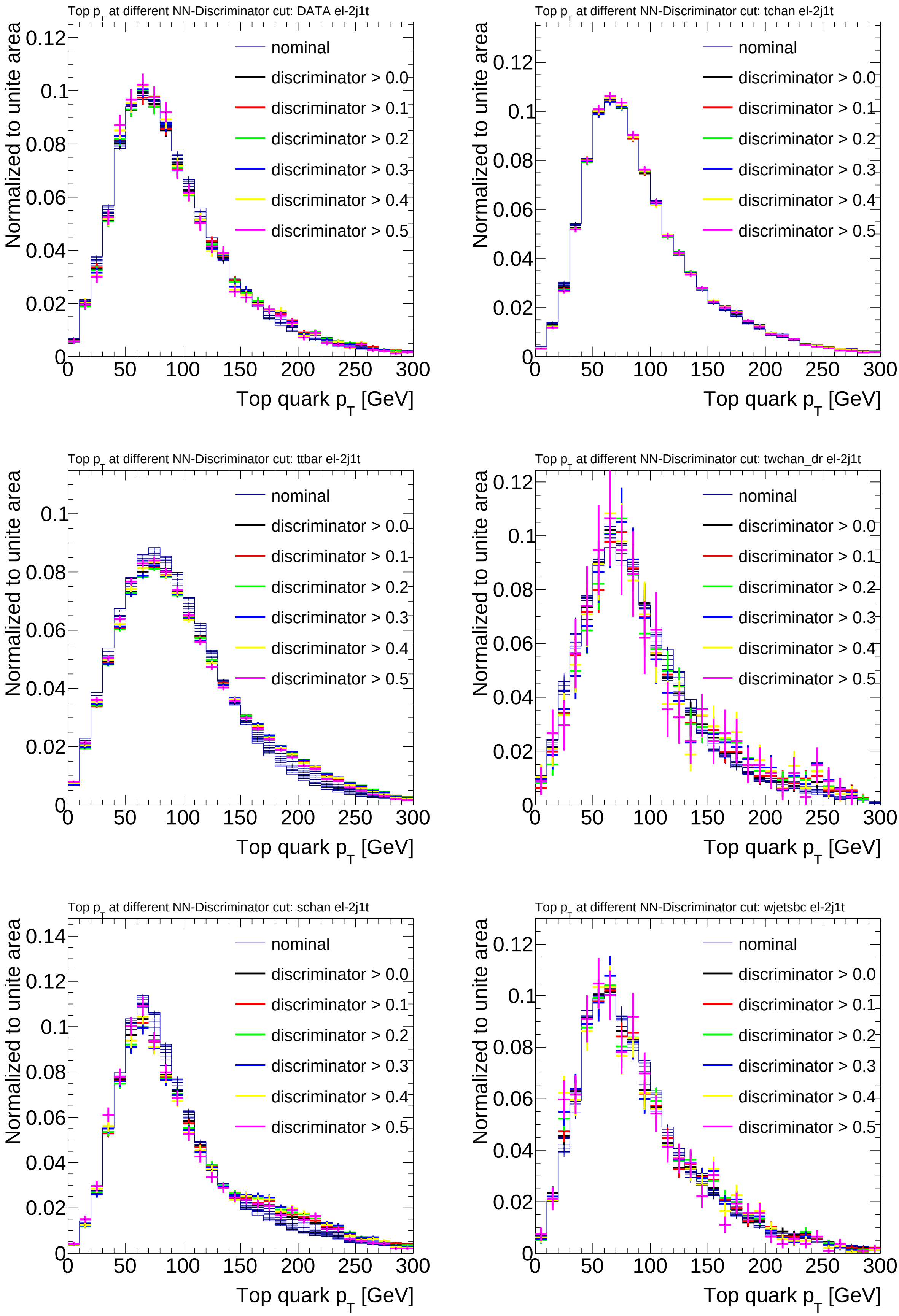

Figure 6.40: Electron channel: The top-quark p_{T} shape in the 2j1t region for various cut values of the discriminator. The comparison is shown for data (top left), signal MC (top right), and background monte carlo simulation.

6.5.2 Top-quark-$|y|$ for Different NN Cut Values

The possible impact of the cut value on the NN discriminator on the distribution of the rapidity of the top-quark is studied in both channels by comparing the shapes of this distribution for various cut values (see Fig. 6.41, 6.42). Within the uncertainties no shape differences could be observed.

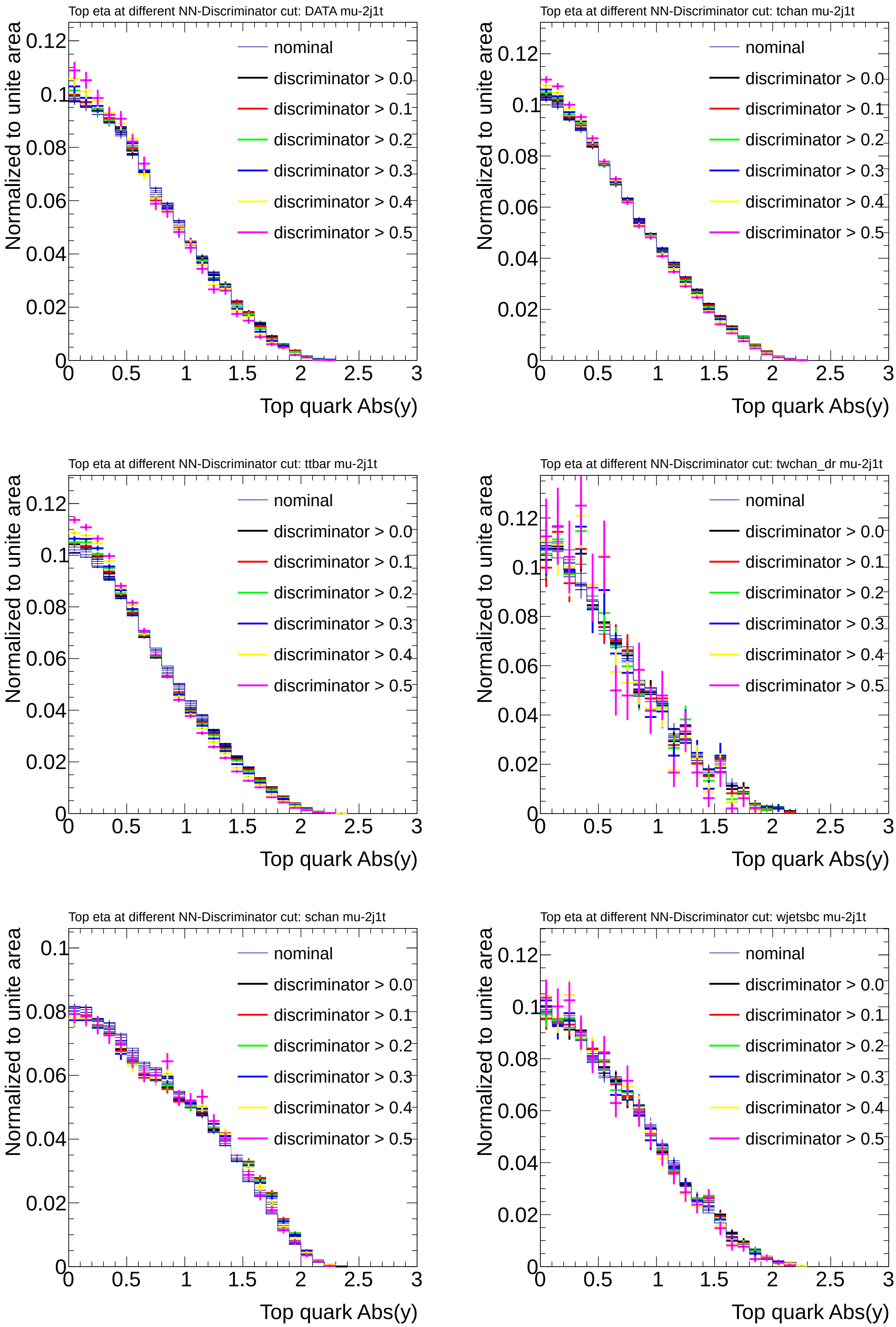

Figure 6.41: Muon channel: The top-quark-$|y|$ in the 2j1t region for various cut values of the discriminator. The comparison is shown for data (top left), signal MC (top right), and background monte carlo simulation.

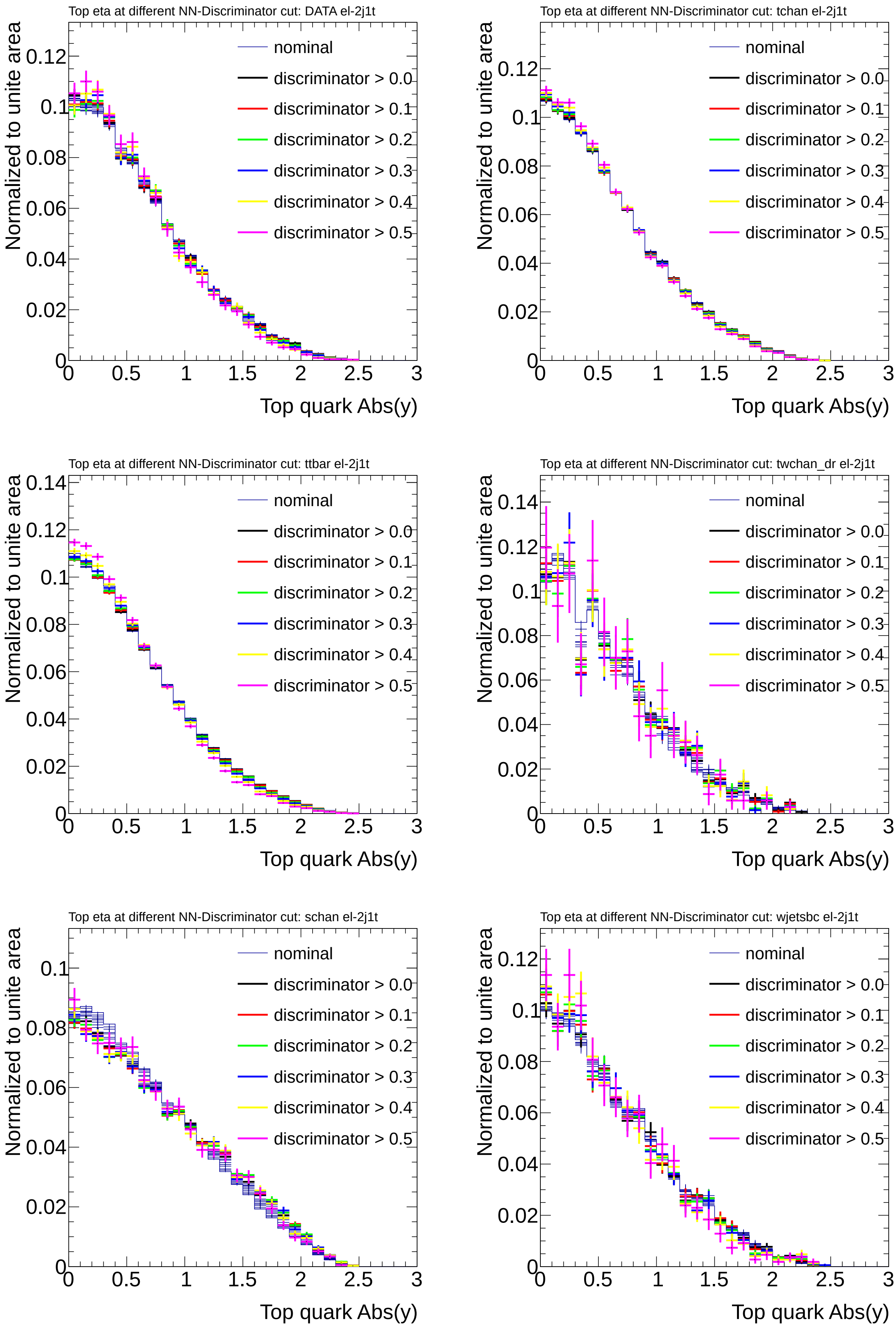

Figure 6.42: Electron channel: The top-quark-$|y|$ in the 2j1t region for various cut values of the discriminator. The comparison is shown for data (top left), signal MC (top right), and background monte carlo simulation.

6.6 Unfolding

Unfolding is a method used in experimental high energy physics to correct measured distributions for detector and background effects. The `TUnfold` algorithm [189] can be interfaced and used in the `ROOT` package and is based on least-square fitting and Tikhonov regularization [190]. Due to the detector effects it is not possible to have a 100% reconstruction efficiency and as a result there is a nonzero probability for events to be found in the wrong reconstructed bin. In each bin we have a linear combination of signal and background events. We are interested to see a physical observable in the detector without having any detector effects and backgrounds. In all such cases the observed numbers of events in each bin have to be corrected for the detector effects. The physics problem comes out to be solving an inverse problem i.e. getting a true distribution from a measured one. Mathematically, the problem can be written as:

$$\bar{y}_i = \sum_{j=1}^{m} A_{ij}\bar{x}_j; \qquad 1 \leq i \leq n, \tag{6.6.1}$$

where $\bar{y}_i$ represents the averages expected event count at the detector level m represents the number of bins, $\bar{x}_j$ represents the true distribution and A_{ij} represents the matrix which transforms the true distribution to the reconstructed or measured ones. Schematically the unfolding can be represented as shown in Fig. 6.43.

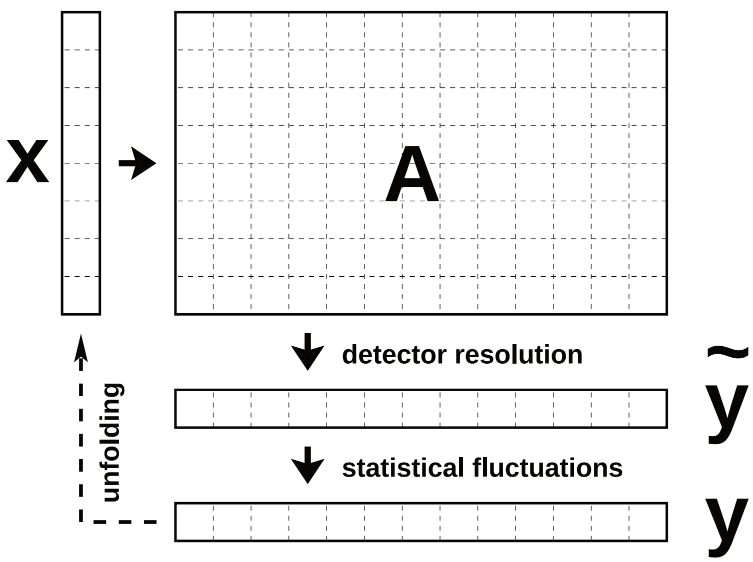

(a)

Figure 6.43: The Schematic view of migration effects and statistical unfolding [189].

However the situation gets more complicated when the backgrounds are included. With the inclusion of backgrounds, y_i now gets the additional contribution, which can be written mathematically as:

$$\bar{y}_i = \sum_{j=1}^{m} A_{ij}\bar{x}_j + b_i; \qquad 1 \leq i \leq n, \tag{6.6.2}$$

where b_i is the background showing up in the bin i. Both background and probability matrix have systematic uncertainties which are to be treated in addition to statistical uncertainties.

If $\bar{y}_i \rightarrow y_i$ and $\bar{x}_i \rightarrow x_i$ in equation 6.6.1 and in equation 6.6.2 one can solve for the values of x_j by inverting the probability matrix but the statistical fluctuations are amplified in y_i. Those statistical fluctuations are often damped by imposing the smoothness conditions on x_j. In technical terms this process is called "Regularization". The `TUnfold` algorithm used in this thesis tries to estimate x_j using the least square method with Tikhonov regularisation [190] and an optional area constraint. Since the process of estimating the x_j is based on least square minimization and to get best from least square minimization the numbers of degrees of freedom $m - n$ has to be greater than zero, i.e., $m - n > 0$. This would mean that the data y_i has to be measured with finner binning. Since the unfolding results depend largely on the number of bins taken into account in the measured distribution and true distribution. In this analysis, the number of bins used for measured distribution are twice as compared to the true distribution. There are some other algorithms available in which the condition $n = m$ is chosen as compared to $n > m$ [191,192]. Examples which do not use $n = m$ condition can be found at [193,194].

Algorithm

The algorithm gives an estimator of a set of truth parameters by using a single measurement of a set of observables. Let $\boldsymbol{y}$[1] be a vector of random variables of n rows. The random variables $\boldsymbol{y}$ are taken to have a multi-variant Gaussian distribution with mean $\tilde{\boldsymbol{y}} = \mathbf{A}\tilde{\boldsymbol{x}}$, where $\tilde{\boldsymbol{x}}$ is a vector corresponding to set of true values and $\mathbf{A}$ is a matrix usually called migration matrix. The variance covariance matrices of $\boldsymbol{x}, \boldsymbol{y}$ are given by $\mathbf{V_{xx}}, \mathbf{V_{yy}}$. The algorithm tries to find out the stationary point of the Lagrangian. Mathematically it can be written as:

$$
\begin{aligned}
\mathcal{L}(x,\lambda) &= \mathcal{L}_1 + \mathcal{L}_2 + \mathcal{L}_3 \qquad \text{where} \qquad (6.6.3)\\
\mathcal{L}_1 &= (\boldsymbol{y} - \mathbf{A}\boldsymbol{x})^{\mathsf{T}}\mathbf{V_{xx}}(\boldsymbol{y} - \mathbf{A}\boldsymbol{x})\\
\mathcal{L}_2 &= \tau^2(\boldsymbol{x} - f_b\boldsymbol{x_0})^{\mathsf{T}}(\mathbf{L^T L})(\boldsymbol{x} - f_b\boldsymbol{x_0})\\
\mathcal{L}_3 &= \lambda(Y - e^{\mathbf{T}}\boldsymbol{x}) \qquad \text{and}\\
Y &= \sum_i y_i,\\
e_j &= \sum_i A_{ij},
\end{aligned}
$$

where $\mathcal{L}_1$ term arises from least square minimisation. The covariance matrix $\mathbf{V_{xx}}$ is a diagonal matrix in most of the cases and the diagonal elements are the uncertainties. The vector $\boldsymbol{x}$ is the corresponding unfolding result which has m rows. The elements A_{ij} of the matrix $\mathbf{A}$ describe for each row j of $\boldsymbol{x}$ the probabilities to migrate to bin i of $\boldsymbol{y}$. As described earlier the migration matrix, $\mathbf{A}$, is determined from the MC simulations. The $\mathcal{L}_2$ describes the regularisation which acts as a damping factor for $\boldsymbol{x}$. The $\mathcal{L}_3$ is an optional area constraint, λ is the Lagrangian parameter, Y gives the sum over all observations, $\boldsymbol{e}$ is

[1]The matrices and vectors are written in bold.

the efficiency vector which has m rows and is calculated from **A**.

This thesis describes the measurement of the differential cross-section as a function of top-quark-p_T and $|y|$. The Transverse momentum distributions and the pseudorapidity distribution of the top-quark at the generator level and at the reconstruction level are shown in Fig. 6.45(a) and Fig. 6.45(c). Similarly the Fig. 6.45(b) and Fig. 6.45(d) represents transverse momentum distributions and the pseudorapidity distribution of the top-quark at the generator level and at the reconstruction level but for the same bins in which the unfolding will be performed. Due to the detector acceptance and selection efficiencies the reconstruction of top-quark kinematics is not perfect. Therefore the distributions have to be corrected before they can be compared to the theoretical predictions. The regularized unfolding method is used for the treatment of imperfections arising during the reconstruction process. In the following we describe the various steps of the unfolding procedure.

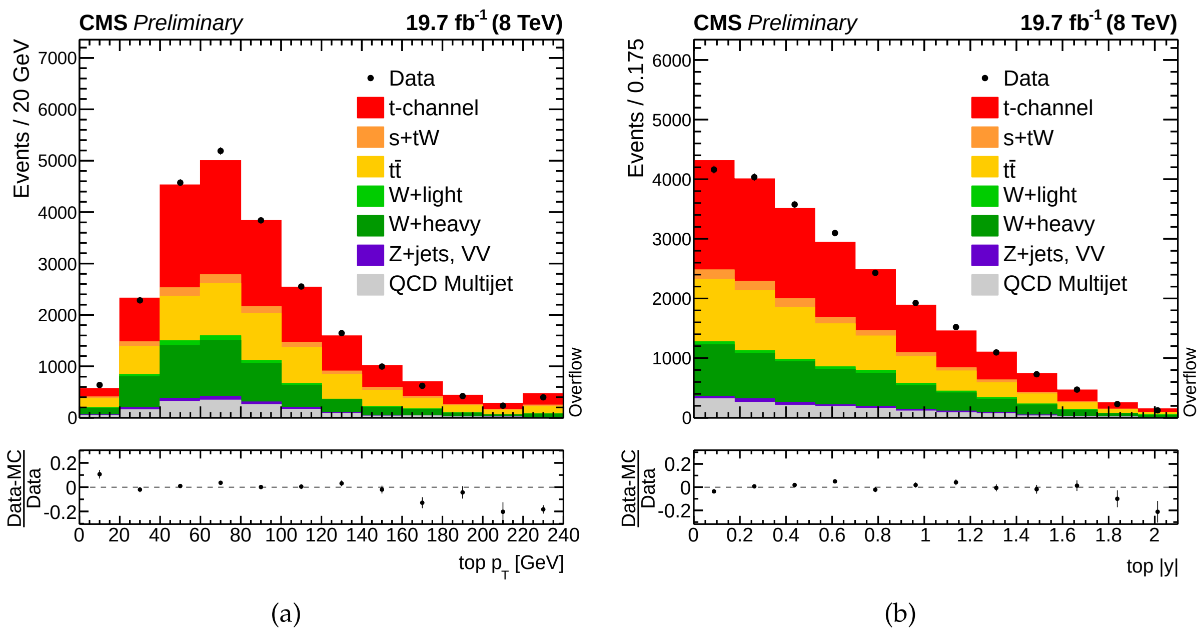

Figure 6.44: The transverse momentum and the absolute value of the rapidity of the top-quark after cutting on the NN discriminator in the lepton+jets channel. The different processes are normalized to the fit results.

The distributions of the transverse momentum and the absolute value of the rapidity of the reconstructed top-quark four-vectors are shown in Fig. 6.44. In addition to the contamination from background processes, resolution effects and ambiguities in the reconstruction affect the shape of these kinematic distributions. To enable comparison to theory predictions, these effects have to be corrected.

Background Subtraction

In the first step, the reconstructed spectra are corrected for background contributions. Background templates, normalized to the respective fitted amount of background events, are subtracted from the reconstructed data distributions. The statistical uncertainties and correlation between the fit parameters in the fit results are taken into account. Therefore the background templates $\vec{b}_i$, where i represents the different background processes, are transformed into orthogonal templates $\vec{b}'_j$ with uncorrelated normalization uncertainties. For this purpose the covariance matrix of the background estimation fit V_b is used:

$$\vec{b}'_j = \sum_{i=1}^{N} s_j(\vec{v}_{j_i} \cdot \vec{b}_i), \tag{6.6.4}$$

where $\vec{v}_{j_i}$ is the i^{th} element of the eigenvector $\vec{v}_j$ of the covariance matrix and s_j are scale factors chosen such that the normalizations of the original contributions are preserved during the transformation. These properly normalized templates are than subtracted from the data distribution with the assumption that uncertainties on background rates and on statistical fluctuations in background processes are Gaussian.

Regularized Unfolding

The distributions of the transverse momentum and of the absolute value of the rapidity of the top-quark at the different stages of the analysis are shown in Fig. 6.45. From these distributions it can be seen that how the selection and reconstruction steps introduces distortions in the original distributions. We correct these distortions by applying a regularized unfolding procedure [195]. The regularized unfolding actually solves the inverse problem by correcting the migration and selection efficiencies by applying the generalized matrix inverse method [196, 197]. We try to get the true underlying distribution from the measured distribution. It can be written mathematically as $\vec{w} = S\vec{x}$, where $\vec{x}$ is the true underlying spectrum and S is the smearing matrix which takes into account the migration (see Fig. 6.47) and selection efficiency (see Fig. 6.46). The smearing matrix is obtained by multiplying the migration matrix with a diagonal matrix with the selection efficiencies on the diagonal elements. The problem is solved by transforming the $\vec{w} = S\vec{x}$ into a least-square problem by minimizing:

$$\chi^2(\vec{x}) = (S\vec{x} - \vec{w})^T V_w^{-1} (S\vec{x} - \vec{w}), \tag{6.6.5}$$

where V_w is the covariance matrix of the measured distribution $\vec{w}$. In general the solution can be written as:

$$\vec{x}_{\chi^2} = S^\dagger \vec{w}, \quad \text{where} \quad S^\dagger = (S^T V_w^{-1} S)^{-1} S^T V_w^{-1}. \tag{6.6.6}$$

However, the solution is not stable and it shows large fluctuations with a small change in $\vec{w}$. To make the solution more stable, two additional terms are introduced in the χ^2 function to reduce the fluctuations.

$$\chi^2(\vec{x}, \kappa) = \chi^2(\vec{x}) + \tau||L(\vec{x} - \vec{x}_{bias})||^2 + \kappa(N_{obs} - \sum_{i=1}^{n}(S\vec{x}_i))^2\ . \tag{6.6.7}$$

The two additional terms are the regularization term proportional to the regularization parameter τ and the normalization term proportional to the normalization constant κ. In the regularization term a matrix L is introduced such that $L(\vec{x} - \vec{x}_{bias})$ is proportional to the second derivatives of $(\vec{x} - \vec{x}_{bias})$. This is a standard regularisation method to force the solution to be smoother and to suppress unphysical fluctuations. The term $\vec{x}_{bias}$ signifies a bias distribution generated from our MC signal sample and allows the curvature to be weighted correctly despite remaining inequity in the statistics of the bins. The bias distribution is normalized to the observed number of events divided by the overall scalar selection efficiency. The parameter τ denotes the strength of the applied regularisation and its value is determined by the Minimum of Global Correlation method [190,191,195], where the optimal value of τ is found as the value which minimizes the mean value of the global correlation coefficient. The global correlation coefficient can be defined as the measure of the total amount of correlation between an element of $\vec{x}$ and all other elements.

The second additional term fixes the norm of the solution. The number of observed events is given by N_{obs}. The parameter κ is a Lagrangian multiplier. The minimization is performed with respect to $\vec{x}$ and κ simultaneously. The constraint on the normalization is important for a reconstructed distribution $\vec{w}$ with non-Gaussian errors, which is for instance the case for small numbers of observed events in some bins of w where the statistical uncertainties are Poisson-like and cannot be approximated by Gaussian uncertainties [198].

Twelve bins are used for the reconstructed spectrum and six bins are used for the unfolded distributions. How reasonable the chosen binning scheme is can be estimated by looking at the purity P and the stability S of each bin out of the six bins in the unfolded spectra. The purity is defined as:

$$P = \frac{N_{\text{rec,gen}}}{N_{\text{rec}}}, \tag{6.6.8}$$

and purity measures the probability for events with a reconstructed top-quark p_{T} (or $|y|$) value in a certain range, also have a generated value in this range. As we use twice the number of reconstructed bins compared to the generated spectrum always two reconstructed bins are compared to one generated bin. The stability is defined as:

$$S = \frac{N_{\text{rec,gen}}}{N_{\text{gen}}}, \tag{6.6.9}$$

and stability measures the probability for events with a generated top-quark p_{T} (or $|y|$) value in a certain range also have a reconstructed value in this range. Values above 50% for both quantities are considered "good".
For the measurement in top-quark p_{T} we found purity values between 50 and 75% and stability values between 50 and 85%. For the measurement in top-quark $|y|$ the purity lies between 53 and 67% and the stability between 41 and 81%, only the sixth bin is a bit low here with only 32%. While events with top-quark-p_{T} (top-quark-$|y|$) values beyond 240 GeV (2.1) are collapsed into the last visible bin in the reconstructed distributions shown in Fig. 6.44 (overflow bin), these events are not considered in the unfolding, i.e. only events with top-quark-$p_{\text{T}} < 240$ GeV (top-quark-$|y| < 2.1$) are used to get the unfolded differential cross-sections.

Performance Test of Unfolding Method

The results of the unfolding method are tested using pseudo experiments with simulated pseudo data sets. For each pseudo experiment the unfolded top-quark p_{T} ($|y|$) is compared to the true value. We checked the pull and relative difference between the generated and unfolded distribution of top-quark p_{T} ($|y|$) in six bins of top-quark p_{T} ($|y|$). The pull for each of the six bins is defined as the difference of unfolded and generated spectrum in that bin divided by the uncertainty on the unfolded spectrum in that bin. The relative difference is the difference between unfolded and generated p_{T} ($|y|$) spectra divided by the generated spectrum in that bin. The pull and relative difference are shown for six bins in top-quark p_{T} ($|y|$) in Fig. 6.50 (Fig. 6.51) and Fig. 6.48 (Fig. 6.49). For the pull distribution a mean around zero and a width around one indicate that the errors are estimated correctly. Similarly a mean of the relative difference around zero indicates that the unfolding is unbiased.

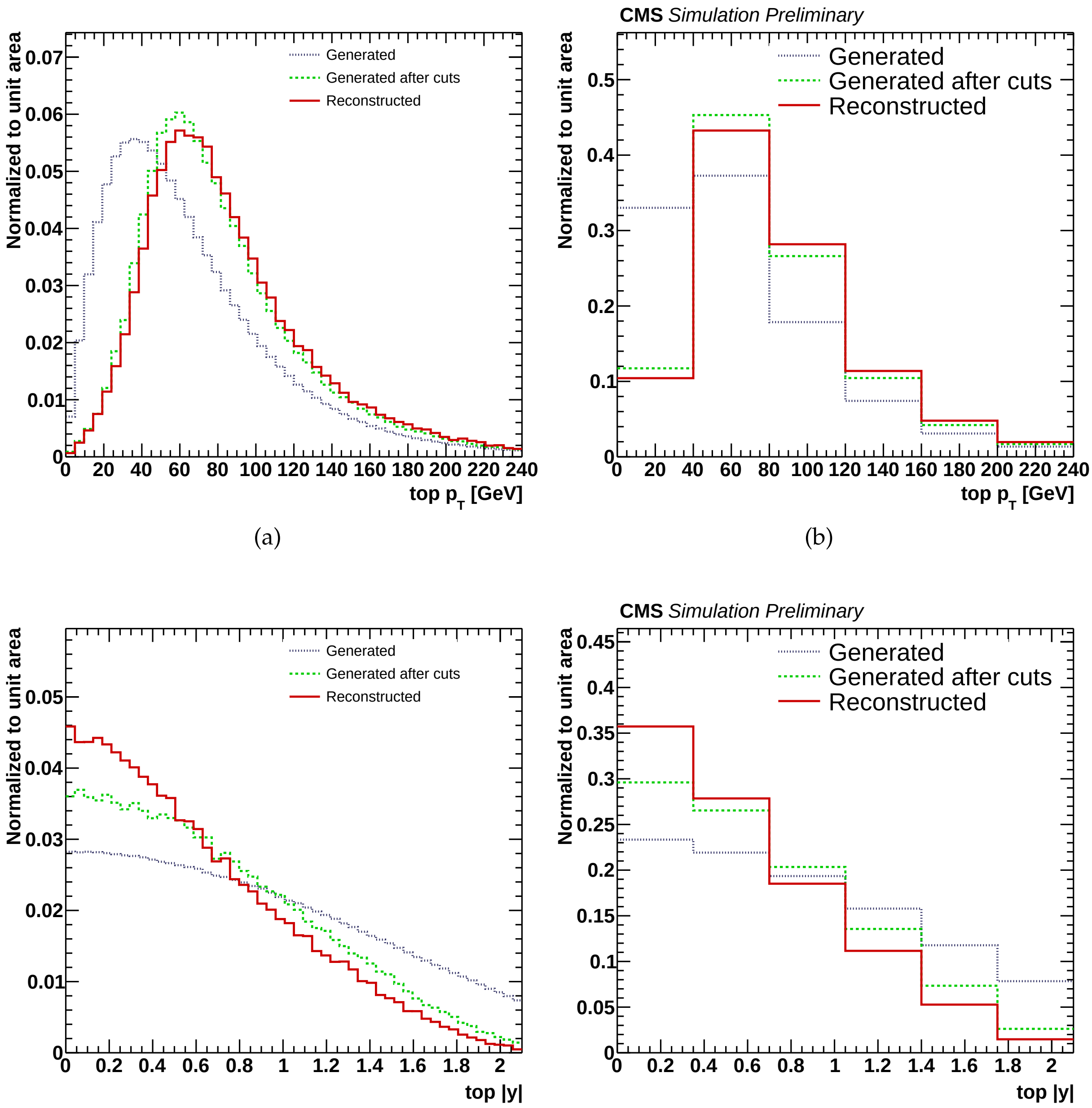

Figure 6.45: Shape comparison of the transverse momentum ((a) and (b)) and the absolute value of the rapidity ((c) and (d)) of the single-top-quark on generator level without any selection, generated after selection cuts, and reconstructed after selection cuts in the combined lepton+jet channel. The comparison is shown in two different binning:(a) and (c) 50 bins; (b) and (d) six bins.

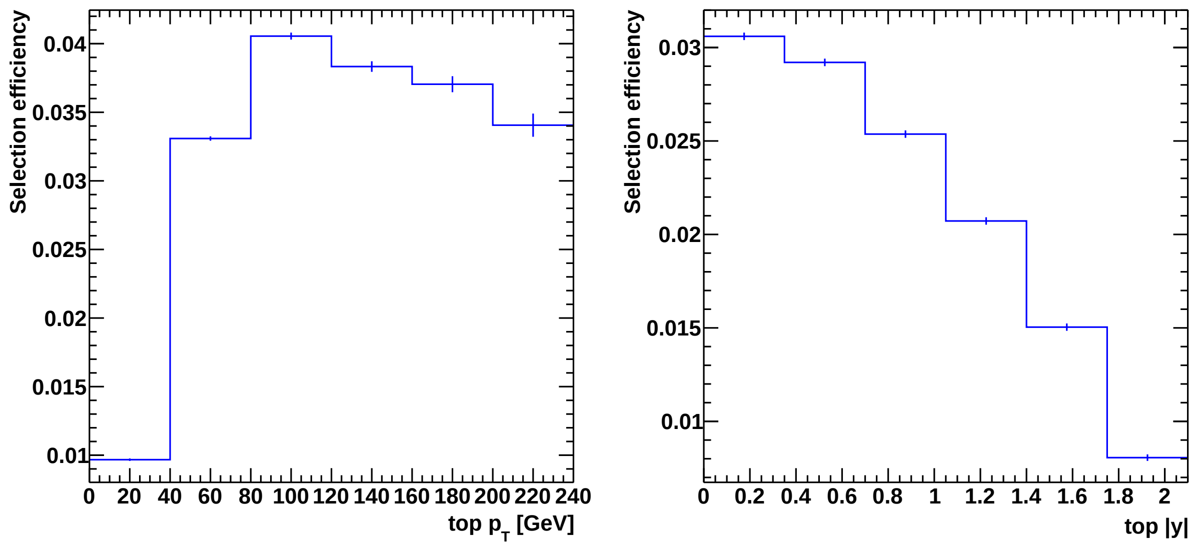

(a) (b)

Figure 6.46: (a) The selection efficiency as a function of the true transverse momentum and $|y|$ distribution of top-quark for the combined lepton+jets channel.

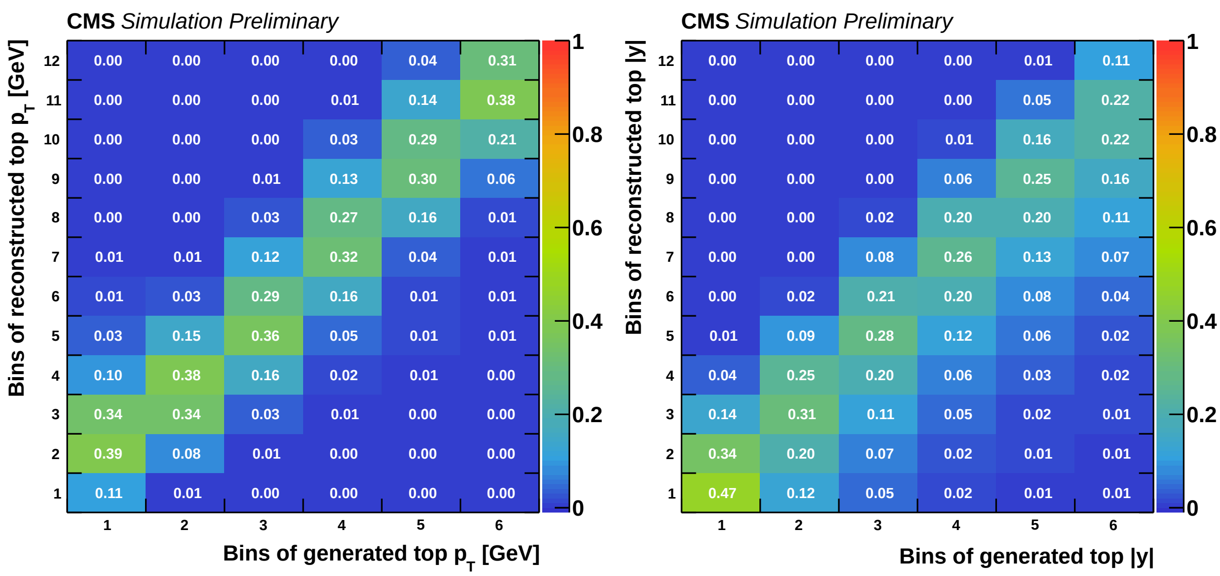

(a) (b)

Figure 6.47: The migration matrix gives the probability of an event with a certain true top-quark p_T to show up in one of the bins of the reconstructed top-quark p_T (a). The migration matrix for the top-quark $|y|$ unfolding (b).

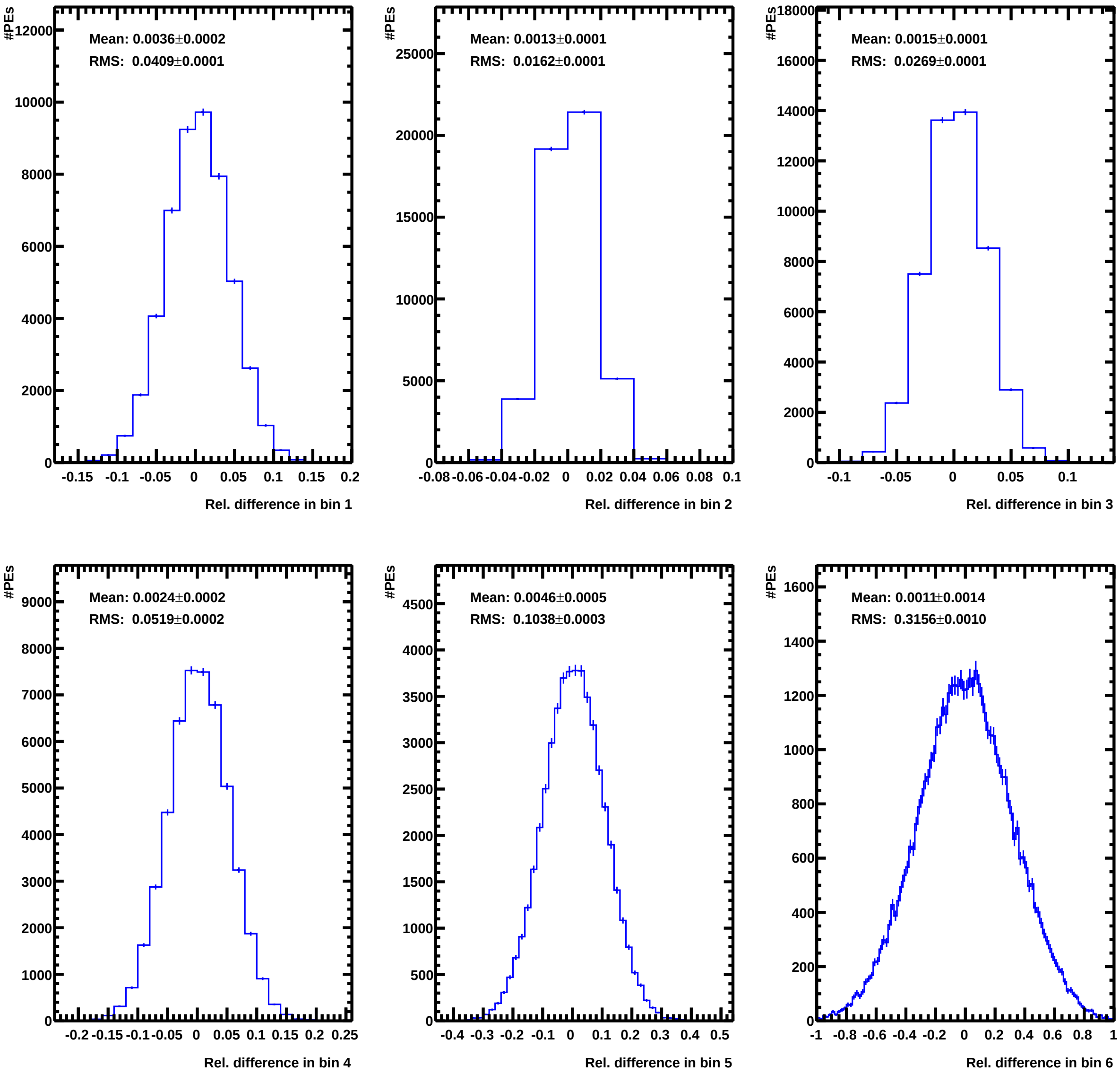

(a)

Figure 6.48: The relative difference between unfolded and true top-quark p_T in the combined lepton+jets channel.

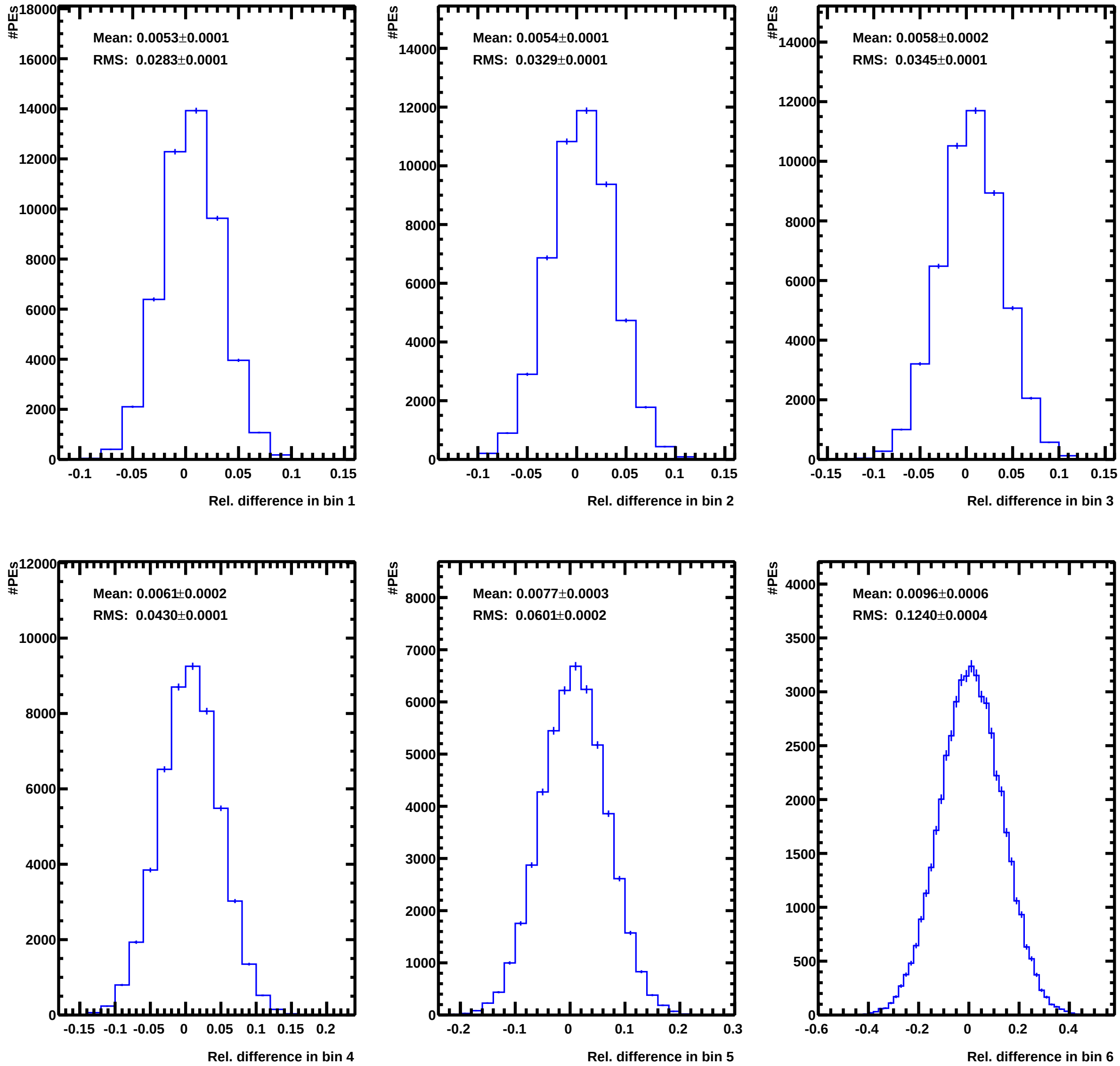

(a)

Figure 6.49: The relative difference between unfolded and true top-quark $|y|$ in the combined lepton+jets channel.

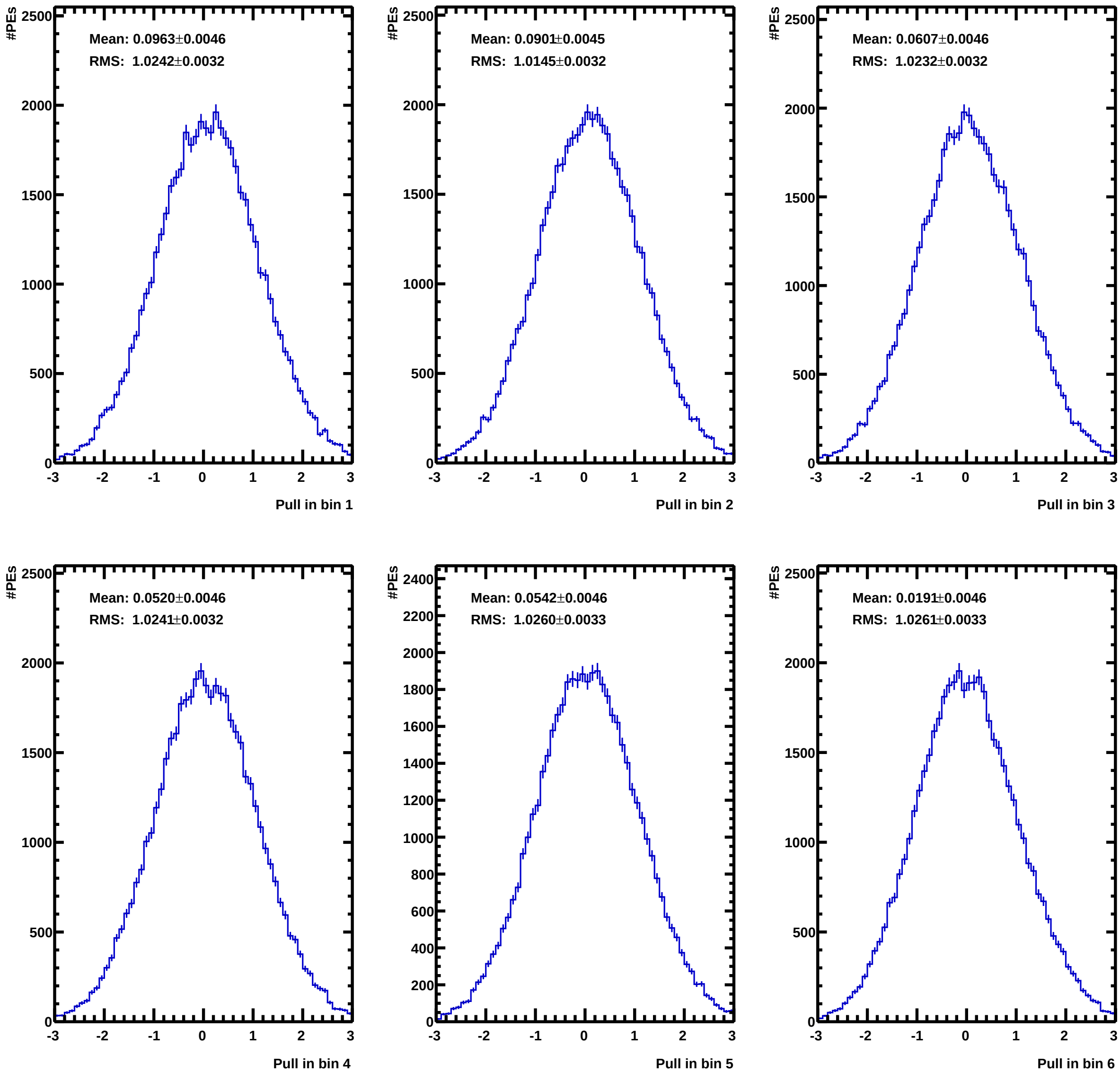

(a)

Figure 6.50: The pull distribution for the unfolded and generated top-quark transverse momentum in 6 different bins in the combined lepton+jets channel.

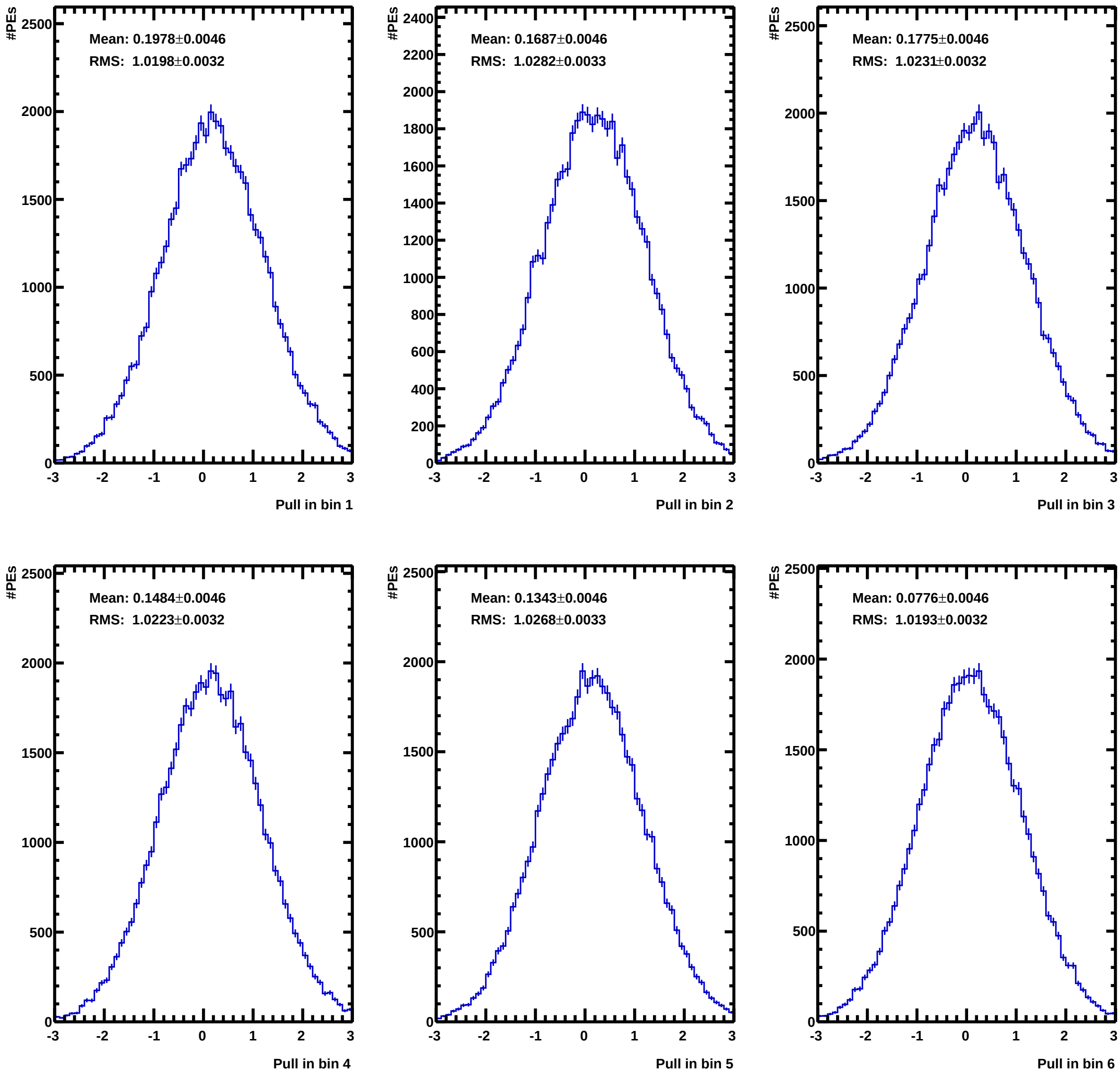

(a)

Figure 6.51: The pull distribution for the unfolded and generated top-quark$|y|$ in 6 different bins in the combined lepton+jets channel.

6.7 Systematics Uncertainties

The resulting spectra of the top-quark p_{T} and top-quark η can be affected by various sources of systematic uncertainties, either due to detector resolution and reconstruction efficiencies or theoretical uncertainties in the modeling of signal and background processes. As the result is a normalized differential cross-section, where the resulting spectrum is divided by the measured inclusive cross-section, some of the systematic variations cancel out. Nevertheless one expects changes in the result due to variations in various parameters. The impact of the individual sources on the spectra is estimated in the following way. The full chain of the analysis is repeated on the measured data, using signal and/or background templates for the background estimation and the unfolding procedure that are affected by the systematic uncertainty under study. The varied background templates are used for the background subtraction, normalized to the new background yields that are estimated using the very same varied templates. The smearing matrix for the unfolding is determined from the varied signal MC templates, in case the source of systematic uncertainty under study affects also the signal process.

The various sources of systematic uncertainty that have been studied are:

- **Jet Energy Scale (JES):** The uncertainty due to JES is estimated from the jet energy corrections (JEC). The effect is propagated to $\not{E}_{\mathrm{T}}$.

- **Jet Energy Resolution (JER):** Jet asymmetry measurements suggest that resolutions in jet p_{T} are about 5% to 29% worse in data compared to simulation, depending on the jet's $|\eta|$ value. For that reason the distribution of reconstructed p_{T} for a fixed generated jet p_{T} is broader by the given percentage. The uncertainty on this measurement is about 6 to 20 percent points, again depending on the jet $|\eta|$. To account for this difference, all jets in the simulated samples are scaled accordingly. The systematic uncertainty on this correction is estimated based on further smearing within the uncertainties of the used correction factors [199].

- **Unclustered Energy in $\not{E}_{\mathrm{T}}$:** The energy contribution from all jets with $p_{\mathrm{T}} < 10\,\mathrm{GeV}$ and PFCandidates not clustered to jets is called "unclustered energy". This energy contribution is varied by $\pm 10\%$ and the resulting uncertainty is propagated to the calculation of the missing transverse energy.

- **Pileup Modelling (PU):** All monte carlo simulation used in this analysis are re-weighted such that the number of simulated pileup events matches the number of pileup events inferred from data. To account for uncertainties in the pileup distribution of data events, the measurement is performed with samples re-weighted to shifted versions of the data pileup distribution, as described at [200]. This corresponds to a $\pm 6\%$ variation in reference to the nominal total inelastic cross-section of 69.4 mb.

- **b-tagging:** In order to estimate the uncertainty related to b-tagging, the applied b-tagging scale factors are varied within their uncertainties [201]. The variations are performed simultaneously for ąnd b–quark jets, and they are combined in a common uncertainty. The scale factors for light-flavor jets are varied independently from the heavy-flavor scale factors and are treated as an independent mis-tag uncertainty.

- **Top-quark p_{T} Re weighting:** Differential cross-sections measurements have shown that the p_{T} spectrum of the top-quarks in $\mathrm{t\bar{t}}$ events is significantly softer than the one generated by simulation programs. To correct for this effect the used events are re weighted according to scale factors derived from these measurements. As a measure of the resulting uncertainty, the measurement is performed with samples lacking any re-weighting and with samples that have been re-weighted twice.

- **top-quark Mass:** Impact of different top-quark mass on the nominal one of 172.5 GeV is estimated by using different samples for t-channel and $t\bar{t}$ with a top-quark mass of ± 1.5 GeV.
- **Electron and Muon Trigger Efficiencies:** The uncertainties on the globally derived scale factors for electron and muon trigger, isolation and ID are added in quadrature to the already applied scale factors.
- Q^2 **scale:** The uncertainties on the renormalization and factorization scales are studied with dedicated samples for $t\bar{t}$, W+jets and t-channel. These samples are generated with twice and half the nominal Q value of the hard scattering process.
- **Matching Threshold:** The impact of a higher and lower matching threshold for MADGRAPH processes is studied with dedicated samples for $t\bar{t}$ and W+jets.
- **Muon Resolution:** The reconstruction of muons has been studied in Z decays. A transverse momentum resolution uncertainty of 0.6% is applied to all muons.
- **QCD Multijet Modeling:** The estimated rate of the QCD mulitjet template is scaled up by a factor of two to account for a potential mis-modeling from the anti-isolated region.
- **Parton Distribution Functions (PDFs):** The impact of different PDF sets (CT10, NNPDF2.1 and MSTW2008) and their uncertainty bands has been taken into account for the signal modeling according to the PDF4LHC recommendation.

A breakdown of the different contributions to the systematic uncertainty in each bin of the unfolded distribution is given in Table 7.3 for top-quark p_{T} and in Table 7.4 for top-quark $|y|$.

Chapter 7

Results and Conclusions

In the following, the results for the inclusive and differential cross-sections of the single-top-quark t-channel production are presented, which are based on the event selection described in Chapter 4. Both the inclusive and differential cross-section measurements use the same amount of data $\mathcal{L}$ = 19.7 fb^{-1}.

7.1 Inclusive Cross-section Measurement

The measured inclusive production cross-section of the t-channel single-top-quark production is:

$$\sigma_{t-\mathrm{ch.}} = 83.6 \pm 2.3\,(\mathrm{stat.}) \pm 7.4\,(\mathrm{syst.})\,\mathrm{pb}. \tag{7.1.1}$$

The measured single t and $\bar{\mathrm{t}}$ production cross-sections in the t-channel is

$$\sigma_{t-\mathrm{ch.}}(\mathrm{t}) = 53.8 \pm 1.5\,(\mathrm{stat.}) \pm 4.4\,(\mathrm{syst.})\,\mathrm{pb}. \tag{7.1.2}$$

$$\sigma_{t-\mathrm{ch.}}(\bar{\mathrm{t}}) = 27.6 \pm 1.3\,(\mathrm{stat.}) \pm 3.7\,(\mathrm{syst.})\,\mathrm{pb}. \tag{7.1.3}$$

The top-quark(t) and the anti-top-quark($\bar{\mathrm{t}}$) are separated on the basis of charge of lepton which is coming from the decay of W-boson which is subsequently coming from the decay of the top-quark. The lepton inherits its charge from the top-quark. Thus, if one can determine the charge of lepton, indirectly it is actually the charge of the top-quark. The inclusive cross-section measurements done are than compared with standard model expectations where the QCD is computed at NLO using a package known as Monte Carlo for FeMtobarn (MCFM) in the 5-flavour scheme (5FS) and at NLO+NNLL (next-to-next-to-leading-logarithmic). Further details can be found at [202,203].

The inclusive measurement is also compared with the previous measurements done at CMS at $\sqrt{s}$ = 7 TeV and the measurements done at the Tevatron at $\sqrt{s}$ = 2 TeV [204–207]. Figure 7.1 shows the NLO t-channel production cross-section plotted as a function of center-of-mass energy for Tevatron and LHC experiments. The measurements are compared with QCD expectations computed at NLO with MCFM in the 5FS and at NLO+NNLL. The error band shown in the plot is the uncertainty arising due to the top mass variations [208,209], and the PDF uncertainties are estimated according to the HEP-DATA recommendations [171]. Similarly the scale uncertainty is estimated by varying the factorization and renormalization scales simultaneously up and down by a factor of two. The theoretical predictions made for the inclusive cross-section of the single-top-quark in a proton-proton collision can also be compared with the p$\bar{\mathrm{p}}$ because the cross-section

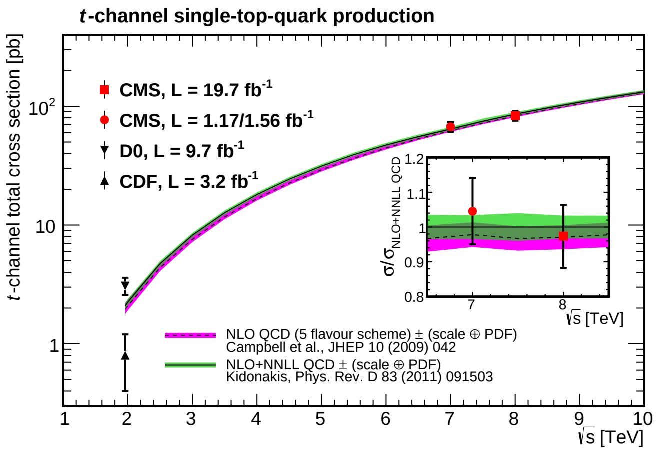

Figure 7.1: The NLO t-channel production cross-section plotted as a function of center-of-mass energy for Tevatron and the LHC experiments.

does not depend on the origin of light quark whether it originates from a proton or from an anti-proton.

7.2 Cross-section Ratio

The ratio of inclusive production cross-section of the single-top-quark t-channel at $\sqrt{s} = 8$ and 7 TeV is extracted from the measurement done in this thesis and to the result reported in [204] for the single-top-quark t-channel cross-section at $\sqrt{s}$ = 7 TeV. The $R_{8/7}$ ratio is obtained from the three measurements, two multivariate analysis Boosted Decision Trees (BDT), Artificial Neural Networks (ANN) and $\eta_{j'}$ analysis, are combined together. The three analysis make use of same selection and methodology so that the final result can be combined together. However the correlation among the various sources of systematics uncertainties considered in the inclusive measurements done at $\sqrt{s}$ = 8 TeV and those taken into account in [204] are determined as follows. The uncertainties which are related to the signal extraction and background estimation from data are considered as fully uncorrelated for the 7 TeV and 8 TeV analysis, while the rest of the uncertainties in 7 and 8 TeV are considered as fully correlated with respect to its 7 TeV $\eta_{j'}$ analysis. Similarly the choices are taken for 8 TeV $\eta_{j'}$ analysis and the two 7 TeV multivariate analysis. The measured cross-section ratio $R_{8/7}$ is

$$R_{8/7} = \sigma_{t-\text{ch.}}(8\,\text{TeV})/\sigma_{t-\text{ch.}}(7\,\text{TeV}) = 1.24 \pm 0.08\,(\text{stat.}) \pm 0.12\,(\text{syst.}). \tag{7.2.1}$$

The measured cross-section for the top-quark(t) and the anti-top-quark($\bar{\text{t}}$) when separated on the basis of their charge at $\sqrt{s}$ = 8 TeV is

$$R_{t-\text{ch.}} = \sigma_{t-\text{ch.}}(\text{t})/\sigma_{t-\text{ch.}}(\bar{\text{t}}) = 1.95 \pm 0.10\,(\text{stat.}) \pm 0.19\,(\text{syst.}). \tag{7.2.2}$$

A comparison of measured production cross-section for the top-quark(t) and the anti-top-quark($\bar{\text{t}}$) with the predictions obtained using different the parton distribution functions (PDF) MSTW2008NLO [210], HERAPDF1.5 NLO [211], ABM11 [212], CT10 and CT10w

Table 7.1: The impact of systematic uncertainties in the combined lepton+jets channel.

Uncertainty source	$\sigma_{\text{t-ch}}$ (%)
Stat. Uncertainty	± 2.7
JES, JER, MET, and Pileup	± 4.3
b-tagging and mis-tag	± 2.5
Lepton reconstruction/trig.	± 0.6
QCD multijet estimation	± 2.3
W+jets, $t\bar{t}$ extraction	± 2.2
Other backgrounds ratio	± 0.3
Signal Modeling	± 5.7
PDF uncertainty	± 1.9
Simulation sample size	± 0.7
Luminosity	± 2.6
Total Systematics	± 8.9
Total Uncertainty	± 9.3
Measured cross-section ± uncertainty	83.6±7.8 pb

Table 7.2: The relative impact of systematic uncertainties on the t and $\bar{t}$ production cross-section and on their ratio.

Uncertainty source	$\sigma_{\text{t-ch}}(\text{t})$ (%)	$\sigma_{\text{t-ch}}(\bar{\text{t}})$ (%)	$R_{\text{t-ch}}$ (%)
Stat. Uncertainty	± 2.7	± 4.9	± 5.1
JES, JER, MET, and Pile-up	± 4.2	± 5.2	± 1.1
b-tagging and mis-tag	± 2.6	± 2.6	± 0.2
Lepton reconstruction/trig.	± 0.5	± 0.5	± 0.3
QCD Multijet estimation	± 1.6	± 3.5	± 1.9
W+jets, $t\bar{t}$ extraction	± 1.7	± 3.6	± 3.0
Other backgrounds ratio	± 0.1	± 0.2	± 0.6
Signal Modeling	± 4.9	± 9.4	± 6.1
PDF uncertainty	± 2.5	± 4.8	± 6.2
Simulation sample size	± 0.6	± 1.1	± 1.2
Luminosity	± 2.6	± 2.6	-
Total systematics	± 8.2	± 13.4	± 9.6
Total uncertainty	± 8.7	± 14.2	± 10.9
Measured cross-section or ratio	53.8±4.7 pb	27.6±3.9 pb	1.95±0.21

[213], and NNPDF [186] is shown in Fig. 7.2. For MSTW2008NLO, NNPDF, ABM, and CT10w the fixed 4-flavour scheme (4FS) PDFs are used together with the PowHEG 4-flavour scheme calculation. The PowHEG calculation in the 5-flavour scheme is used for all other PDFs, as they are derived from a variable flavour scheme. The error bars on the different PDF sets includes the statistical uncertainty, uncertainty due to mass of the top-quark and factorization and renormalization scale. The uncertainty due to mass of the top-quark is derived by varying the top quark mass between 172.0 and 174.0 GeV. The nominal value used for the top-quark mass is 173.0 GeV. The factorization and renormalization scale uncertainty is derived by varying both of them by a factor of 1/2 and 2.

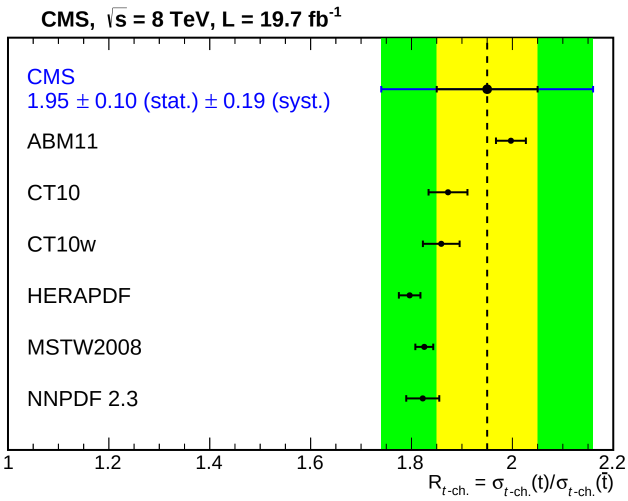

Figure 7.2: The comparison of measured $R_{t-\rm ch.}$ with the predictions obtained using different PDF function. The yellow band shows the statistical uncertainty and the green band shows the systematic uncertainty on the measurement.

7.3 Extraction of $|V_{\rm tb}|$

The three single-top-quark production modes have a unique feature of Wtb vertex and the production cross-section is directly proportional to the $|V_{\rm tb}|$. Thus measuring the production cross-section allows us to measure indirectly the CKM matrix element $|V_{\rm tb}|$. Anomalous form factors can be produced due to the anomalous couplings present at Wtb vertex. These anomalous form factors [214–216] which are parametrised as $f_{\rm Lv}$, where "Lv" stands for the left handed coupling strength. Under the assumption that $|V_{\rm td}|, |V_{\rm ts}| \ll |V_{\rm tb}|$ the top-quark decaying into Wb with a branching ratio $\mathcal{B}$ to be almost equal to 1, we get $|f_{\rm Lv} V_{\rm tb}| = \sqrt{\sigma_{t-\rm ch.}/\sigma^{\rm theo.}_{t-\rm ch.}}$. In the SM case, $f_{\rm Lv} = 1$, the measurement of cross-section puts a direct constraint on $|V_{\rm tb}|$. Inserting the measured and theoretical cross-section values we get:

$$|f_{\rm Lv} V_{\rm tb}| = 0.979 \pm 0.045\,(\text{exp.}) \pm 0.016\,(\text{theo.}) \tag{7.3.1}$$

7.4 Differential Cross-section Measurements

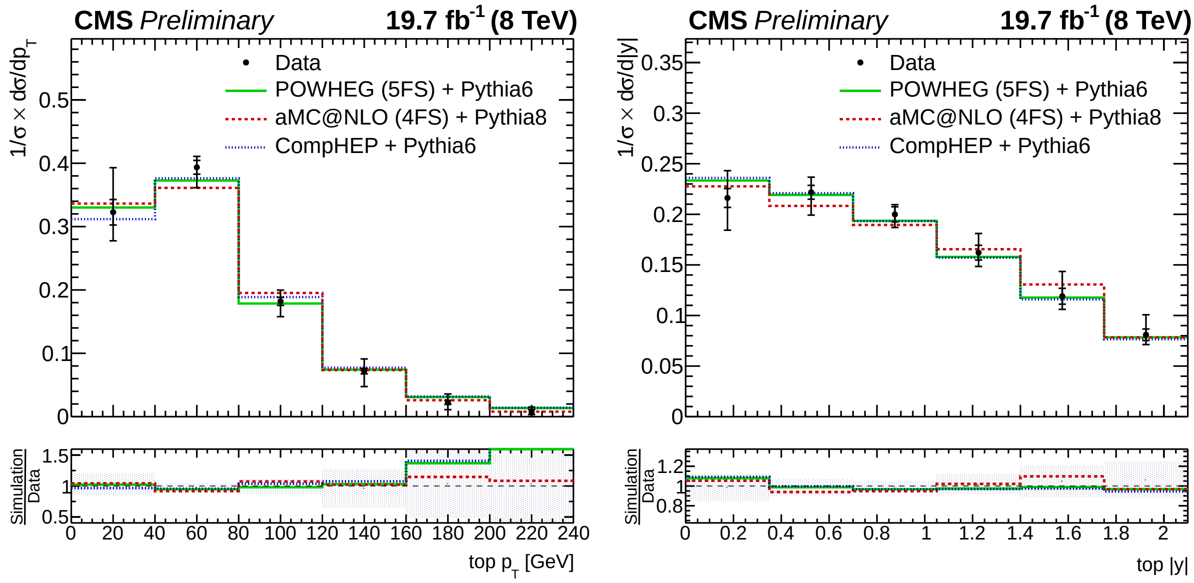

(a) (b)

Figure 7.3: The unfolded top-quark p_T (a) and the top-quark $|y|$ (b) spectra in the combined lepton+jets channel. The distributions are normalized to 1.0 by multiplying with one over the inclusive cross-section corresponding to the fitted event yields. (The uncertainties show statistical and systematic uncertainties.)

The unfolded distributions of the transverse momentum and the absolute value of the rapidity of the top-quark in the combined lepton+jets channel are shown in Fig. 7.3, normalized to the measured inclusive cross-section of the t-channel single-top-quark production, being the integral over all bins. The distributions from data are compared to the distribution generated with different MC generators: two NLO event generators, PowHEG and aMC@NLO, and CompHEP [127, 217]. The main difference between the two NLO generators is the used flavor scheme. aMC@NLO uses the four-flavor scheme while PowHEG uses the five-flavor scheme, i.e. the b quarks in the initial state are included in the proton PDF. The CompHEP sample consists of two separate samples, one with simulated $2 \to 2$ processes and one with simulated $2 \to 3$ processes, matched based on the p_T spectrum of the second b-quark. For all three generators, the hadronization and parton shower is modelled by Pythia. All three simulations describe the unfolded data distribution well within the statistical and systematic uncertainties. The results of the individual channels can be seen in Appendix A and in Appendix B.

Table 7.3: Systematics table for top p_{T}.

Uncertainty / Δ [%]	Bin 1	Bin 2	Bin 3	Bin 4	Bin 5	Bin 6
JES	+12.2 -0.0	+1.0 -2.1	+0.0 -6.2	+0.0 -16.1	+0.0 -26.7	+0.0 -41.0
JER	+3.4 -0.0	+0.1 -1.0	+0.3 -1.6	+0.0 -2.2	+0.0 -11.1	+0.0 -29.6
met	+10.4 -12.1	+1.9 -2.3	+8.9 -8.5	+25.5 -23.4	+42.1 -28.0	+55.4 -31.6
PU	+2.9 -0.0	+0.0 -0.2	+0.0 -1.0	+0.0 -3.0	+0.0 -13.1	+0.0 -21.0
btagcb	+0.7 -1.1	+0.2 -0.1	+1.1 -0.9	+2.4 -1.9	+1.1 -0.6	+1.2 -0.6
btaglight	+0.2 -0.6	+0.3 -0.2	+0.1 -0.0	+0.3 -0.0	+0.9 -0.3	+0.4 -0.0
PT	+1.5 -1.0	+0.3 -1.0	+0.6 -0.3	+3.4 -2.5	+10.6 -10.3	+17.3 -18.5
mass	+2.8 -0.0	+0.7 -0.0	+0.0 -1.4	+0.0 -5.6	+0.0 -12.5	+0.0 -35.8
LEP	+1.0 -0.0	+0.7 -0.0	+0.0 -0.3	+0.0 -2.5	+0.0 -10.2	+0.0 -18.6
scale tchan	+0.0 -1.0	+0.9 -0.0	+0.0 -0.3	+0.4 -0.9	+0.8 -0.0	+13.6 -3.2
scale wjetsbc	+11.1 -0.0	+0.4 -6.7	+0.0 -5.7	+0.0 -7.5	+20.3 -0.0	+6.2 -0.0
scale ttbar	+3.8 -0.9	+1.5 -1.2	+1.5 -0.9	+0.0 -3.4	+0.0 -12.9	+0.0 -19.1
matching wjetsbc	+2.8 -1.5	+1.3 -1.3	+0.0 -3.5	+0.0 -13.1	+29.0 -0.0	+72.0 -0.0
matching ttbar	+1.7 -0.0	+0.3 -0.2	+0.5 -0.4	+0.0 -2.8	+0.0 -9.0	+0.0 -31.1
MuRes	+1.0 -0.0	+0.0 -0.5	+0.2 -0.0	+0.2 -0.0	+0.0 -3.9	+0.0 -9.4
QCD	+0.0 -1.2	+0.8 0.0	+0.0 -0.9	+1.4 0.0	+7.2 0.0	+0.0 -4.1
PDF	+0.1 -0.9	+0.0 -0.1	+0.5 -0.1	+1.8 -0.3	+3.5 -0.6	+3.8 -1.6
Total systematic uncertainty	+20.9 -12.5	+3.4 -7.7	+9.1 -12.8	+26.0 -33.4	+56.6 -49.2	+93.7 -86.1

Table 7.4: Systematics table for top $|y|$.

Uncertainty / Δ [%]	Bin 1	Bin 2	Bin 3	Bin 4	Bin 5	Bin 6
JES	+0.7 -5.1	+2.4 -2.3	+0.6 -0.2	+3.6 -2.2	+5.8 -1.9	+2.6 -0.8
JER	+0.0 -2.9	+1.9 -0.0	+0.8 -0.0	+1.4 -0.9	+1.3 -1.7	+0.0 -2.2
met	+6.1 -9.2	+4.2 -3.2	+1.9 -0.5	+5.1 -5.0	+7.3 -6.8	+7.4 -6.6
PU	+0.0 -1.5	+0.5 -0.0	+0.1 -0.2	+0.5 -0.0	+1.2 -0.0	+1.6 -0.0
btagcb	+0.0 -0.5	+1.0 -0.0	+0.4 -0.0	+0.0 -0.2	+0.0 -0.9	+0.0 -1.1
btaglight	+0.0 -0.7	+1.0 -0.0	+0.4 -0.0	+0.0 -0.4	+0.0 -1.0	+0.0 -1.2
PT	+0.3 -0.2	+0.1 -0.2	+0.0 -0.2	+0.3 -0.2	+0.4 -0.1	+0.0 -0.3
mass	+2.1 -1.1	+1.4 -0.0	+0.6 -0.6	+0.0 -1.6	+0.0 -1.8	+0.0 -1.2
LEP	+0.0 -0.2	+1.1 -0.0	+0.2 -0.0	+0.0 -0.5	+0.0 -1.2	+0.0 -0.9
scale tchan	+2.2 -0.0	+1.5 -0.0	+0.3 -0.0	+0.0 -1.2	+0.0 -3.3	+0.0 -3.3
scale wjetsbc	+9.4 -0.0	+0.0 -2.9	+0.0 -3.5	+0.8 -3.7	+3.7 -1.8	+4.5 -4.6
scale ttbar	+0.4 -1.6	+0.3 -0.4	+0.4 -0.0	+0.9 -0.0	+1.1 -0.6	+1.5 -2.3
matching wjetsbc	+0.0 -7.5	+0.0 -8.2	+1.8 -3.9	+8.3 -0.0	+16.0 -0.0	+20.8 -0.0
matching ttbar	+0.3 -0.1	+0.2 -0.2	+0.5 -0.2	+0.3 -0.0	+0.0 -0.5	+0.0 -1.1
MuRes	+1.1 -0.0	+0.4 -0.0	+0.0 -0.2	+0.0 -0.6	+0.0 -0.9	+0.0 -1.3
QCD	+0.0 -3.6	+0.0 -1.5	+0.1 0.0	+1.6 0.0	+3.7 0.0	+4.8 0.0
PDF	+0.9 -1.7	+0.4 -0.9	+0.2 -0.2	+1.1 -0.6	+2.1 -1.1	+2.1 -1.1
Total systematic uncertainty	+11.7 -14.1	+6.0 -9.7	+3.0 -5.3	+10.8 -7.1	+19.5 -8.7	+23.4 -9.7

Table 7.5: Normalized differential cross-section $\frac{1}{\sigma} \times \frac{d\sigma}{dp_{\mathrm{T}}}$ as function of the transverse momentum p_{T} of the top-quark compared to different theory predictions.

	Normalized differential cross-section: $\frac{1}{\sigma} \times \frac{d\sigma}{dp_{\mathrm{T}}}$	
p_{T}	Unfolded	Generated PowHEG
$[0.0, 40.0]$	$0.323 \pm 0.020\,(\mathrm{stat.})^{+0.067}_{-0.040}\,(\mathrm{syst.})$	0.330
$[40.0, 80.0]$	$0.394 \pm 0.011\,(\mathrm{stat.})^{+0.013}_{-0.030}\,(\mathrm{syst.})$	0.373
$[80.0, 120.0]$	$0.182 \pm 0.006\,(\mathrm{stat.})^{+0.017}_{-0.023}\,(\mathrm{syst.})$	0.179
$[120.0, 160.0]$	$0.072 \pm 0.004\,(\mathrm{stat.})^{+0.019}_{-0.024}\,(\mathrm{syst.})$	0.074
$[160.0, 200.0]$	$0.023 \pm 0.003\,(\mathrm{stat.})^{+0.013}_{-0.011}\,(\mathrm{syst.})$	0.031
$[200.0, 240.0]$	$0.007 \pm 0.004\,(\mathrm{stat.})^{+0.007}_{-0.006}\,(\mathrm{syst.})$	0.014

Table 7.6: Normalized differential cross-section $\frac{1}{\sigma} \times \frac{d\sigma}{d|y|}$ as function of the rapidity of the top-quark compared to different theory predictions.

	Normalized differential cross-section: $\frac{1}{\sigma} \times \frac{d\sigma}{d\|y\|}$	
$\|y\|$	Unfolded	Generated PowHEG
$[0.0, 0.35]$	$0.216 \pm 0.009\,(\mathrm{stat.})^{+0.025}_{-0.030}\,(\mathrm{syst.})$	0.233
$[0.35, 0.7]$	$0.222 \pm 0.007\,(\mathrm{stat.})^{+0.013}_{-0.022}\,(\mathrm{syst.})$	0.219
$[0.7, 1.05]$	$0.200 \pm 0.007\,(\mathrm{stat.})^{+0.006}_{-0.011}\,(\mathrm{syst.})$	0.193
$[1.05, 1.4]$	$0.162 \pm 0.007\,(\mathrm{stat.})^{+0.018}_{-0.012}\,(\mathrm{syst.})$	0.158
$[1.4, 1.75]$	$0.119 \pm 0.008\,(\mathrm{stat.})^{+0.023}_{-0.010}\,(\mathrm{syst.})$	0.118
$[1.75, 2.1]$	$0.081 \pm 0.006\,(\mathrm{stat.})^{+0.019}_{-0.008}\,(\mathrm{syst.})$	0.078

7.5 Summary and Outlook

In this thesis the measurements of the inclusive and differential cross-sections of the electroweak production of the t-channel single-top-quarks at a $\sqrt{s}$ = 8 TeV with a muon or electron in the final state at the CMS detector has been presented. The data set used in this thesis corresponds to a total integrated luminosity of $\mathcal{L}$ = 19.7 fb^{-1}. In the final state, there is one isolated lepton (muon or electron) along with the corresponding neutrino coming from the decay of W-boson, a light quark jet and exactly one b-jet stemming from the decay of the top-quark.

The production cross-section of the single-top-quark t-channel and the ratio of t and $\bar{\mathrm{t}}$ comes out to be in very good agreement with the standard model predictions. The CKM matrix element extracted from the cross-section measurements is than combined with the 7 TeV measurements to get the most precise value of $|V_{\mathrm{tb}}|$. The assumption $|V_{\mathrm{tb}}| < 1$, the 95% confidence level limit is found to be $|V_{\mathrm{tb}}| > 0.92$. The measurements of differential cross-section as a function of p_{T} and $|y|$ of the top-quark come out in very good agreement with various SM predictions.

The single-top-quark t-channel inclusive and differential cross-sections are well understood at 8 TeV. The LHC will start operating in 2015 at a center-of-mass energy of 13 TeV. The single-top-quark t-channel production cross-section at this energy is $\sigma_{t-\mathrm{ch.}}$

$\approx 217.04\,\text{pb}$, which is almost 3 times more than at 8 TeV. As a result there will be lot more statistics which will be available for the higher precision of the cross-section measurement and the study of the various top-quark properties. Next to the inclusive cross-section measurement with higher statistics one can study the fiducial cross-section measurement and CP violation in the single-top-quark t-channel production.

Appendix A

Differential Cross-section Measurements in Muon Channel

The main results of this analysis are the differential cross section measurements in the combined lepton+jets channel. For that purpose the background contributions fitted in the muon and electron channels are subtracted from the combined lepton+jets distributions. These background subtracted distributions are than subjected to the unfolding procedure, where efficiency and migration matrix (the two components of the smearing matrix used in the unfolding) are constructed from the single efficiencies and migration matrices in the two exclusive channels (muon+jets and electron+jets), taking the relative contribution of each channel to the combined lepton+jets channel into account.

However, also the results of the individual channels are of interest and for that reason this Appendix shows the reconstructed distributions, the inputs to the unfolding and the final results, including the estimation of the systematic uncertainties. The unfolding is done as described for the combined lepton+jets channel with the exception that efficiencies and migration matrices are determined exclusively on events of the respective channel.
The Figure A.1 shows the reconstructed top quark p_{T} and top quark $|y|$ distributions in muon+jets channel along with the templates for the signal and background processes normalized to the fit results. For the unfolding procedure in the muon+jets channel, efficiency and migration matrix are determined based solely on simulated muon+jets events. Figure A.2 shows the selection efficiencies as a function of the true top quark p_{T} and top quark $|y|$ in the muon+jets channel, while the migration matrices are presented in figure A.3. These inputs are used to apply the unfolding to the distributions shown in Figure A.1. The resulting differential cross section distributions for the exclusive muon+jets channel are shown in Figure A.4.

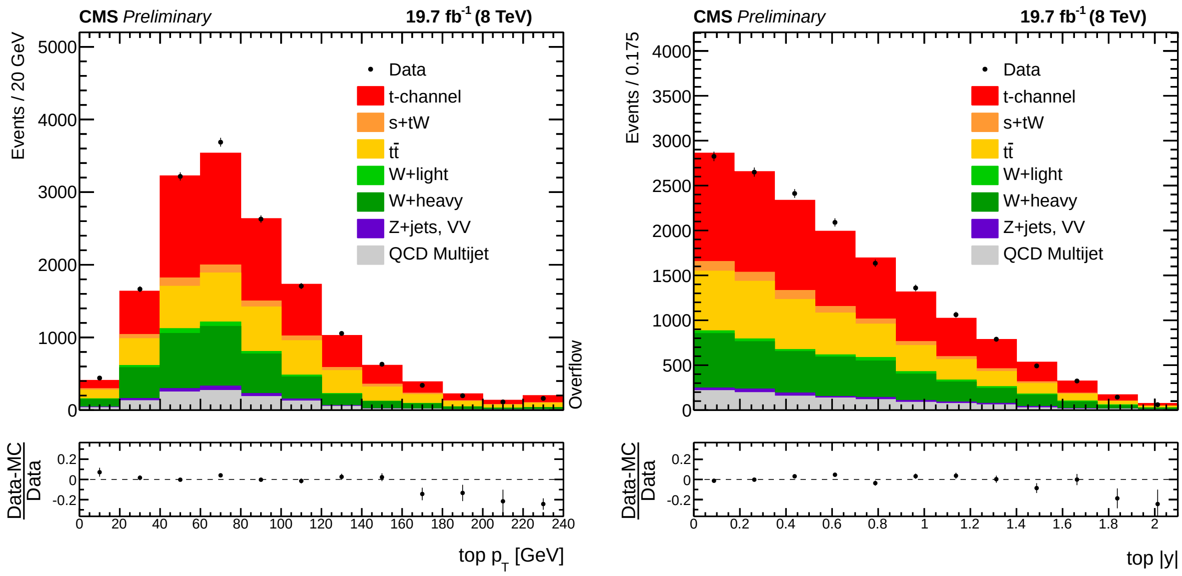

(a) (b)

Figure A.1: Muon channel: The transverse momentum and the pseudorapidity of the top quark after cutting on the NN discriminator in the muon+jets channel. The templates for the different processes are normalized to the fit results.

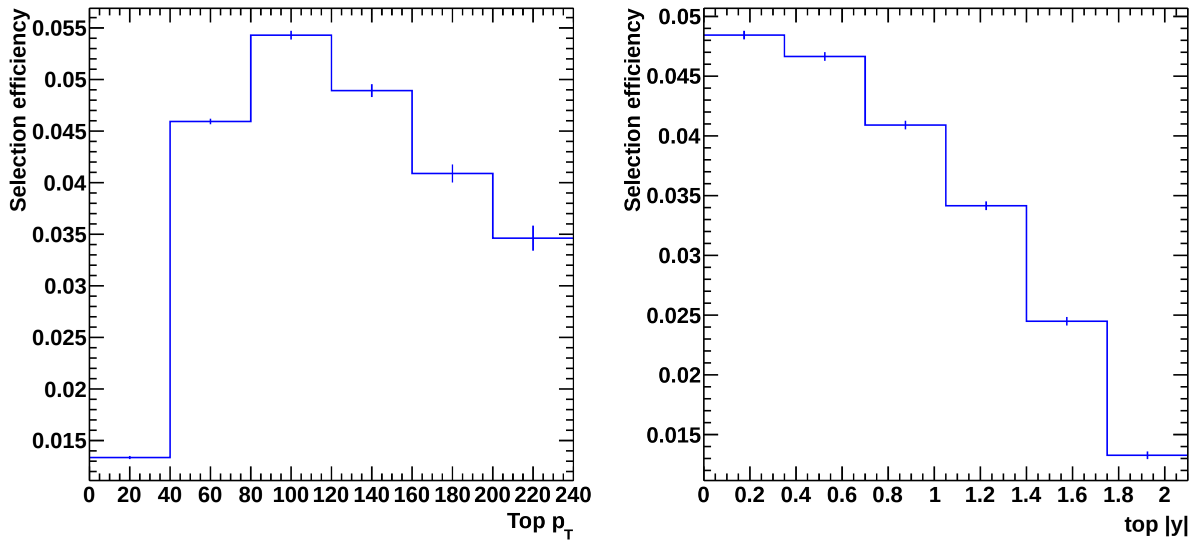

(a) (b)

Figure A.2: Muon channel: The selection efficiency as a function of the true top quark p_T (a) and as function of the true top quark $|y|$ (b) for the muon+jets channel.

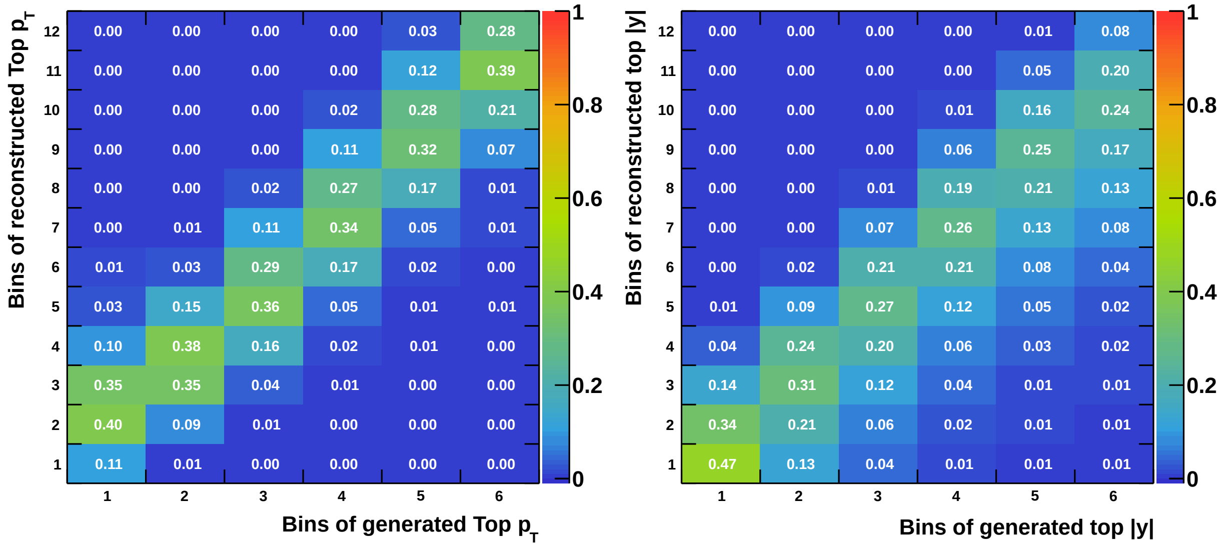

(a) (b)

Figure A.3: Muon channel: The migration matrix gives the probability of an event with a certain true top quark p_T to show up in one of the bins of the reconstructed top quark p_T (a). The migration matrix for the top quark $|y|$ unfolding (b).

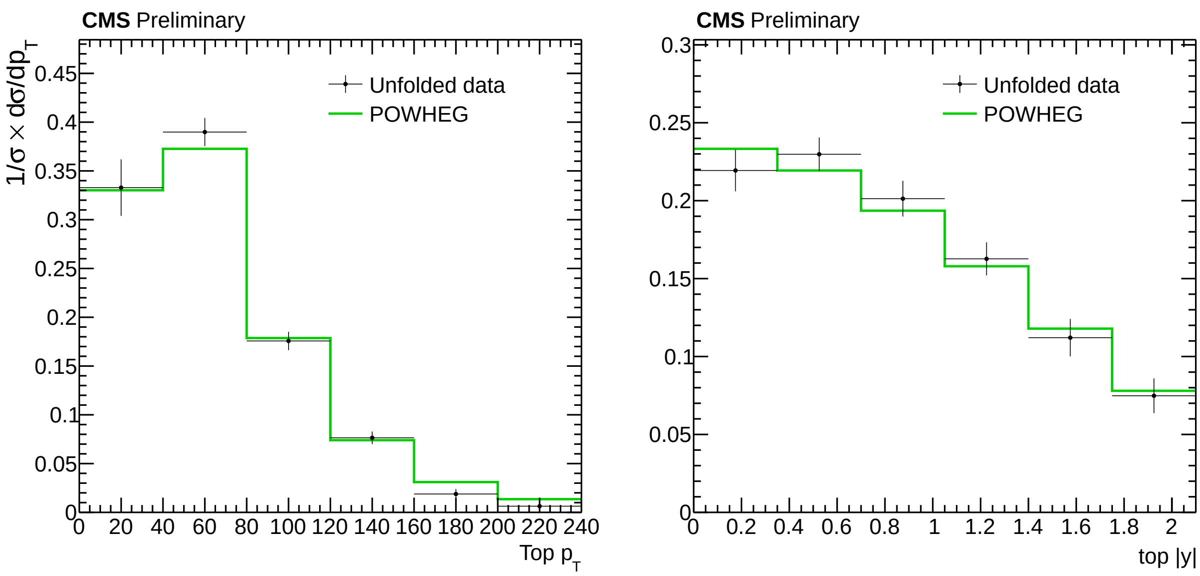

(a) (b)

Figure A.4: Muon channel: Unfolded top quark p_T (a) and top quark $|y|$ (b) spectra in the muon+jets channel. The distributions are normalized to 1.0 by multiplying with one over the inclusive cross section corresponding to the fitted event yields.

Appendix B

Differential Cross-section Measurements in Electron Channel

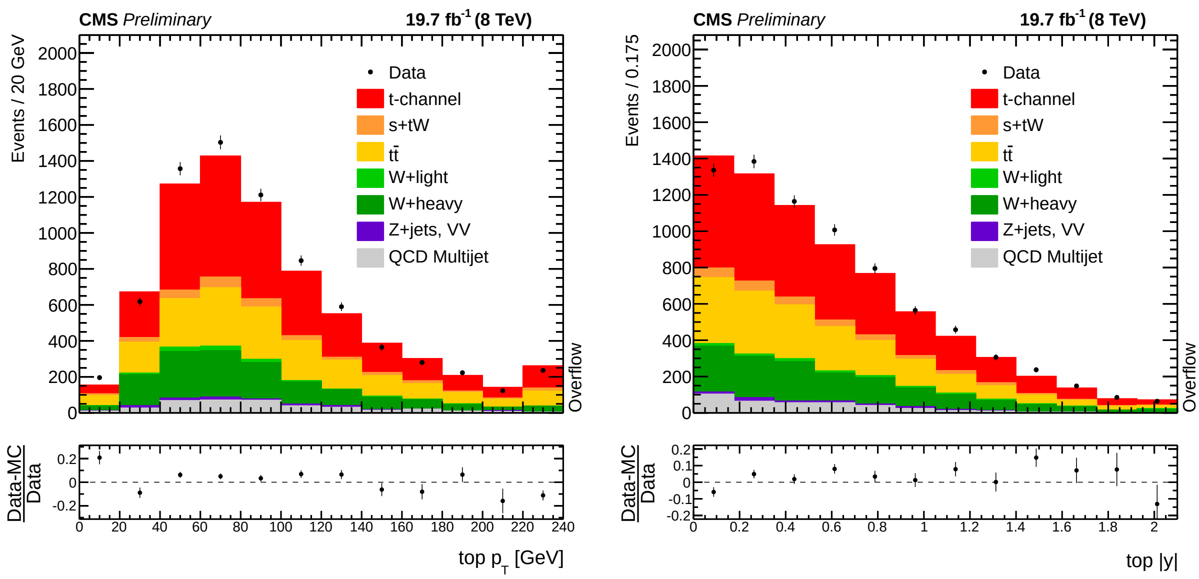

(a) (b)

Figure B.1: Electron channel: The transverse momentum and the rapidity of the top-quark after cutting on the NN discriminator in the electron+jets channel. The templates for the different processes are normalized to the fit results.

The Figure B.1 shows the reconstructed top-quark p_T and top-quark $|y|$ distributions in the electron+jets channel along with the templates for the signal and background processes normalized to the fit results. For the unfolding procedure in the electron+jets channel, efficiency and migration matrix are also determined based solely on simulated electron+jets events. Figure B.2 shows the selection efficiencies as a function of the true top-quark p_T and top-quark $|y|$ in the electron+jets channel, while the migration matrices are presented in Fig. B.3.
The resulting differential cross section distributions for the exclusive electron+jets channel are shown in Figure B.4.

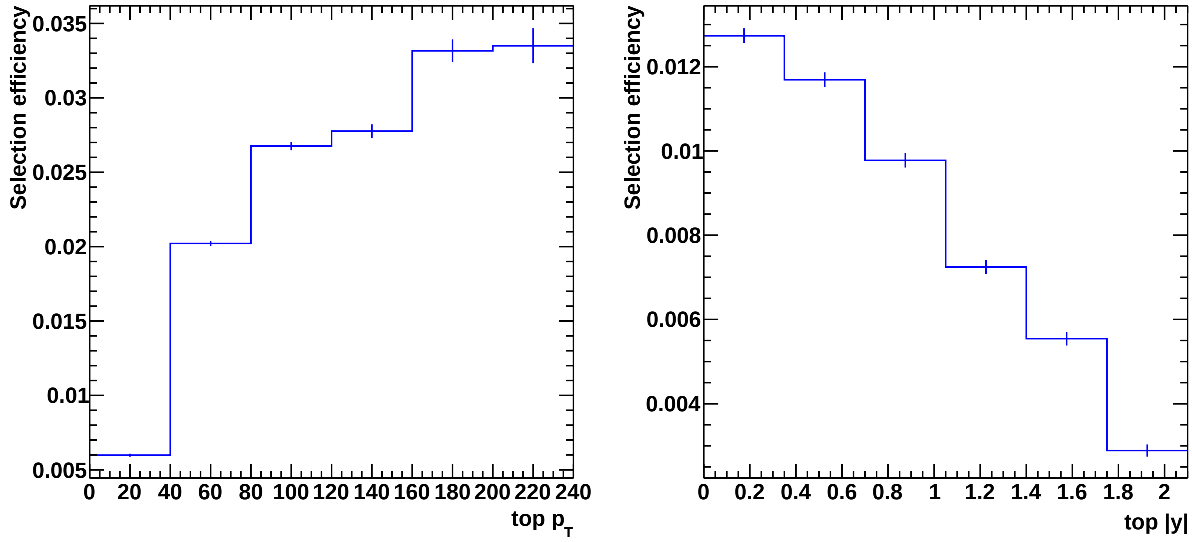

(a) (b)

Figure B.2: Electron channel: The selection efficiency as a function of the true top-quark p_T (a) and as function of the true top-quark $|y|$ (b) for the electron+jets channel.

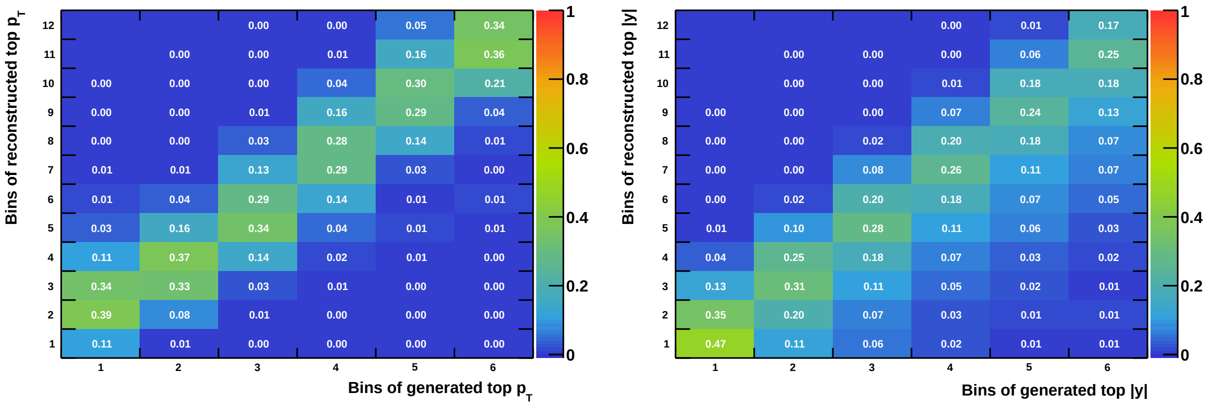

(a) (b)

Figure B.3: Electron channel: The migration matrix gives the probability of an event with a certain true top-quark p_T to show up in one of the bins of the reconstructed top-quark p_T (a). The migration matrix for the top-quark $|y|$ unfolding (b).

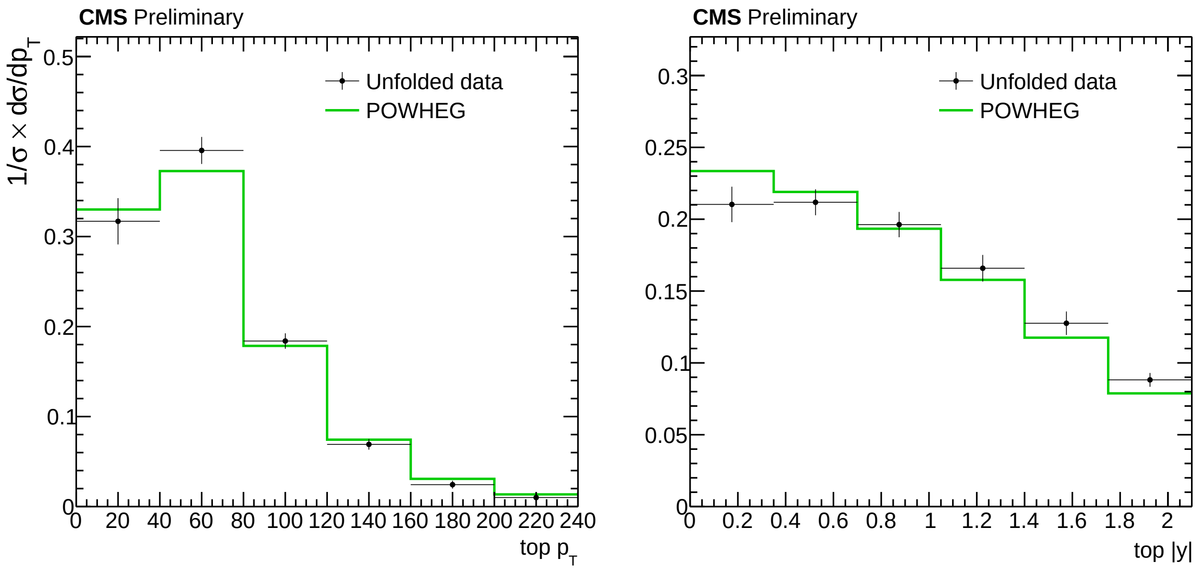

(a) (b)

Figure B.4: Electron channel: Unfolded top-quark p_T (a) and top-quark $|y|$ (b) spectra in the electron+jets channel. The distributions are normalized to 1.0 by multiplying with one over the inclusive cross section corresponding to the fitted event yields.

Bibliography

[1] F. Abe et al. Observation of Top-quark Production in $p\overline{p}$ Collisions with the Collider Detector at Fermilab. *Phys. Rev. Lett.*, 1995.

[2] M. Kobayashi and T. Maskawa. CP Violation in the Renormalizable Theory of Weak Interaction. *Prog. Theor. Phys.*, 49:652:657, 1973. doi: 10.1143/PTP.49.652.

[3] Nicola Cabibbo. Unitary Symmetry and Leptonic Decays. *Phys. Rev. Lett.*, 10:531–533, Jun 1963.

[4] T. Aaltonen et al. First Observation of Electroweak Single-top-quark Production. *Phys. Rev. Lett.*, 103:092002, 2009.

[5] G. Aad et al. Measurement of the Top-quark-pair Production Cross-section with ATLAS in pp Collisions at $\sqrt{s} = 7\,\mathrm{TeV}$. *Eur. Phys. J.*, C71:1577, 2011.

[6] V. Khachatryan et al. First Measurement of the Cross-section for Top-quark Pair Production in pp Collisions at $\sqrt{s} = 7\,\mathrm{TeV}$. *Phys. Lett.*, B695: 424:443, 2011.

[7] R. Schwienhorst. Single-top-quark Production with the ATLAS Detector in pp Collisions at $\sqrt{s} = 7\,\mathrm{TeV}$. 2011.

[8] S. Chatrchyan et al. Measurement of the *t*–channel Single-top-quark Production Cross-section in pp Collisions at $\sqrt{s} = 7\,\mathrm{TeV}$. *Phys. Rev. Lett.*, 107:091802, 2011.

[9] Vardan Khachatryan et al. Measurement of the *t*–channel Single-top-quark Production Cross-section and of the $|V_{\mathrm{tb}}|$ CKM Matrix Element in pp Collisions at $\sqrt{s} = 8\,\mathrm{TeV}$. *JHEP*, 1406:090, 2014.

[10] Single-top *t*-channel differential Cross-section at $\sqrt{s} = 8\,\mathrm{TeV}$. Technical Report CMS-PAS-TOP-14-004, CERN, Geneva, 2014.

[11] Tevatron Electroweak Working Group. Combination of CDF and DØ Results on the Mass of the Top-quark. FERMILAB-TM-2466-E, 2010.

[12] M. Gell-Mann. A Schematic Model of Baryons and Mesons. *Phys. Rev. Lett.*, 8, 214-215, 1964.

[13] S. Weinberg. A Model of Leptons. *Phys. Rev. Lett.*, 19, 1264-1266, 1967.

[14] A. Salam and C. J. Ward. Electromagnetic and Weak Interactions. *Phys. Rev. Lett.*, 13, 168 - 171, 1964.

[15] S. L. Glashow. Partial Symmetries of Weak Interactions. *Nucl. Phys.*, 22, 579-588, 1961.

[16] J. Iliopoulos S. L. Glashow and L. Maiani. Weak Interactions with Lepton-Hadron Symmetry. *Phys. Rev.*, D2, 1285-1292, 1970.

[17] H. Georgi and S. L. Glashow. Unified Weak and Electromagnetic Interactions without Neutal Currents. *Phys. Rev. Lett.*, 28, 1494-1497, 1972.

[18] G. ť Hooft and M. J. G. Veltman. Regularization and Renormalization of Guage Fields. *Nucl. Phys.*, B4, 189-213, 1972.

[19] G. ť Hooft. Renormalizable Lagrangian For Massive Yang-Mills Fields. *Nucl. Phys.*, B35, 167-188, 1971).

[20] G. ť Hooft and M. J. G. Veltman. Combinatorics Of Guage Fields. *Nucl. Phys.*, B50, 318-353, 1972.

[21] D. J. Gross and F. Wilczek. Asymptotically Free Guage Theories. *Phys. Rev.*, D8, 3633-3652, 1973.

[22] H. D. Politzer. Reliable Perturbative Results for Strong Interactions. *Phys. Rev. Lett.*, 30, 1343-1346, 1973.

[23] R. P. Feynman. Theory of Positrons. *Phys. Rev.*, 76, 749-759, 1949.

[24] R. P. Feynman. Space-Time Approach to Quantum Electrodynamics. *Phys. Rev.*, 76, 769-789, 1949.

[25] R. P. Feynman. Mathematical Formulation of the Quantum Theory of Electromagnetic Interaction. *Phys. Rev.*, 80, 440-457, 1950.

[26] J. S. Schwinger. Quantum Electrodynamics-I: A Covariant Formulation. *Phys. Rev.*, 74, 1439, 1948.

[27] J. S. Schwinger. Quantum Electrodynamics-II: Vaccum Polarization and Self Energy. *Phys. Rev.*, 75, 651, 1948.

[28] J. S. Schwinger. Quantum Electrodynamics-III: The Electromagnetic Properties of the Electron: Radiative Corrections to Scattering. *Phys. Rev.*, 76, 790-817, 1949.

[29] J. W. F. Valle. Neutrino Physics Overview. *J. Phys. Conf. Ser.*, 3, 473-505, 2006.

[30] Y. Fukuda et al. Evidance for Oscillation of Atmospheric Neutrinos. *Phys. Rev. Lett.*, 87, 071301, 2001.

[31] Q. R. Ahmad et al. Direct Evidance for Neutrino Flavor Transformation from Neutral Current Interaction in the Sudbury Neutrino Obervatory. *Phys. Rev. Lett.*, 87, 011301, 2002.

[32] S. Khalil and E. Torrente-Lujan. Neutrino Mass and Oscillation as Probes of Physics beyond the Standard Model. *J. Egyptian Math. Soc.*, 9, 91-141, 2001.

[33] P. Ramond. Neutrinos: A Glimpse Beyound the Standard Model. *Nucl. Phys. Proc. Suppl.*, 77, 3-9, 1999.

[34] O. W. Greenberg. Spin and Unitary Spin Independence in a Paraquark Model of Bayrons and Mesons. *Phys. Rev. Lett.*, 13, 598-602, 1964.

[35] M. Y. Han and Y. Nambu. Three-Triplet Model with Double SU(3) Symmetry. *Phys. Rev. Lett.*, 139, B1006-B1010, 1965.

[36] M. Gell-Mann H. Fritzsch and H. Leutwyler. Advantages of the Colour Octet Gluon Picture. *Phys. Rev. Lett.*, B47, 365-368, 1973.

[37] C. Amsler et. al. Review of Particle Physics. *Phys. Rev. Lett.*, B667, 1 (2008).

[38] K. Nakamura et al. Review of Particle Physics. *J. Phys.*, G37:075021, 2010.

[39] J. R. Musser et al. Measurement of the Michel Parameter ρ in Muon Decay. *Phys. Rev. Lett.*, 94:101805, 2005.

[40] A. Salam J. Goldsone and W. Weinberg. Broken Saymmetries. *Prog. Rev.*, 127, 965 - 970 (1962).

[41] S. Peris R. D. Peccei and X. Zhang. Non Standard Couplings of the Top-quark and Precision Measurements of the Electroweak Teory. *Nucl. Phys.*, B349, 305 - 322, 1991.

[42] H. J. Behrend et al. CELLO Collaboration. Search for New Heavy Quarks in e^+e^-Collisions up to 46.78 GeV Center-of-mass Energy. *Phys. Lett.*, B144,297, 1984.

[43] W. Bartel et al. JADE Collaboration. Total Cross-section for Hadron Production by e^+e^-Annihilation at Petra Energies. *Phys. Lett.*, B88, 171, 1979.

[44] W. Bartel et al. JADE Collaboration. Search for New Flavor Production at PETRA. *Phys. Lett.*, B89, 136, 1979.

[45] W. Bartel et al. JADE Collaboration. Experimental Limits on the Strength of Weak Neutral Currents in Lepton Pair Production at PETRA Energies. *Phys. Lett.*, B99, 281, 1981.

[46] D. P. Barber et al. The MARK-J Collaboration. Study of Electron-Positron Collisions at the Highest Petra Energy. *Phys. Lett.*, B85, 463, 1979.

[47] D. P. Barber et al. The MARK-J Collaboration. Search for the Production of a New Quark Flavor at c.m. system Energies between 33 and 35.8 GeV. *Phys. Rev. Lett.*, 44, 1722, 1980.

[48] B. Adeva et al. The MARK-J Collaboration. Search for Top-quark and a Test of Models without Top-quark up to 38.54 GeV at PETRA. *Phys. Rev. Lett.*, 50, 799, 1983.

[49] B. Adeva et al. The MARK-J Collaboration. Experimental Study of Inclusive Muon Spectra at PETRA from Electron-Positron collisions in the Energy Region $33 < \sqrt{s} < 38.54$ GeV. *Phys. Rev. Lett.*, 51, 443, 1983.

[50] B. Adeva et al. The MARK-J Collaboration. New Particles Searches. *Phys. Lett.*, B152, 439, 1985.

[51] B. Adeva et al. The MARK-J Collaboration. Study of Hadron and Inclusive Muon Spectra from Electron-Positron Annihilation at $39.79 < \sqrt{s} < 46.78$ GeV. *Phys. Rev. Lett.*, D34, 681, 1986.

[52] C. Berger et al. The PLUTO Collaboration. Search for a 'Top' Threshold in Hadronic e^+e^-Annihilation at Energies Between 22 GeV and 31.6 GeV. *Phys. Lett.*, B86, 413, 1979.

[53] R. Brandelik et al. The TASSO Collaboration. A Measurement of Sigma(tot) $e^+e^- \rightarrow$ Hadrons for CM Energies Between 12.0 GeV and 36.7 GeV. *Phys. Lett.*, B113, 499, 1982.

[54] M. Althoff et al. The TASSO Collaboration. Jet Production and Fragmentation in e^+e^-Annihilation at 12 GeV to 43 GeV. *Z. Phys.*, C22, 307, 1984.

[55] M. Althoff et al. The TASSO Collaboration. Measurement of r and Search for the Top-quark in e^+e^-Annihilation Between 39.8 GeV and 45.2 GeV. *Phys. Lett.*, B138, 441, 1984.

[56] H. Sagawa et al. The AMY Collaboration. Measurements of R and a Search for Heavy Quark Production in e^+e^-Annihilation at $\sqrt{s}$ = 50 GeV and 52 GeV. *Phys. Rev. Lett.*, 60, 93, 1988.

[57] S. Igarashi et al. The AMY Collaboration. Search for Isolated leptons in Low Thrust e^+e^-Annihilation Events at $\sqrt{s}$ = 50 GeV and 52 GeV. *Phys. Rev. Lett.*, 60, 2359, 1988.

[58] I. Adachi et al. The TOPAZ Collaboration. Search for Top-quark in e^+e^-Collisions at $\sqrt{s}$ = 52 GeV. *Phys. Rev. Lett.*, 60, 97, 1988.

[59] H. Yoshida et al. Measurement of R and Search for New Heavy Quarks in e^+e^-Annihilation at 50 GeV and 52 GeV Center-of-mass Energies. *Phys. Lett.*, B198:570, 1987.

[60] K. Abe et al. Measurement of R and Search for New Quark Flavors Decaying into Multi-Jet Final States in e^+e^-Collisions between 54 GeV and 61.4 GeV Center-of-mass Energies. *Phys. Lett.*, B234:382, 1990.

[61] G. S. Abrams et al. Searches for New Quarks and Leptons Produced in Z-boson Decay. *Phys. Rev. Lett.*, 63:2447, 1989.

[62] D. Decamp et al. A Search for New Quarks and Leptons From Z^0 Decay. *Phys. Lett.*, B236:511, 1990.

[63] P. Abreu et al. Search for the Top and b' Quarks in Hadronic Decays of the Z^0 boson. *Phys. Lett.*, B242:536, 1990.

[64] M. Z. Akrawy et al. A Search for the Top and b' Quarks in Hadronic Z^0 Decays. *Phys. Lett.*, B236:364, 1990.

[65] C. Albajar et al. Search for New Heavy Quarks at the CERN Proton Anti-Proton Collider. *Z. Phys.*, C37:505–525, 1988.

[66] C. Albajar et al. Search For New Heavy Quarks in $p\overline{p}$ Collisions at $\sqrt{s}$ = 0.63 TeV. *Z. Phys.*, C48:1–12, 1990.

[67] T. Akesson et al. Search for Top-quark Production at the CERN $p\overline{p}$ Collider. *Z. Phys.*, C46:179, 1990.

[68] F. Abe et al. Search for the Top-quark in the Reaction $p\overline{p}$ to Electron+jets at $\sqrt{s}$ = 1.8 TeV. *Phys. Rev. Lett.*, 64:142–146, 1990.

[69] F. Abe et al. Search For New Heavy Quarks in Electron-Muon Events at the Fermilab Tevatron Collider. *Phys. Rev. Lett.*, 64:147–151, Jan 1990.

[70] F. Abe et al. Top-quark Search in the Electron + jet Channel in $p\overline{p}$ collisions at $\sqrt{s}$ = 1.8 TeV. *Phys. Rev.*, D43:664–686, 1991.

[71] F. Abe et al. A Lower Limit on the Top-quark Mass From Events with Two Leptons in $p\overline{p}$ Collisions at $\sqrt{s}$ = 1.8 TeV. *Phys. Rev. Lett.*, 68:447–451, 1992.

[72] F. Abe et al. A Limit on the Top-quark Mass From $p\overline{p}$ collisions at $\sqrt{s}$ = 1.8 TeV. *Phys. Rev.*, D45:3921–3948, 1992.

[73] S. Abachi et al. Top-quark Search with the DØ 1992–1993 Data Sample. *Phys. Rev. D*, 52:4877–4919, Nov 1995. `http://link.aps.org/doi/10.1103/PhysRevD.52.4877`.

[74] S. Abachi et al. Search for the Top-quark in $p\overline{p}$ Collisions at $\sqrt{s} = 1.8$ TeV. *Phys. Rev. Lett.*, 72:2138–2142, Apr 1994. `http://link.aps.org/doi/10.1103/PhysRevLett.72.2138`.

[75] S. Abachi et al. Observation of the Top-quark. *Phys. Rev. Lett.*, 74:2632–2637, 1995.

[76] W. Bernreuther. Top-quark physics at the LHC. *J. Phys.*, G35, 083001, 2008.

[77] S. Mochad P. Uwer. Top-quark Production and QCD. *Eur. Phys. J. C.*, 2011.

[78] S. Weinzierl. Theoratical overview on Top pair production and single-top production. *HCP2011, Paris*, 2011.

[79] John C. Collins, Davison E. Soper, and Sterman George F. Heavy Particle Production in High-Energy Hadron Collisions. *Nucl. Phys.*, B263:37, 1986.

[80] B. R. Webber R. K. Ellis, W. J. Stirling. QCD and Collider Physics, Cambridge Monographs on Particle Physics, Nuclear Physics and Cosmology, (Cambridge Univ. Press, Cambridge). 1996.

[81] A. D. Martin, W. J. Stirling, R. S. Thorne, and G. Watt. Parton Distributions for the LHC. *Eur. Phys. J.*, C63:189–285, 2009.

[82] M. Cacciari, S. Frixione, M. L. Mangano, P. Nason, and G. Ridolfi. The $t\bar{t}$ Cross-section at 1.8 TeV and 1.96 TeV: A Study of the Systematics Due to Parton Densities and Scale Dependence. *JHEP*, 0404:068, 2004.

[83] Nikolaos Kidonakis and Ramona Vogt. Next-to-next-to-Leading Order Soft Gluon Corrections in Top-quark Hadroproduction. *Phys. Rev.*, D68:114014, 2003.

[84] Roberto Bonciani, Stefano Catani, Michelangelo L. Mangano, and Paolo Nason. NLL Resummation of the Heavy Quark Hadroproduction Cross-section. *Nucl. Phys.*, B529:424–450, 1998.

[85] Nikolaos Kidonakis. Differential and Total Cross-sections for Top Pair and Single-top Production. pages 831–834, 2012.

[86] S. Willenbrock and D. Dicus. Production of Heavy from W-gluon Fusion. *Phys. Rev.*, D34:155, 1986.

[87] C. P. Yuan. A New Method to Hetect Heavy Top-quark at the Tevatron. *Phys. Rev.*, D41:42, 1990.

[88] R. K. Ellis and S. J. Parke. Top-quark by W-gluon Fusion. *Phys. Rev.*, D46:3785–3788, 1992.

[89] A. S. Belyaev A. P. Heinson and E. E. Boss. Single-top-quark at the Fermilab Tevatron. *Phys. Rev.*, D56:3114–3128, 1997. `http://arxiv.org/abs/hep-ph/9612424`.

[90] Z. Sullivan T. Stelzer and S. Willenbrock. Single-top-quark Production via W-gluon Fusion at Next to Leading Order. *Phys. Rev.*, D56:5919–5927, 1997.

[91] Z. Sullivan T. Stelzer and S. Willenbrock. Single-top-quark Production at Hadron Collider. *Phys. Rev.*, D58:094021, 1998.

[92] Z. Sullivan et al B. W. Harris. Fully Differential Single-top-quark Cross-section in Next to Leading Order QCD. *Phys. Rev.*, D66:054024, 2002.

[93] John Campbell, R. K. Ellis, and Francesco Tramontano. Single-top Production and Decay at Next-to-Leading Order. *Phys. Rev.*, D70:094012, 2004.

[94] M. Jezabek and Johann H. Kuhn. QCD Corrections to Semileptonic Decays of Heavy Quarks. *Nucl. Phys.*, B314:1, 1989.

[95] The Measurement of Single-top Polarization with 3.2 fb^{-1}. Technical Report Conference Note CDF/PUB/TOP/PUBLIC/9920, FNAL, 2009.

[96] Measurement of Top-quark Polarization in t-channel Single-top Production. Technical Report CMS-PAS-TOP-13-001, CERN, Geneva, 2013.

[97] The Large Hadron Collider Project. `http://lhc.web.cern.ch/lhc`.

[98] The Compact Muon Solenoid Experiment. `http://cms.cern.ch`.

[99] The ATLAS Experiment. `http://atlas.web.cern.ch/Atlas/index.html`.

[100] The LHC-b Experiment. `http://lhcb.web.cern.ch/lhcb`.

[101] The ALICE Experiment. `http://aliceinfo.cern.ch`.

[102] Lefevre. C. LHC: The Guide (English version). Guide du LHC (Version Anglaise). Feb 2009.

[103] Michel Della Negra et al. CMS Physics Technical Design Report. *CERN/LHCC 2006-001*, CMS TDR 8.1, 2006.

[104] Chatrchyan. S. and others. The CMS experiment at the CERN LHC. *JINST*, 3:S08004, 2008.

[105] Karimaki. V. The CMS Tracker System Project Technical Design Report. CERN/LHCC-98-6. CMS-TDR-005, 1997.

[106] The CMS Collaboration and S Chatrchyan et al. The CMS experiment at the CERN LHC. *Journal of Instrumentation*, 3(08):S08004, 2008. `http://stacks.iop.org/1748-0221/3/i=08/a=S08004`.

[107] The CMS Collaboration. Missing Transverse Energy Performance of the CMS Detector. *Journal of Instrumentation*, 6(09):P09001, 2011.

[108] G.L. Bayatian et al. CMS physics: Technical design report. CERN-LHCC-2006-001, 2006.

[109] The CMS Collaboration. The CMS Muon Project: Technical Design Report. CERN/LHCC-97-32, CMS-TDR-003, 1997.

[110] The CMS Collaboration. The Trigger and Data Acquisition Project, Volume 1, The High Level Trigger: Technical Design Report. CERN/LHCC 2000-038, CMS-TDR-6.1, 2000.

[111] The CMS Collaboration. The Trigger and Data Acquisition Project, Volume 1, The L-1 Trigger: Technical Design Report. CERN/LHCC 2002-26, CMS-TDR-6.2, 2002.

[112] R. Adolphi et al. The CMS experiment at the CERN LHC. *JINST*, 3(S08004), 2008.

[113] WLCG Collaboration. LHC Computing Grid: Technical Design Report. *CERN-LHCC-2002-024*, LCG-TDR-CERN, 2005.

[114] V. N. Gribov and L. N. Lipatov. Deep Inelastic ep Scattering in Perturbation Theory. *Sov. J. Nucl. Phys.*, 15:438–450, 1972.

[115] Guido Altarelli and G. Parisi. Asymptotic Freedom in Parton Language. *Nucl. Phys.*, B126:298, 1977.

[116] Yuri L. Dokshitzer. Calculation of the Structure Functions for Deep Inelastic Scattering and e^+e^-Annihilation by Perturbation Theory in Quantum Chromodynamics. *Sov. Phys. JETP*, 46:641–653, 1977.

[117] Flip Tanedo. When Feynman Diagrams Fail. , 2010. `http://www.quantumdiaries.org/2010/12/11/when-feynman-diagrams-fail`.

[118] M. A. Dobbs, S. Frixione, Eric Laenen, K. Tollefson, H. Baer, et al. Les Houches Guidebook to Monte Carlo generators for Hadron Collider Physics. pages 411–459, 2004.

[119] Alioli, Simone and Nason, Paolo and Oleari, Carlo and Re, Emanuele. A General Framework for Implementing NLO Calculations in Shower Monte Carlo Programs: The Powheg Box. *JHEP*, 1006:043, 2010.

[120] Frixione, Stefano and Nason, Paolo and Oleari, Carlo. Matching NLO QCD Computations with Parton Shower Simulations: The Powheg Method. *JHEP*, 0711:070, 2007.

[121] Paolo Nason. A New Method for Combining NLO QCD with Shower Monte Carlo Algorithms. *JHEP*, 0411:040, 2004.

[122] T. Stelzer and W. F. Long. Automatic Generation of Tree Level Helicity Amplitudes. *Nucl. Phys. Proc. Suppl.*, 37B:158–162, 1994.

[123] Fabio Maltoni and Tim Stelzer. MadEvent: Automatic Event Generation with MadGraph. *JHEP*, 0302:027, 2003.

[124] Torbjorn Sjostrand, Stephen Mrenna, and Peter Z. Skands. A Brief Introduction to PYTHIA 8.1. *Comput. Phys. Commun.*, 178:852–867, 2008.

[125] Andy Buckley, Jonathan Butterworth, Stefan Gieseke, David Grellscheid, Stefan Hoche, et al. General Purpose Event Generators for LHC Physics. *Phys. Rept.*, 504:145–233, 2011.

[126] Johan Alwall, A. Ballestrero, P. Bartalini, S. Belov, E. Boos, et al. A Standard format for Les Houches event files. *Comput. Phys. Commun.*, 176:300–304, 2007.

[127] E. Boos et al. CompHEP 4.4: Automatic Computations from Lagrangians to Events. *Nucl. Instrum. Meth.*, A534:250–259, 2004.

[128] S. Agostinelli et al. GEANT4: A Simulation Toolkit. *Nucl. Instrum. Meth.*, A506:250–303, 2003.

[129] CMS Single-top Group. Samples for Single-top analysis 2013 (specific to *t*–channel). 2013. `https://twiki.cern.ch/twiki/bin/viewauth/CMS/SingleTopMC`.

[130] CMS Data Quality Monitoring Group. `https://cms-service-dqm.web.cern.ch/cms-service-dqm/CAF/certification`.

[131] Pumplin, J. and Stump, D. R. and Huston, J. and Lai, H. L. and Nadolsky, Pavel M. and others. New Generation of Parton Distributions with Uncertainties from Global QCD Analysis. *JHEP*, 0207:012, 2002.

[132] Adam, Wolfgang and Mangano, Boris and Speer, Thomas and Todorov, Teddy. Track Reconstruction in the CMS tracker. CMS NOTE 2006-041, Dec 2006.

[133] Cervera-Villanueva, A. and do Couto e Silva, E. and Ellis, Malcolm and Ferrere, D. and Gomez-Cadenas, J. J. and others. Kalman Filter Tracking and Vertexing in a Silicon Detector for Neutrino Physics. *Nucl. Instrum. Meth.*, A486:639–662, 2002.

[134] Adam, Wolfgang and Frhwirth, R and Strandlie, Are and Todor, T. Reconstruction of Electrons with the Gaussian-Sum Filter in the CMS Tracker at the LHC. CMS-NOTE-2005-001, Jan 2005.

[135] Piergiulio Lenzi, Chiara Genta, and Boris Mangano. Track Reconstruction of Real Cosmic Muon Events with CMS Tracker Detector. *J. Phys. Conf. Ser.*, 119:032030, 2008.

[136] The CMS Collaboration. Particle-Flow Event Reconstruction in CMS and Performance for Jets, Taus, and MET. CMS-PAS-PFT-09-001, 2009.

[137] The CMS Collaboration. CMS public Software Guide - Description of the Particle Flow Algorithm. `https://twiki.cern.ch/twiki/bin/view/CMSPublic/SWGuideParticleFlow#Description_of_the_Algorithm`.

[138] F. Beaudette. Performance of the Particle Flow Algorithm in CMS. Presentation at ICHEP - 35th International Conference on High Energy Physics, Paris, July 2010. `http://indico.cern.ch/event/73513/session/45/contribution/825/material/slides/0.pdf`.

[139] M. Mulders, I. Bloch, E. James et al. Muon Identification in CMS. CMS Analysis-Note 2008-098, 2008.

[140] Baseline Muon Selections for 2012 Data. `https://twiki.cern.ch/twiki/bin/view/CMSPublic/SWGuideMuonId`.

[141] The CMS Collaboration. CMS Physics, Technical Design Report Detector Performance and Software. Volume-1, 2006. `http://cmsdoc.cern.ch/cms/cpt/tdr/`.

[142] J. Gruschke. Observation of Top-quarks and First Measurement of the $t\bar{t}$ Production Cross-section at a Centre-of-mass Energy of 7 TeV with the CMS Experiment at the LHC. PhD Thesis, 2011.

[143] Gavin P. Salam and Gregory Soyez. A Practical Seedless Infrared-safe Cone Jet Algorithm. *JHEP*, 0705:086, 2007.

[144] S. Catani, Yuri L. Dokshitzer, M. H. Seymour, and B. R. Webber. Longitudinally Invariant k_T Clustering Algorithms for Hadron Hadron Collisions. *Nucl. Phys.*, B406:187–224, 1993.

[145] M. Wobisch and T. Wengler. Hadronization Corrections to Jet Cross-sections in Deep Inelastic Scattering. 1998.

[146] Yuri L. Dokshitzer, G. D. Leder, S. Moretti, and B. R. Webber. Better Jet Clustering Algorithms. *JHEP*, 9708:001, 1997.

[147] Matteo Cacciari, Gavin P. Salam, and Gregory Soyez. The Anti-k_T Jet Clustering Algorithm. *JHEP*, 0804:063, 2008.

[148] Plans for Jet Energy Corrections at CMS. Technical Report CMS-PAS-JME-07-002, CERN, 2008. Geneva, Jul 2008.

[149] CMS Jet Energy Resolution and Corrections Group. Jet Energy Corrections in CMS. `https://twiki.cern.ch/twiki/bin/viewauth/CMS/JetEnergyScale`.

[150] Jet Energy Corrections Determination at 7 TeV. Technical Report CMS-PAS-JME-10-010, CERN, Geneva, 2010.

[151] The CMS Collaboration. 8 TeV Jet Energy Corrections and Uncertainties Based on 19.8 fb^{-1} of Data in CMS. CMS Detector Performance Note CMS-DP-2013-033, 2013.

[152] Cacciari, Matteo and Salam, Gavin P. and Soyez, Gregory. The Catchment Area of Jets. *JHEP*, 0804:005, 2008.

[153] Cacciari, Matteo and Salam, Gavin P. Pileup Subtraction Using Jet Areas. *Phys. Lett.*, B659:119–126, 2008.

[154] Jet Performance in pp Collisions at 7 TeV. Technical Report CMS-PAS-JME-10-003, CERN, Geneva, 2010.

[155] Brian Dorney. http://www.quantumdiaries.org/2011/06/10/to-b-or-not-to-bbar-b-tagging-via-track-counting/.

[156] The CMS Collaboration. Identification of b-quark Jets with the CMS Experiment. *JINST*, 8:P04013, 2013.

[157] The ALEPH Collaboration. A precise measurement of $\Gamma_{Z\to b\bar{b}}/\Gamma_{Z\to \mathrm{hadrons}}$. *Phys. Lett. B*, 313:535–548, 1993.

[158] G. Borisov and C. Mariotti. Fine Tuning of Track Impact Parameter Resolution of the DELPHI Detector. *Nucl. Instrum. Meth.*, A372:181–187, 1996.

[159] CMS b- Tag and Vertexing Physics Object Group. b-jet Identification in CMS. https://twiki.cern.ch/twiki/bin/viewauth/CMS/BtagPOG.

[160] Missing Transverse Energy Analysis. https://twiki.cern.ch/twiki/bin/view/CMSPublic/WorkBookMetAnalysis.

[161] Compact Muon Solenoid Software. https://github.com/cms-sw/cmssw.

[162] M. Feindt. A Neural Bayesian Estimator for Conditional Probability Densities. *ArXiv Physics e-prints*, 2004. http://arxiv.org/abs/physics/0402093.

[163] M. Feindt and U. Kerzel. The neurobayes neural network package. *Nuclear Instruments and Methods in Physics Research Section A: Accelerators, Spectrome- ters, Detectors and Associated Equipment*, 559(1):190–194, April, 2006. http://www.sciencedirect.com/science/article/pii/S0168900205022679.

[164] ROOT: A Data Analysis Framework. http://root.cern.ch/drupal/.

[165] J. Ott Th. Muller and J. Wagner-Kuhr. http://www.theta-framework.org.

[166] Z. Albrecht, T. Allmendinger, G. Barker, M. Feindt, C. Haag, et al. BSAURUS: A Package for Inclusive B Reconstruction in DELPHI. 2001.

[167] Kjell Magne Fauske. Example: Neural network. Dec 2006. http://www.texample.net/tikz/examples/neural-network/.

[168] Chrislb. Diagram of an Artificial Neuron. Wikipedia. 2005.

[169] D. E. Rumelhart, G. E. Hinton, and R. J. Williams. Parallel Distributed Processing: Explorations in the Microstructure of Cognition, Vol. 1. pages 318–362, 1986. http://dl.acm.org/citation.cfm?id=104279.104293.

[170] H. Byrd and J. Nocedal. A Limited Memory Algorithm for Bound Constrained Optimization. *Technical Report*, 1995.

[171] John M. Campbell, J. W. Huston, and W. J. Stirling. Hard Interactions of Quarks and Gluons: A Primer for LHC Physics. *Rept. Prog. Phys.*, 70:89, 2007.

[172] J. P. Chou et al. Anomalous HB/HE Noise at Startup: Characteristics and Rejection Algorithms. *CMS Internal Note*, 2010-006, 2010.

[173] https://twiki.cern.ch/twiki/bin/view/CMS/TriggerTables.

[174] https://twiki.cern.ch/twiki/bin/view/CMS/MuonReferenceEffs.

[175] https://twiki.cern.ch/twiki/bin/view/CMS/EgammaCutBasedIdentification.

[176] Top Jet-MET Analysis. https://twiki.cern.ch/twiki/bin/viewauth/CMS/TopJME.

[177] JEC Recommendations for CMS analyses. https://twiki.cern.ch/twiki/bin/viewauth/CMS/JECAnalysesRecommendations.

[178] Serguei Chatrchyan et al. Determination of Jet Energy Calibration and Transverse Momentum Resolution in CMS. *JINST*, 6:P11002, 2011.

[179] Serguei Chatrchyan et al. Identification of b-quark jets with the CMS experiment. *JINST*, 8:P04013, 2013.

[180] Vardan Khachatryan et al. Measurements of Inclusive W and Z Cross-sections in pp Collisions at $\sqrt{s} = 7$ TeV. *JHEP*, 1101:080, 2011.

[181] Serguei Chatrchyan et al. Measurement of the Lepton Charge Asymmetry in Inclusive W Production in pp Collisions at $\sqrt{s} = 7$ TeV. *JHEP*, 1104:050, 2011.

[182] Nikolaos Kidonakis. Top-quark Production. 2013.

[183] Matteo Cacciari, Michal Czakon, Michelangelo Mangano, Alexander Mitov, and Paolo Nason. Top-pair production at hadron colliders with next-to-next-to-leading logarithmic soft-gluon resummation. *Phys. Lett.*, B710:612–622, 2012.

[184] John M. Campbell and R. K. Ellis. MCFM for the Tevatron and the LHC. *Nucl. Phys. Proc. Suppl.*, 205-206:10–15, 2010.

[185] Hung-Liang Lai, Marco Guzzi, Joey Huston, Zhao Li, Pavel M. Nadolsky, et al. New Parton Distributions for Collider Physics. *Phys. Rev.*, D82:074024, 2010.

[186] Richard D. Ball, Valerio Bertone, Stefano Carrazza, Christopher S. Deans, Luigi Del Debbio, et al. Parton Distributions with LHC Data. *Nucl. Phys.*, B867:244–289, 2013.

[187] CMS Luminosity Based on Pixel Cluster Counting - Summer 2013 Update. Technical Report CMS-PAS-LUM-13-001, CERN, Geneva, 2013.

[188] Lück, J. bservation of Electroweak Single-top-quark Production with the CDF II Experiment. *PhD Thesis, Karlsruhe Institute of Technology,*, IEKP-KA/2009-22, 2009.

[189] S Schmitt. TUnfold, An Algorithm for Correcting Migration Effects in High Energy Physics. *Journal of Instrumentation*, 7(10):T10003, 2012. http://stacks.iop.org/1748-0221/7/i=10/a=T10003.

[190] A. Tikhonov. Solution of Incorrectly Formulated Problems and the Regularization Method. *Soviet Mathematics Doklady*, 4:1035–1038, 1963.

[191] Hocker et al. SVD Approach to Data Unfolding. *Nucl. Instrum. Meth.*, A372:469–481, 1996.

[192] G. D'Agostini. A Multidimensional Unfolding Method Based on Bayes' Theorem. *Nucl. Instrum. Meth.*, A362:487–498, 1995.

[193] Georgios Choudalakis. Fully Bayesian Unfolding. 2012.

[194] G. D'Agostini. Improved Iterative Bayesian Unfolding. Oct 2010. `http://arxiv.org/abs/1010.0632v1`.

[195] V. Blobel. Unfolding - Linear Inverse Problems. *Notes for the Terascale Workshop on Unfolding and Data Correction at DESY*, 2010.

[196] Serguei Chatrchyan et al. Measurement of the Charge Asymmetry in Top-quark Pair Production in proton-proton Collisions at $\sqrt{s} = 7\,\mathrm{TeV}$. *Phys. Lett.*, B709:28–49, 2012.

[197] Serguei Chatrchyan et al. Inclusive and Differential Measurements of the $\mathrm{t\bar{t}}$ Charge Asymmetry in proton-proton Collisions at $\sqrt{s} = 7\,\mathrm{TeV}$. *Phys. Lett.*, B717:129–150, 2012.

[198] Steve Baker and Robert D. Cousins. Clarification of the Use of chi-square and Likelihood Functions in Fits to Histograms. *Nuclear Instruments and Methods in Physics Research*, 221(2):437 – 442, 1984.

[199] `https://twiki.cern.ch/twiki/bin/view/CMS/JetResolution#JER_Uncertainty`.

[200] `https://twiki.cern.ch/twiki/bin/viewauth/CMS/PileupSystematicErrors`.

[201] `https://twiki.cern.ch/twiki/bin/viewauth/CMS/BtagPOG#2012_Data_and_MC_EPS13_prescript`.

[202] John M. Campbell, Rikkert Frederix, Fabio Maltoni, and Francesco Tramontano. NLO Predictions for t-channel Production of Single-top and Fourth Generation Quarks at Hadron Colliders. *JHEP*, 0910:042, 2009.

[203] Nikolaos Kidonakis. Next-to-Next-to-Leading-Order Collinear and Soft Gluon Corrections for t-channel Single-top-quark Production. *Phys. Rev.*, D83:091503, 2011.

[204] Chatrchyan et al. Measurement of the Single-top-quark t-channel Cross-section in pp Collisions at $\sqrt{s} = 7\,\mathrm{TeV}$. *JHEP*, 1212:035, 2012.

[205] Aaltonen et al. Observation of Single-top-quark Production and Measurement of $|V_{\mathrm{tb}}|$ with CDF. *Phys. Rev.*, D82:112005, 2010.

[206] Victor Mukhamedovich Abazov et al. Evidence for s-channel Single-top-quark Production in pp Collisions at $\sqrt{s} = 1.96\,\mathrm{TeV}$. *Phys. Lett.*, B726:656–664, 2013.

[207] Timo Antero Aaltonen et al. Observation of s-channel Production of Single-top-quarks at the Tevatron. *Phys. Rev. Lett.*, 112:231803, 2014.

[208] T. Aaltonen et al. Combination of the Top-quark Mass Measurements from the Tevatron Collider. *Phys. Rev.*, D86:092003, 2012.

[209] Mathew Muether. Combination of CDF and DØ results on the mass of the Top-quark using up to $8.7\,\mathrm{fb}^{-1}$ at the Tevatron. 2013.

[210] A. D. Martin, W. J. Stirling, R. S. Thorne, and G. Watt. Parton distributions for the LHC. *Eur. Phys. J.*, C63:189–285, 2009.

[211] F. D. Aaron et al. Combined Measurement and QCD Analysis of the Inclusive $\mathrm{e}^{\pm}\mathrm{p}$ Scattering Cross-sections at HERA. *JHEP*, 1001:109, 2010.

[212] S. Alekhin, J. Blumlein, and S. Moch. Parton Distribution Functions and Benchmark Cross-sections at NNLO. *Phys. Rev.*, D86:054009, 2012.

[213] Hung-Liang Lai, Marco Guzzi, Joey Huston, Zhao Li, Pavel M. Nadolsky, et al. New Parton Distributions for Collider Physics. *Phys. Rev.*, D82:074024, 2010.

[214] Thomas G. Rizzo. Single-top-quark Production as a Probe for Anomalous Moments at Hadron Colliders. *Phys. Rev.*, D53:6218–6225, 1996.

[215] Johan Alwall, R. Frederix, J. M. Gerard, A. Giammanco, M. Herquet, et al. Is $|V_{\mathrm{tb}}| \simeq 1$? *Eur. Phys. J.*, C49:791–801, 2007.

[216] Louis Lyons, Duncan Gibaut, and Peter Clifford. How to Combine Correlated Estimates of a Single Physical Quantity. *Nucl. Instrum. Meth.*, A270:110, 1988.

[217] A. Pukhov, E. Boos, M. Dubinin, V. Edneral, V. Ilyin, et al. CompHEP: A Package for Evaluation of Feynman Diagrams and Integration Over Multiparticle Phase Space. 1999.